Photoswitchable Dyes for Super-Resolution Microscopy

Yaoyao Xiong

Keble College, University of Oxford

A thesis submitted for the degree of Doctor of Philosophy

Michaelmas Term 2018

Photoswitchable Dyes for Super-Resolution Microscopy

Yaoyao Xiong, Keble College, University of Oxford

Abstract of thesis submitted for the degree of Doctor of Philosophy, September 2018

This thesis describes the synthesis and characterisation of photoswitchable synthetic dyes for application in super-resolution microscopy of biological systems.

Chapter 1 introduces the field of super-resolution microscopy. A variety of techniques are described, with a particular focus on the reversible saturable optical fluorescence transitions (RESOLFT) approach. For RESOLFT application, a dyad molecular design is proposed, which comprises a reversible photoswitch and an emissive dye. Major classes of these components are presented, followed by a discussion of the criteria required for RESOLFT dyes.

Chapter 2 reports preparation of spiropyran photoswitches and a derived dyad. Properties of the switches are characterised, including photoconversion and resistance to photodegradation. The dyad system is also examined by live cell confocal imaging.

Chapter 3 focuses on switches from the spirooxazine family that is closely related to the spiropyran family. Synthesis and crystal structure are described, and detailed examination of the photoswitching behaviour by spectroscopic measurements is then presented. Subsequent switching kinetic investigations using ultrafast spectroscopies are reported.

Chapter 4 continues to describe a series of spirooxazine-based dyads. Their switching behaviour is assessed in live cells, and the applicability in RESOLFT microscopy is also tested. The photophysical properties of these dyads are comprehensively characterised and compared, providing insights into the molecular design for future work.

Chapter 5 explores the possibility of selectively labelling biomolecules of interest by incorporating bioconjugation techniques into the dyad design. Several synthetic approaches led to a series of compounds, and comparison of their cell images suggests key factors for further considerations.

Chapter 6 demonstrates the RESOLFT potential of the dyad in liposomes. The switching behaviour is investigated in different types of liposomes, and detailed imaging analyses are reported, highlighting the varying performance of the dyad in different systems.

Chapter 7 summarises the conclusions described in this work.

Acknowledgements

First and foremost, I would like to thank my supervisor, Prof. Harry L. Anderson for always being supportive, encouraging and understanding regardless positive or negative research outcomes. Thanks to the HLA group members who have worked on this project: Dr Andreas Vargas Jentzsch, Prof. Pablo Rivera-Fuentes, Dr Andrew Frawley, Dr Virginia Wycisk, Johannes Osterrieth, and Xinyu Qiu. Great support from other HLA group members is much appreciated: Dr Bart Limburg (Bartie), Dr Michel Rickhaus (Mike), Dr Renee Haver, Dr Przemyslaw Gawel (Przemek), Dr Steffen Woltering, Dr James Thomas, Dr Keith Andrews, Dr Huawei Jiang, Dr Jonathan Cremers, Dr Daniel Kohn, Dr Anjul Khadria, Dr Martin Peeks, Dr Ibrahim Bulut, Dr Nuntaporn Kamonsutthipaijit (Nun), Dr Cécile Roche, Dr Anne Jeppesen, Dr Jennifer Le Roy, Dr René Oetterli, William Kendrick, Michael Jirasek, Sabine Weidlich, Isabell Gruebner, Lorel Scriven, Pernille Bols, Wenjun Xu, Hiromu Kubo, Jamie Duburg, Takayuki Kobatake, Yutaka Hisamune, Josh Sauer. A big thank you goes to Andrew (particularly), Virginia, and Bartie for taking time to proofread this thesis and for their enormous encouragement.

Productive collaboration with the group of Prof. Christian Eggeling is much appreciated; thanks particularly go to Dr Silvia Galiani, Dr Erdinc Sezgin, Dr Katharina Reglinski, Dr Dilip Shrestha, and Falk Schneider. I must also take the opportunity to thank Prof. Anthony Parker and Dr Igor Sazanovich for collaboration on the ultrafast time-resolved spectroscopies.

I must also take the opportunity to thank Prof. Paul Beer and the group for the support and care during my rotation project: Dr Matthew Langton, Dr Asha Brown, Dr Lim Yuan Chong (Jason), Dr Timothy Barendt, Dr Lydia Gilday, Dr Sean Robinson, Dr Will Arter, Hena Bagha, Thanthapatra Bunchuay (Valentine), Thomas Mole, Stuart Cornes, Sam Sutton, Alexander Hess, Anna Spearing-Ewyn, Daniel Lucy, Ewan MacAuley.

I must also give credit to Dr Amber Thompson, Prof. Richard Cooper and Dr Kirsten Christensen for training me on small-molecule X-ray crystallography. I would also thank Prof. Tim Claridge for helping with analysis of NMR data. Support by the EPSRC Centre for Doctoral Training in Synthesis for Biology and Medicine (EP/L015838/1) is acknowledged. I gratefully acknowledge the University of Oxford Clarendon Fund

Scholarship, without which I would have not been able to study for my DPhil degree and spend four most amazing years at Oxford.

I would like to say a big thank you to Prof. Anthony Hill who has provided enormous support for over 7 years even when I was not in his group anymore. Acknowledgements also go to the Hill group members: Dr Jas Ward, Dr Torsten Schwich, Dr Manab Sharma, Dr Annie Colebatch, Dr Caitlin McQueen, Ritchie Manzano, Cathy Ma, Yong-shen Han, Lily Dixon, Joseph Wang.

I also want to thank my caring, supportive and lovely housemates for three memorable years together, Tom Fleming (Tommie), Sam Ellis (Sammie), Dimitri Caputo (Dimi), and Steve Mansfield (Ste). A big thank you also goes to other loving friends, Khushboo Borah, Alice Schwarze, Ruchuta Ardkhean (Nod), Fei Song, Susan Leung, Hana Mazuri. Last but not least, I want to say thank you to my loving, supportive and wise parents who are always there for me.

Yaoyao Xiong

Oxford, September 2018

List of publications

'Polyyne formation via skeletal rearrangement induced by atomic manipulation'
N. Pavliček, P. Gawel, D. R. Kohn, Z. Majzik, Y. Xiong, G. Meyer, H. L. Anderson, L. Gross, *Nat. Chem.* **2018**, *10*, 853–858.

'Synthesis of polyynes using dicobalt masking groups'
D. R. Kohn, P. Gawel, Y. Xiong, K. E. Christensen, H. L. Anderson, *J. Org. Chem.* **2018**, *83*, 2077–2086.

'Spironaphthoxazine switchable dyes for biological imaging'
Y. Xiong, A. Vargas Jentzsch, J. W. M. Osterrieth, E. Sezgin, I. V. Sazanovich, K. Reglinski, S. Galiani, A. W. Parker, C. Eggeling, H. L. Anderson, *Chem. Sci.* **2018**, *9*, 3029–3040.

'Detecting mechanochemical atropisomerization within an STM break junction'
E. Leary, C. Roche, H.-W. Jiang, I. Grace, M. T. González, G. Rubio-Bollinger, C. Romero-Muñiz, Y. Xiong, Q. Al-Galiby, M. Noori, M. A. Lebedeva, K. Porfyrakis, N. Agrait, A. Hodgson, S. J. Higgins, C. J. Lambert, H. L. Anderson, R. J. Nichols, *J. Am. Chem. Soc.* **2018**, *140*, 710–718.

'Unexpected interactions between alkyl straps and pyridine ligands in sulfur-strapped porphyrin nanorings'
C. Roche, Q. Luo, G. Gil-Ramírez, H.-W. Jiang, D. R. Kohn, Y. Xiong, A. L. Thompson, H. L. Anderson, *J. Org. Chem.* **2017**, *82*, 7446–7462.

'Photoswitchable spiropyran dyads for biological imaging'
Y. Xiong, P. Rivera-Fuentes, E. Sezgin, A. Vargas Jentzsch, C. Eggeling, H. L. Anderson, *Org. Lett.* **2016**, *18*, 3666–3669.

'Cascade polycyclizations in natural product synthesis'
R. Ardkhean, D. F. J. Caputo, S. M. Morrow, H. Shi, Y. Xiong, E. A. Anderson, *Chem. Soc. Rev.* **2016**, *45*, 1557–1569.

'Active-metal template synthesis of a halogen-bonding rotaxane for anion recognition'
M. J. Langton, Y. Xiong, P. D. Beer, *Chem. – Eur. J.* **2015**, *21*, 18910–18914.

Oral presentations

Discussion leader for the session 'Biological applications and inspiration'
Gordon Research Seminar: Artificial Molecular Switches and Motors, Holderness, US, June 2017.

'Photoswitchable synthetic dyes for super-resolution microscopy'
Synthesis for Biology and Medicine CDT roadshow, GSK Stevenage, June 2017.

'Spirooxazine-based switchable dyes for biological imaging'
Synthesis for Biology and Medicine CDT Science Day, Inorganic Chemistry Laboratory, Oxford, September 2017.

'Photoswitchable synthetic dyes for super-resolution microscopy'
Synthesis for Biology and Medicine CDT roadshow, UCB, Chemistry Research Laboratory, Oxford, January 2018.

'Switchable synthetic dyes for super-resolution microscopy'
AstraZeneca final year graduate symposium, Chemistry Research Laboratory, Oxford, October 2018.

Poster presentations

'Photoswitchable synthetic dyes for biological imaging'
Gordon Research Conference: Artificial Molecular Switches and Motors, Holderness, US, June 2017.

'A reversibly photoswitchable dye for biological imaging'
International Conference on Nanoscopy, Basel, Switzerland, June 2016.

List of abbreviations

°C	Celsius degrees
Å	Angstrom, 10^{-10} m
abs.	absorbance
aq.	aqueous
Bn	benzyl
Boc	*tert*-butoxycarbonyl
br.	broad
BSA	bovine serum albumin
Bu	butyl
Cbz	benzyloxycarbonyl
CCD	charge-coupled device
CHO	Chinese hamster ovary (cells)
COS-7	fibroblast cell line from monkey kidney tissues
CuAAC	copper(I)-catalysed azide-alkyne cycloaddition
CW	continuous wave
δ	chemical shift
d	spatial resolution; deuterated
d	doublet
Δ	difference
DCM	dichloromethane
dd	doublet of doublets
DFT	density functional theory
DIPEA	*N*,*N*-diisopropylethylamine
DMAP	4-dimethylaminopyridine
DMEM	Dulbecco's modified Eagle medium
DMF	dimethylformamide
DMSO	dimethyl sulfoxide
ε	molar absorption coefficient
EDC	*N*-(3-dimethylaminopropyl)-*N'*-ethylcarbodiimide
EI	electron ionisation
ESI	electrospray ionisation
Et	ethyl
ex.	excitation
Φ	quantum yield
f	femto, 10^{-15}
FCS	fetal calf serum
fl.	fluorescence
Fmoc	9-fluorenylmethoxycarbonyl

FOV	field of view
FRET	Förster resonance energy transfer
FWHM	full width at half maximum
G	giga, 10^9
GM5756	human skin fibroblast cell line
GUV	giant unilamellar vesicle
h	hours
HBTU	*N*,*N*,*N′*,*N′*-tetramethyl-*O*-(1*H*-benzotriazol-1-yl)uronium hexafluorophosphate
HDLEC	human dermal lymphatic endothelial cells
HEK 293	human embryonic kidney 293 (cell line)
HeNe	helium-neon (laser)
HPLC	high performance liquid chromatography
HR	high resolution
Hz	Hertz
I	intensity
J	coupling constant; spectral overlap integral
K	Kelvin
k	kinetic rate constant
k	kilo, 10^3
LED	light emitting diode
LR	low resolution
LSM	laser scanning microscopy
LUV	large unilamellar vesicle
M	moles per litre
m	milli, 10^{-3}
m/z	mass/charge ratio
MALDI	matrix assisted laser desorption/ionisation
MC	merocyanine
Me	methyl
min	minute
MLV	multilamellar vesicle
MM	molecular mechanics
mol	mole
MS	mass spectrometry
n	nano, 10^{-9}
NA	numerical aperture
NHS	*N*-hydroxysuccinimide
NMR	nuclear magnetic resonance
NSOM	near-field scanning optical microscopy
p	pico, 10^{-12}

PALM	photoactivated localisation microscopy
PBS	phosphate buffered saline
PET	photoinduced electron transfer
Ph	phenyl
pH	$-\log_{10}[H^+]$
PLL	polylysine
POI	protein of interest
POPC	1-palmitoyl-2-oleoyl-sn-glycero-3-phosphocholine
ppm	parts per million
Pr	propyl
PSF	point spread function
PSS	photostationary state
q	quartet
R_0	Förster radius
R^2	coefficient of determination
RESOLFT	reversible saturable optical fluorescence transitions
R_f	retention factor
RP	reversed phase
s	singlet
SIM	structured illumination microscopy
SMLM	single molecule localisation microscopy
SO	spirooxazine
SP	spiropyran
STED	stimulated emission depletion
STFC	Science and Technology Facilities Council
STORM	stochastic optical reconstruction microscopy
SUV	small unilamellar vesicle
τ	lifetime
t	triplet
$t_{1/2}$	half lifetime
TA	transient absorption
TD-DFT	time dependent-density functional theory
TFA	trifluoroacetic acid
THF	tetrahydrofuran
TLC	thin layer chromatography
ToF	time-of-flight
TRIR	time-resolved infrared
UV-vis	ultraviolet-visible
WIMM	Weatherall Institute of Molecular Medicine
λ	wavelength
µ	micro, 10^{-6}

Table of contents

Chapter 1

Introduction

1 Introduction

Microscopy is an indispensable tool in life science, as it enables direct observation of cellular organisation and interactions that are otherwise too small to observe with the human eye. Compared to other branches, such as electron and scanning probe microscopies, optical microscopy is more commonly used in biomedical research due to its minimal invasiveness and thus, compatibility with living specimens. To allow in-depth imaging of relatively thick living specimens, optical microscopy is generally performed in the far-field. In this experimental setup, the light is gathered and focused by lenses, which are positioned sub- or millimetres away from the specimen. In contrast, the less common near-field optical microscopy places the sample at a distance of less than a single wavelength, which limits its application to imaging of flat surfaces (see later). When far-field optical microscopy is coupled with fluorescent markers, such techniques possess unrivalled benefits, i.e. sensitive and specific detection of biomolecules of interest in a non-invasive way.

Far-field fluorescence microscopes are set up in either the widefield or confocal mode. In the widefield mode, the entire specimen is illuminated, and photons are collected by a camera, e.g. CCD camera (**Figure 1-1**a).[1] The alternative confocal mode uses a pinhole (small aperture) to excite a small defined volume of the specimen, emission photons are collected by a point detector, e.g. photomultiplier, and the final image is obtained by raster scanning across the sample (**Figure 1-1**b).[1] The pinhole on confocal microscopes eliminates out-of-focus light, and hence offers improved image contrast compared to the widefield mode. Both widefield and confocal microscopes employ objective lenses to focus the excitation and emission light. Because of the lens system, far-field optical microscopy suffers from limited spatial resolution; that is, the resolving power of distinguishing two objects in close proximity is not limitless. This is known as Abbe's diffraction limit,[2] and arises from a fundamental barrier that as light propagates away from a point source in both excitation and fluorescence detection pathways, diffraction is inevitable and the outcome is an ellipsoid pattern, i.e. a point spread function (PSF) of a finite size rather than an infinitely small spot (**Figure 1-1**). In other words, even on a perfect far-field fluorescence microscope, when two objects simultaneously emit within the volume of the PSF, they cannot be discerned, and instead a blurred image is formed. The achievable spatial resolution is expressed as the lateral (*x*,*y*) (**1.1**) and axial (*z*) dimensions (**1.2**) of the PSF,[3]

$$d_{x,y} = \frac{\lambda}{2n\sin\alpha} = \frac{\lambda}{2\mathrm{NA}} \quad \textbf{(1.1)} \qquad d_z = \frac{2\lambda}{(n\sin\alpha)^2} = \frac{2\lambda}{\mathrm{NA}^2} \quad \textbf{(1.2)}$$

where λ is the wavelength of the excitation light, n is the refractive index of the medium, α is half of the maximum angle that light can enter the objective lens. The combined term $n\sin\alpha$, known as the objective numerical aperture (NA), is generally less than 1.5 ($\alpha <$ 70°) for commercial instruments. In practice, using visible light of the shortest wavelength (~400 nm), the achievable resolution is 200 nm ($\lambda/2$) and 500 nm in the lateral and axial directions, respectively.[3] This limited spatial resolution of conventional optical microscopy hampers direct visualisation of many important features in live cells, such as cell membranes, synaptic vesicles and dynamic molecular interactions.[4]

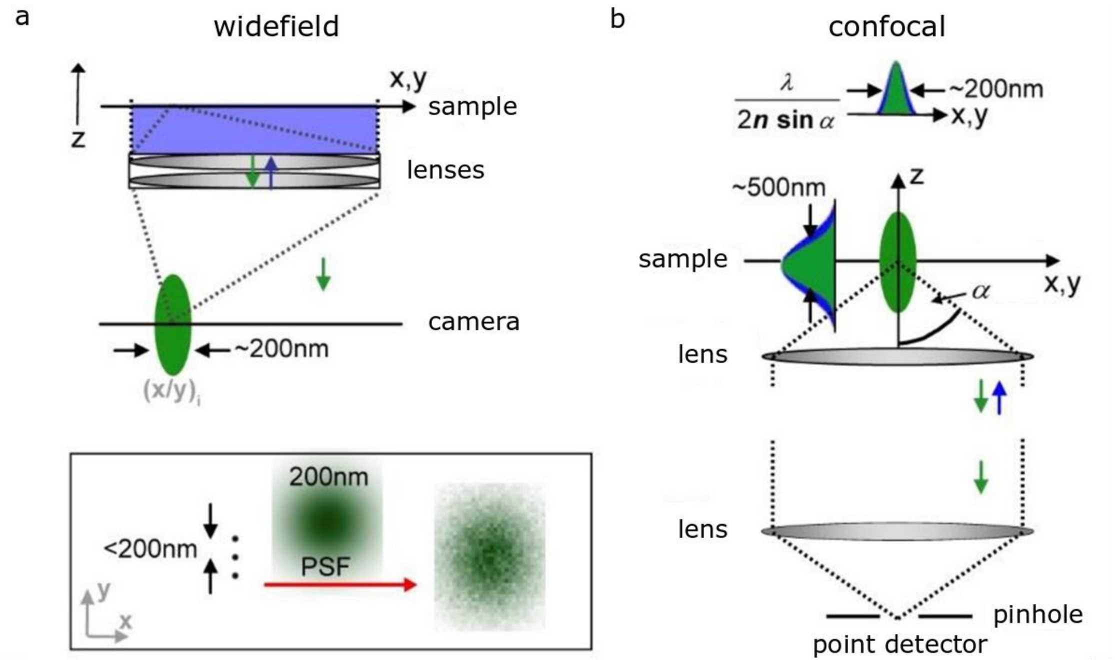

Figure 1-1 Schematic representations of far-field fluorescence microscopes in the widefield and confocal modes. Both employ lenses and are limited in spatial resolution due to the diffraction of light. a) Widefield fluorescence microscope setup. The entire sample is illuminated, and fluorescence photons are collected by a camera. b) Confocal fluorescence microscope setup. Only a small volume of the sample is illuminated by excitation light through a pinhole, and emission photons are collected by a point detector, e.g. photomultiplier. The final image is built by raster scanning the entire sample. The figure is adapted from *Q. Rev. Biophys*, **2015**, *48*, 178-243, and used with permission from Cambridge University Press.

For over a century, it was believed that the diffraction limit could not be overcome, until a major breakthrough was first made in the 1990's.[5,6] Since then, a number of super-resolution microscopy (SRM or nanoscopy) techniques have been developed, making it possible to observe cellular constituents and dynamics with unprecedented spatial resolution. The 2014 Nobel Prize in Chemistry was jointly awarded to William Moerner, Eric Betzig and Stefan Hell for their pioneering work in the 'development of super-resolved fluorescence microscopy'. All existing SRM techniques bypass Abbe's diffraction limit by exploiting photophysical and photochemical properties of fluorescent markers (fluorophores) rather than fighting against the diffraction law. In the following sections, I will first introduce fundamental photophysical concepts using a Jablonski energy diagram, followed by description of different SRM techniques along with their principles, advantages and disadvantages. The discussion will then be focused on reversible saturable optical fluorescence transitions (RESOLFT) microscopy, for which a number of molecular approaches will be presented. Lastly, our molecular design, along with criteria for our system to be applied in RESOLFT microscopy, will be detailed.

1.1 Jablonski diagram

A Jablonski energy diagram (**Figure 1-2**) represents molecular processes that occur after absorption of a photon by a molecule.[7,8] The singlet electronic states S_0, S_1 and S_2 stand for the ground state, first and second excited states respectively, and T_1 is the first triplet state. Within each electronic state, there are multiple vibrational states notated as 0, 1, etc. Absorption of a photon promotes the molecule from the ground state to an excited singlet state, and this occurs on the femtosecond (10^{-15} s) timescale. The vertical line reflects the instantaneous nature of light absorption, during which the positions of nuclei do not change given the short time, as described in the Franck-Condon principle. According to Kasha's rule,[9] following absorption, molecules first rapidly relax to the lowest vibrational state in S_1 by internal conversion and vibrational relaxation that occur on a picosecond (10^{-12} s) timescale. From there, several processes can take place to depopulate the excited state. Decay from the ground state in S_1 to S_0 can occur radiatively, i.e. fluorescence emission, with lifetime in the nanosecond (10^{-9}) range. An alternative pathway is stimulated emission, where an incoming photon of a matched frequency interacts with the excited state electron to cause the emission of two photons of the same frequency. Because of the energy loss during internal conversion and vibrational relaxation, the wavelength of emitted photons from fluorescence and stimulated emission is longer (red-shifted) than the absorption wavelength. The difference between the absorption and emission wavelengths is known as the Stokes shift. Nonradiative decays from S_1 to S_0 can also occur (10^{-9}–10^{-5} s). Alternatively, S_1 can undergo intersystem crossing, i.e. nonradiative transitions from the singlet state to the triplet state T_1. This process is formally forbidden due to spin inversion, and it occurs on a timescale 10^{-11}–10^{-6} s. Similarly, transitions from T_1 to S_0 are relatively slow (10^{-3}–10^{2} s), and happen either nonradiatively or radiatively, with the latter termed phosphorescence.

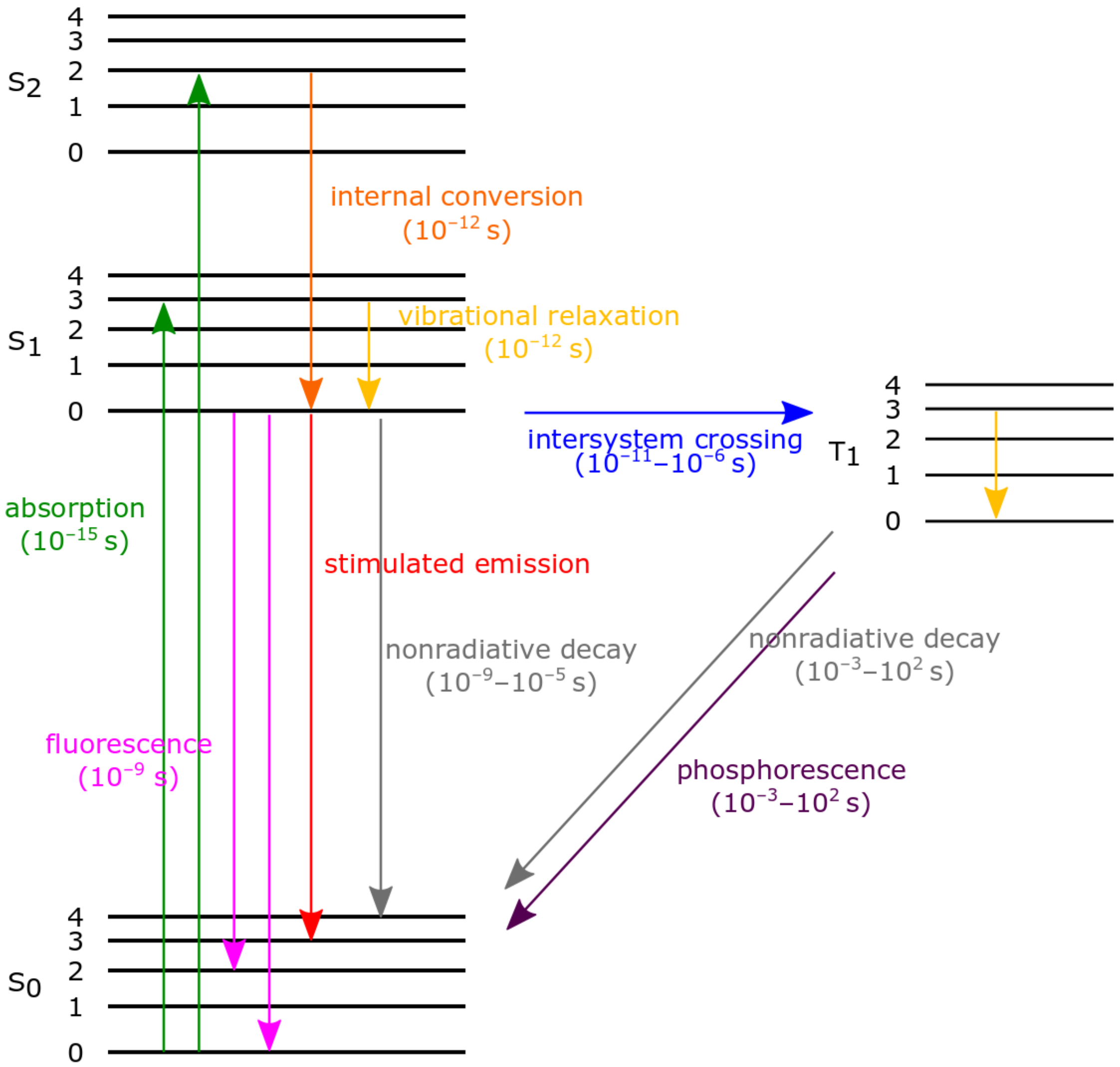

Figure 1-2 Jablonski energy diagram. Adapted from references.[7,8]

Alternative pathways to depopulate the S$_1$ state are nonradiative transitions, including Förster resonance energy transfer (FRET) and photoinduced electron transfer (PET). In FRET, energy of an excited donor fluorophore is transferred to an acceptor in its ground state *via* a transition dipole-transition dipole interaction, and the acceptor can be fluorescent or non-fluorescent. FRET can occur when there is a sufficient spectral overlap between the emission of the donor and the absorption of the acceptor, and the separation distance of the donor and acceptor is within a characteristic distance, i.e. Förster radius. On the other hand, PET processes depend on redox potentials as well as separation distances of the species involved. The difference between FRET and PET can be illustrated by molecular orbital schemes as shown in **Figure 1-3**. In an oversimplified picture, absorption of light by the donor raises one electron from the highest-occupied molecular orbital (HOMO) to the lowest-unoccupied molecular orbital (LUMO). During

FRET, the excited electron in the donor returns to the ground state, and the energy released results in the excitation of one electron in the acceptor from HOMO to LUMO (**Figure 1-3**a). On the other hand, when PET occurs, one electron of a donor is transferred to an acceptor, and a charge separated complex is generated (**Figure 1-3**b). In PET, an excited fluorophore can be either the electron donor or acceptor, whereas in FRET, a fluorophore is always the energy donor.

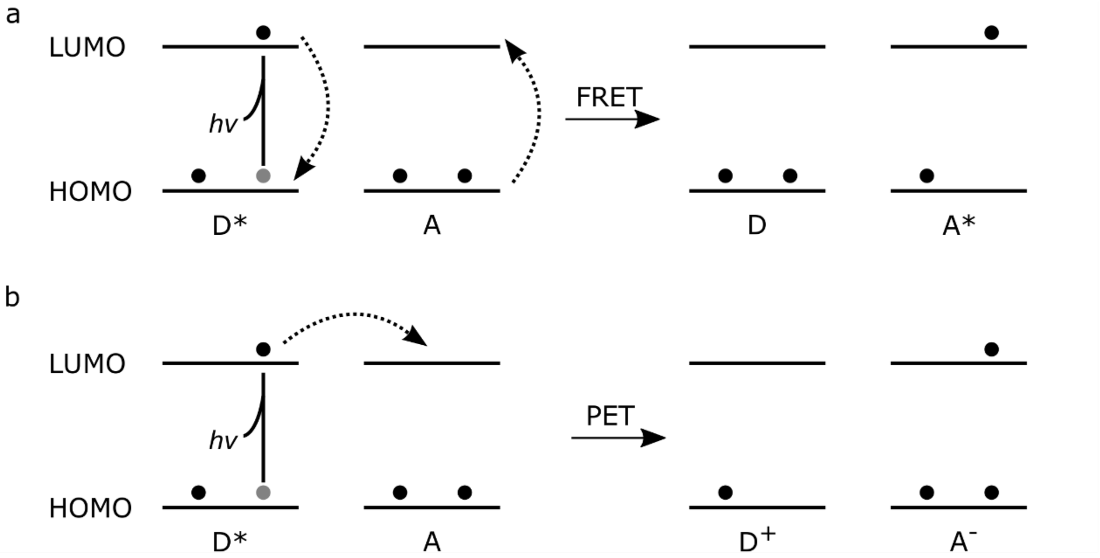

Figure 1-3 Schemes of molecular orbitals for the processes of a) Förster resonance energy transfer (FRET) and b) photoinduced electron transfer (PET). Vertical solid lines: absorption of a photon; dotted lines: electron transitions that occur during FRET and PET processes respectively. LUMO = lowest-unoccupied molecular orbital, HOMO = highest-occupied molecular orbital. Adapted from reference.[8]

In this project, absorption and fluorescence, along with other related and competing transitions, are crucial processes to be taken into consideration in our molecular design. For relatively diluted solutions, the absorption behaviour follows the Beer-Lambert Law, $A = -\log_{10} T = -\log_{10} (I/I_0)$, where A is the absorbance of a sample at a specific wavelength, T is transmittance, I and I_0 are the light intensities after and before passing through a sample. Another expression is $A = \varepsilon c d$, where c is the concentration (M), d is the path length of the light (cm), and ε is the molar absorption coefficient ($\mathrm{M}^{-1}\ \mathrm{cm}^{-1}$). The molar absorption coefficient is an intrinsic property of a molecule. Regarding fluorescence, arguably the two most important properties are quantum yield, Φ_f, and lifetime, τ (**Figure 1-4**).[8] Quantum yield in general is defined as the number of a particular event that occurs per photon absorbed by the system.[10] Fluorescence quantum yield is the ratio of photons emitted to photons absorbed, and is calculated as $\Phi_f = k_R/(k_{NR} + k_R)$, where k_R is the emissive rate constant and k_{NR} is the term for the collective nonradiative processes. That is, the quantum yield approaches 1 when fluorescence emission is much faster than the combined nonradiative decays. Fluorescence lifetime, τ, is defined as the average time that a molecule spends in the electronic excited state; mathematically, $\tau = 1/(k_{NR} + k_R)$.[10] If fluorescence emission follows a single exponential decay, i.e. $I(\mathrm{t}) = I_0 e^{-t/\tau}$, $(1-1/e)$%, i.e. 63%, of the population emits before time τ, and 37% after time τ. Many organic fluorophores have fluorescence lifetimes in the nanosecond range.

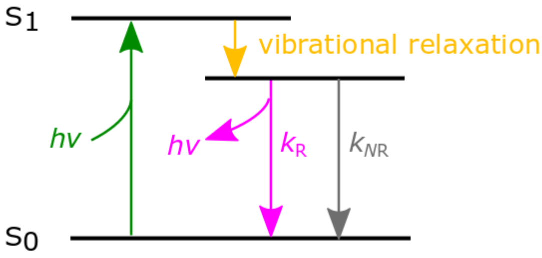

Figure 1-4 Simplified Jablonski diagram to explain fluorescence quantum yield (Φ_f) and lifetime (τ). $\Phi_f = k_R/(k_{NR} + k_R)$; $\tau = 1/(k_{NR} + k_R)$. Adapted from reference.[8]

Many of the above concepts will be revisited throughout this report. With this basic understanding of molecular transitions, I will continue to describe a variety of SRM techniques in which different photophysical and photochemical processes are exploited.

1.2 Super-resolution near-field optical microscopy

As described earlier, the diffraction limit arises from the fact that light diffracts when travelling between the objective lens and the sample. Near-field scanning optical microscopy (NSOM) removes the need for lenses. Instead, a small aperture is used to confine the illumination light, and its size is much smaller than the wavelength of the light, usually a few nanometres.[11–13] As illustrated in **Figure 1-5**, illumination light from the back of an opaque screen is confined to the dimension of the small aperture, and in close proximity (i.e. less than a wavelength) to the sample surface, non-propagating waves are detected to form the image, which imparts the sub-diffraction resolving power of NSOM.[14] Essentially, the resolution no longer depends on the wavelength, but mainly the size of the aperture,[15,16] and spatial resolutions below 20 nm have been reported.[17,18] Considerable research efforts have been devoted to application of NSOM in the biological sciences,[19–27] but a few of its intrinsic limitations prevent the extensive use in more advanced studies, e.g. dynamic processes in live cells. Firstly, the light substantially diffracts with the slightly increasing distance from the screen, impairing the sub-diffraction resolving power.[28] As a consequence, NSOM is limited to membrane/surface studies in fixed cells[21–23,25,27] or thinly sectioned tissues;[26] very few live-cell studies can be found, and these lack dynamic information.[29] Additionally, despite its theoretical simplicity, it is technically challenging to implement the setup, hindering its routine use in the biological laboratory. In conclusion, while NSOM provides a powerful imaging tool with diffraction-unlimited resolution capacity, its widespread application in complex biological samples is yet to be realised.

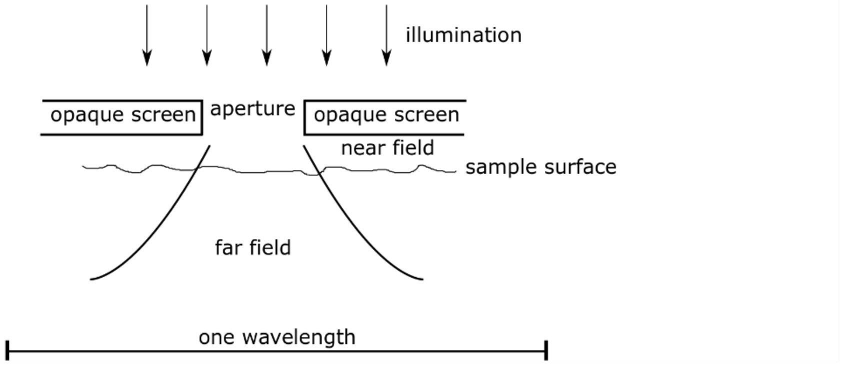

Figure 1-5 Schematic representation of NSOM, modified from the reference.[28] The sub-wavelength sized aperture determines the resolving power of NSOM, rather than the wavelength of the illumination light.

1.3 Super-resolution far-field optical microscopy

In contrast to NSOM, far-field super-resolution microscopy has provided completely different approaches to bypassing Abbe’s diffraction limit, and mainly due to its compatibility with live specimens, it has attracted more interest in life science. The techniques fall into three categories: structured illumination microscopy (SIM), single molecule localisation microscopy (SMLM), and reversible saturable optical fluorescence transitions (RESOLFT) microscopy. Each of these techniques will be briefly discussed below. For comprehensive reviews of super-resolution approaches and their biological applications, many recent reviews are available elsewhere.[1,30–35]

1.3.1 Structured illumination microscopy (SIM)

Based on widefield microscopy, super-resolution structured illumination microscopy (SR-SIM) extends the spatial resolution by exploiting the moiré effect. The sample, which contains an unknown distribution pattern of fluorescent dyes, is overlaid with a known spatial structure of excitation illumination. As a result, moiré fringes are generated, the frequency of which is lower than the original patterns (**Figure 1-6**a).[36] The fact that such moiré fringes are more observable to optical microscopes means retrieval of higher resolution information that was previously inaccessible. This effect is easier to understand when the structure is considered in the frequency space or reciprocal space, i.e. its Fourier transform. In the frequency space, the observable region of a finite size is equivalent to the diffraction limit in the real space, and this circle with the radius $k_0 = 1/d = 2\mathrm{NA}/\lambda$ dictates structural details that are retained on a far-field optical microscope (**Figure 1-6**b). While low resolution information is near the centre of the region, high resolution information is further away and anything outside the circle is unobservable.[36] SR-SIM uses a known illumination pattern to relocate high resolution information from outside to inside of the observable region by forming moiré fringes. Take a simple sinusoidal pattern as an example, 3 spots exist in the frequency space, and their relative orientation is determined by the stripe direction of the pattern, with distance k_1 inversely proportional to the line spacing in the real space (**Figure 1-6**c).[36] The superimposition of the pattern and sample forms moiré fringes, and essentially, an additional observable region of a circle is available, with the offset from the centre by k_1 and the radius k_1 (**Figure 1-6**d). By rotating the pattern in different directions, spatial resolution can be improved by a factor up to 2 due to the fact that the illumination pattern is limited by light diffraction in the same way as the sample and thus, $k_1 \leq k_0$ (**Figure 1-6**e).

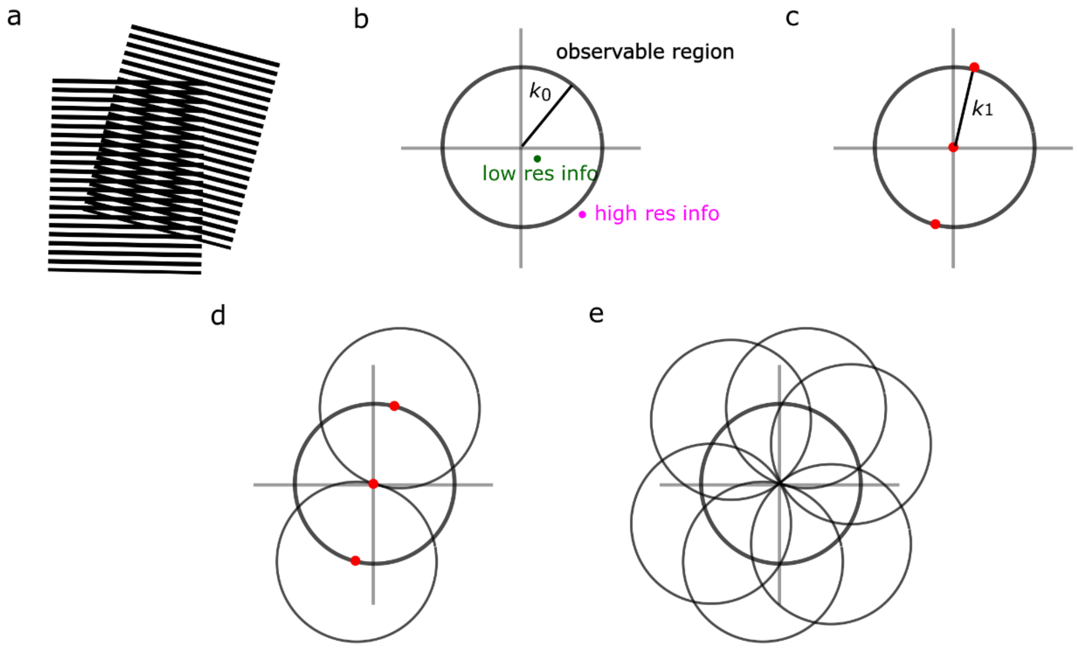

Figure 1-6 The principle of linear super-resolution structured illumination microscopy. a) Superimposition of two structures gives moiré fringes. b) The observable region in the reciprocal space is equivalent to the diffraction limit in the real space on a conventional optical microscope. The circular observable region has a radius $k_0 = 1/d = 2\mathrm{NA}/\lambda$. Low resolution information residues close to the centre, whereas high resolution information is further away and anything outside the circle cannot be detected. c) Presence of 3 spots in the reciprocal space arising from a simple sinusoidal pattern. The locations of the two offset spots define the observable region in the same way as in b). d) When the sample is illuminated with excitation intensities of the pattern in c), the generated moiré fringes contain additional high-resolution information that has been relocated into the observable region. e) By repeating step in d) with different stripe directions, the observable region can be doubled, representing a two-fold improvement in the spatial resolution.

The two-fold improvement can be extended to theoretical infinity by using photoswitchable dyes in non-linear SIM. In non-linear SIM, the excited states of dye molecules are saturated when the illumination intensity is above the threshold that the molecules cannot respond linearly, i.e. one molecule can only absorb one photon within its fluorescence lifetime. In the simplest term, the non-linearity effectively introduces more frequency dots at distances of multiple k_1 in the frequency space, and thus, more high-resolution information is shifted into the observable region (**Figure 1-7**).[37] For both linear and non-linear SIM techniques, the final image is mathematically reconstructed by reallocating the data to original coordinates after removing the known illumination structure. SR-SIM generally requires lower illumination intensities relative to other super-resolution techniques, and acquisition speed is faster, making it an extremely powerful tool to monitor dynamics in three dimensions of living cells for an extended period of time.[38–41] Nevertheless, significant challenges/disadvantages of this method are the complex and time-consuming data processing, and that image quality is very susceptible to artefacts introduced by sample preparation, labelling, microscope, and quantitative data analysis.[33]

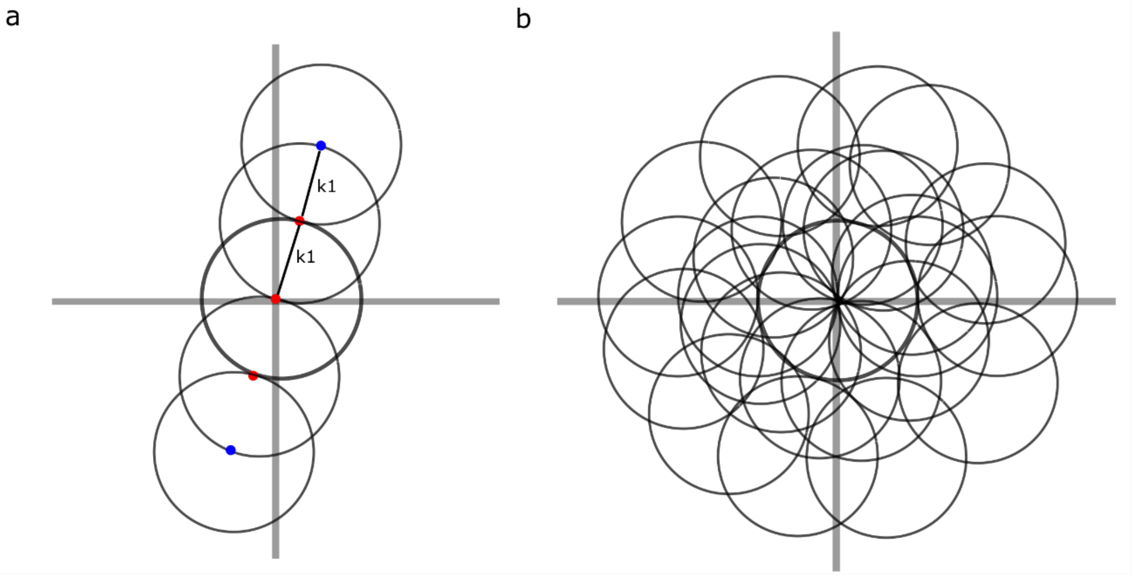

Figure 1-7 The principle of nonlinear super-resolution structured illumination microscopy. a) Non-linearity of illumination introduces additional observable circles, the centres of which are offset by multiples of k_1 (e.g. $2k_1$, blue dots), along with those of k_1 (red dots) as in linear SIM. b) By rotating the illumination pattern in different phases, the area of the observable regions is much larger, and after data processing, this leads to higher spatial resolution. In theory, the resolution improvement can be infinite.

1.3.2 Single molecule localisation microscopy (SMLM)

On account of different types of fluorophores and imaging conditions, single molecule localisation microscopy (SMLM) methods appear under multiple acronyms, dominantly

STORM (stochastic optical reconstruction microscopy),[42] and (F)PALM ((fluorescence) photoactivated localisation microscopy).[43,44] Nevertheless, they are based on the same principle: in widefield microscopy, fluorescence of well-separated individual molecules is stochastically turned on and off temporally, and by precise determination of the centres of their positions, an image with sub-diffraction resolution is reconstructed (**Figure 1-8**).

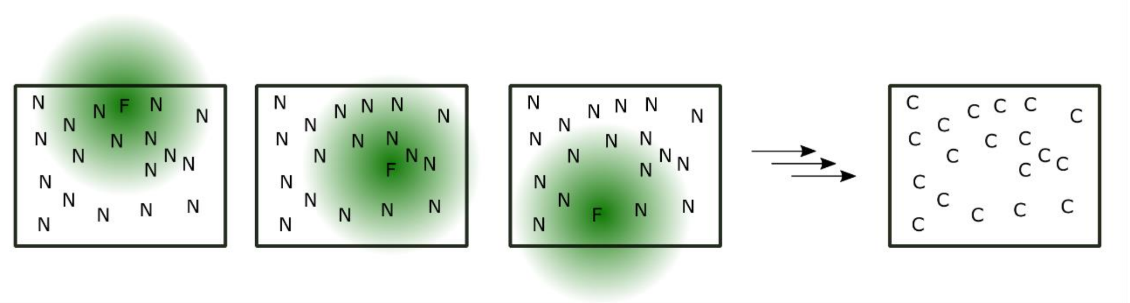

Figure 1-8 The principle of SMLM. A scarce population of well-separated fluorophores are switched on when the majority remain in the dark state. The centre of each diffraction-limited spot is calculated by fitting a Gaussian function. Repeated cycles of photoactivation, imaging and photobleaching are performed, and the image is reconstructed by summation of the localised central positions. N = non-fluorescent fluorophore, F = fluorescent fluorophore, C = centre of fluorophores.

The exact mechanism of photoswitching between bright and dark states varies, for example, through reacting a cyanine dye with a primary thiol[45] or uncaging a rhodamine spiroamide.[46] Given a sufficient number of emission photons are collected, the central position of a diffraction-limited spot generated by an individual emitter can be located by fitting a Gaussian function with nanometric precision. Such a precision is expressed by the following equation,[47]

$$\sigma^2 = \frac{s^2 + a^2/12}{N} + \frac{8\pi s^4 b^2}{a^2 N^2} \qquad \mathbf{(1.1)}$$

where σ is the localisation accuracy (standard error of the mean), s the size of the PSF, a the size of the pixels on the camera, b the background intensity, and N the number of detected photons. The final structural resolution is determined by localisation precision and the Nyquist criterion, i.e. the separation between two fluorescent labels must be shorter than half of the desired spatial resolution.[48] The mathematical equation of the SMLM resolution[49] is

$$d_{\mathrm{final}} = \sqrt{d^2_{\substack{\mathrm{localisation}\\ \mathrm{precision}}} + d^2_{\mathrm{Nyquist}}} = \sqrt{(2\sqrt{2ln2}\bar{\sigma})^2 + (\frac{2}{\rho^{1/l}})^2} \qquad \mathbf{(1.2)}$$

Where d is the resolution, $\bar{\sigma}$ the mean localisation accuracy, l the dimension of the image (e.g. 2-dimensional image), and ρ the local density of fluorescent markers. Because of simplicity in both the concept and instrumentation, SMLM has received considerable attention, and become increasingly commercially available for routine application in biology laboratories. For example, 3D imaging[50–53] and time-lapse imaging of relatively slow dynamic processes in live cells[54–56] have been demonstrated using SMLM techniques. However, as indicated in the equations of image reconstruction, SMLM imposes strict criteria of high photon outputs/brightness, implying intense excitation illumination, low background noise, and high labelling density. Another severe disadvantage of SMLM is the slow acquisition due to its stochastic approach.

1.3.3 Reversible saturable optical fluorescence transitions (RESOLFT) microscopy

A third category of super-resolution microscopy, RESOLFT (reversible saturable optical fluorescence transitions) microscopy circumvents the diffraction limit by exploiting reversibly photoswitchable transitions between states with different fluorescence characteristics, commonly a bright state and a dark state, of dyes at predefined coordinates.[33,57–61] The exact nature could be photoswitching between ground and excited singlet states of a fluorophore in STED (stimulated emission depletion) microscopy,[5,6,62] excited singlet and triplet states in GSD (ground state depletion) microscopy,[63–65] or fluorescent and non-fluorescent forms of a reversibly photoswitchable fluorophore.[57–59,66] In the earliest RESOLFT modality, i.e. STED microscopy, a depletion beam featuring a local intensity minimum (typically of a donut shape) is superimposed with the diffraction-limited excitation illumination to suppress fluorescence in a defined region *via* stimulated emission process.[5] Usually a donut-shaped STED beam with a zero intensity centre is created by inserting a phase plate or grating in the wave-front of the depletion laser. With use of a shortpass filter, red-shifted stimulated emission appears dark to the detector, and thus, fluorescence emission is only observed from the zero intensity centre and registered for a known position, resulting in an effective PSF smaller than the diffraction limit (**Figure 1-9**a). Raster-scanning (point by point or parallel[67,68]) the entire sample reconstructs the image with fine structural details that are otherwise indiscernible by conventional confocal microscopy (**Figure 1-9**b). It is obvious that in order to acquire super-resolved images, the scanning step size must be smaller than the diffraction limit, and increased spatial resolution is achieved with a decreasing step size. This necessitates the fluorophore switching between bright and dark states multiple times when the superimposed excitation and depletion beams are scanned across the sample.

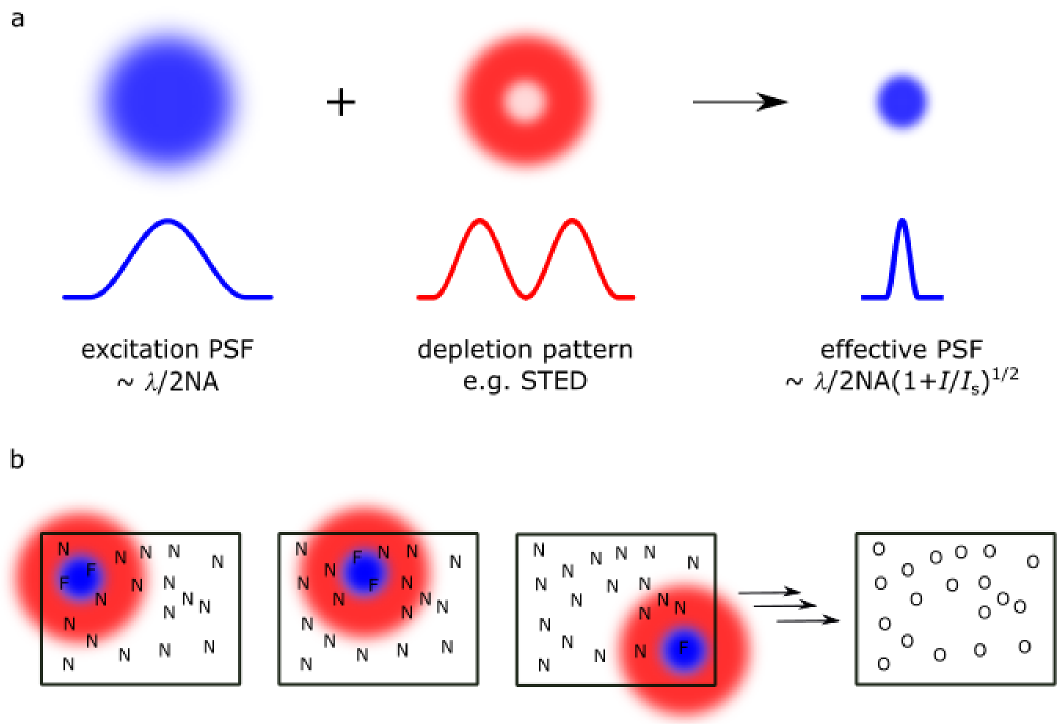

Figure 1-9 The principle of RESOLFT microscopy. a) The diffraction-limited excitation spot (Gaussian-shaped, width λ/2NA) is overlaid with a fluorescence-depletion beam featuring a local intensity minimum (donut-shaped intensity distribution). Provided that the depletion beam deactivates the fluorescence of the dye, any fluorescence must come from the diffraction unlimited difference spot. b) The superimposition of the excitation and depletion beams creates a sub-diffraction spot, and scanning over the entire sample builds up the image with increased resolution than what is provided by conventional confocal microscopy. N = non-fluorescent fluorophore, F = fluorescent fluorophore, O = objects.

Mathematically, the spatial resolution of RESOLFT/STED images is modified to[57,69]

$$d \approx \frac{\lambda}{2n\sin\alpha\sqrt{1+I/I_s}} = \frac{\lambda}{2NA\sqrt{1+I/I_s}} \qquad \textbf{(1.3)}$$

where I is the maximum value of the intensity distribution of the depletion beam, and I_s is the saturation intensity of the fluorophore. For the stimulated emission process, increasing the STED power decreases the fluorescence emission in a non-linear manner (**Figure 1-10**a). Saturation intensity, I_s, is a function of the depletion light and intrinsic properties of the fluorophore (involving absorption cross-section of the transition and lifetimes of the states), and defines the depletion intensity required to outperform competing transitions. In STED microscopy, I_s is usually defined as the STED power at which 50% of the dye population is turned to the dark state *via* stimulated emission process (**Figure 1-10**a).[1,57] In other words, by applying depletion powers above the saturation intensity, it becomes highly likely that one of the incident photons would initiate the photo-event, e.g. stimulated emission in STED microscopy. Equation (**1.3**) indicates that increasing depletion laser powers sharpens the effective PSF, i.e. higher spatial resolution (**Figure 1-10**b). In theory, an unlimited resolution is possible as the term I/I_s approaches ∞.

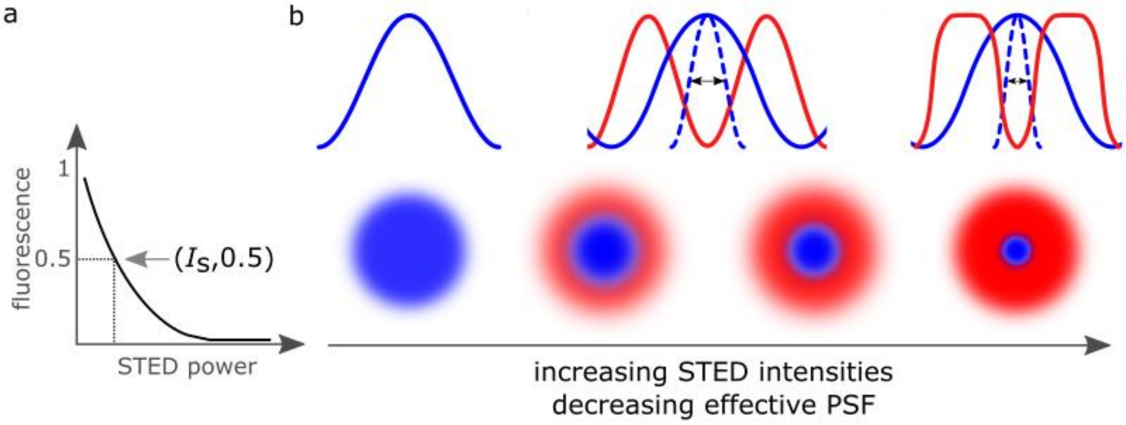

Figure 1-10 Dependence of spatial resolution on STED laser intensities in STED microscopy. a) Fluorescence depletion as a function of STED power in a non-linear manner. Saturation intensity I_s is defined as the power required to deplete the original fluorescence by 50% *via* stimulated emission process. b) Schematic representation of decreasing effective PSF, i.e. increasing spatial resolution, with stronger STED intensities.

In recent years, STED microscopy has been successfully applied to unveil previously undiscernible details of subcellular structures in live specimens,[70–74] and even neural movement in the brain of a living (anaesthetised) mouse.[75] However, notably intense (picosecond pulsed) powers ($MW/cm^2 – GW/cm^2$) are typically applied in STED imaging because of high saturation intensity (I_s) in STED. The calculation of saturation intensity is given by $I_s = (\tau\,\sigma_{STED})^{-1}$, where σ_{STED} is the photon cross-section of stimulated emission at the wavelength λ_{STED} and τ is the lifetime of the excited S_1 state.[1] The lifetime τ is typically in the range of 1–5 ns, stimulated emission cross-section σ is $\sim 10^{-17}$ cm^2, and given the typical stimulated emission wavelength of 590–990 nm, photon cross-section $\sigma_{STED} = \sigma/E = \sigma\lambda/hc \approx 30–50$ cm^2/J. Thus, $I_s \sim 20–35$ MW/cm^2 and the applied intensity I needs to be significantly higher. Such strong laser powers can cause permanent photobleaching of the fluorophore and phototoxicity to the specimen.[1,33,76–80]

One solution is to replace the photophysical switching of stimulated emission depletion by photochemical processes of switchable fluorophores, so that the depletion and emission processes are no longer in direct competition, allowing use of lower laser intensities. From here onwards, when RESOLFT is discussed, it refers to this photochemical method, while other RESOLFT sub-categories such as STED and GSD will be specified.

1.4 Switchable fluorophores for RESOLFT microscopy

The most commonly applied fluorophores in RESOLFT microscopy are reversibly switchable fluorescent proteins (rsFPs), and many working examples have been demonstrated in biological systems using light intensities at a magnitude of kW/cm^2, which is three to six orders of magnitude lower than required for STED microscopy.[58–60,67,81] The photoswitching behaviour of rsFPs arises from fluorophores that reside inside the barrel structure of the proteins, and structural cores of the fluorophores in different rsFP families are quite similar.[82] The popularity of (photoswitchable) fluorescent proteins is mainly attributed to their creation by genetic encoding, which inherently gives them live-cell compatibility, and the concomitant absolute specificity to target specific sites.[83] The first rsFP employed in RESOLFT imaging was asFP595[84] which enabled 50–100 nm spatial resolution to be attained on a groove-crafted glass-slide despite the disadvantages of low contrast, low quantum yield and existence as a tetramer.[59] Well-known rsFPs include Dronpa,[85] which achieved 30–50 nm spatial resolution in live-cell 3D RESOLFT imaging when combined with 4Pi setup (using two opposing objectives to improve the axial resolution),[86] and rsEGFP that achieved <50 nm resolution in living cells.[60,81,87] rsFPs have been continuously developed, with very recent examples including rsFusionRed[88] and rsLOV1.[89] Arguably the most promising rsFP may be Skylan-NS, although it has only been demonstrated in PALM microscopy.[90]

Notwithstanding the advantages arising from genetic encoding, rsFPs and FPs in general are associated with several drawbacks. Firstly, their brightness and photostability are relatively low. Additionally, there is a very small number of fluorescence colours available presumably due to a limited variety of chromophores and switching mechanisms available in FPs,[82] which limits the use of multi-colour imaging. In the meanwhile, the above problems are by no means easy to solve given the absence of predictable rational design for fluorophores that are buried deeply inside the proteins.[91–93]

An alternative switchable label is small-molecule synthetic dyes. Unlike FPs, synthetic dyes generally lack specificity for particular proteins, but they are more versatile than FPs, and available in a wider spectrum of colours due to commercial interest in organic fluorescent dyes.[94] Synthetic dyes also offer advantages of higher brightness, photostability,[95] and the possibility of labelling endogenous proteins.[96] Given these unrivalled advantages, significant effort has also been dedicated to the development of small-molecule organic dyes for use in RESOLFT microscopy. The following sections will summarise the strategies of constructing synthetic dyes for RESOLFT microscopy, followed by detailed description of our molecular design in this work.

1.5 Approaches to photoswitchable synthetic dyes

There are three general approaches to RESOLFT synthetic dyes, which have the potential of being applied in the majority of other SRM techniques:

1. A single molecular switch that has a brightly fluorescent form, and a comparatively dark state (**Figure 1-11**a).[97,98] At least one of the directions is photochemically driven.

2. A bimolecular reaction between a fluorophore and a reactant under illumination conditions (**Figure 1-11**b).[99,100] For example, it could be a nucleophilic addition reaction that interrupts the electronic conjugation of the fluorophore, and this transiently stops fluorescence emission, resulting in a dark state.

3. A dyad construct, in which the fluorescence of a fluorophore is modulated by a photoswitch (**Figure 1-11**c).[101–104] Such a system could result from simply mixing the two components,[105] or permanently linking them by a covalent bond.[106] A bright state is present when the photoswitch is in the inactive form, and the dye fluoresces without being affected. A dark state is generated when the photoswitch resides in the active fluorescence quenching form. Light is used to convert the photoswitch from the inactive to active form, or *vice versa*. The two forms of the photoswitch must have different photophysical or photochemical properties, e.g. different absorption spectra, to be responsible for different behaviour resulting in bright and dark states. In theory, the quenching mechanism could be any process that competes with fluorescence, as described in Section 1.1, e.g. photoinduced electron transfer (PET),[107] or Förster resonance energy transfer (FRET) processes.[104,108,109]

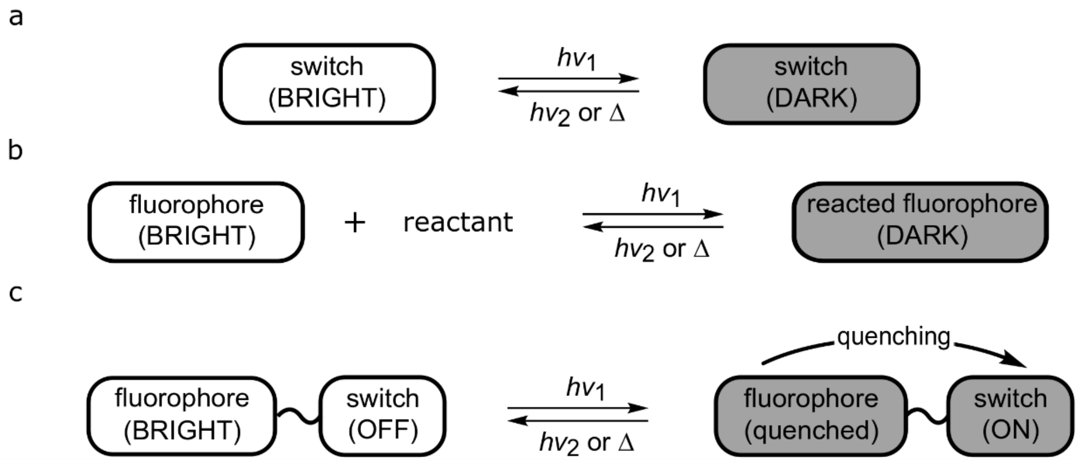

Figure 1-11 Approaches to photoswitchable synthetic dyes for super-resolution microscopy. a) The molecular switch acts as fluorophore itself. b) The bimolecular reaction of a fluorophore with a reactant, which interrupts the electronic conjugated system of the fluorophore to generate a dark state. c) The emission of a bright fluorophore can be modulated by a (covalently or non-covalently attached) photoswitch in a dyad construct, e.g. quenching by PET or FRET processes.

Despite considerable research efforts, very few synthetic dyes have been demonstrated in biological systems under RESOLFT microscopy. The earliest of such working examples adopts the third approach, where a synthetic polymer containing a FRET pair of a naphthalimide dye and a diarylethene photoswitch was applied (**Figure 1-12**).[104] When the diarylethene is in the open form, its absorption spectrum does not overlap with the emission spectrum of the naphthalimide dye. Therefore, no FRET quenching occurs, and the dye fluoresces normally. Upon irradiation at 302 nm, the diarylethene is converted to its closed form, which absorbs at longer wavelengths due to its extended conjugation. Its absorption spectrum now overlaps with the naphthalimide dye emission spectrum, and FRET quenching of the dye can occur, resulting in a dark state. Using the photoswitching capacity of this dyad, RESOLFT images were acquired of lysosomes in live HeLa cells, and the spatial resolution of 40 nm was reported.[104] However, a 405 nm laser was used as the excitation and recovery light, and 302 nm was used as depletion light, both of which would likely cause photobleaching to dyes and phototoxicity to cells. Use of longer illumination wavelengths in the visible region would be preferred, but it would require significant changes to the molecular design. In this work, consideration of factors, such as water-solubility and specific site localisation, resulted in a complex molecule that succeeded in achieving live-cell RESOLFT imaging. However, the molecular construct is not generalisable. Targeting a different site/organelle would mean a new molecule incorporating another unique unit for site recognition if such selective recognition units exist for every organelle of interest.

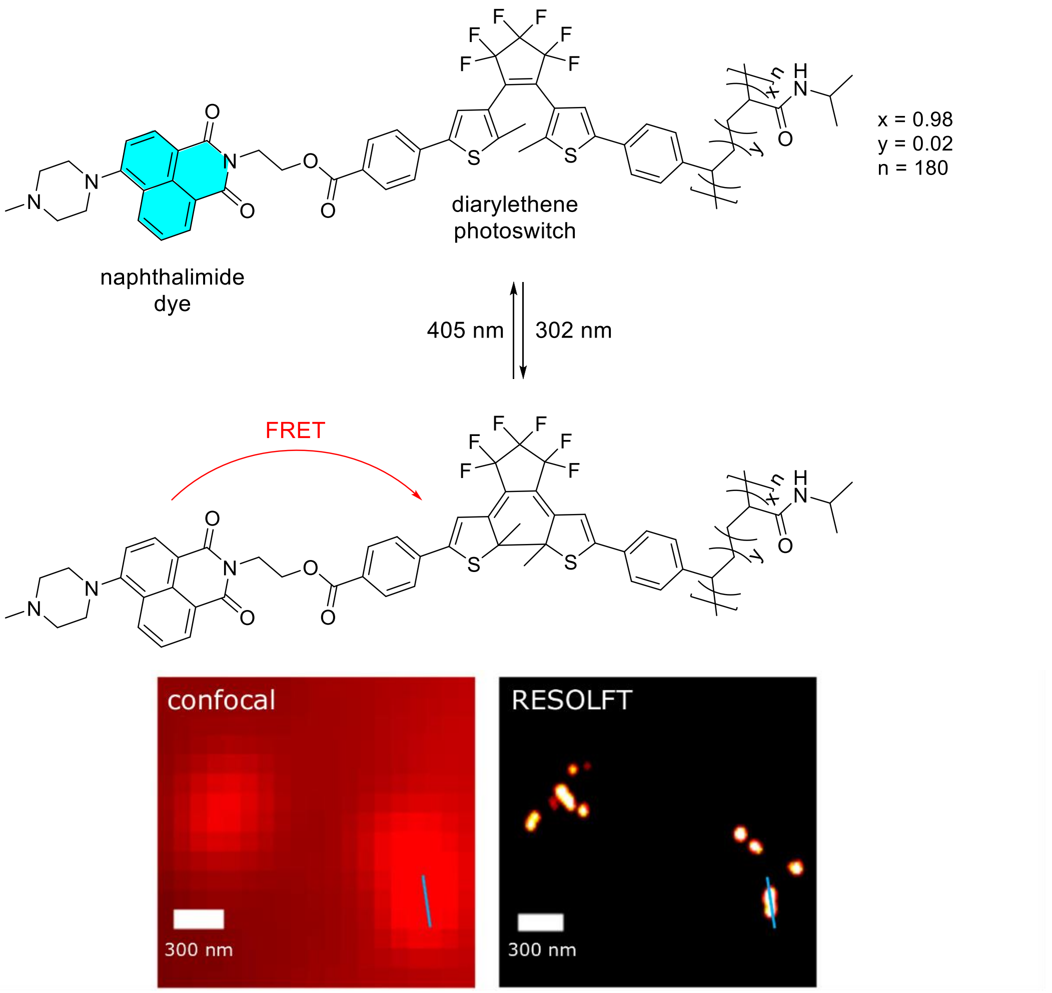

Figure 1-12 The first example of a small-molecule RESOLFT dye, utilising an emissive naphthalimide whose emission is reversibly modulated by a diarylethene switch. Resolution of 40 nm was reported in the lysosomes of live HeLa cells.[104]

The second approach, i.e. utilisation of a bimolecular reaction, was validated by RESOLFT imaging of multiple subcellular structures by applying a Cy3-Alexa647 heterodimer and a primary thiol (RSH) in the presence of KI in fixed cells (**Figure 1-13**).[100] The dark state likely results from the nucleophilic addition of RSH to one conjugated double bond of the Alexa647 unit,[99] which prevents the dye absorbing at the excitation wavelength (658 nm). Using an indirect immunolabelling method by relying on primary and secondary antibodies,[110] nuclear pore complexes in fixed NIH3T3 cells as well as mitochondria and microtubules in fixed primary human-skin-fibroblast cells, were specifically labelled and imaged. Three lasers, 532 nm, 633 nm and 658 nm were used as activation, depletion and excitation light, respectively. With optimised buffer conditions and laser parameters, 75 nm resolution was reported on nuclear pore complexes, and the hollow structures of mitochondria and microtubules separated by ~130 nm were also discerned. One advantage of the method is the generalisability of the immunolabelling method, making it possible to target many proteins of interest using the same molecule. However, a number of limitations might prevent its general application. Firstly, the optimisation of the system seems complicated, including the addition of an appropriate concentration of KI to promote the photochemical switching without compromising brightness, and the employment of an oxygen scavenging system of glucose oxidase and catalase[111] to alleviate photobleaching. Furthermore, the imaging was performed in fixed cells, which is commonly associated with immunolabelling due to the large size of antibodies.

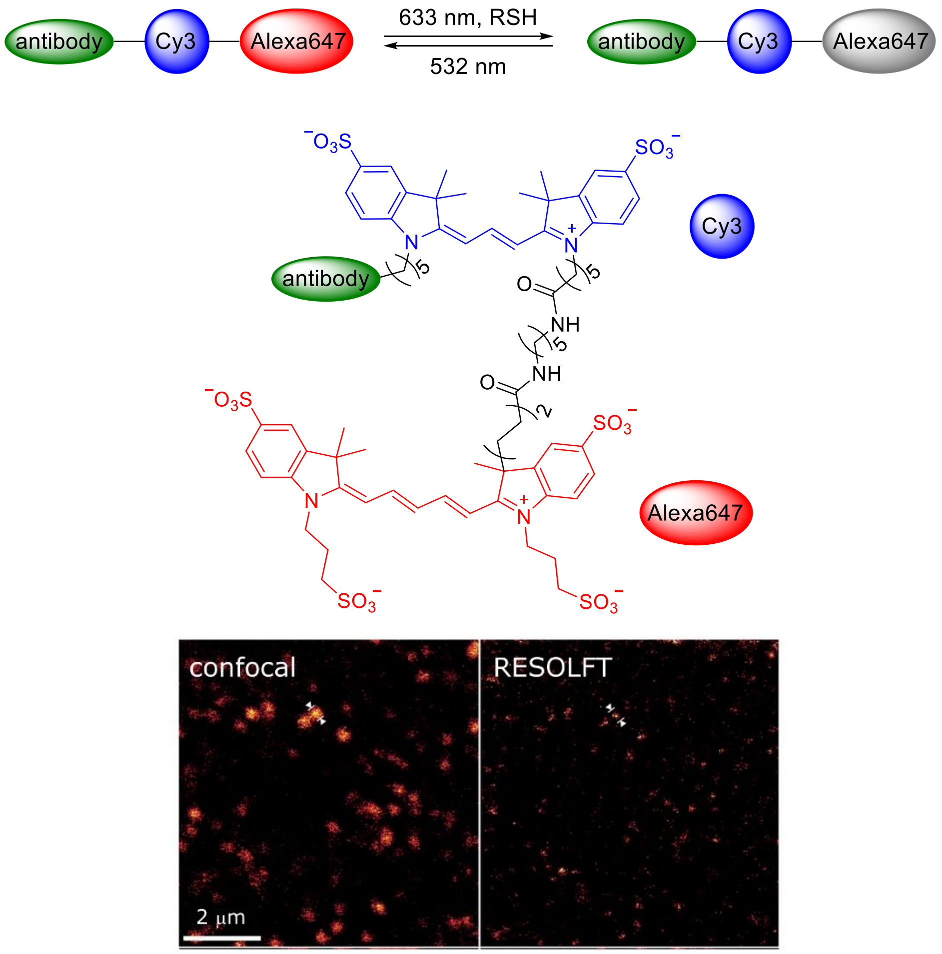

Figure 1-13 RESOLFT example based on a reversible bimolecular reaction of a Cy3-Alexa647 heterodimer and a primary thiol RSH in the presence of KI and an oxygen scavenging system employing glucose oxidase and catalase. The RESOLFT images were obtained of nuclear pore complexes in fixed NIH3T3 cells (as shown), and of mitochondria and microtubules in fixed primary human-skin-fibroblast cells.[100]

Among the successful examples of RESOLFT imaging in biological systems, the one based on seemingly the simplest approach, i.e. one molecule that reversibly switches between a bright and dark state, is the most recent to be reported. In this system, a sulfone-based diarylethene photoswitch was used to stain tubulin filaments in fixed Vero cells using an indirect immunolabelling method (**Figure 1-14**).[98] Using activation light at 355 nm and both excitation and depletion at 488 nm, RESOLFT images were recorded with 75 nm resolution. In the work, the notorious hydrophobicity of diarylethenes was overcome by presence of multiple (4 or 8) water-solubilising carboxylic acid groups. The simplicity of the molecular construct is also an encouraging advantage. However, like the previous example, the imaging was performed in fixed cells. The use of phototoxic 355 nm UV light is another significant drawback that is not simple to solve. Additionally, exciting fluorescence causes conversion to the dark state, which would potentially result in an insufficient number of emitted photons.

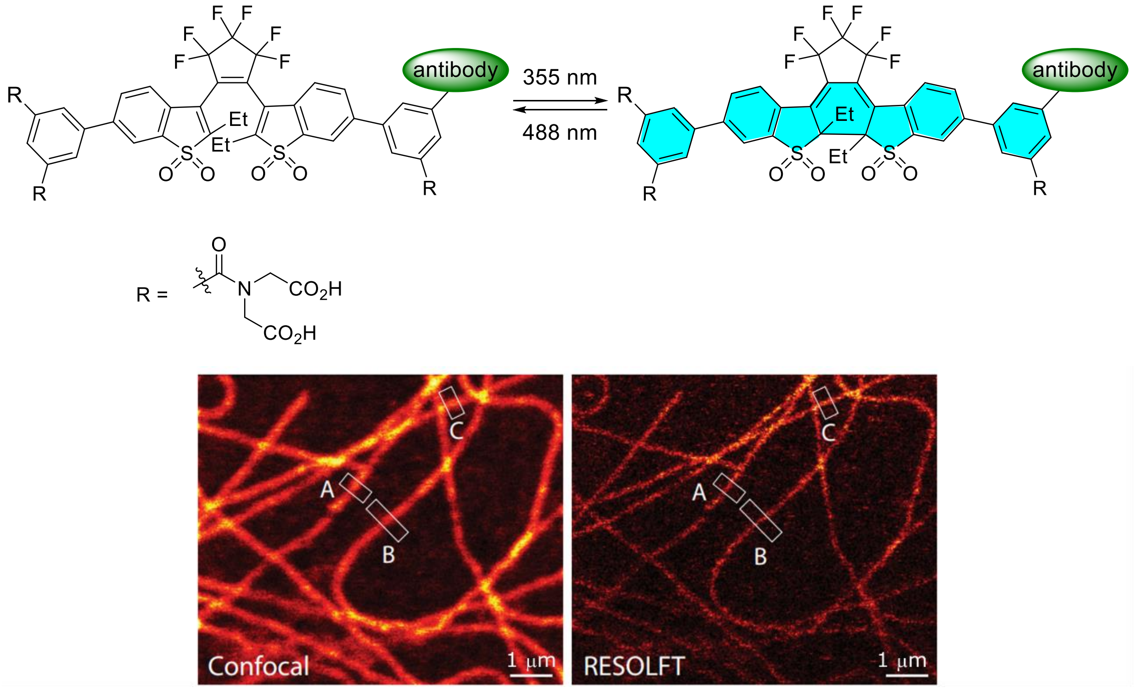

Figure 1-14 RESOFLT dye based on a diarylethene photoswitch which can interconvert between a dark state and bright state upon irradiation with UV and visible light. RESOLFT images with 75 nm resolution were obtained of stained tubulin filaments in fixed Vero cells.[98]

1.6 Our molecular design

Among the three general approaches to switchable dyes, we consider the dyad approach to have three main advantages: the modular construct allows combination of the optimal individual components, less stringent criteria are imposed on each component, and the possibility of using different fluorescent dyes enables multi-colour imaging. In this work, we choose the design of covalently linked dyads utilising FRET as the fluorescence quenching mechanism. This is because FRET can be reliably predicted when the spectral properties of the fluorophore and switch are suitable, and the two components are within a certain distance.[8] In theory, the relative orientation of the two could prevent the occurrence of FRET, but it is very rare.[8] In addition, the extent of FRET is readily predictable.[8] These points will be elaborated in the following section.

1.6.1 FRET theory

As briefly introduced in Section 1.1, FRET occurs between a donor in an excited state and an acceptor in the ground state through transition dipole-transition dipole interactions, typically over 10–100 Å.[8] In our design, FRET works as a nonradiative competing pathway to fluorescence emission of the donor fluorophore. The rate constant of FRET is given by the equation:

$$k\,(r) = \frac{1}{\tau_\mathrm{D}}\left(\frac{R_0}{r}\right)^6 \qquad \textbf{(1.4)}$$

where τ_D is the fluorescence lifetime of the donor in the absence of the acceptor, r is the separation distance between the donor and acceptor, and R_0 is the Förster radius, defined as the distance at which FRET efficiency is 50%. That is, at $r = R_0$, the fluorescence intensity of the donor is decreased to half of the original emission without the acceptor.

The formal equation for $k\,(r)$ that includes the calculation of R_0 is presented below,

$$k(r) = \frac{\Phi_\mathrm{D}\kappa^2}{\tau_\mathrm{D} r^6}\left(\frac{9000\,(\ln 10)}{128\pi^5 N n^4}\right)\int_0^\infty F_\mathrm{D}(\lambda)\varepsilon_\mathrm{A}\,(\lambda)\lambda^4 d\lambda \qquad \textbf{(1.5)}$$

where in addition to τ_D and r described above, Φ_D is the fluorescence quantum yield of the donor in the absence of the acceptor, N is the Avogadro constant, and n is the refractive index of the medium. The dipole orientation factor κ^2 describes the relative orientation of the transition dipoles of the donor and acceptor, and the value can range from 0 to 4. For example, $\kappa^2 = 4$ for head-to-tail parallel orientation, $\kappa^2 = 1$ for parallel orientation and $\kappa^2 = 0$ for perpendicular orientation. It is usually assumed to be 2/3, which is reasonable for dynamic random averaging between the donor and acceptor. $F_\mathrm{D}(\lambda)$ is the fluorescence intensity of the donor in the range λ to $\lambda+\Delta\lambda$ after the total intensity (the area under the curve) is normalised to 1. $\varepsilon_\mathrm{A}(\lambda)$ is the molar absorption coefficient of the acceptor at λ. A combined term $J(\lambda)$ is used to define the extent of the spectral overlap between the donor emission and acceptor absorption:

$$J(\lambda) = \int_0^\infty F_\mathrm{D}(\lambda)\varepsilon_\mathrm{A}\,(\lambda)\lambda^4 d\lambda \qquad \textbf{(1.6)}$$

Because $F_\mathrm{D}(\lambda)$ is dimensionless, if $\varepsilon_\mathrm{A}(\lambda)$ is in the unit of $\mathrm{M}^{-1}\mathrm{cm}^{-1}$, and λ is in nm, then $J(\lambda)$ is in the unit of $\mathrm{M}^{-1}\mathrm{cm}^{-1}\mathrm{nm}^4$.

From the above equations, R_0^6 can be expressed as

$$R_0^6 = \left(\frac{\Phi\mathrm{D}\kappa^2 9000\ (\ln 10)}{128\pi^5 N n^4}\right)\int_0^\infty F_{\mathrm{D}}(\lambda)\varepsilon_{\mathrm{A}}\,(\lambda)\lambda^4 d\lambda = \frac{\Phi\mathrm{D}\kappa^2 9000\ (\ln 10)}{128\pi^5 N n^4} J(\lambda) \qquad \mathbf{(1.7)}$$

This equation allows the calculation of the Förster radius based on the spectral properties of the donor and the acceptor, and the fluorescence quantum yield of the donor. In terms of units, when $J(\lambda)$ is in the unit of $\mathrm{M}^{-1}\mathrm{cm}^{-1}\mathrm{nm}^4$, R_0^6 is in the unit of Å^6.

In this report, a numerical version of equation (**1.7**) is used for convenient calculations of R_0:

$$R_0 = 0.2108\left[\frac{\kappa^2\,\Phi\mathrm{D}J(\lambda)}{n^4}\right]^{\frac{1}{6}} \qquad \mathbf{(1.8)}$$

Once the R_0 value is calculated, the rate constant of FRET can be easily obtained using equation (**1.4**). If this FRET rate constant is much larger than the fluorescence decay, the energy transfer is efficient.

Another way to look at the FRET process is the FRET efficiency E, which is the percentage of photons absorbed by the donor that are transferred to the acceptor. E is expressed as

$$E = \frac{k(r)}{\tau_{\mathrm{D}}^{-1} + k(r)} \qquad \mathbf{(1.9)}$$

Because $k\,(r) = \frac{1}{\tau_{\mathrm{D}}}\left(\frac{R_0}{r}\right)^6$ (**1.4**), E can be expressed as

$$E = \frac{1}{1 + \left(\frac{r}{R_0}\right)^6} \qquad \mathbf{(1.10)}$$

This equation shows that the FRET efficiency is strongly dependent on the separation distance of the donor and acceptor r (**Figure 1-15**).

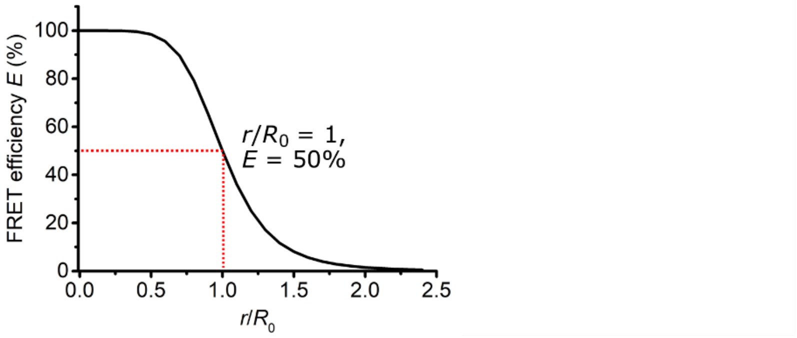

Figure 1-15 Dependence of FRET efficiency E (%) on r/R_0 ratio. r is the separation distance of the donor and acceptor, and R_0 is the calculated Förster radius.

As shown in **Figure 1-15**, the efficiency rapidly increases as the donor-acceptor distance decreases below R_0. For example, when r/R_0 is 0.1–0.3, the FRET efficiency is calculated to be 0.99999–0.99927, so the fluorescence emission of the donor would be hardly observed. In contrast, when r is greater than R_0, the efficiency quickly decreases. In our dyad molecular design, high FRET efficiency is crucial because along with the photostationary state of the switch (discussed later), it controls the darkness of the dark state. In turn, strong contrast between bright and dark states is a key factor in achieving diffraction-unlimited resolution in RESOLFT microscopy.

1.6.2 RESOLFT dye precedents based on FRET process

While fluorescence modulation using FRET has been long recognised,[101–103] application of a FRET pair in super-resolution microscopy has only been realised recently. Although the theoretical analysis was conducted in 2009 and 2012 to confirm the practicability of the FRET based approach to RESOLFT microscopy,[112,113] the idea was first proposed by the Hell group in 2006,[106] and experimentally verified by the same group in the same year.[105] In the latter work, the researchers employed a FRET pair of a Coumarin 6 dye as the donor, and a furyl-fulgide photoswitch, Aberchrome670, as the acceptor (**Figure 1-16**). A bright state exists when Aberchrome670 is in the open form. The 375 nm illumination triggers ring closure of Aberchrome670, and the closed form absorbs at a longer wavelength due to the extended conjugation. The spectral overlap between this longer wavelength absorption and the emission of Coumarin 6 results in FRET quenching of the fluorescence, and thus, a dark state. Coumarin 6 and Aberchrome670 were simply mixed and embedded in a poly(methyl methacrylate) (PMMA) matrix, and RESOLFT imaging was performed on grooves of known patterns that had been spin-coated with the PMMA mixture. The spatial resolution of ~50 nm was reported using 375 nm and 543 nm switching light.

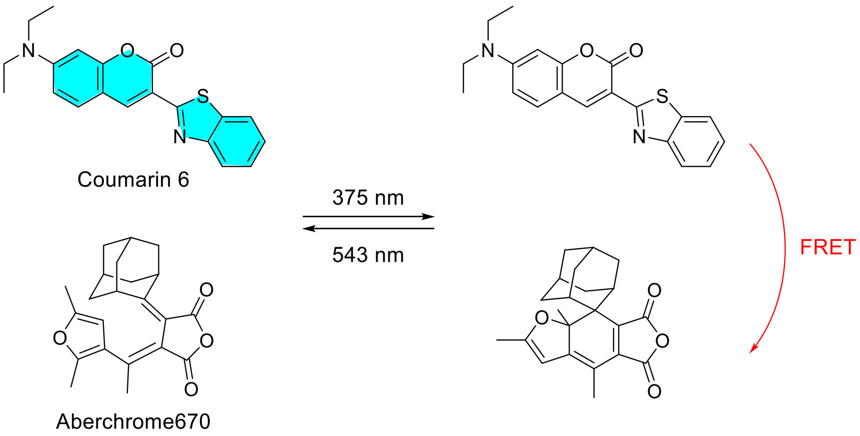

Figure 1-16 The earliest RESOLFT example using a FRET pair. The Coumarin 6 dye and the Aberchrome670 photoswitch were mixed and embedded in a PMMA matrix, and such a PMMA mixture was used to stain grooves of known patterns. The RESOLFT images of the grooves were obtained with ~50 nm resolution.[105]

Following the first example, a number of switchable molecules based on FRET pairs have been proposed, and some have shown promising properties required for RESOLFT microscopy.[107,114–118] Nevertheless, only few have been successfully demonstrated in RESOLFT imaging. A pair formed from a diarylethene switch and a Rhodamine101 dye was covalently linked to silica nanoparticles (**Figure 1-17**a), and particles that were separated by ~230 nm were clearly resolved.[108] In the second example, three diarylethene units were attached to one perylenemonoimide dye (**Figure 1-17**b), and RESOLFT images with ~35 nm resolution were obtained of artificial vesicles that were stained with the four-unit 'dyad'.[109] For these two molecules, imaging of more biologically relevant environments may be challenging due to their hydrophobic nature. To the best of our knowledge, only one RESOLFT synthetic dye based on the FRET approach has been employed in the biological system, which is already described in Section 1.5.

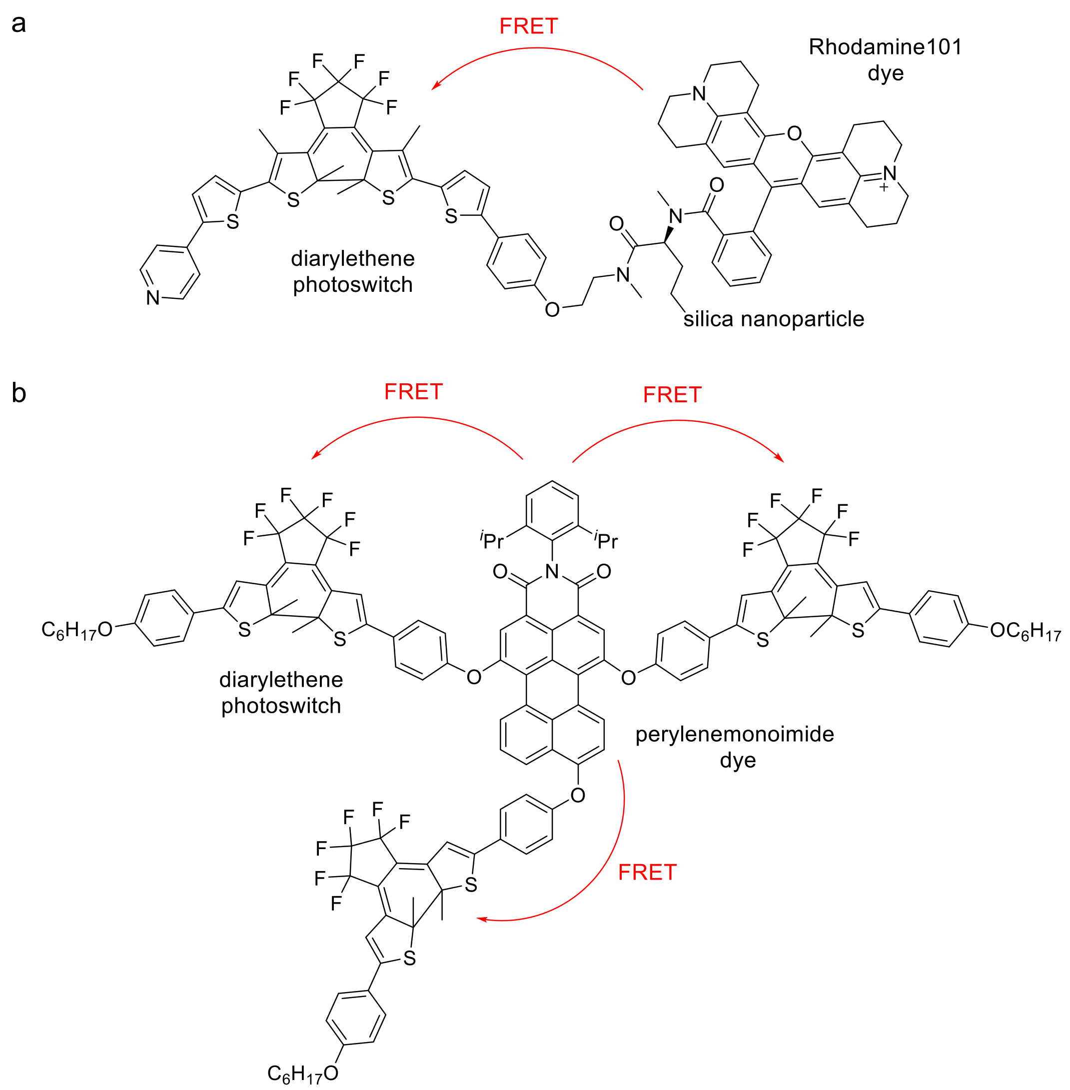

Figure 1-17 Synthetic dyes based on the FRET approach, which have been applied in RESOLFT microscopy to image non-biological systems. a) A FRET pair of a diarylethene switch and a Rhodamine101 dye was used to image covalently-linked silica nanoparticles. Particles ~230 nm apart were resolved.[108] b) Three diarylethene units were attached to one perylenemonoimide dye, and this compound was used to stain artificial vesicles. ~35 nm resolution was reported for the RESOLFT images of the vesicles.[109]

1.7 Photoswitches

1.7.1 Photochromism

A photoswitch in our FRET approach refers to an organic photochromic compound. Photochromism is defined as a reversible transformation of a molecule, induced by light in one or both directions, between two states **A** and **B** that have different absorption spectra (**Figure 1-18**).[119] In the context of FRET based dyad design, only one of the states acts as an effective fluorescence quencher given the sufficient spectral overlap with the fluorophore, whereas the other state does not affect the fluorescence emission.

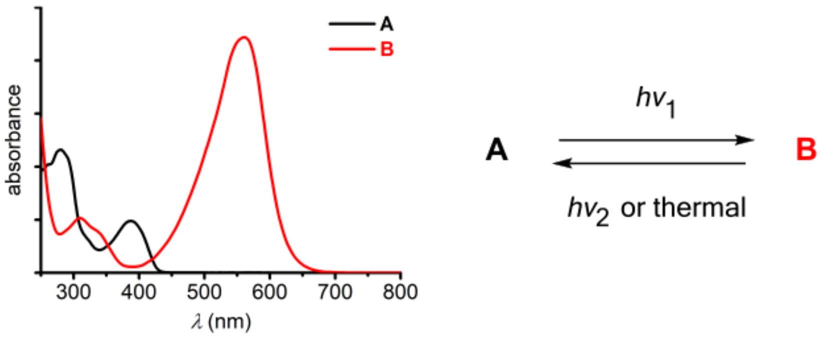

Figure 1-18 An example of organic photochromism. **A** absorbs light of $h\nu_1$, and is transformed into **B**. The back reaction from **B** to **A** is either thermal or photochemically driven by light of $h\nu_2$.

Upon light of a particular frequency, $h\nu_1$, the thermodynamically stable form **A** is transformed into form **B**. The back reaction is either thermal or photochemically driven by absorption at $h\nu_2$, which categorises photochromism as type **T** and type **P** respectively. For most cases, type T systems can also be photochemically accelerated.

In order to fully describe photoswitching behaviour, it is necessary to define a few terms first as follows.

If the thermodynamically stable form **A** is colourless or only slightly coloured and form **B** is strongly coloured, the phenomenon is called **positive photochromism**. The reverse is **negative photochromism**.

Photostationary state (**PSS**) refers to the composition ratio of forms **A** and **B** when the system reaches an equilibrium upon illumination of light at a particular frequency. It is the steady state when the formation and disappearance rates of transient species are equal. High PSS ratios in both directions are crucial for our FRET dyad based approach as along with FRET efficiency, it dictates the contrast of bright and dark states, which in turn determines the achievable spatial resolution.

Fatigue resistance is the resistance to light-induced degradation, and is manifested in the number of cycles a system can be switched effectively before decomposition. A cycle is the transformation from **A** to **B** and then **B** back to **A**. In the context of our dyad design, fatigue can arise from irreversible side reactions of either the dye or the photoswitch components. As a result of photochromic behaviour of the photoswitch, the dyad undergoes conversion between bright and dark states. The ratio of the average photon counts from bright and dark states in a single cycle is called the **contrast**. Another related parameter is **quenching efficiency**, which is calculated as ($1-I_{\text{dark}}/I_{\text{bright}}$), where I_{dark} and I_{bright} stand for intensities of fluorescence signals in dark and bright states within a cycle.

That is, quenching efficiency describes the extent to which the switch depletes the fluorescence in a single cycle. Unlike fatigue resistance, it presents the performance of the switch *without* considering the effects from factors like decomposition of the dye component.

Thermal half-life $t_{1/2}$ is the time required for a coloured form to thermally bleach to half of its original absorbance at a given wavelength. This parameter is influenced by the choice of the solvent and temperature, among other factors.

Quantum yield of a photochemical reaction refers to the amount of a product formed per photon absorbed by the system, e.g. how much of **B** generated from **A** per photon absorbed by **A** at a particular frequency.

1.7.2 Photoswitch families

The most common organic photochromic systems involve unimolecular reactions, though bimolecular processes also exist. Representative photoswitch families are shown in **Figure 1-19**, where $h\nu_1 > h\nu_2$.[119]

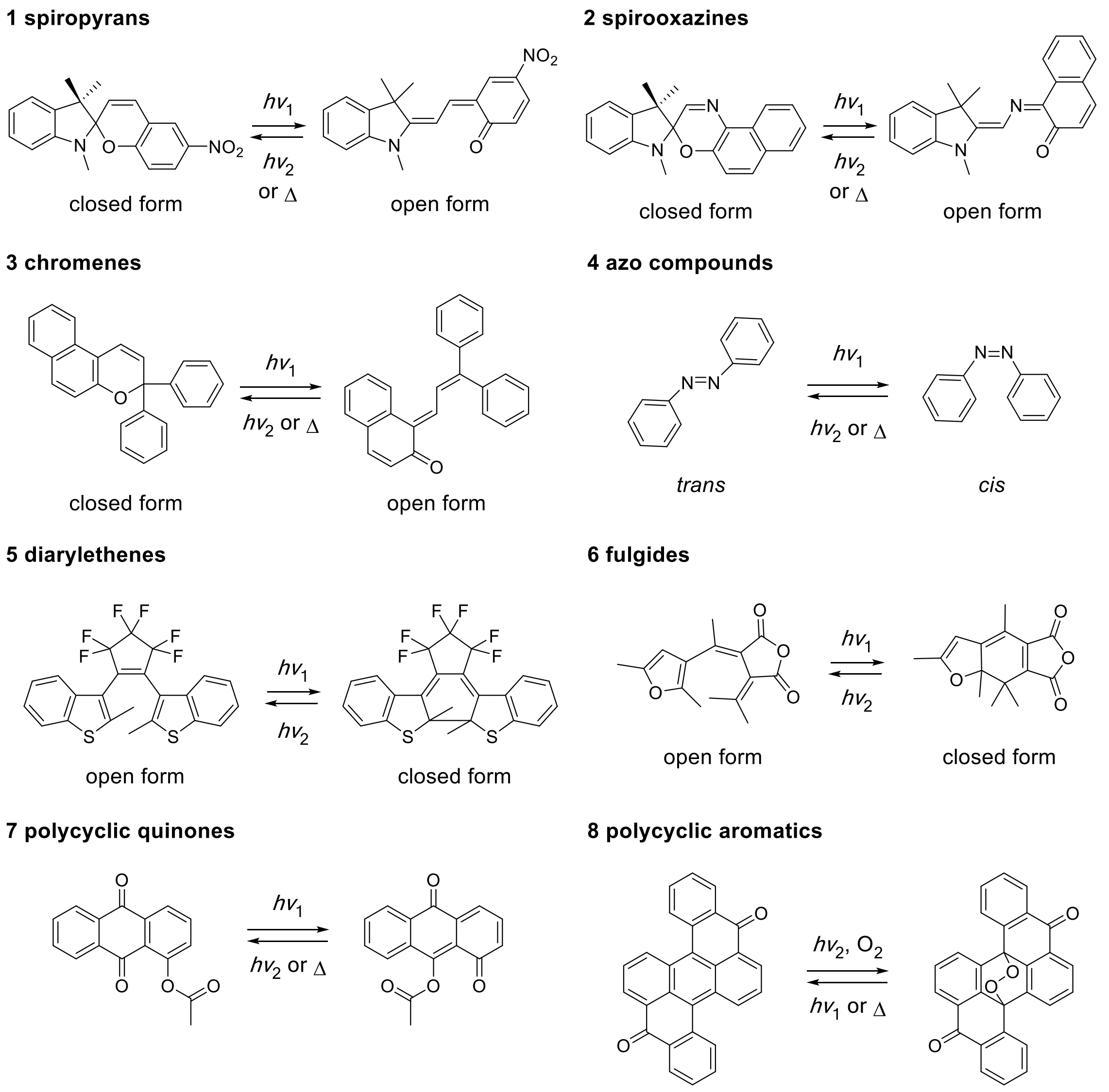

Figure 1-19 Representative photoswitch families.[119] $h\nu_1 > h\nu_2$; Δ = thermal conditions.

Spiropyrans,[120] spirooxazines[121] and chromenes[122] belong to a broad spiroheterocyclic class of type T photoswitches. These structurally closely related families undergo similar photoinduced transformations from a closed form to an open form *via* either $C_{(spiro)}$–O bond cleavage or an electrocyclic reaction. The reverse isomerisation occurs spontaneously in the dark, and can be photochemically enhanced by excitation at wavelengths longer than those for the forward reaction. While spiropyrans have been extensively studied by the academic community, spirooxazines and chromenes appear mostly in patents for industrial applications such as photochromic sunglasses.[123] A considerable amount of previous research means that compounds of varied structures are synthetically available from different methods, and rational design of molecular structures may be possible to tune photophysical and photochemical properties. For example, the known structure-property relationships allow us to envision a switch that undergoes isomerisation in response to visible light in both directions. The use of visible light is important for RESOLFT imaging because visible light is less phototoxic than UV light, causing less damage to cells and less photobleaching to dyes. The precedented structural variability of spiroheterocyclic switches also makes it possible to have open forms that have different colours, and accordingly have different dyes in FRET pairs for the purpose of multi-colour imaging. Furthermore, the closed and open forms of a photoswitch from these families usually have very different absorption spectra, which allows high PSS ratios in either direction using different wavelengths. Lastly, the lack of examples using a spiroheterocyclic photoswitch in a FRET dyad for RESOLFT microscopy provides us opportunities to develop novel systems.

Another type T family is azo compounds. They undergo *trans* and *cis* isomerisation upon light absorption. A significant number of biological studies have been carried out using azo aromatic compounds to probe and manipulate protein functions,[124–126] and even restore visual responses in blind mice.[127] However, the majority of azo compounds suffer incomplete photoswitching due to the significant overlap of the absorption spectra of the *cis* and *trans* isomers.[128]

Unlike the spiroheterocyclic and azo families above, diarylethenes are type P photoswitches, i.e. the back reaction occurs photochemically only. The photoswitching mechanism is electrocyclisation in both directions by exposure to light of different wavelengths. The diarylethene family has been extensively investigated[129–131] due to their unrivalled fatigue resistance reported in organic solvents and polymers, and a broad range of structural variations is synthetically accessible. Compared to all other photoswitches, diarylethenes have been the most advanced in terms of being employed in super-resolution microscopy. As described in Section 1.5, they have been used to achieve super-resolved imaging in biological systems, either by themselves (**Figure 1-14**) [98] or in a FRET pair (**Figure 1-12**).[104] Another type P family is fulgides, which share a similar photoswitching mechanism with diarylethenes. The fatigue resistance of fulgides is generally believed to be lower than diarylethenes because of more undesired side-reactions, particularly in the presence of oxygen.[132]

Polycyclic quinones are another type T family, but the switching mechanism is very different from the others. Upon irradiation, a polycyclic quinone undergoes intramolecular group transfer to form a product of an extended conjugation, and the reverse reaction occurs in a similar way either thermally or photochemically.[133] Compared to other type T switches, photochromism of polycyclic quinones has received significantly less attention as the variation of switching wavelengths are limited as well as the variation of migrating groups.

All the families described above involve unimolecular reactions. On the other hand, polycyclic aromatics are a representative family in which a bimolecular reaction is responsible for photochromic behaviour.[134] These compounds undergo reactions with singlet oxygen to form a product in which the conjugated system is interrupted. The reverse reaction is either thermal or photochemical by absorption at a shorter wavelength than that for the forward reaction.

As described so far, although considerable research has been devoted to studies of organic photochromism, only limited success has been reported using photoswitches from one or two families for application in RESOLFT microscopy. This impasse reflects the demanding list of requirements that such a dye must fulfill to be suitable for RESOLFT imaging (see Section 1.9). In this thesis, we focus on spiropyrans and spirooxazines, while other families like diarylethenes and fulgides have also been explored by other researchers in our group.

For RESOLFT microscopy, choosing a switch with desirable properties is critical because there are numerous requirements on this unit. For example, the scanning nature of RESOLFT microscopy imposes the criteria of strong fatigue resistance on the switch, which is notoriously difficult to achieve in aqueous media. In addition, the spectral properties of a photoswitch in the quencher form are very important but difficult to predict when the quencher form is short-lived. Starting with the choice and synthesis of the photoswitch allows us to investigate such important properties at the earliest stage. Furthermore, compared to the choice of the switch, there is large flexibility in the choice of the dye as a variety of commercial dyes are available.

1.8 Dyes and linker

A broad range of fluorescent dyes are commercially available[135] due to industrial optimisation of brightness, photostability and wavelength range.[94] Selected dyes (Thermo Fischer Scientific) from major classes[136–138] are shown in **Figure 1-20**: coumarin, e.g. Alexa430 ($\lambda_{ex}/\lambda_{em}$ = 431/540 nm in PBS); fluorescein ($\lambda_{ex}/\lambda_{em}$ = 498/517 nm in PBS); rhodamine, e.g. Atto565 ($\lambda_{ex}/\lambda_{em}$ = 564/590 nm in PBS); BODIPY, e.g.

BODIPY 581/591 ($\lambda_{ex}/\lambda_{em}$ = 589/597 nm in PBS); cyanine, e.g. Alexa647 ($\lambda_{ex}/\lambda_{em}$ = 650/671 nm in PBS). They cover a broad spectrum of colours, and possess different properties such as lipophilicity and pH sensitivity, which are important factors to consider for biological applications.

class	core structure	commercial example
coumarin	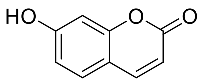	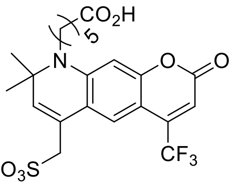 Alexa430
fluorescein		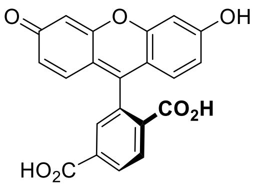
rhodamine	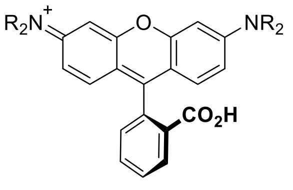	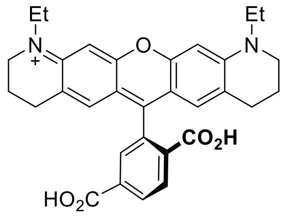 Atto565
BODIPY	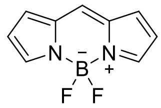	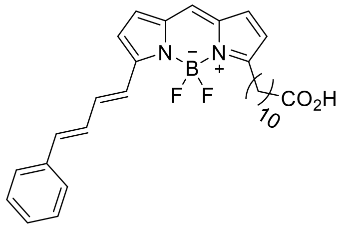 BODIPY 581/591
cyanine	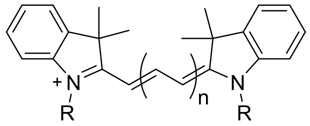	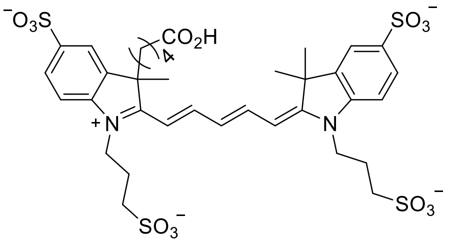 Alexa647

Figure 1-20 Selected dyes (Thermo Fischer Scientific) from major structural classes.

The choice of the covalently linked dye is made mainly based on the consideration of FRET efficiency, which largely depends on the spectral overlap between the dye emission and the switch absorption in the quenching form. The decision to prioritise the choice of the photoswitch over the dye is because requirements for the photoswitch are more demanding than the dye for RESOLFT applications (see Section 1.7.2).

After the FRET consideration narrows down a colour range for the dye, other properties like membrane permeability and aqueous solubility are taken into consideration. This may involve compromises on some properties. For example, use of lipophilic dyes potentially improves membrane penetration, but there might be self-quenching by aggregation in aqueous environments.

Another significant factor is the choice of the linker. In addition to the length limit imposed by the FRET consideration, the linker can be exploited for improved solubility in aqueous media by incorporation of a polyethylene glycol (PEG) unit. Additional functionalities can also be included for specific site labelling in cellular environments. For instance, a carboxylic acid group is converted to an *N*-hydroxysuccinimide, which is the most common reactive group for immunolabelling of proteins of interest.[139]

1.9 Requirements for synthetic RESOLFT dyes

The following is a list of criteria that a synthetic dye must fulfill before being applied in RESOLFT microscopy:

(1) A stable emissive form that persists for µs–ms and that can be switched off photochemically using visible light.

(2) High contrast of bright and dark states, which is mainly determined by the darkness of the dark state. Firstly, FRET efficiency for the individual dye-photoswitch pair needs to be high for efficient fluorescence quenching in the dark state. Secondly, the photostationary state (PSS) ratio of the switch must be high in both directions. This is important as with a low PSS, the residual fluorescence can interfere in distinguishing true ‘on’ molecules from ‘off’ molecules that are actually emissive and therefore, leads to low spatial resolution. In turn, the PSS is governed by photochemical quantum yields and molar absorption coefficients of the switch in different states.

(3) Strong fatigue resistance in biological media; this directly determines the achievable resolution under the RESOLFT principle. An n-fold increase in resolution requires the dye to show only minor degradation after n^2 switching cycles for 2D-imaging.

(4) Use of visible light illumination to trigger switching. This is important because commercial microscopes typically do not have UV lasers, and their optics have poor transmission at wavelengths shorter than 400 nm. Furthermore, UV light is damaging for cells, and it has a short penetration depth through biological tissues.

(5) Rapid switching between bright and dark states on the μs–ms timescale. Either thermal or photochemical reactions can be used. Fast switching increases image acquisition speed, which allows real-time imaging of dynamic processes.

(6) High brightness, which is the product of fluorescence quantum yield and molar absorption coefficient ($B = \Phi_f \times \varepsilon$).

(7) Low toxicity and minimal interference on the natural behaviour of cells.

(8) Cellular membrane permeability to allow intracellular staining in living cells.

(9) High labelling specificity and affinity. This can be achieved by either relying on the intrinsic properties of the molecule, or exploiting labelling techniques like immunolabelling which require incorporation of additional functionalities.

(10) Preferably dyes that fluoresce at long wavelengths in the visible region. Specifically, the red/near-infrared region is where autofluorescence and phototoxicity is minimal, and where optical transparency of tissues is maximal.[140]

1.10 Project aim

The goal of the project is to develop a generalisable strategy of constructing photoswitchable synthetic dyes, and accomplish practical applications of such dyes in RESOLFT imaging of biological systems. In this work, we exploit intramolecular FRET process in a modular dyad design, in which the reversible change in spectral properties of a photoswitch is used to modulate the fluorescence states of an appended dye. In particular, we will focus on photoswitches from spiroheterocyclic families, and a variety of compounds comprising optimal switches and dyes will be investigated with the aim of achieving live-cell super-resolved imaging.

Chapter 2 details synthesis and characterisation of spiropyran photoswitches and a dyad that consists of a red-emitting rhodamine dye and a spirothiopyran switch. The potential of the dyad system is examined by live cell imaging.

Chapter 3 introduces spirooxazine photoswitches with comprehensive characterisation of their photophysical and photochemical properties. In addition to X-ray crystallography analysis and DFT calculations, ultrafast spectroscopies are also performed to elucidate the photoswitching kinetics.

Chapter 4 continues to describe dyads based on a spirooxazine switch and an orange rhodamine dye. Photophysical characterisation is detailed, followed by exploring the capacity of dyads in RESOLFT live cell imaging. Investigation into property improvement is also presented.

Chapter 5 advances the dyad design by exploiting strategies of selectively labelling biomolecules of interest. Additional functionalities are incorporated into the molecular construct, and several synthetic approaches to such triads are developed. Detailed examination of their switching behaviour in cells is discussed.

Chapter 6 explores the performance of our compounds in cell-mimicking vesicles, and the possibility for their application in RESOLFT microscopy.

Chapter 7 presents conclusions from this project and prospective work.

1.11 References

[1] C. Eggeling, K. I. Willig, S. J. Sahl, S. W. Hell, *Q. Rev. Biophys.* **2015**, *48*, 178–243.
[2] E. Abbe, *Arch. Für Mikrosk. Anat.* **1873**, *9*, 413–418.
[3] M. Born, E. Wolf, *Principles of Optics*, Cambridge University Press, **2007**.
[4] S. W. Hell, *Angew. Chem. Int. Ed.* **2015**, *54*, 8054–8066.
[5] S. W. Hell, J. Wichmann, *Opt. Lett.* **1994**, *19*, 780–782.
[6] T. A. Klar, S. W. Hell, *Opt. Lett.* **1999**, *24*, 954–956.
[7] W. Reusch, “Photochemistry,” can be found under https://www2.chemistry.msu.edu/faculty/reusch/virttxtjml/photchem.htm, **2018**.
[8] J. R. Lakowicz, *Principles of Fluorescence Spectroscopy*, Springer Science & Business Media, **2007**.
[9] M. Kasha, *Discuss. Faraday Soc.* **1950**, *9*, 14–19.
[10] J. W. Verhoeven, *Pure Appl. Chem.* **1996**, *68*, 2223–2286.
[11] E. H. Synge, *Lond. Edinb. Dublin Philos. Mag. J. Sci.* **1928**, *6*, 356–362.
[12] E. H. Synge, *Lond. Edinb. Dublin Philos. Mag. J. Sci.* **1931**, *11*, 65–80.
[13] E. H. Synge, *Lond. Edinb. Dublin Philos. Mag. J. Sci.* **1932**, *13*, 297–300.
[14] R. C. Dunn, *Chem. Rev.* **1999**, *99*, 2891–2928.
[15] A. Lewis, M. Isaacson, A. Harootunian, A. Muray, *Ultramicroscopy* **1984**, *13*, 227–231.
[16] D. W. Pohl, W. Denk, M. Lanz, *Appl. Phys. Lett.* **1984**, *44*, 651–653.
[17] E. Betzig, J. K. Trautman, *Science* **1992**, *257*, 189–195.
[18] Y. Oshikane, T. Kataoka, M. Okuda, S. Hara, H. Inoue, M. Nakano, *Sci. Technol. Adv. Mater.* **2007**, *8*, 181–185.
[19] F. de Lange, A. Cambi, R. Huijbens, B. de Bakker, W. Rensen, M. Garcia-Parajo, N. van Hulst, C. G. Figdor, *J. Cell Sci.* **2001**, *114*, 4153–4160.
[20] M. Hausmann, B. Liebe, B. Perner, M. Jerratsch, K.-O. Greulich, H. Scherthan, *Micron* **2003**, *34*, 441–447.
[21] A. Ianoul, M. Street, D. Grant, J. Pezacki, R. S. Taylor, L. J. Johnston, *Biophys. J.* **2004**, *87*, 3525–3535.

[22] S. Rieti, V. Manni, A. Lisi, L. Giuliani, D. Sacco, E. D'Emilia, A. Cricenti, R. Generosi, M. Luce, S. Grimaldi, *J. Microsc.* **2004**, *213*, 20–28.

[23] A. Ianoul, D. D. Grant, Y. Rouleau, M. Bani-Yaghoub, L. J. Johnston, J. P. Pezacki, *Nat. Chem. Biol.* **2005**, *1*, 196–202.

[24] C. Höppener, J. P. Siebrasse, R. Peters, U. Kubitscheck, A. Naber, *Biophys. J.* **2005**, *88*, 3681–3688.

[25] B. I. de Bakker, F. de Lange, A. Cambi, J. P. Korterik, E. M. H. P. van Dijk, N. F. van Hulst, C. G. Figdor, M. F. Garcia-Parajo, *ChemPhysChem* **2007**, *8*, 1473–1480.

[26] M. Zweyer, B. Troian, V. Spreafico, S. Prato, *J. Microsc.* **2008**, *229*, 440–446.

[27] E. Trevisan, E. Fabbretti, N. Medic, B. Troian, S. Prato, F. Vita, G. Zabucchi, M. Zweyer, *NeuroImage* **2010**, *49*, 517–524.

[28] E. Betzig, A. Lewis, A. Harootunian, M. Isaacson, E. Kratschmer, *Biophys. J.* **1986**, *49*, 269–279.

[29] T. S. van Zanten, A. Cambi, M. F. Garcia-Parajo, *Biochim. Biophys. Acta BBA - Biomembr.* **2010**, *1798*, 777–787.

[30] S. J. Sahl, S. W. Hell, S. Jakobs, *Nat. Rev. Mol. Cell Biol.* **2017**, *18*, 685–701.

[31] S. W. Hell, S. J. Sahl, M. Bates, X. Zhuang, R. Heintzmann, M. J. Booth, Joerg Bewersdorf, G. Shtengel, H. Hess, P. Tinnefeld, et al., *J. Phys. Appl. Phys.* **2015**, *48*, 443001.

[32] A. G. Godin, B. Lounis, L. Cognet, *Biophys. J.* **2014**, *107*, 1777–1784.

[33] L. Schermelleh, R. Heintzmann, H. Leonhardt, *J. Cell Biol.* **2010**, *190*, 165–175.

[34] B. Huang, M. Bates, X. Zhuang, *Annu. Rev. Biochem.* **2009**, *78*, 993–1016.

[35] S. W. Hell, *Science* **2007**, *316*, 1153–1158.

[36] M. G. L. Gustafsson, *J. Microsc.* **2000**, *198*, 82–87.

[37] M. G. L. Gustafsson, *Proc. Natl. Acad. Sci.* **2005**, *102*, 13081–13086.

[38] D. Li, L. Shao, B.-C. Chen, X. Zhang, M. Zhang, B. Moses, D. E. Milkie, J. R. Beach, J. A. Hammer, M. Pasham, et al., *Science* **2015**, *349*, aab3500.

[39] C. Lesterlin, G. Ball, L. Schermelleh, D. J. Sherratt, *Nature* **2014**, *506*, 249–253.

[40] E. H. Rego, L. Shao, J. J. Macklin, L. Winoto, G. A. Johansson, N. Kamps-Hughes, M. W. Davidson, M. G. L. Gustafsson, *Proc. Natl. Acad. Sci.* **2012**, *109*, E135–E143.

[41] L. Shao, P. Kner, E. H. Rego, M. G. L. Gustafsson, *Nat. Methods* **2011**, *8*, 1044–1046.

[42] M. J. Rust, M. Bates, X. Zhuang, *Nat. Methods* **2006**, *3*, 793–796.

[43] E. Betzig, G. H. Patterson, R. Sougrat, O. W. Lindwasser, S. Olenych, J. S. Bonifacino, M. W. Davidson, J. Lippincott-Schwartz, H. F. Hess, *Science* **2006**, *313*, 1642–1645.

[44] S. T. Hess, T. P. K. Girirajan, M. D. Mason, *Biophys. J.* **2006**, *91*, 4258–4272.

[45] M. Heilemann, S. van de Linde, A. Mukherjee, M. Sauer, *Angew. Chem. Int. Ed.* **2009**, *48*, 6903–6908.

[46] V. N. Belov, M. L. Bossi, J. Fölling, V. P. Boyarskiy, S. W. Hell, *Chem. – Eur. J.* **2009**, *15*, 10762–10776.

[47] R. E. Thompson, D. R. Larson, W. W. Webb, *Biophys. J.* **2002**, *82*, 2775–2783.

[48] H. Shroff, C. G. Galbraith, J. A. Galbraith, E. Betzig, *Nat. Methods* **2008**, *5*, 417–423.

[49] M. Lakadamyali, H. Babcock, M. Bates, X. Zhuang, J. Lichtman, *PLOS ONE* **2012**, *7*, e30826.

[50] B. Huang, S. A. Jones, B. Brandenburg, X. Zhuang, *Nat. Methods* **2008**, *5*, 1047–1052.

[51] B. Huang, W. Wang, M. Bates, X. Zhuang, *Science* **2008**, *319*, 810–813.

[52] K. Xu, H. P. Babcock, X. Zhuang, *Nat. Methods* **2012**, *9*, 185–188.

[53] K. Xu, G. Zhong, X. Zhuang, *Science* **2013**, *339*, 452–456.

[54] S. T. Hess, T. J. Gould, M. V. Gudheti, S. A. Maas, K. D. Mills, J. Zimmerberg, *Proc. Natl. Acad. Sci.* **2007**, *104*, 17370–17375.

[55] P. Dedecker, G. C. H. Mo, T. Dertinger, J. Zhang, *Proc. Natl. Acad. Sci.* **2012**, *109*, 10909–10914.

[56] S. Wilmes, M. Staufenbiel, D. Liße, C. P. Richter, O. Beutel, K. B. Busch, S. T. Hess, J. Piehler, *Angew. Chem. Int. Ed.* **2012**, *51*, 4868–4871.

[57] S. W. Hell, *Nat. Biotechnol.* **2003**, *21*, 1347–1355.

[58] S. W. Hell, S. Jakobs, L. Kastrup, *Appl. Phys. A* **2003**, *77*, 859–860.

[59] M. Hofmann, C. Eggeling, S. Jakobs, S. W. Hell, *Proc. Natl. Acad. Sci.* **2005**, *102*, 17565–17569.

[60] T. Grotjohann, I. Testa, M. Leutenegger, H. Bock, N. T. Urban, F. Lavoie-Cardinal, K. I. Willig, C. Eggeling, S. Jakobs, S. W. Hell, *Nature* **2011**, *478*, 204–208.

[61] I. Testa, E. D’Este, N. T. Urban, F. Balzarotti, S. W. Hell, *Nano Lett.* **2015**, *15*, 103–106.

[62] G. Vicidomini, P. Bianchini, A. Diaspro, *Nat. Methods* **2018**, *15*, 173–182.

[63] S. W. Hell, M. Kroug, *Appl. Phys. B* **1995**, *60*, 495–497.

[64] S. Bretschneider, C. Eggeling, S. W. Hell, *Phys. Rev. Lett.* **2007**, *98*, 218103:1–4.

[65] J. Fölling, M. Bossi, H. Bock, R. Medda, C. A. Wurm, B. Hein, S. Jakobs, C. Eggeling, S. W. Hell, *Nat. Methods* **2008**, *5*, 943–945.

[66] S. W. Hell, *Phys. Lett. A* **2004**, *326*, 140–145.

[67] A. Chmyrov, J. Keller, T. Grotjohann, M. Ratz, E. d’Este, S. Jakobs, C. Eggeling, S. W. Hell, *Nat. Methods* **2013**, *10*, 737–740.

[68] P. Bingen, M. Reuss, J. Engelhardt, S. W. Hell, *Opt. Express* **2011**, *19*, 23716–23726.

[69] V. Westphal, S. W. Hell, *Phys. Rev. Lett.* **2005**, *94*, 143903:1–4.

[70] K. I. Willig, R. R. Kellner, R. Medda, B. Hein, S. Jakobs, S. W. Hell, *Nat. Methods* **2006**, *3*, 721–723.

[71] B. Hein, K. I. Willig, S. W. Hell, *Proc. Natl. Acad. Sci.* **2008**, *105*, 14271–14276.

[72] J. Tønnesen, G. Katona, B. Rózsa, U. V. Nägerl, *Nat. Neurosci.* **2014**, *17*, 678–685.

[73] U. V. Nägerl, K. I. Willig, B. Hein, S. W. Hell, T. Bonhoeffer, *Proc. Natl. Acad. Sci.* **2008**, *105*, 18982–18987.

[74] V. Westphal, S. O. Rizzoli, M. A. Lauterbach, D. Kamin, R. Jahn, S. W. Hell, *Science* **2008**, *320*, 246–249.

[75] S. Berning, K. I. Willig, H. Steffens, P. Dibaj, S. W. Hell, *Science* **2012**, *335*, 551.

[76] S. Wäldchen, J. Lehmann, T. Klein, S. van de Linde, M. Sauer, *Sci. Rep.* **2015**, *5*, 15348.

[77] P. Tinnefeld, C. Eggeling, S. W. Hell, Ebook Library, *Far-Field Optical Nanoscopy,* Springer Science & Business Media, **2015**.

[78] J. Hotta, E. Fron, P. Dedecker, K. P. F. Janssen, C. Li, K. Müllen, B. Harke, J. Bückers, S. W. Hell, J. Hofkens, *J. Am. Chem. Soc.* **2010**, *132*, 5021–5023.

[79] C. Eggeling, J. Widengren, R. Rigler, C. A. M. Seidel, *Anal. Chem.* **1998**, *70*, 2651–2659.

[80] M. Dyba, S. W. Hell, *Appl. Opt.* **2003**, *42*, 5123–5129.

[81] T. Grotjohann, I. Testa, M. Reuss, T. Brakemann, C. Eggeling, S. W. Hell, S. Jakobs, *eLife* **2012**, *1*, e00248.

[82] A. Acharya, A. M. Bogdanov, B. L. Grigorenko, K. B. Bravaya, A. V. Nemukhin, K. A. Lukyanov, A. I. Krylov, *Chem. Rev.* **2017**, *117*, 758–795.

[83] K. M. Marks, G. P. Nolan, *Nat. Methods* **2006**, *3*, 591–596.

[84] K. A. Lukyanov, A. F. Fradkov, N. G. Gurskaya, M. V. Matz, Y. A. Labas, A. P. Savitsky, M. L. Markelov, A. G. Zaraisky, X. Zhao, Y. Fang, et al., *J. Biol. Chem.* **2000**, *275*, 25879–25882.

[85] R. Ando, H. Mizuno, A. Miyawaki, *Science* **2004**, *306*, 1370–1373.

[86] U. Böhm, S. W. Hell, R. Schmidt, *Nat. Commun.* **2016**, *7*, 10504.

[87] T. Brakemann, A. C. Stiel, G. Weber, M. Andresen, I. Testa, T. Grotjohann, M. Leutenegger, U. Plessmann, H. Urlaub, C. Eggeling, et al., *Nat. Biotechnol.* **2011**, *29*, 942–947.

[88] F. Pennacchietti, E. O. Serebrovskaya, A. R. Faro, I. I. Shemyakina, N. G. Bozhanova, A. A. Kotlobay, N. G. Gurskaya, A. Bodén, J. Dreier, D. M. Chudakov, et al., *Nat. Methods* **2018**, *15*, 601–604.

[89] C. Gregor, S. C. Sidenstein, M. Andresen, S. J. Sahl, J. G. Danzl, S. W. Hell, *Sci. Rep.* **2018**, *8*, 2724.

[90] X. Zhang, M. Zhang, D. Li, W. He, J. Peng, E. Betzig, P. Xu, *Proc. Natl. Acad. Sci.* **2016**, *113*, 10364–10369.

[91] R. E. Campbell, O. Tour, A. E. Palmer, P. A. Steinbach, G. S. Baird, D. A. Zacharias, R. Y. Tsien, *Proc. Natl. Acad. Sci.* **2002**, *99*, 7877–7882.

[92] K. A. Lukyanov, D. M. Chudakov, S. Lukyanov, V. V. Verkhusha, *Nat. Rev. Mol. Cell Biol.* **2005**, *6*, 885–890.

[93] M. Fernández-Suárez, A. Y. Ting, *Nat. Rev. Mol. Cell Biol.* **2008**, *9*, 929–943.

[94] B. N. G. Giepmans, S. R. Adams, M. H. Ellisman, R. Y. Tsien, *Science* **2006**, *312*, 217–224.

[95] G. Lukinavičius, K. Umezawa, N. Olivier, A. Honigmann, G. Yang, T. Plass, V. Mueller, L. Reymond, I. R. Corrêa Jr, Z.-G. Luo, et al., *Nat. Chem.* **2013**, *5*, 132–139.

[96] L. Xue, I. A. Karpenko, J. Hiblot, K. Johnsson, *Nat. Chem. Biol.* **2015**, *11*, 917–923.

[97] J. C. Crano, R. J. Guglielmetti, Eds. , *Organic Photochromic and Thermochromic Compounds: Volume 1: Main Photochromic Families*, Kluwer Academic Publishers, **2002**.

[98] B. Roubinet, M. L. Bossi, P. Alt, M. Leutenegger, H. Shojaei, S. Schnorrenberg, S. Nizamov, M. Irie, V. N. Belov, S. W. Hell, *Angew. Chem. Int. Ed.* **2016**, *55*, 15429–15433.

[99] G. T. Dempsey, M. Bates, W. E. Kowtoniuk, D. R. Liu, R. Y. Tsien, X. Zhuang, *J. Am. Chem. Soc.* **2009**, *131*, 18192–18193.

[100] J. Kwon, J. Hwang, J. Park, G. R. Han, K. Y. Han, S. K. Kim, *Sci. Rep.* **2015**, *5*, 17804–17811.

[101] F. M. Raymo, M. Tomasulo, *J. Phys. Chem. A* **2005**, *109*, 7343–7352.

[102] I. Yildiz, E. Deniz, F. M. Raymo, *Chem. Soc. Rev.* **2009**, *38*, 1859–1867.

[103] D. Bléger, S. Hecht, *Angew. Chem. Int. Ed.* **2015**, *54*, 11338–11349.

[104] C. Li, Z. Hu, M. P. Aldred, L.-X. Zhao, H. Yan, G.-F. Zhang, Z.-L. Huang, A. D. Q. Li, M.-Q. Zhu, *Macromolecules* **2014**, *47*, 8594–8601.

[105] M. Bossi, J. Fölling, M. Dyba, V. Westphal, S. W. Hell, *New J. Phys.* **2006**, *8*, 275.

[106] M. Bossi, V. Belov, S. Polyakova, S. W. Hell, *Angew. Chem. Int. Ed.* **2006**, *45*, 7462–7465.

[107] T. Fukaminato, T. Doi, N. Tamaoki, K. Okuno, Y. Ishibashi, H. Miyasaka, M. Irie, *J. Am. Chem. Soc.* **2011**, *133*, 4984–4990.

[108] J. Fölling, S. Polyakova, V. Belov, A. van Blaaderen, M. L. Bossi, S. W. Hell, *Small* **2008**, *4*, 134–142.

[109] C. Li, H. Yan, L.-X. Zhao, G.-F. Zhang, Z. Hu, Z.-L. Huang, M.-Q. Zhu, *Nat. Commun.* **2014**, *5*, 5709.

[110] D. E. Chandler, R. W. Roberson, *Bioimaging: Current Concepts in Light & Electron Microscopy*, Jones & Bartlett Publishers, **2009**.

[111] S. C. Blanchard, H. D. Kim, R. L. Gonzalez, J. D. Puglisi, S. Chu, *Proc. Natl. Acad. Sci.* **2004**, *101*, 12893–12898.

[112] J. Chen, Y. Cheng, *Opt. Lett.* **2009**, *34*, 1831–1833.

[113] J. Chen, Y. Cheng, *Opt. Commun.* **2012**, *285*, 1404–1407.

[114] K. Mutoh, M. Sliwa, J. Abe, *J. Phys. Chem. C* **2013**, *117*, 4808–4814.

[115] J. Wang, Y. Lv, W. Wan, X. Wang, A. D. Q. Li, Z. Tian, *ACS Appl. Mater. Interfaces* **2016**, *8*, 4399–4406.

[116] J.-X. Liu, B. Xin, C. Li, N.-H. Xie, W.-L. Gong, Z.-L. Huang, M.-Q. Zhu, *ACS Appl. Mater. Interfaces* **2017**, *9*, 10338–10343.

[117] Y. Xiong, P. Rivera-Fuentes, E. Sezgin, A. Vargas Jentzsch, C. Eggeling, H. L. Anderson, *Org. Lett.* **2016**, *18*, 3666–3669.

[118] Y. Xiong, A. Vargas Jentzsch, J. W. M. Osterrieth, E. Sezgin, I. V. Sazanovich, K. Reglinski, S. Galiani, A. W. Parker, C. Eggeling, H. L. Anderson, *Chem. Sci.* **2018**, *9*, 3029–3040.

[119] H. Bouas-Laurent, H. Dürr, *Pure Appl. Chem.* **2001**, *73*, 639–665.

[120] R. C. Bertelson, in *Org. Photochromic Thermochromic Compd. Vol. 1 Main Photochromic Fam.* (Eds.: J.C. Crano, R.J. Guglielmetti), Kluwer Academic Publishers, **2002**, pp. 11–83.

[121] M. Shuichi, in *Org. Photochromic Thermochromic Compd. Vol. 1 Main Photochromic Fam.* (Eds.: J.C. Crano, R.J. Guglielmetti), Kluwer Academic Publishers, **2002**, pp. 85–110.

[122] V. G. Barry, in *Org. Photochromic Thermochromic Compd. Vol. 1 Main Photochromic Fam.* (Eds.: J.C. Crano, R.J. Guglielmetti), Kluwer Academic Publishers, **2002**, pp. 111–206.

[123] S. N. Corns, S. M. Partington, A. D. Towns, *Color. Technol.* **2009**, *125*, 249–261.

[124] D. B. Konrad, J. A. Frank, D. Trauner, *Chem. – Eur. J.* **2016**, *22*, 4364–4368.

[125] Y. Guo, T. Wolter, T. Kubař, M. Sumser, D. Trauner, M. Elstner, *PLOS ONE* **2015**, *10*, e0135399.

[126] J. A. Frank, D. A. Yushchenko, D. J. Hodson, N. Lipstein, J. Nagpal, G. A. Rutter, J.-S. Rhee, A. Gottschalk, N. Brose, C. Schultz, et al., *Nat. Chem. Biol.* **2016**, *12*, 755–762.

[127] A. Polosukhina, J. Litt, I. Tochitsky, J. Nemargut, Y. Sychev, I. De Kouchkovsky, T. Huang, K. Borges, D. Trauner, R. N. Van Gelder, et al., *Neuron* **2012**, *75*, 271–282.

[128] B. L. Feringa, W. R. Browne, Eds. , *Molecular Switches*, Wiley VCH, Weinheim, Germany, **2011**.

[129] M. Irie, *Chem. Rev.* **2000**, *100*, 1685–1716.

[130] V. A. Barachevsky, Y. P. Strokach, Y. A. Puankov, M. M. Krayushkin, *J. Phys. Org. Chem.* **2007**, *20*, 1007–1020.

[131] M. Irie, T. Fukaminato, K. Matsuda, S. Kobatake, *Chem. Rev.* **2014**, *114*, 12174–12277.

[132] F. Mei-gong, Y. Lianhe, Z. Weih, in *Org. Photochromic Thermochromic Compd. Vol. 1 Main Photochromic Fam.* (Eds.: J.C. Crano, R.J. Guglielmetti), Kluwer Academic Publishers, **2002**, pp. 141–206.

[133] N. P. Gritsan, L. S. Klimenko, *J. Photochem. Photobiol. Chem.* **1993**, *70*, 103–117.

[134] H.-D. Brauer, in *Photochromism Mol. Syst.* (Eds.: D. Heinz, H. Bouas-Laurent), Elsevier, **2003**, pp. 631–653.
[135] R. P. Haugland, *The Handbook: A Guide to Fluorescent Probes and Labeling Technologies*, Molecular Probes, **2005**.
[136] L. D. Lavis, R. T. Raines, *ACS Chem. Biol.* **2008**, *3*, 142–155.
[137] L. D. Lavis, R. T. Raines, *ACS Chem. Biol.* **2014**, *9*, 855–866.
[138] Q. Zheng, L. D. Lavis, *Curr. Opin. Chem. Biol.* **2017**, *39*, 32–38.
[139] G. Mattson, E. Conklin, S. Desai, G. Nielander, M. D. Savage, S. Morgensen, *Mol. Biol. Rep.* **1993**, *17*, 167–183.
[140] U. Kubitscheck, Ed. , *Fluorescence Microscopy: From Principles to Biological Applications*, Wiley VCH, **2013**.

Chapter 2

Spiropyrans

2 Spiropyrans

2.1 Introduction

Within the wealth of photochromic switches, we have chosen to focus on the spiroheterocyclic families,[1,2] i.e. spiropyrans and spirooxazines. For both families, reversible photochromism arises from interconversion between a closed form (e.g. spiropyran, **SP**) that is colourless or slightly yellow, and an open form (merocyanine, **MC**) that is intensely coloured. Upon photoactivation, the closed form undergoes ring opening *via* either heterolytic cleavage of the $C_{(spiro)}$–O bond, or electrocyclisation, to give the open form, which absorbs at a longer wavelength due to an extended π system (**Figure 2-1**).[3] Both families belong to thermal (T) type of photoswitches, i.e. the forward reaction is driven by light and the reversion occurs spontaneously in the dark. Additionally, the thermal back reaction can be photochemically accelerated.[4]

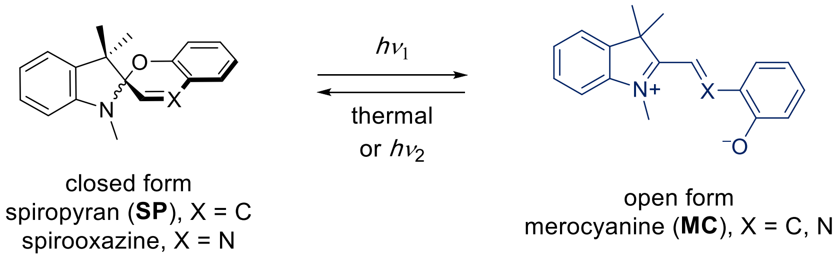

Figure 2-1 Photochromism of spiropyrans and spirooxazines, both of which belong to thermal (T) type of photoswitch families. $h\nu_1 > h\nu_2$.

Since the first report on the photochromic behaviour in 1952,[5] spiro(benzo)pyrans have been investigated extensively as molecular photoswitches for diverse applications, including information storage and optical memory, biopolymers, photocontrol of biomolecules, light-responsive lenses, and molecular devices, to name a few.[3,6–9] For application in RESOLFT microscopy, use of visible light illumination to trigger switching is crucial as discussed in Chapter 1. This is because in contrast to UV light, visible light causes less phototoxicity to cells and less photobleaching to dyes, allows deeper tissue penetration and is more compatible with commercial microscopes. Extending the π-conjugation from benzopyran to naphthopyran induces a red shift in the absorption spectrum of the closed SP form, and shifts the wavelength of light required for ring-opening into the visible region,[8] providing an ideal platform for multi-colour fluorescence quenching.

In this Chapter, we report a photoswitchable, far-red emitting, small-molecule dyad, comprising the bright biocompatible fluorophore, silicon rhodamine (SiR),[10,11] and a spironaphthothiopyran as a photoswitchable quencher. Despite the large amount of research on spirobenzopyrans,[6,8,12–14] spironaphthopyrans have received little attention,[8] and spironaphthothiopyrans have not previously been reported. The majority of the work presented here has been published.[15]

2.2 Synthesis

The compounds used in this study were prepared as shown in **Scheme 2-1**. The synthesis starts with Duff formylation of naphthol **1** to give aldehyde **2**. The sulfur analogue **3** was synthesised from the reaction of **2** with dimethylthiocarbamoyl chloride, *via* a Newman-Kwart rearrangement and deprotection. Compound **4** was used to prepare photochromes **5** and **6** by Knoevenagel condensation with aldehydes **2** and **3**. Compound **6** was subsequently attached to the silicon rhodamine (SiR) derivative **7** to afford **Dyad 1**. We chose SiR dye because its emission has a strong spectral overlap with the absorption spectrum of the open form of the switch, which gives high FRET efficiency (see later).

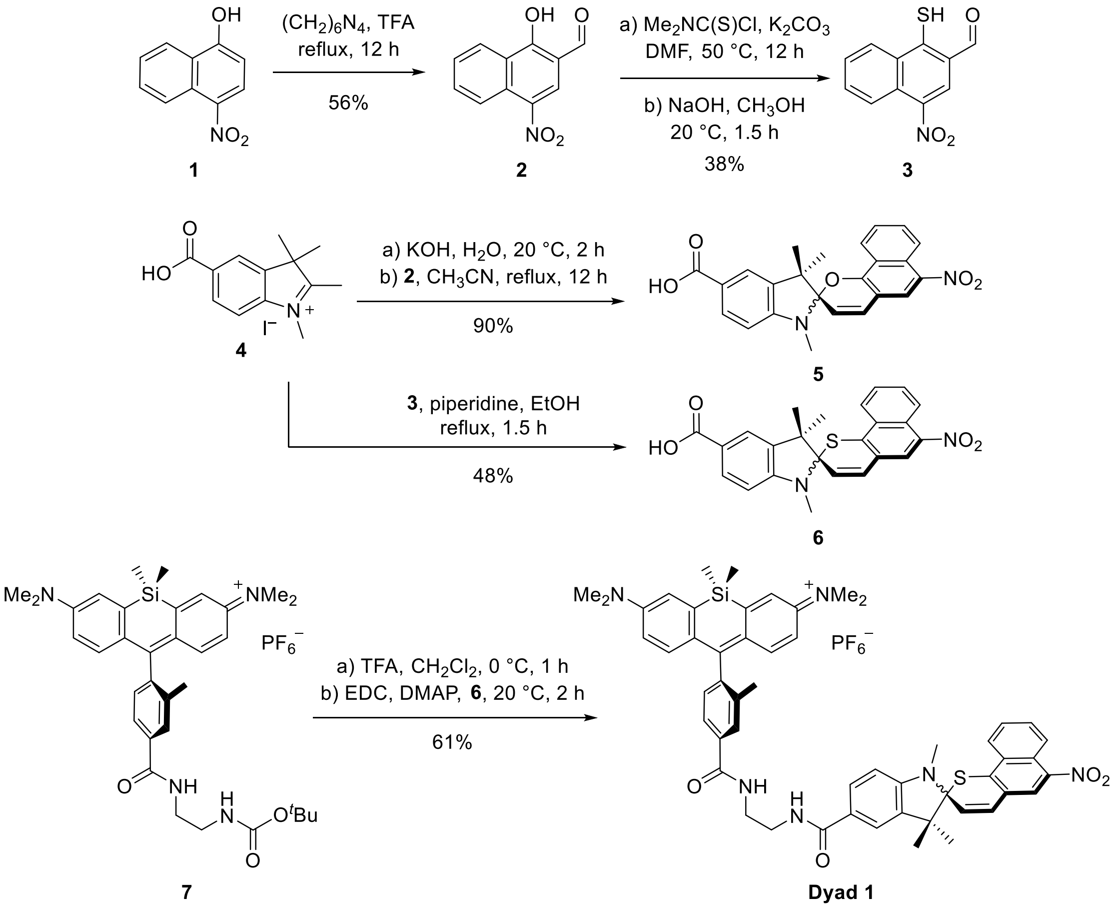

Scheme 2-1 Synthesis of **Dyad 1**.

2.3 Characterisation of switches

The photophysical and photochemical properties of spironaphthopyran **5** and spironaphthothiopyran **6** were characterised to check whether they are suitable photoswitchable FRET quenchers in our molecular design.

2.3.1 Photochromic behaviour

Upon exposure of 405 nm irradiation, organic solutions of both compounds rapidly change colour as the pale yellow SP isomers are converted to the blue-green MC forms (example of switch **6** in **Figure 2-2**). The absorption spectrum of the photostationary state (PSS) displays a new peak at λ_{max} = 630 nm due to the MC form. The experiments were carried out using 1.1 W/cm^2 of 405 nm and 2.1 W/cm^2 of 630 nm LED light sources. The intensity and duration of the irradiation were adjusted to optimise the switching performance and minimise photobleaching (**Figure 2-3**).

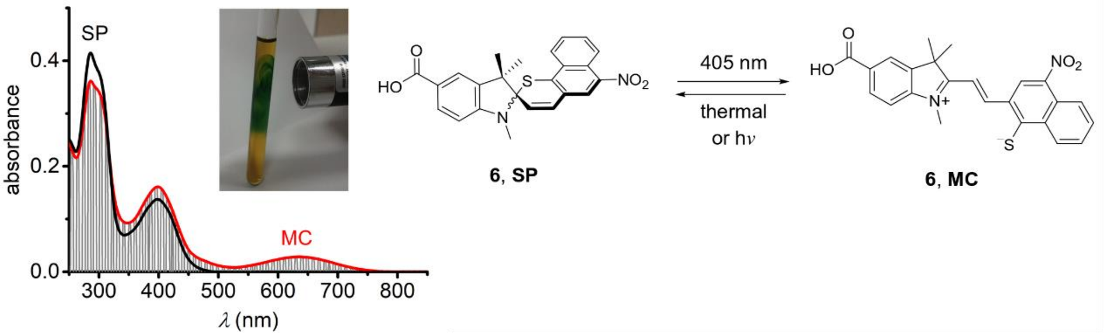

Figure 2-2 UV-vis absorption spectra of switch **6** in CH_3OH (14 μM) before (black line, SP) and after (red line, MC/PSS) irradiation at 405 nm. Before the second spectrum was recorded, the sample was irradiated for 5.5 s (1.1 W/cm^2); it was then irradiated with 100 ms pulses every 300 ms while recording the spectrum to maintain the presence of the MC form. The inset shows a solution of switch **6** in DMSO under irradiation with a blue laser pointer (405 nm, 1 mW); irradiation causes a colour change from yellow to green.

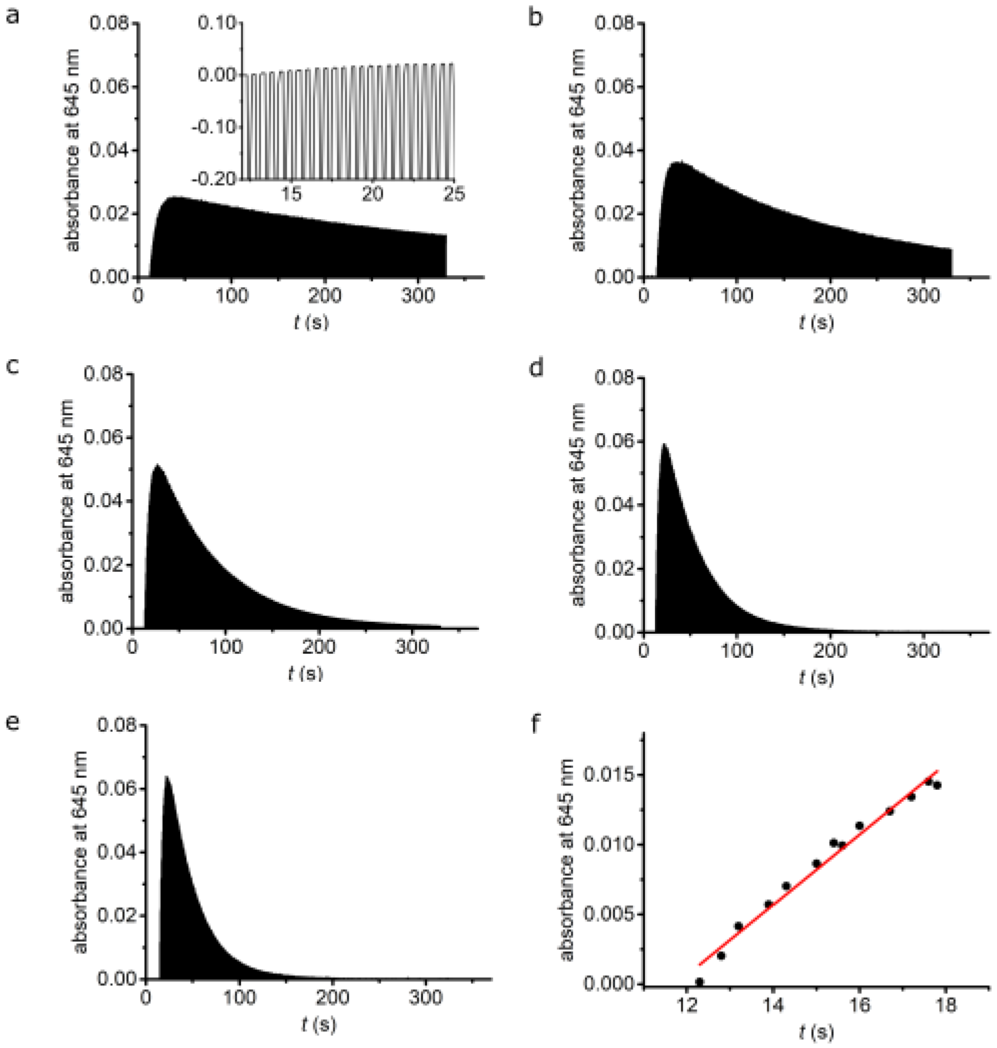

Figure 2-3 Optimisation of irradiation length and power intensity of 405 nm light. A methanol solution of compound **6** (13.8 µM, 2.0 mL) was irradiated with pulses of 405 nm LED light at an indicated power intensity, and a kinetic trace of absorbance at 645 nm was recorded over 330 s. $t_{opt} = t_{max,abs} \times$ [150 ms/(150 + 400) ms], where 150 ms is the irradiation length and 400 ms is the interval between each pulse. a) 45 mW, t_{opt} ~ 7.0 s. The inset is the zoom-in kinetic trace at t = 12–25 s; b) 80 mW, t_{opt} ~ 5.5 s; c) 184 mW, t_{opt} ~ 4.0 s; d) 288 mW, t_{opt} ~ 3.0 s; e) 358 mW, t_{opt} ~ 2.0 s. f) Part of the reconstructed kinetic trace of a), and the linear fit. m = 0.00277 s^{-1} (used in calculation of quantum yield of ring opening), R^2 = 0.981.

In the absence of ambient light, the SP/MC equilibrium of compound **5** is sensitive to the solvent polarity, with the MC form becoming more stable in polar solvents, e.g. DMSO and H_2O (**Figure 2-4**). In aqueous solution, **5** exists mainly as the MC isomer and no evidence of photoswitching was detected (**Figure 2-5**).

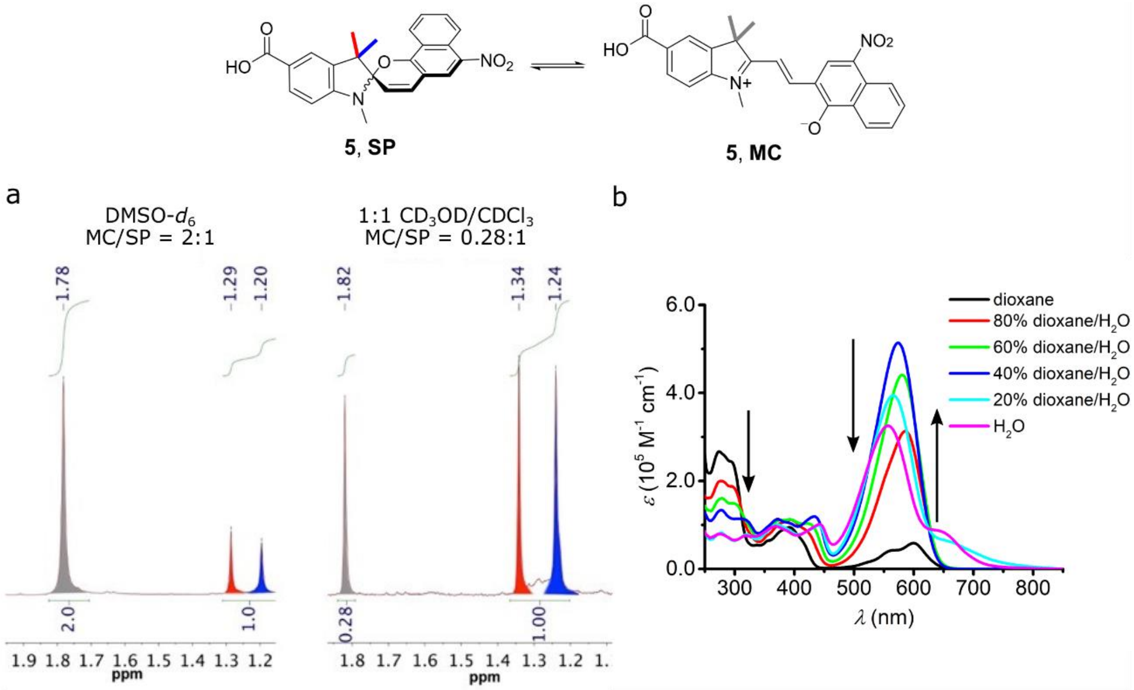

Figure 2-4 Equilibrium between the SP and MC forms of compound **5**. a) NMR signals of compound **5** in DMSO-d_6 and 1:1 mixture of CD_3OD:$CDCl_3$. The sections of the ^1H NMR (400 MHz, 25 °C) spectra show the resonances for the *gem*-dimethyl groups in compound **5**. The signals are present for both MC and SP forms, with the ratio 2:1 in DMSO-d_6 and 0.28:1 in 1:1 mixture of CD_3OD:$CDCl_3$. b) UV-vis absorption spectra of compound **5** in mixtures of 1,4-dioxane/H_2O at 25 °C. The equilibrium of the SP and MC forms is shifted towards the MC form upon increasing the fraction of H_2O.

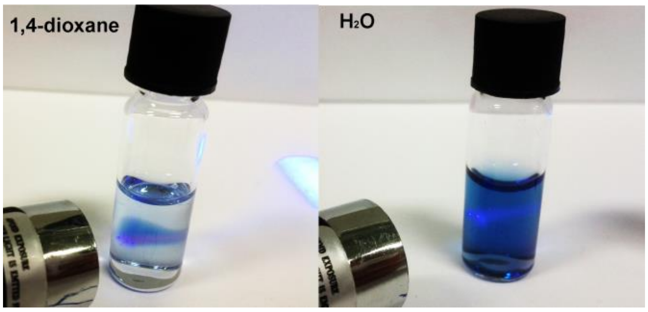

Figure 2-5 Solvent-dependent photochromism of compound **5** in pure 1,4-dioxane (left) and H_2O (right). No photoswitching was observed in H_2O. Photochromism was induced by illumination of the sample with a laser pointer (405 nm, 1 mW).

In contrast, spironaphthothiopyran **6** exhibits excellent positive photochromism in polar and apolar media. ^1H NMR spectroscopy in polar solvents shows that this compound exists exclusively in the SP form (**Figure 2-6**a), as confirmed by the UV-vis absorption spectra; the MC form is not detected at equilibrium in pure water, i.e. no signals beyond 600 nm (**Figure 2-6**b). In the context of a dyad design, it is important that the photoswitch is fully in the inactive quencher form, i.e. SP state in the absence of light in order to have high contrast between bright (photoswitch in SP state) and dark (photoswitch in MC state) states. Hence, the following experiments focus on compound **6**.

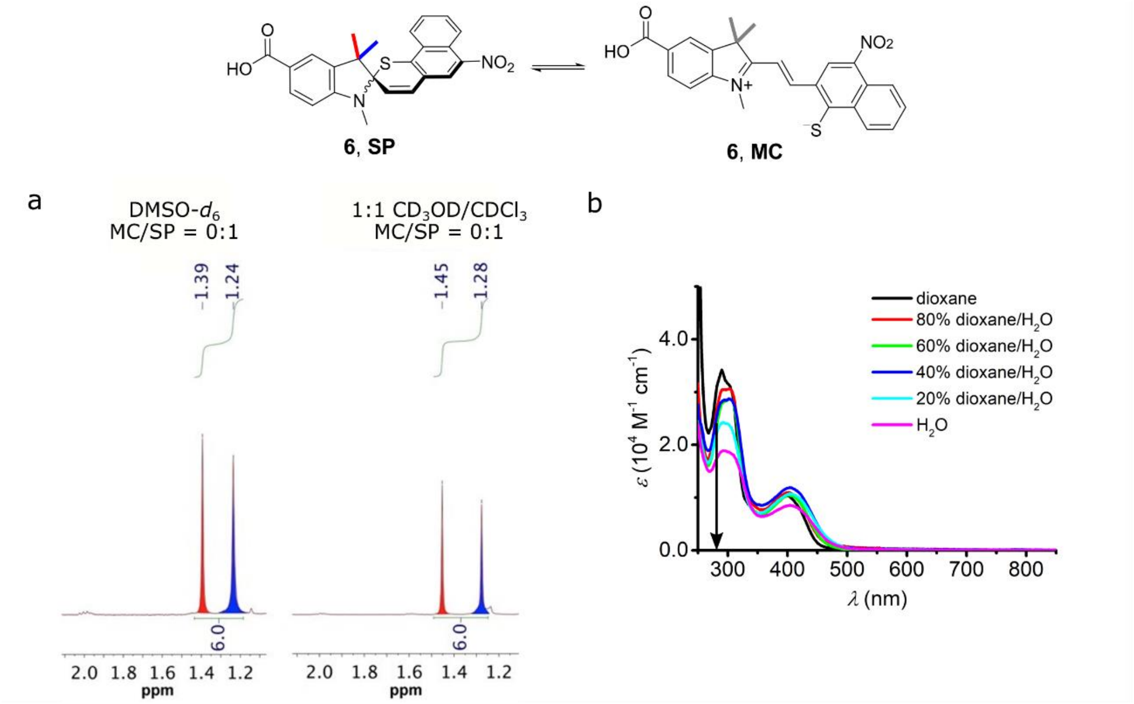

Figure 2-6 Equilibrium between the SP and MC forms of compound **6**. a) NMR signals of compound **6** in DMSO-d_6 and 1:1 mixture of CD_3OD:$CDCl_3$. The sections of the ^{1}H NMR (400 MHz, 25 °C) spectra show the resonances for the *gem*-dimethyl groups in compound **6**. Only the signals for the SP form are observed. b) UV-vis absorption spectra of compound **6** in mixtures of 1,4-dioxane/H_2O at 25 °C. There is no increase in absorbance around 650 nm, indicating that the equilibrium between the SP and MC forms is not affected even in pure H_2O.

The quantum yield of the photochemical opening reaction for compound **6** in CH_3OH was estimated to be around 1%, which is comparable to those of similar spirobenzopyrans.[16] The value was estimated based on the method of Heckel et al.[13] using the following equation,

$$\Phi_0 = \frac{mVN_Ahc}{P\lambda(1-10^{-A})\varepsilon_{\mathrm{prod}}d} \qquad \mathbf{(2.1)}$$

where m is the slope of the linear fit from the time-dependent change in absorbance at 645 nm during irradiation at 405 nm (m = 0.00277 s^{-1}, **Figure 2-3**f), V is the sample volume (2.0 mL), N_A, h, and c are Avogadro, Planck and speed of light constants, P is the power intensity (0.0455 W), λ is the excitation wavelength (405 nm), A is the absorbance at excitation wavelength (0.134), $\varepsilon_{\mathrm{prod}}$ is the molar absorption coefficient of the MC form at 645 nm, d is the path length (1.00 cm). It is difficult to determine $\varepsilon_{\mathrm{prod}}$ because there is no direct way to find out the composition of the PSS due to the fast MC→SP back reaction. Values of the quantum yield Φ_0 were calculated from Equation **2.1** using four different approaches to estimate $\varepsilon_{\mathrm{prod}}$, as listed below. During the measurement of photoswitching, an isosbestic point at ca. 320 nm was observed, which indicates the presence of only two coloured species, i.e. SP and MC forms. All these approaches are crude approximations, but they provide a rough value of Φ_o:

(i) In this method, we assume that the MC form of **6** has negligible absorption at 285 nm compared with the SP form. The change in absorbance at 285 nm is attributed to conversion of the SP to MC form, and indicates 13% of the SP form was photoswitched to the MC form in the PSS (**Figure 2-2**). Therefore, $\varepsilon_{\text{prod}} = A_{645\text{ofPSS}}/(0.13\ [\text{SP}]_0) = 1.5 \times 10^4\ \text{M}^{-1}\ \text{cm}^{-1}$. This approach gives $\Phi_o = 0.88\%$. In reality, the MC form of **6** must have some absorption at 285 nm, implying that $\Phi_o > 0.88\%$.

(ii) In this method, we assume that the PSS consists entirely of the MC form, i.e. photoisomerisation is completed from the SP to MC form. $[\text{SP}]_0 = [\text{MC}]_{\text{PSS}} = 13.8\ \mu\text{M}$. $\varepsilon_{\text{prod}} = A_{645\text{ofPSS}}/([\text{MC}]_{\text{PSS}}) = 2.0 \times 10^3\ \text{M}^{-1}\ \text{cm}^{-1}$. This approach gives $\Phi_o = 6.7\%$. In reality, the PSS must contain some of the SP form of **6**, implying that $\Phi_o < 6.7\%$.

(iii) In this method, we assume that the $\varepsilon_{\text{prod}}$ of the MC form for compound **6** is the same as that of compound **5**, $\varepsilon = 3.4 \times 10^4\ \text{M}^{-1}\ \text{cm}^{-1}$. The molar absorption coefficient of compound **5** in its MC form can easily be measured because this isomer predominates in CH_3OH, as shown by NMR spectroscopy and supported by the fact that the spectrum shows no change before and after irradiation at 405 nm. This approach gives $\Phi_o \approx 0.40\%$.

(iv) In this method, we attempted to determine the composition of the PSS by ^{1}H NMR spectroscopy. Compound **6** (0.53 mL of an 18 mM solution in DMSO-d_6) was transferred to a 5-mm NMR tube. The sample was locked and shimmed, and a single-scan ^{1}H NMR spectrum was recorded at 25 °C. The sample was ejected, and the solution was evenly irradiated for 2 min with a laser pointer (405 nm, 1 mW). The tube was quickly inserted into the probe, the sample was locked, and a single-scan spectrum was recorded at 25 °C. The total time between the end of irradiation and acquisition of the single-scan spectrum was 25 s. The resulting spectrum revealed that after this time only 1.5% of **6** exists in the MC form (estimated by integration of two different pairs of signals and two independent measurements). A kinetic trace was obtained by measuring the decrease in absorbance at 645 nm as a function of time after irradiation. For this experiment, compound **6** (2 mL of a 0.48 mM solution in DMSO) was transferred to a 1-cm cuvette. The sample was irradiated for 12 s with a laser pointer (405 nm, 1 mW), and the decrease in absorbance was recorded as a function of time at 25 °C. After 25 s, the absorbance at 645 nm was 0.57. Knowing that at 25 s after irradiation the fraction of MC is 1.5%, the concentration of MC in the cuvette is approximately 7.3 μM, and therefore the molar absorption coefficient of the MC form is approximately $\varepsilon_{\mathrm{prod}} = 7.9 \times 10^{4}\ \mathrm{M}^{-1}\ \mathrm{cm}^{-1}$, which gives $\Phi_{\mathrm{o}} \approx 0.17\%$.

Following photochemical ring opening, the thermal recovery of the SP forms of compounds **5** and **6** occurs rapidly in polar solvents. Dependence of thermal ring closing kinetics on the solvent viscosity was measured in a mixture of ethylene glycol (EG) and CH_3OH to vary the viscosity of the medium without significant variation in the polarity.[17] The half-life of thermal ring closure ($t_{1/2}$) for compound **6** at 20 °C ranges from 83 s in ethylene glycol (EG) to 14 s in CH_3OH, increasing nonlinearly as a function of solvent viscosity[10] (**Figure 2-7**, **Figure 2-8**).

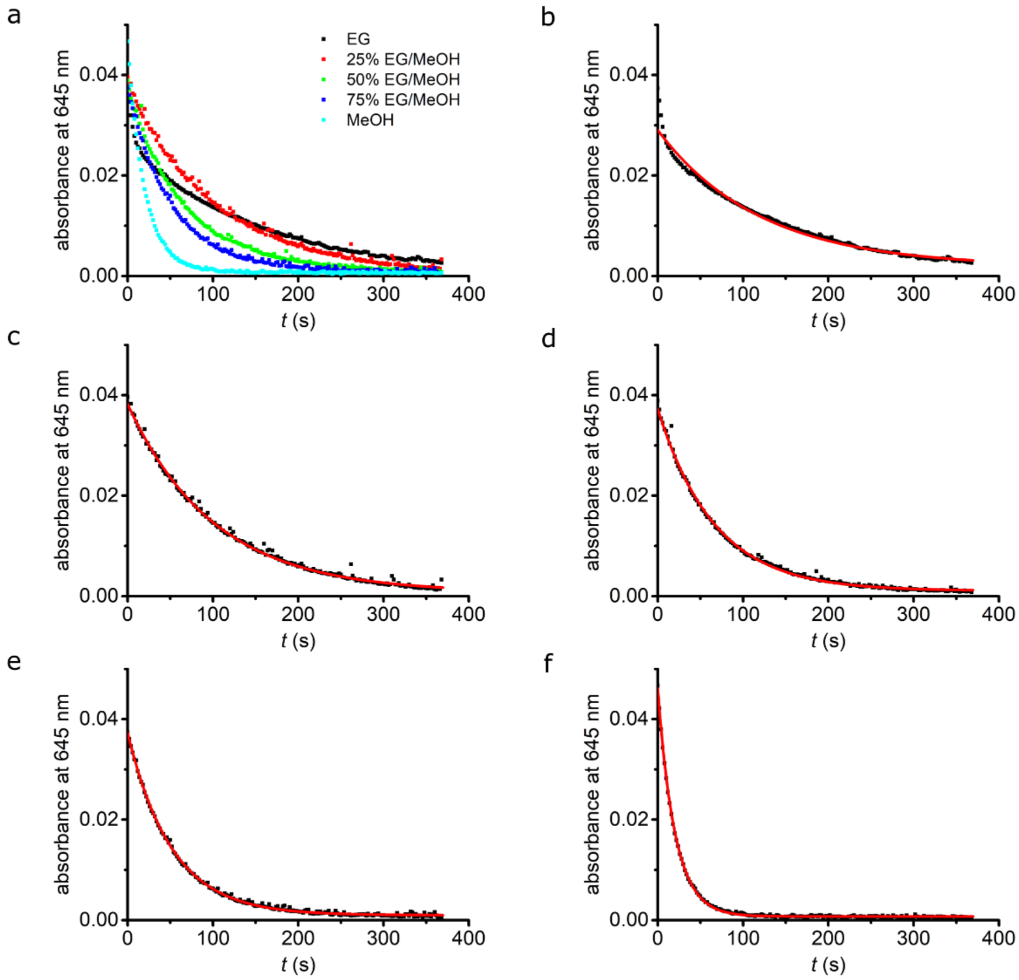

Figure 2-7 Kinetic traces of thermal ring closing after 405 nm irradiation (80 mW, 5.5 s) of compound **6** (12 μM, 2.0 mL) in the indicated mixtures of ethylene glycol (EG) and CH_3OH at 20 °C. Individual traces can be formulated as a single exponential equation, and the following parameters are derived. a) Overlay of all traces; b) 100% EG: $R^2 = 0.985$, $k = 0.008\ \mathrm{s}^{-1}$, $t_{1/2} = 83$ s; c) 75% EG: $R^2 = 0.998$, $k = 0.010\ \mathrm{s}^{-1}$, $t_{1/2} = 70$ s; d) 50% EG: $R^2 = 0.999$, $k = 0.015\ \mathrm{s}^{-1}$, $t_{1/2} = 46$ s; e) 25% EG: $R^2 = 0.998$, $k = 0.019\ \mathrm{s}^{-1}$, $t_{1/2} = 36$ s; f) 0% EG: $R^2 = 0.999$, $k = 0.049\ \mathrm{s}^{-1}$, $t_{1/2} = 14$ s.

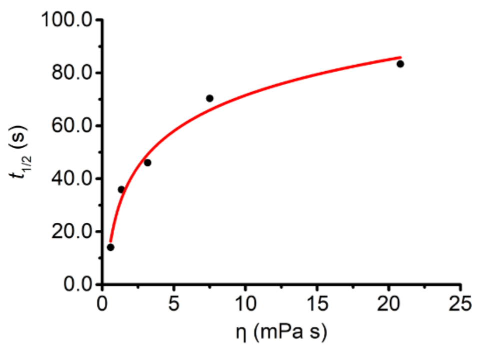

Figure 2-8 The half-life of thermal ring closing of compound **6** has a non-linear dependence on dynamic viscosity (η) in mixtures of ethylene glycol (EG)/CH_3OH at 20 °C. Fitting model: $t_{1/2} = [19.5\ln(\eta)] + 26.7$; $R^2 = 0.977$.

In addition, thermal ring closing kinetics of compound **6** were measured at different temperatures (**Figure 2-9**). To induce ring opening, the samples were irradiated with 405 nm LED light (80 mW, 5.5 s) from the side of a square quartz cuvette (10 mm) immediately before measuring the decay of absorbance at 645 nm as a function of time. The kinetics were also measured for compound **5** (see Experimental 2.7.5).

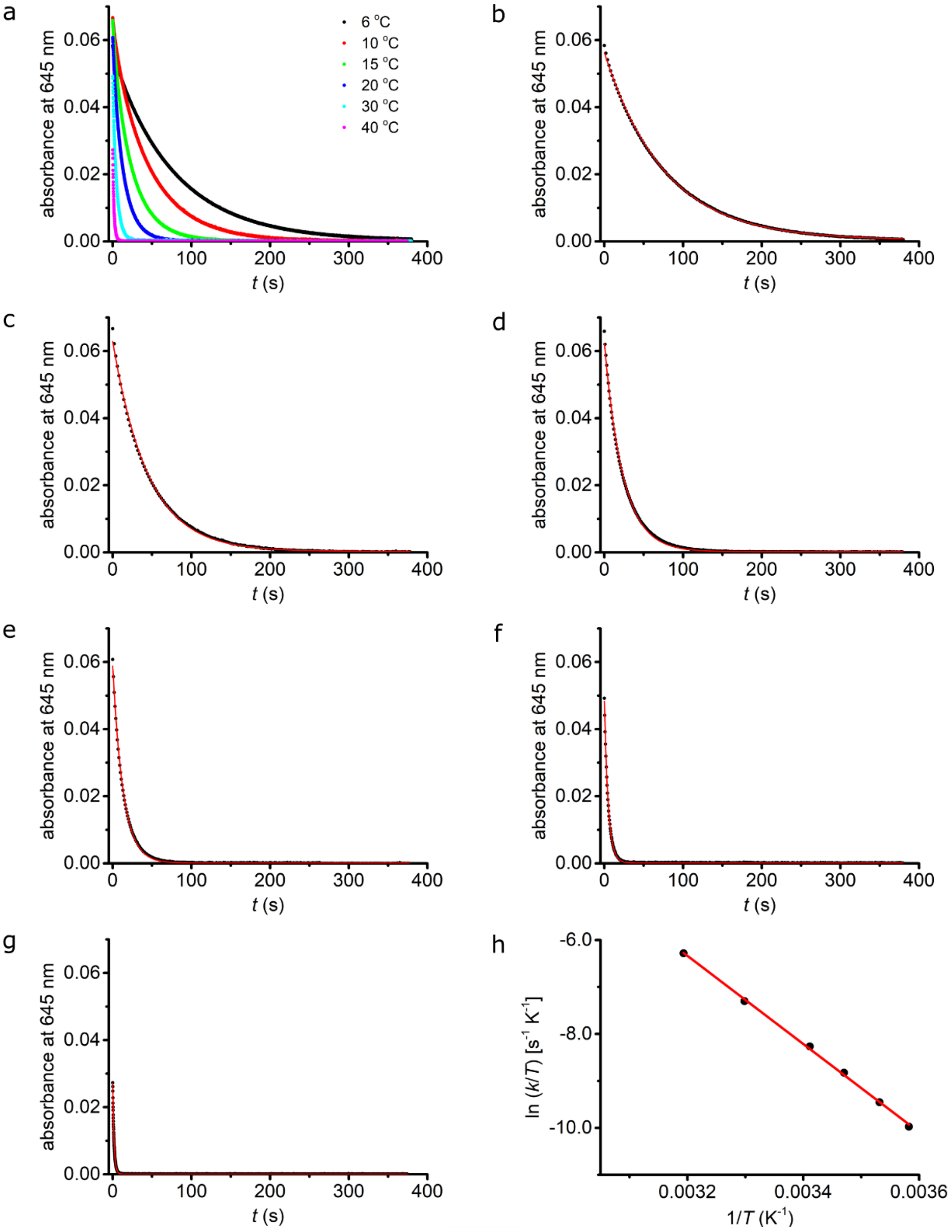

Figure 2-9 Kinetic traces of thermal ring closing after irradiation of compound **6** in CH_3OH (13.8 μM, 2.0 mL) using 405 nm LED (80 mW, 5.5 s) at a range of temperatures. Individual traces are fit to a single exponential function. a) Overlay of all traces; b) 6 °C: $R^2 = 0.999$, $k = 0.013\ s^{-1}$; c) 10 °C: $R^2 = 0.999$, $k = 0.022\ s^{-1}$; d) 15 °C: $R^2 = 0.999$, $k = 0.042\ s^{-1}$; e) 20 °C: $R^2 = 0.999$, $k = 0.075\ s^{-1}$; f) 30 °C: $R^2 = 0.999$, $k = 0.204\ s^{-1}$; g) 40 °C: $R^2 = 0.998$, $k = 0.586\ s^{-1}$; h) a linear correlation between ln(k/T) and $1/T$, i.e. Eyring equation. $y = 23.7 - 9384.7x$, $R^2 = 0.999$, $\Delta H^{\ddagger} = 78.0$ kJ mol^{-1}, $\Delta S^{\ddagger} = -0.54$ J $mol^{-1}\ K^{-1}$, $\Delta G^{\ddagger} = 78.2$ kJ mol^{-1} at 25 °C.

Activation enthalpy ($\Delta H^{\ddagger}$) and activation entropy ($\Delta S^{\ddagger}$) were calculated based on the Eyring equation,

$$\ln\left(\frac{k}{T}\right) = \frac{-\Delta H^{\ddagger}}{R} \times \left(\frac{1}{T}\right) + \left(\ln\frac{k_{\mathrm{B}}}{h} + \frac{\Delta S^{\ddagger}}{R}\right)$$

where k is the rate constant (s^{-1}), T is the absolute temperature (K), R is the universal gas constant (8.3145 J mol^{-1} K^{-1}), k_B is the Boltzmann constant (1.381×10^{-23} J K^{-1}), h is the Planck constant (6.626×10^{-34} J s). The free energy of activation ($\Delta G^{\ddagger}$) was calculated from $\Delta G^{\ddagger} = \Delta H^{\ddagger} - T\Delta S^{\ddagger}$.

Based on the Eyring equation, the Gibbs energies of activation ($\Delta G^{\ddagger}$) are almost the same for switches **5** and **6** in CH_3OH at 25 °C (75 and 78 kJ mol^{-1} respectively), which are at the same magnitude of the values previously reported for analogues.[13] There is a small enthalpy difference ($\Delta H^{\ddagger}$ = 77.8 and 78.0 kJ mol^{-1}), whereas an entropic gain ($\Delta S^{\ddagger}$ = 9.2 J mol^{-1} K^{-1}) was calculated for compound **5**, and an entropic loss ($\Delta S^{\ddagger}$ = –0.5 J mol^{-1} K^{-1}) for compound **6**. The opposite sign for the entropy values is probably attributed to the different steric hindrance associated with the two chalcogen atoms. With a bigger sulfur atom next to the spiro-carbon centre, the transition from the MC to SP state presumably involves generation of restraints and loss of disorder.

As with many spirobenzopyrans, ring-closure of the MC form of **6** is accelerated by irradiation with red light (**Figure 2-10**).[4] Relative to thermal recovery in the dark (k = 0.042 s^{-1}), excitation at 630 nm significantly increases the rate of ring-closure (k_1 = 0.15 s^{-1}, k_2 fixed at 0.042 s^{-1}). This ability to switch the system photochemically in both directions using different wavelengths is ideal for RESOLFT microscopy.

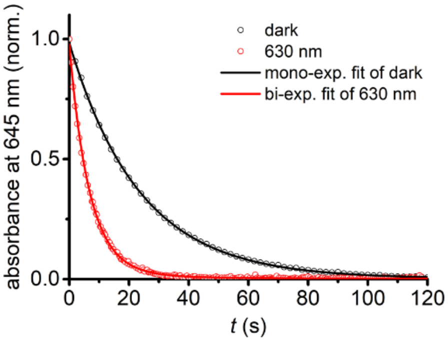

Figure 2-10 Kinetic traces for the ring-closure reaction MC→SP after irradiation of compound **6** in CH_3OH (14 µM, 2.0 mL) either thermally (black, open circle) or photochemically with irradiation at 630 nm (2.1 W/cm^2, 200 ms irradiation + 500 ms intervals). The thermal kinetic trace is fit to a mono-exponential decay (k = 0.042 s^{-1}, R^2 = 1.00), and the photochemical kinetic trace is fit to a bi-exponential decay (k_1 = 0.15 s^{-1}, k_2 fixed at 0.042 s^{-1}, R^2 = 0.999).

2.3.2 *In vitro* fatigue resistance

Strong fatigue resistance, i.e. a large number of switching cycles before photodegradation, is an important requirement for a photoswitchable dye for RESOLFT microscopy due to the nature of the scanning process. We tested the fatigue resistance of switch **6** in methanol solution in a cuvette. Under aerobic conditions, it shows significant decomposition after 10 cycles (**Figure 2-11**), whereas there is less fatigue under anaerobic conditions, implying that switch **6** suffers oxygen-dependent photochemical decomposition, which is consistent with previous reports.[18]

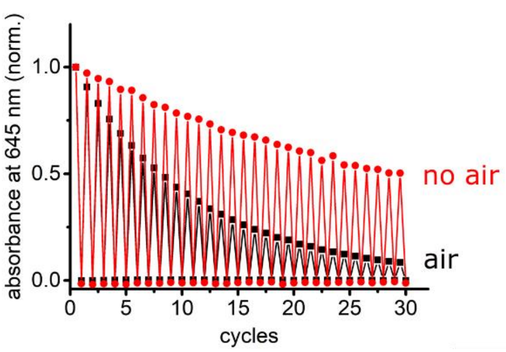

Figure 2-11 Photochemical fatigue resistance of compound **6** in CH_3OH (14 μM, 2.0 mL) in the presence (black squares) and absence of air (red circle) by purging with argon. Samples were irradiated for 5.5 s at the beginning of each cycle using a 405 nm LED (1.1 W/cm^2) and then thermal ring closure was allowed to reach completion before the next cycle.

2.4 Characterisation of Dyad 1

For **Dyad 1**, the choice of silicon rhodamine (SiR) dye was made based on the expected high FRET efficiency, given the almost perfect spectral overlap between the emission of SiR dye and the absorption of switch **6** in the MC form (**Figure 2-12**). The Förster radius calculated from this spectral overlap is R_0 = 36 Å (**Figure 2-12**; Experimental 2.7.4), and the distance between the SiR and MC units is 9–19 Å (**Figure 2-13**), corresponding to an energy transfer efficiency of > 97% (see Experimental 2.7.4). The computational calculations of the MC conformations were carried out by Dr Pablo Rivera-Fuentes.

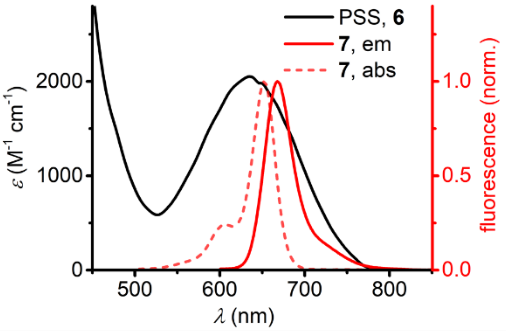

Figure 2-12 Overlap of the reconstructed PSS spectrum of compound **6** (13.8 μM in CH_3OH; black line) and normalised emission spectrum of compound **7** (red solid line). Based on the spectral overlap, a Förster radius of 36 Å was obtained, indicating that FRET efficiencies of > 97% are expected for interchromophore distance smaller than 20 Å. The normalised UV-vis absorption spectrum of compound **7** is included.

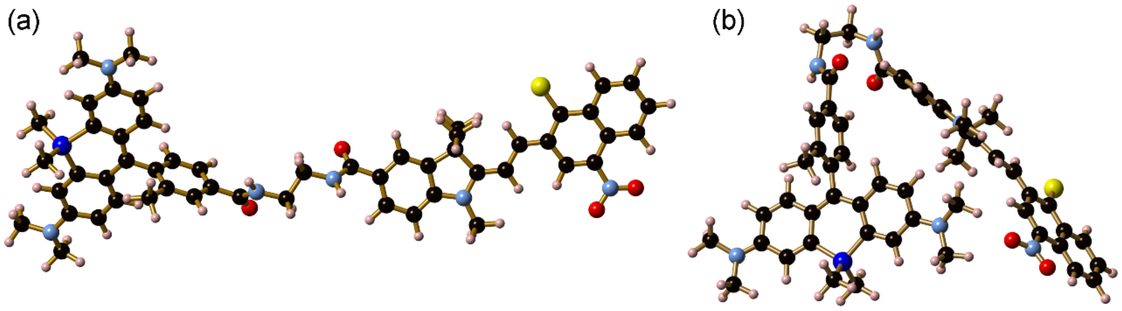

Figure 2-13 Two low-energy conformations of the MC-form of **Dyad 1** from calculations at the PM6 level of theory with Gaussian 09. The distances from the centre of the SiR unit to the centre of the MC unit are (a) r = 19.0 Å and (b) r = 9.3 Å.

The UV-vis absorption spectra of **Dyad 1** demonstrate that the spironaphthothiopyran remains in the SP form in polar solvents and pure water, as expected from the properties of switch **6**. Additionally, the SP form is insensitive to the physiological pH range in aqueous solutions (**Figure 2-14**). This is important to ensure maximal brightness at the resting state and the resulting strong contrast between bright and dark states.

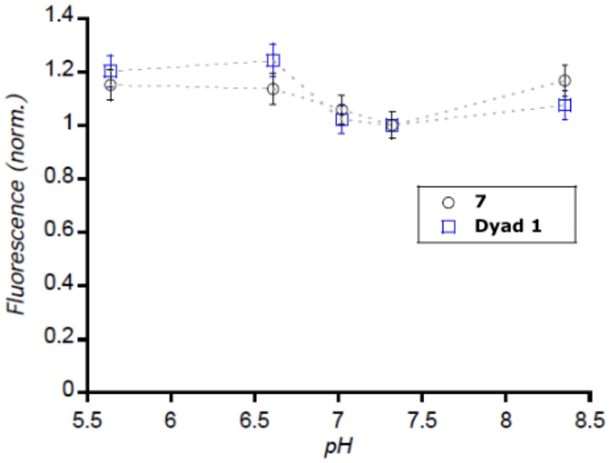

Figure 2-14 Normalised fluorescence intensities of compound **7** and **Dyad 1** as a function of pH at a concentration of ca. 0.8 μM in phosphate-buffered saline in the biologically relevant pH region (5.5–8.5). The values are normalised to 1 at pH 7.3. The subtle variation in fluorescence intensity is attributed solely to the SiR fluorophore, since compounds **7** and **Dyad 1** exhibit very similar behaviour. These results show that the spironaphthothiopyran unit **6** remains closed in the SP form over this pH range, in contrast to the spironaphthopyran unit **5** which exists mainly as the open MC form even in the dark under these conditions.

The fluorescence quantum yield of **Dyad 1** (Φ_f = 0.17; **Figure 2-15**b) in the aqueous solution is only slightly lower than that of SiR derivative **7** (Φ_f = 0.24; **Figure 2-15**a), which indicates that the SP form of the photochrome does not significantly quench the emission of the fluorophore.

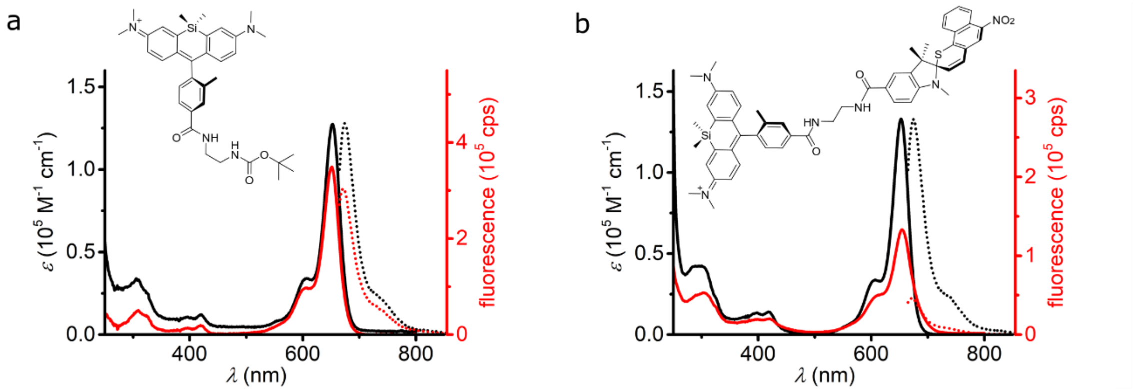

Figure 2-15 Comparison of photophysical properties of compound **7** and **Dyad 1** in different solvents at 25 °C. a) UV-vis absorption (solid lines) and fluorescence (dotted lines) spectra of compound **7** (1 μM) in CH_3CN (black lines) and H_2O (red lines). b) UV-vis absorption (solid lines) and fluorescence (dotted lines) spectra of **Dyad 1** (0.8 μM) in CH_3CN (black lines) and H_2O (red lines).

2.5 Biological imaging

The ability of **Dyad 1** to operate in biological environments was tested on a confocal laser scanning microscope (Zeiss LSM 780 inverted confocal microscope) using human dermal lymphatic endothelial cells (HDLEC). **Dyad 1** crosses the plasma membrane readily (15 min incubation at 37 °C), and it appears to accumulate in the mitochondria of HDLEC (**Figure 2-16**).

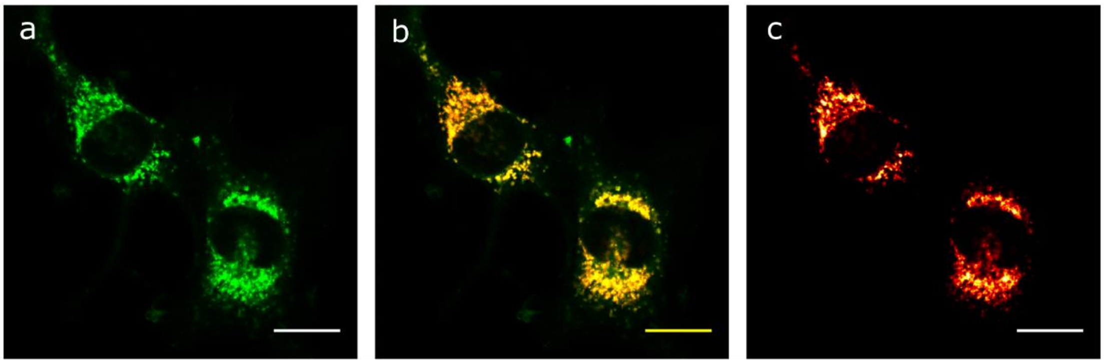

Figure 2-16 Mitochondrial localisation of **Dyad 1** in live HDLEC in comparison to MitoTracker Green. a) Confocal image of MitoTracker Green (excited at 488 nm, readout at 500–550 nm). b) Colocalisation of MitoTracker Green and **Dyad 1**. c) Confocal image of **Dyad 1** (excited at 633 nm, readout at 640–710 nm). Scale bar: 20 μm.

Dyad 1 shows good contrast using a 633 nm laser to excite the fluorophore, and photoisomerisation of the quencher could be accomplished using a 405 nm laser, confirming the photochromic behaviour. The photoswitching efficiency depends on the intensities of the excitation (I_{633}) and switching (I_{405}) irradiation, as well as on the duration of the irradiation. We therefore optimised these parameters as detailed in **Figure 2-17** and **Figure 2-18**. The off/on ratio refers to the ratio of average photon counts of dark:bright states as shown in **Figure 2-19**. The optimal photoswitching conditions were found to be I_{405} = 16 µW, I_{633} = 2.4 µW, and pixel dwell time of 5 µs.

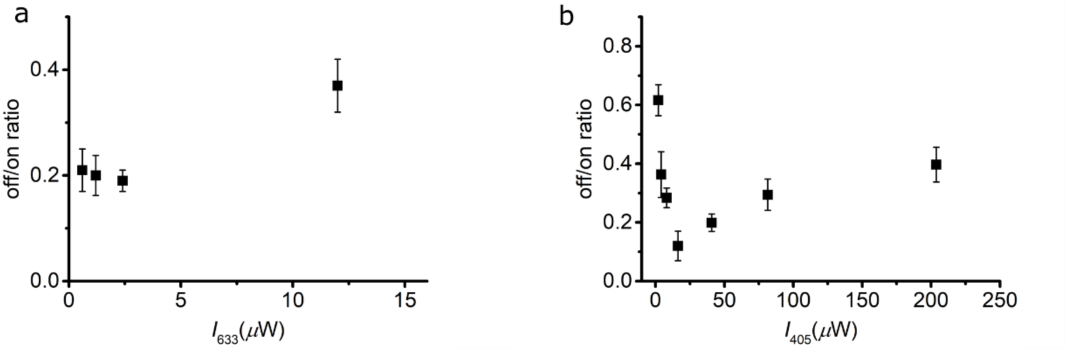

Figure 2-17 Optimisation of laser powers on the confocal microscope. a) Off/on ratio of **Dyad 1** in live HDLEC as a function of I_{633} at fixed I_{405} = 16 µW. b) Off/on ratio of **Dyad 1** in live HDLEC as a function of I_{405} at fixed I_{633} = 2.4 µW.

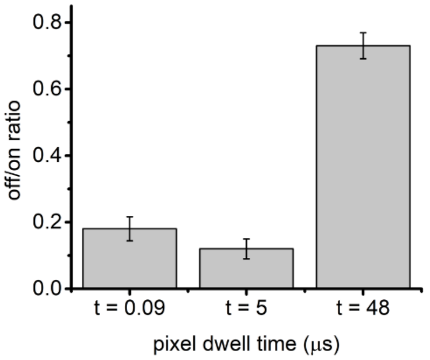

Figure 2-18 Effect of scanning speed (pixel dwell time) on the off/on ratio of **Dyad 1** in live HDLEC.

With these parameters, the three images shown in **Figure 2-19** were obtained. The first image, i.e. bright/‘on’ state (**Figure 2-19**A), shows the fluorescence of **Dyad 1** upon excitation at 633 nm. The dark state was obtained by line-by-line scanning. That is, the first line of the field of view is scanned with a 405 nm laser, followed by immediate readout by excitation at 633 nm. The process was repeated for 2nd, 3rd line etc. until the entire image was built (**Figure 2-19**B). Finally, the cells were scanned again, after 1–2 s, with the 633 nm laser (**Figure 2-19**C). This experiment revealed that irradiation at 405 nm switches off the fluorescence intensity of SiR to about 13% of its original intensity in primary cells, and that this switch-off is reversible (**Figure 2-19**D). We observed almost full recovery of the fluorescence intensity (**Figure 2-19**C) only 2 s after photoswitching, which is consistent with the rapid photochemical ring closure demonstrated in cuvettes.

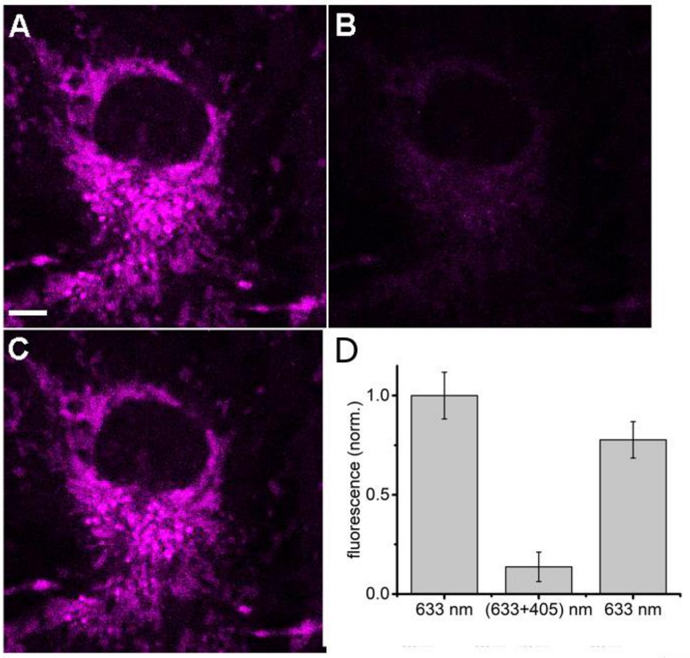

Figure 2-19 Switching performance of **Dyad 1** in live HDLEC under confocal imaging. A) Excitation with 633 nm (2.4 µW); B) Irradiation with 405 nm (16 µW) immediately followed by excitation with 633 nm (2.4 µW); C) Irradiation with 633 nm (2.4 µW) ~2 s after B; D) Quantification of the off/on ratio (fluorescence intensity of B/A and of C/A). Scale bar: 5 µm.

The off/on ratio of about 0.13 implies that after 405 nm irradiation, **Dyad 1** must be at least 87% in the MC form, and that the fluorescence from the SiR component must be at least 87% quenched in this isomer.[19,20] The MC form has significant absorption at 405 nm (**Figure 2-2**), making it impossible to achieve complete SP → MC conversion by excitation at this wavelength. A darker off state and a lower off/on ratio would be ideal, but a ratio of 0.13 is high enough for RESOLFT microscopy.[21,22]

The fatigue resistance was also investigated during live cell imaging of **Dyad 1**. Several cycles of alternating irradiation with 633 nm and 405 nm + 633 nm revealed that the fluorescence off/on ratio decreases rapidly after only a few cycles (**Figure 2-20**). The ratio decreases mainly because the fluorescence intensity of the dark state increases. This result is consistent with the cuvette experiment, and confirms that the photoswitch, rather than the SiR fluorophore, is responsible for the poor fatigue resistance of **Dyad 1**. Mainly due to the poor fatigue resistance, it is difficult to justify the application of **Dyad 1** in RESOLFT microscopy. Improvement in this aspect will be addressed in the following chapters.

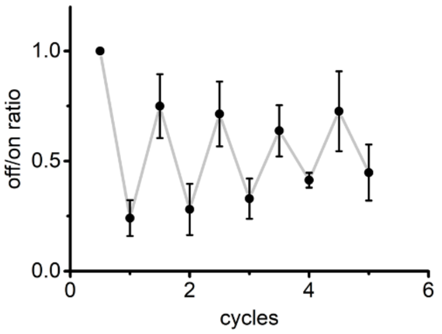

Figure 2-20 Fatigue resistance of **Dyad 1** in live HDLEC. Switching was repeated using I_{405} = 16 µW and I_{633} = 2.4 µW with a pixel dwell time of 5 µs.

2.6 Conclusions

We have developed a reversibly photoswitchable dyad based on a silicon rhodamine fluorophore and a spironaphthothiopyran switch. This dyad possesses several desirable traits, including fast and reversible modulation of its fluorescence using visible light, high brightness in the far-red region, and a high off/on ratio in live cells using low laser powers. These results show that spironaphthothiopyrans have significant advantages compared with their oxygen counterparts. Unfortunately, **Dyad 1** does not display good enough fatigue resistance for RESOLFT microscopy; this limitation will be addressed in the following chapters.

2.7 Experimental

2.7.1 General procedures

All reagents were purchased from commercial sources and used as received. Solvents were procured from Merck, formerly Sigma Aldrich at HPLC or analytical grade purity. Dry solvents were obtained by elution through activated Al_2O_3 under N_2 atmosphere. Column chromatography was carried out using SiO_2 60A (particle size 35–70 µm, Fisher, UK) as the stationary phase, and the eluent mixtures are given in volume ratios.

2.7.1.1 NMR

NMR spectra were acquired on a Bruker AVII400, AVIII400, or AVII500 instrument at 25 °C. ^1H NMR chemical shifts are reported in ppm relative to $SiMe_4$ ($\delta = 0$) and were referenced internally with respect to residual protons in the solvent ($\delta = 7.26$ for $CDCl_3$; 2.50 for DMSO-d_6; 3.31 for CD_3OD; 5.32 for CD_2Cl_2). $^{13}C\{^1H\}$ NMR chemical shifts are reported in ppm relative to $SiMe_4$ ($\delta = 0$) and were referenced internally with respect to solvent signal ($\delta = 77.2$ for $CDCl_3$; 39.5 for DMSO-d_6; 49.0 for CD_3OD; and 53.8 for

CD_2Cl_2). Standard abbreviations indicating multiplicity were used as follows: s = singlet, d = doublet, dd = doublet of doublets, t = triplet, q = quartet, m = multiplet, br. = broad signal.

2.7.1.2 Mass spectrometry

High-resolution mass spectra (HRMS) were obtained on a Bruker µTOF instrument or a Waters GCT.

2.7.1.3 Spectroscopic measurements

Stock solutions of all compounds were prepared in DMSO at concentrations in the range 0.1–5 mM and stored at –20 °C, and thawed immediately before each experiment. Samples were prepared at a concentration to have absorbance below 0.1 at the excitation wavelength in order to avoid the inner filter effect. Spectroscopic measurements were conducted in HPLC grade solvents at 25 °C unless specified. UV-vis absorption spectra were acquired on a Perkin Elmer Lambda 20 or Lambda 25 spectrometer using quartz cuvettes from Starna (10 mm path length). All measurements were conducted at 25 °C unless otherwise stated, and the temperature controlled by a PTP-1 Peltier unit from Perkin Elmer.

2.7.1.4 Custom LED setup

Photoswitching experiments in the cuvette were carried out using a custom setup within the UV-vis spectrometer. The irradiation sources were mic-LED-405 (from Prizmatix Ltd.; centred at 405 nm, FWHM = 15 nm) up to 360 mW, and mic-LED-630 (from Prizmatix Ltd.; centred at 630 nm, FWHM = 15 nm) up to 150 mW. The two LEDs were joined into one output beam *via* a beam combiner, which was coupled to a liquid light guide (diameter = 3 mm). The liquid light guide was wired close to the cell holder and orthogonal to the beamline of the spectrometer. The irradiation was performed using Matlab programs to control light sources, irradiation and interval lengths, and the number of cycles. Where necessary, Matlab and OriginLab softwares were used for data treatment.

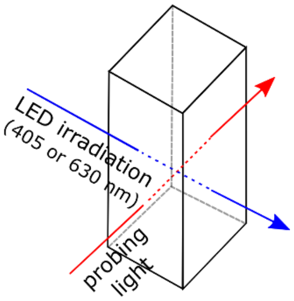

Figure 2-21 Schematic representation of the geometrical arrangement of the sample holder in the UV-vis spectrometer, for measurements of the PSS spectrum, fatigue resistance, and photochemical ring closure.

2.7.1.5 Relative fluorescence quantum yields

Fluorescence spectra were acquired using a Fluoromax-2 fluorimeter. Fluorescence emission spectra were integrated from 600 to 850 nm. With 4-carboxy-2-methyl silicon rhodamine (Φ_f = 0.39 in H_2O) as standard,[10] fluorescence quantum yields were calculated using the following equation[23]:

$$\Phi_X = \Phi_S \times \frac{I_X}{I_S} \times \frac{A_S}{A_X} \times \left(\frac{\eta_X}{\eta_S}\right)^2$$

Where Φ is the relative fluorescence quantum yield, *I* is the integrated emission area, *A* is the absorbance at the excitation wavelength (630 nm), η is the refractive index of the medium, $_X$ stands for the measured sample, and $_S$ stands for the standard.

2.7.2 Determination of the power intensities

The power intensities of the Prizmatix mic-LED-405 and mic-LED-630 light sources were measured with a Coherent® power meter at various points of indicated intensity percentage. These intensity measurements were carried out at the end of the liquid light guide, immediately before the cuvette.

indicated power percentage (%)	power intensity of mic-LED-405 (mW)	power intensity of mic-LED-630 (mW)
2%	16.5	6.5
5%	27.5	11.5
8%	39.0	16.5
10%	45.0	18.9
50%	174.5	78.5
100%	302.0	147.0

The power of the mic-LED-405 was also confirmed by chemical actinometry, as described below.

Ferric oxalate actinometry:[24,25] A solution of ferric oxalate (0.0060 M) was prepared by dissolving $K_3[Fe(C_2O_4)_3]\cdot 3H_2O$ (300 mg, 0.60 mmol) in aqueous sulfuric acid (100 mL of 0.05 M H_2SO_4). 2.00 mL of this solution was placed in a quartz cuvette, and while stirring, irradiated with mic-LED-405 at the power of the indicated output percentage for 10 s, while an identical control sample was kept in the dark. A sample of the irradiated ferric oxalate solution (0.2 mL) and a control sample (0.2 mL) were transferred to vials containing a mixture of 0.1% phenanthroline solution (0.9 mL, prepared by dissolving 13.56 g of CH_3CO_2Na and 0.100 g of phenanthroline in 100 mL of 0.5 M H_2SO_4) and H_2O (0.9 mL). Samples were kept in the dark for 1 h to allow the complexation to occur and absorption spectra were acquired in the 250–850 nm range. The LED power intensities and irradiation lengths were chosen to ensure that the photoconversion of ferric oxalate does not exceed 5% and that the absorbance of the $Fe(phen)_3^{2+}$ complex is within the range 0.5–1.0.

Upon exposure to light, $K_3[Fe(C_2O_4)_3]$ is converted to Fe^{2+}, and the quantum yield Φ_R of formation of Fe^{2+} is well-known for a range of wavelengths (222–500 nm; $\Phi_R = 1.14$ at 405 nm[26]). The photon flux f used can be calculated using Equation **2.2**,

$$f = \frac{\text{no.moles Fe}^{2+}}{\Phi_R t(1-10^{-A})} \qquad \textbf{(2.2)}$$

where Φ_R is the quantum yield of the ferric oxalate conversion at the irradiation wavelength, t (s) is the irradiation time, $(1-10^{-A})$ is the fraction of light absorbed by the ferric oxalate solution while A is the absorbance of 0.006 M solution at the irradiation wavelength. Formation of the coloured $Fe(phen)_3^{2+}$complex (ε_{510} = 11,100 M^{-1} cm^{-1}) allows quantification of Fe^{2+} generated during the irradiation by measuring the absorbance of irradiated and non-irradiated samples (Equation **2.3**).

$$\text{no. moles Fe}^{2+} = \frac{V_1 V_3 \Delta A\ (510\ \text{nm})}{10^3 V_2 l \varepsilon\ (510\ \text{nm})} \qquad \textbf{(2.3)}$$

Where V_1 (mL) is the irradiated volume, V_2 (mL) is the aliquot of the irradiated solution transferred to the solution of buffered phenanthroline, V_3 (mL) is the final volume of the complexation solution, l (cm) is the optical path length of the quartz cuvette used for irradiation, ΔA (510 nm) is the difference in the absorbance between the irradiated solution and control stored in the dark, and ε (510 nm) is the molar absorption coefficient of Fe(phen)$_3^{2+}$ complex at 510 nm.

The calculated value of the photon flux was expressed in E·s^{-1} and was converted to mW using Equation **2.4**.

$$f\ (\mathrm{mW}) = 1000\ \times\ f\ (\mathrm{E{\cdot}s^{-1}}) N_{\mathrm{A}} h \frac{c}{\lambda} \qquad \mathbf{(2.4)}$$

A linear correlation between the power intensity (mW) and indicated output percentage (%) was derived as in **Figure 2-22**. The power intensity obtained from the power meter matches very well with that from the actinometry measurement.

As the output beam was fixed in close contact with the cuvette, the irradiation area was estimated to be the surface area of the end of the liquid light guide, A = 0.071 cm^2. This area was used to calculate the applied power density (W/cm^2).

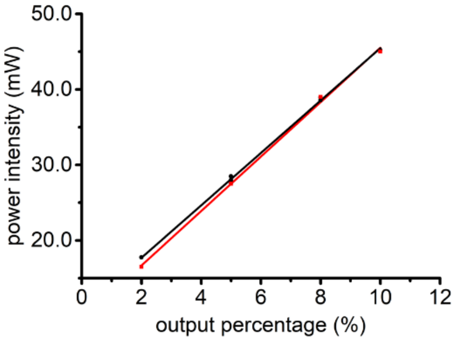

Figure 2-22 Linear correlation between the output percentage and power intensity from actinometry or the power meter for mic-LED-405 light source. The measurement points from actinometry are shown as black circles (linear fit: black line, y = 3.47x + 10.76, R^2 = 0.998). Measurement points from the power meter are shown as red square (linear fit: red line, y = 3.61x + 9.47, R^2 =0.998).

2.7.3 Acquisition of the photostationary state (PSS) absorption spectra

The PSS absorption spectrum was shown in **Figure 2-2**. The measurement procedure is as follows: a methanol solution of compound **6** (13.8 μM, 2.0 mL) was irradiated with 80 mW of mic-LED-405 for 5.5 s, and immediately afterwards, the spectrum was recorded while the sample was given pulses of the same LED intensity with 100 ms irradiation and 200 ms interval lengths. The reconstructed PSS spectrum from Matlab was used to calculate the FRET efficiency of **Dyad 1**.

2.7.4 Calculation of the FRET efficiency (E)

The following equations[27] were used:

$$E = \frac{1}{1+ (^{r}/_{R_0})^6}$$

$$R_0 = 0.2108[\frac{\kappa^2 \Phi_{\mathrm{D}} J(\lambda)}{n^4}]^{\frac{1}{6}}$$

$$J(\lambda) = \int F_{\mathrm{D}}(\lambda)\varepsilon_{\mathrm{A}}(\lambda)\lambda^4 d\lambda$$

where r is the distance between the donor and acceptor, R_0 is the Förster radius (distance at which the energy transfer efficiency is 50%), κ^2 is the dipole orientation factor (assumed to be 2/3 given free rotation between the donor and acceptor),[28] Φ_{D} is the fluorescence quantum yield of the donor in the absence of the acceptor (0.39),[10] n is the refractive index of the solvent (1.33 for water), $J(\lambda)$ is the spectral overlap integral based on the data of **Figure 2-12**, F_{D} is the fluorescence intensity of the donor (in PBS) after the total intensity (the area under the curve) is normalised to 1, ε_{A} is the acceptor molar absorption coefficient (in cyclohexane), and λ is the wavelength. The spectra shown in **Figure 2-12** give $J(\lambda) = 2.97 \times 10^{14}\ \mathrm{M}^{-1}\ \mathrm{cm}^{-1}\ \mathrm{nm}^4$, which corresponds to a Förster radius of $R_0 = 36$ Å.

A conformational search of the MC form of **Dyad 1** using computational calculations at the PM6 level of theory with Gaussian 09 revealed two predominant conformers with distances r of 19.0 and 9.3 Å (see **Figure 2-13**). The equations above indicate the FRET efficiency is $E > 97\%$ in both conformations.

2.7.5 Testing the kinetics of thermal ring closure in cuvettes

Similar to **Figure 2-9**, **Figure 2-23** below shows thermal ring-closing kinetic traces for compound **5** (12.9 μM, 2.0 mL) by monitoring the absorbance change at 570 nm at different temperatures. For comparison with the data of compound **6**, please see Section 2.3.1.

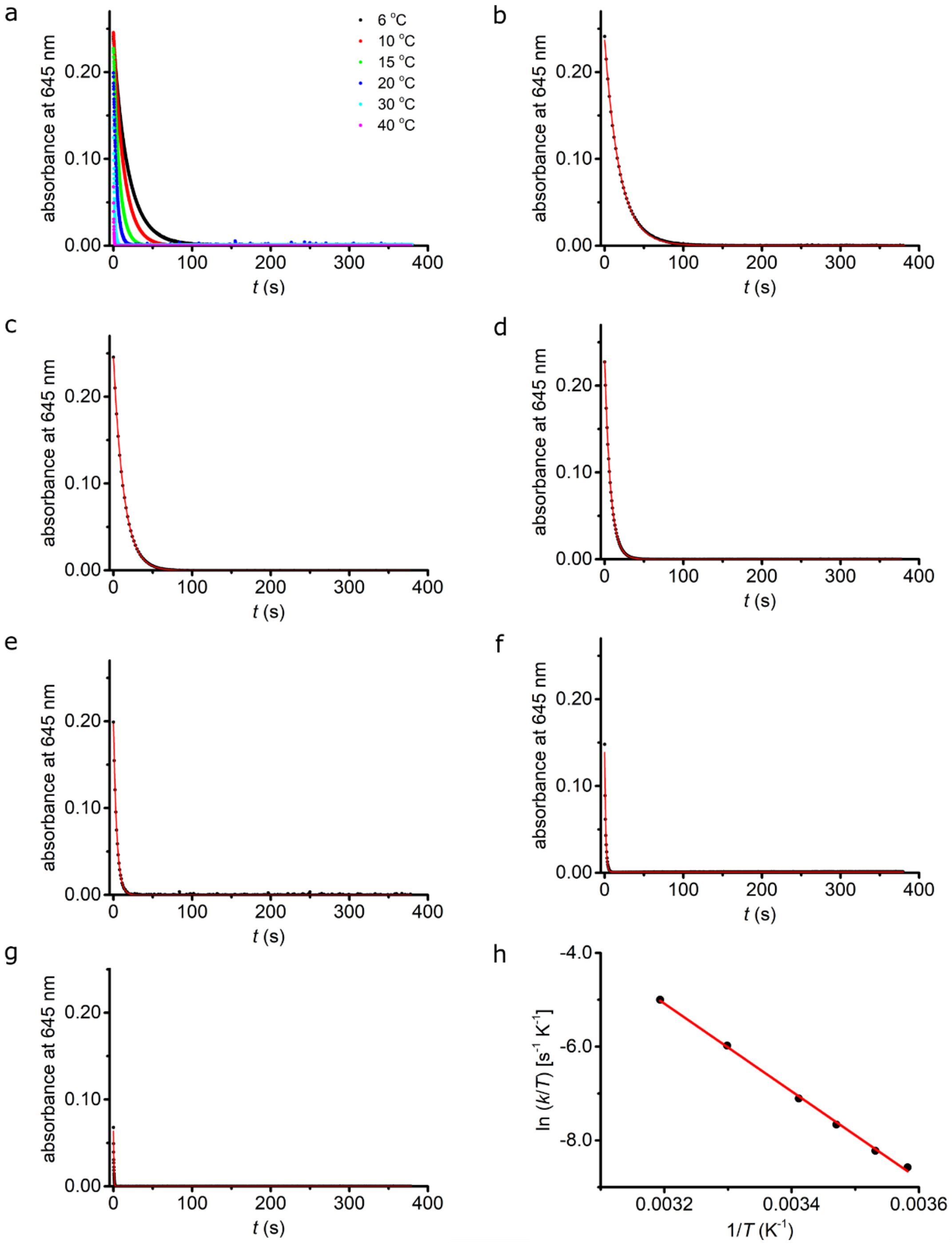

Figure 2-23 Kinetic traces of thermal ring closing after irradiation of compound **5** in CH_3OH (12.9 μM, 2.0 mL) using 80 mW of mic-LED-405 for 5.5 s at a range of temperatures. Individual traces can be formulated as a single exponential equation, and the following parameters are derived. a) Overlay of all traces; b) 6 °C: $R^2 = 0.999$, $k = 0.053\ s^{-1}$; c) 10 °C: $R^2 = 0.999$, $k = 0.0762\ s^{-1}$; d) 15 °C: $R^2 = 0.999$, $k = 0.136\ s^{-1}$; e) 20 °C: $R^2 = 0.999$, $k = 0.240\ s^{-1}$; f) 30 °C: $R^2 = 0.995$, $k = 0.769\ s^{-1}$; g) 40 °C: $R^2 = 0.995$, $k = 2.111\ s^{-1}$; h) a linear relation between $\ln(k/T)$ and $1/T$, $y = 24.9 - 9360.4x$, $R^2 = 0.998$, $\Delta H^{\ddagger} = 77.8\ kJ\ mol^{-1}$, $\Delta S^{\ddagger} = 9.24\ J\ mol^{-1}\ K^{-1}$, $\Delta G^{\ddagger} = 75.1\ kJ\ mol^{-1}$ at 25 °C.

Dependence of thermal ring-closing kinetics of compound **6** on the solvent viscosity (see **Figure 2-7**) was measured using solutions (12 μM, 2.0 mL) in mixtures of ethylene glycol (EG) and CH_3OH to vary the medium viscosity without much change in the polarity.[17]

To induce ring opening, the samples were irradiated for 30 s with a Tesoar hand-held laser pointer (405 nm, 1 mW) from the top of a squared quartz cuvette (10 mm). During the measurements, the solutions were stirred at a constant rate.

2.7.6 Testing accelerated ring closure under irradiation with red light

A methanol solution of compound **6** (13.8 µM, 2.0 mL) was placed in the sample holder of a UV-vis spectrometer and stirred at 25 °C. Immediately after irradiation with 80 mW of mic-LED-405 for 5.5 s, a kinetic trace of absorption intensity at 645 nm was recorded over 120 s to give the thermal ring closure kinetics (**Figure 2-24**a). The photochemically accelerated ring closing was performed under the same conditions, except that the sample was given pulses of 147 mW mic-LED-630 with 200 ms irradiation length and 500 ms interval over the 120 s recording time (**Figure 2-24**b).

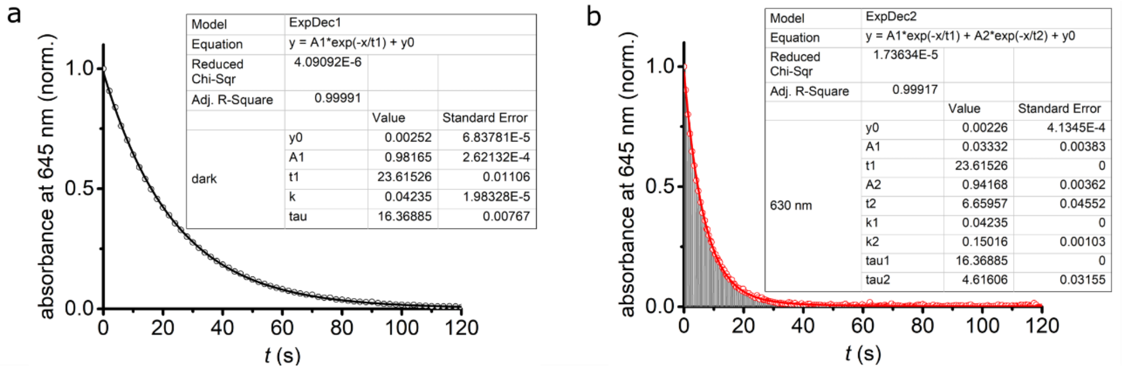

Model	ExpDec1		
Equation	y = A1*exp(-x/t1) + y0		
Reduced Chi-Sqr	4.09092E-6		
Adj. R-Square	0.99991		
		Value	Standard Error
dark	y0	0.00252	6.83781E-5
	A1	0.98165	2.62132E-4
	t1	23.61526	0.01106
	k	0.04235	1.98328E-5
	tau	16.36885	0.00767

Model	ExpDec2		
Equation	y = A1*exp(-x/t1) + A2*exp(-x/t2) + y0		
Reduced Chi-Sqr	1.73634E-5		
Adj. R-Square	0.99917		
		Value	Standard Error
630 nm	y0	0.00226	4.1345E-4
	A1	0.03332	0.00383
	t1	23.61526	0
	A2	0.94168	0.00362
	t2	6.65957	0.04552
	k1	0.04235	0
	k2	0.15016	0.00103
	tau1	16.36885	0
	tau2	4.61606	0.03155

Figure 2-24 Kinetic traces of ring closing of compound **6** in CH_3OH (13.8 µM, 2.0 mL). The absorption intensity of each trace is normalised relative to the respective original absorbance. a) Thermal ring closure (black, open circle), and the corresponding mono-exponential fit (black line). $k = 0.042$ s^{-1}, $R^2 = 1.00$. b) Photochemical ring closure using 147 mW of mic-LED-630 (raw: grey lines; reconstructed: red, open square), and the corresponding bi-exponential fit (red line). $k_1 = 0.15$ s^{-1}, with fixed $k_2 = 0.042$ s^{-1}, $R^2 = 0.999$. The raw data of the decay was processed in Matlab to remove the negative spikes caused by scattering light of the red irradiation during the measurement to give the reconstructed decay.

2.7.7 Testing photochemical fatigue resistance in cuvettes

Please see **Figure 2-11** for fatigue resistance of compound **6** in organic solvents. A methanol solution of compound **6** (13.8 µM, 2.0 mL) was placed in the sample holder of a UV-vis spectrometer and stirred at 25 °C. The samples were irradiated using mic-LED-405 (80 mW) for 5.5 s to generate the MC form. Immediately after irradiation, a kinetic trace of absorption intensity at 645 nm was recorded over 90 s for the MC form to fully recover to the SP form. The above procedure was repeated using the same sample for 30 cycles. For each cycle, the absorbance at $t = 0$ and 90 s are normalised to the maximum absorption intensity that happens at $t = 0$ s of the first cycle. This experiment was also carried out under argon using a distilled and degassed methanol solution under argon in an airtight cuvette.

2.7.8 Cell culture and staining procedures

Human dermal lymphatic endothelial cells (HDLEC) were generously provided by Dr Tess A. Stanly, at Weatherall Institute of Molecular Medicine, University of Oxford. HDLEC were cultured in Dulbecco’s modified Eagle medium (DMEM), supplemented with 10% fetal calf serum (FCS). The cells were grown to confluence at 37 °C with 5% CO_2 on a poly-D-lysine-coated microscope coverslip 24 h before imaging. For staining, **Dyad 1** was added to the growth medium as DMSO stock solution to reach a final concentration of 5 μM, and the cells were incubated for 15 min. The coverslip was taken out of the growth medium, rinsed with dye-free medium, and used for imaging at 37 °C.

2.7.9 Optical microscopy

Confocal images were acquired on a Zeiss confocal laser scanning microscope (Zeiss LSM 780 inverted confocal microscope), using a 63x/1.4 numerical aperture oil immersion objective lens (Plan-Apochromat 63x/1.4 Oil, Zeiss, Germany). The microscope was operated with Zen software. The excitation and depletion light sources were 633 nm (HeNe, 240 μW at 100%) and 405 nm (diode, 815 μW at 100%). The data were processed in ImageJ (Fiji software).

The fatigue resistance in cell imaging is defined as how many switching cycles a dyad (as an entire dyad of the switch and dye) can survive before photodegradation. This property is expressed as the normalised mean photon counts of the same field of view over consecutive cycles, relative to the fluorescence readout at the first bright state.

2.8 Synthetic procedures

Compounds **4** (5-carboxy-1,2,3,3-tetramethyl-3*H*-indol-1-ium iodide),[29] 1,3,3-trimethyl-2-methyleneindoline-5-carboxylic acid,[29] and 4-carboxy-2-methyl silicon rhodamine (precursor to compound **7**),[30] were prepared following published procedures.

1-Hydroxy-4-nitro-2-naphthaldehyde (2)

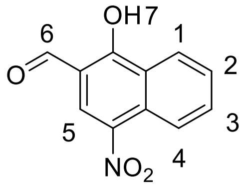

A suspension of 4-nitronaphthalen-1-ol (**1**) (500 mg, 2.65 mmol) and hexamethylene tetramine $(CH_2)_6N_4$ (557 mg, 3.98 mmol) in TFA (5.0 mL) was heated to 80 °C for 12 h. An aqueous solution of HCl (1 M, 17 mL) was added to the mixture, and the suspension was stirred vigorously at 20 °C for 2 h. The suspension was extracted with CH_2Cl_2 (3 × 60 mL) and washed with saturated aqueous NaCl (80 mL). The combined organic fractions were dried over $MgSO_4$, filtered, and the solvent was removed under reduced pressure to give a dark brown residue. The crude product was purified by silica gel chromatography (7:3 CH_2Cl_2/*n*-pentane to 99:1 CH_2Cl_2/CH_3OH). Recrystallisation from CH_2Cl_2/*n*-pentane afforded the product as a yellow solid (321 mg, 56%). R_f (SiO_2, CH_2Cl_2) = 0.49. ^1H NMR (400 MHz, $CDCl_3$) δ (ppm): 13.18 (s, 1H, H7), 10.01 (s, 1H, H6), 8.79 (d, *J* = 8.8 Hz, 1H, H4), 8.59–8.57 (overlapped signals, 2H, H1, H5), 7.92 (m, 1H, H3), 7.71 (m, 1H, H2). $^{13}C\{^1H\}$ NMR (101 MHz, $CDCl_3$) δ (ppm): 195.3, 165.8, 138.6, 133.9, 129.4, 127.7, 127.5, 125.2, 125.1, 124.0, 111.9. HRMS (TOF MS FI +ve) *m/z*: 217.0366, $([M]^+$, $C_{11}H_7NO_4$ requires 217.0375).

S-(2-Formyl-4-nitronaphthalen-1-yl) dimethylcarbamothioate

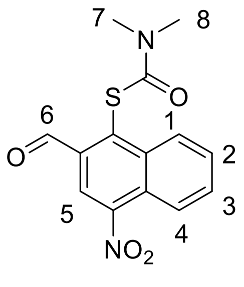

A mixture of 1-hydroxy-4-nitro-2-naphthaldehyde (**2**) (167 mg, 0.77 mmol), K_2CO_3 (256 mg, 1.85 mmol) and dimethylcarbamoyl chloride $Me_2NC(S)Cl$ (358 mg, 2.90 mmol) were placed in a dry Schlenk flask that was evacuated and refilled with nitrogen three times. Dry DMF (2.0 mL) was added and the suspension stirred at 50 °C for 12 h. The resultant was poured onto a mixture of ice (50 g) and an aqueous solution of HCl (5 mL, 10 M), and the suspension was filtered to obtain an orange solid. The crude product was purified by silica gel chromatography (CH_2Cl_2, 99:1 to 98:2 CH_2Cl_2/CH_3OH) to yield the product as a yellow solid (90 mg, 38%). R_f (SiO_2, 98:2 CH_2Cl_2/CH_3OH) = 0.70. ^1H NMR (400 MHz, $CDCl_3$) δ (ppm): 10.64 (s, 1H, H6), 8.81 (d, *J* = 8.3 Hz, 1H, H1), 8.66 (s, 1H, H5), 8.47 (d, *J* = 8.5 Hz, 1H, H4), 7.86

(m, 1H, H3), 7.78 (m, 1H, H2), 3.34 (s, 3H, H8), 3.05 (s, 3H, H7). $^{13}C\{^{1}H\}$ NMR (101 MHz, $CDCl_3$) δ (ppm): 189.7, 162.9, 148.6, 138.3, 136.3, 135.9, 131.8, 129.0, 127.1, 126.9, 123.7, 120.5, 37.5, 37.4. HRMS (TOF MS FI +ve) *m/z*: 304.0520, ($[M]^+$, $C_{14}H_{12}N_2O_4S$ requires 304.0518).

1-Mercapto-4-nitro-2-naphthaldehyde (3)

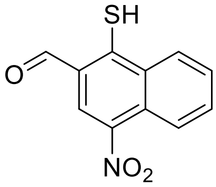

A solution of *S*-(2-formyl-4-nitronaphthalen-1-yl) dimethylcarbamothioate (90 mg, 0.30 mmol) in CH_3OH (8 mL) was degassed in an ultrasonic bath under positive pressure of nitrogen for 15 min. An aqueous solution of NaOH (1.86 mL, 1 M) was degassed for 10 min and added to the first solution. The reaction was stirred at 20 °C for 2 h. The red solution was cooled in an ice bath, and the mixture was acidified by adding an aqueous solution of HCl (3 mL, 1 M). The suspension was diluted with saturated aqueous NaCl (20 mL) and extracted with EtOAc. The combined organic fractions were dried over $MgSO_4$, filtered, and the solvent was evaporated to yield a yellow solid, which was used immediately in the next step without further purification. LRMS (ESI −ve) *m/z*: 232.0, ($[M-H]^-$, $C_{11}H_6NO_3S$ requires 232.0).

1',3',3'-Trimethyl-6-nitrospiro[benzo[*h*]chromene-2,2'-indoline]-5'-carboxylic acid (5)

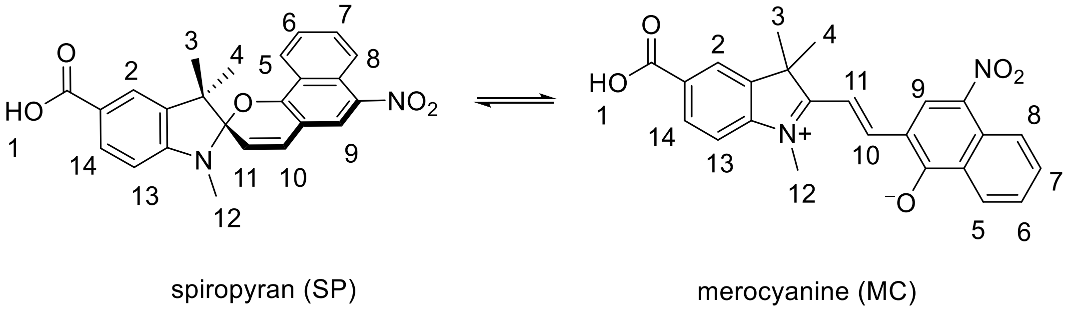

1,3,3-Trimethyl-2-methyleneindoline-5-carboxylic acid (prepared from compound **4**,[29] 41 mg, 0.19 mmol) and 1-hydroxy-4-nitro-2-naphthaldehyde (**2**) (41 mg, 0.19 mmol) were mixed in a dry Schlenk flask that was evacuated and refilled with nitrogen three times. Degassed CH_3CN (8.0 mL) was added and the mixture was heated to 82 °C for 12 h. The suspension was cooled to 0 °C and filtration afforded the product as a blue solid (71 mg, 90%). R_f (SiO_2, 9:1 CH_2Cl_2/CH_3OH) = 0.29. ^{1}H NMR (500 MHz, DMSO-d_6) δ (ppm): 12.92 (br. s, 2.5H, MC-H1, SP-H1), 8.93 (s, 2.4H, MC-H9), 8.67–8.53

(overlapped peaks, 3.4H, SP-H5, MC-H8), 8.52 (s, 1H, SP-H9), 8.35 (d, *J* = 6.2 Hz, 2.4H, MC-H5), 8.22 (s, 2.4H, MC-H2), 8.05 (dd, *J* = 6.6, 0.9 Hz, 2.4H, MC-H14), 7.87 (dd, *J* = 6.5, 1.2 Hz, 1H, SP-H14), 7.83 (d, *J* = 6.8 Hz, 1H, SP-H8), 7.77–7.72 (overlapped peaks, 2H, SP-H6, SP-H2), 7.70 (dd, *J* = 6.6, 6.6 Hz, 2.4H, MC-H7), 7.64 (d, *J* = 6.7 Hz, 2.4H, MC-H13), 7.57 (dd, *J* = 6.2, 6.2 Hz, 1H, SP-H7), 7.47 (dd, *J* = 6.1, 6.1 Hz, 2.4H, MC-H6), 7.35 (d, *J* = 8.3 Hz, SP-H10), 6.75 (d, *J* = 6.6 Hz, SP-H13), 6.04 (d, *J* = 8.2 Hz, 1H, SP-H11), 3.80 (s, 7.1H, MC-H12), 2.77 (s, 3H, SP-H12), 1.78 (s, 14.4H, MC-H3, MC-H4), 1.29 (s, 3H, SP-H3), 1.20 (s, 3H, SP-H4). ^{13}C{^{1}H} NMR (126 MHz, DMSO-*d*$_6$) δ (ppm): 167.5, 166.9, 153.9, 151.0, 145.9, 142.1, 137.8, 136.0, 131.8, 131.2, 130.9, 130.5, 130.4, 129.3, 128.7, 128.3, 127.3, 126.9, 126.1, 125.9, 125.5, 123.7, 123.4, 123.2, 123.0, 122.8, 121.8, 121.6, 118.8, 116.5, 112.1, 111.5, 107.1, 106.5, 51.3, 49.7, 32.2, 28.5, 27.0, 25.4, 19.6. HRMS (ESI –ve) *m/z*: 415.1302, ([M-H]$^-$, $C_{24}H_{19}N_2O_5$ requires 415.1299). UV-vis (H_2O) $\lambda_{\max}$ / nm (ε / M^{-1} cm^{-1}) 369 (1.0×10^4), 443 (1.1×10^4), 559 (3.3×10^4), 650 (8.7×10^3); UV-vis (1,4-dioxane) $\lambda_{\max}$ / nm (ε / M^{-1} cm^{-1}) 274 (2.7×10^4), 392 (9.4×10^3), 567 (4.2×10^3), 599 (5.8×10^3). UV-vis (toluene) $\lambda_{\max}$ / nm (ε / M^{-1} cm^{-1}) 393 (8.9×10^3), 568 (1.8×10^3), 606 (2.3×10^3).

1',3',3'-Trimethyl-6-nitrospiro[benzo[*h*]thiochromene-2,2'-indoline]-5'-carboxylic acid (6)

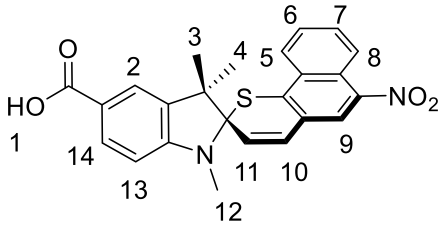

1-Mercapto-4-nitro-2-naphthaldehyde (**3**) (70 mg, 0.30 mmol) and 5-carboxy-1,2,3,3-tetramethyl-3*H*-indol-1-ium iodide (**4**) (104 mg, 0.30 mmol) were mixed in a dry Schlenk flask that was evacuated and refilled with nitrogen three times. Degassed EtOH (5.0 mL) and piperidine (0.11 mL, 1.1 mmol) were added and the mixture was heated to 78 °C for 80 min. The solution was acidified with acetic acid (0.02 mL, 0.3 mmol) and the solvent was removed under reduced pressure. The residue was purified by silica gel chromatography (CH_2Cl_2, 99:1 to 98:2 CH_2Cl_2/CH_3OH) and recrystallisation from 1:1 *n*-pentane/Et_2O afforded the product as a yellow solid (62 mg, 48%). R_f (SiO_2, 95:5 CH_2Cl_2/CH_3OH) = 0.20. ^{1}H NMR (500 MHz, 1:1 $CD_3OD/CDCl_3$) δ (ppm): 8.59 (d, *J* = 8.6 Hz, 1H, H5), 8.26 (d, *J* = 8.5 Hz, 1H, H8), 8.19 (s, 1H, H9), 7.86 (dd, *J* = 8.1, 1.6 Hz, 1H, H14), 7.74 (d, *J* = 1.3 Hz, 1H, H2), 7.68 (m, 1H, H6), 7.57 (m, 1H, H7), 7.12 (d, *J* = 10.7 Hz, 1H, H10), 6.54 (d, *J* = 8.2 Hz, 1H, H13), 6.07 (d, *J* = 10.8 Hz, 1H, H11), 2.77 (s, 3H, H12), 1.46 (s, 3H, H3), 1.29 (s, 3H, H4). ^{13}C{^{1}H} NMR (126 MHz, 1:1

$CD_3OD/CDCl_3$) δ (ppm): 152.0, 143.6, 140.7, 137.1, 132.5, 132.1, 131.6, 130.5, 128.2, 125.57, 125.53, 125.45, 125.2, 124.5, 124.4, 122.7, 107.3, 90.1, 52.8, 30.7, 25.1, 22.4. HRMS (ESI –ve) *m/z*: 431.1079, ($[M\text{-}H]^-$, $C_{24}H_{19}N_2O_4S$ requires 431.1071). UV-vis (H_2O) λ_{max} / nm (ε / M^{-1} cm^{-1}) 297 (1.9×10^4), 405 (8.9×10^3); UV-vis (CH_3CN) λ_{max} / nm (ε / M^{-1} cm^{-1}) 302 (2.5×10^4), 401 (8.6×10^3); UV-vis (1,4-dioxane) λ_{max} / nm (ε / M^{-1} cm^{-1}) 290 (3.5×10^4), 402 (1.0×10^4).

N-(10-(4-((2-((*tert*-Butoxycarbonyl)amino)ethyl)carbamoyl)-2-methylphenyl)-7-(dimethylamino)-5,5-dimethyldibenzo[*b*,*e*]silin-3(5*H*)-ylidene)-*N*-methylmethanaminium hexafluorophosphate (7)

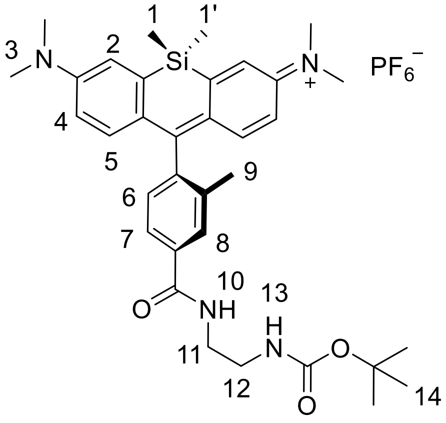

N-(10-(4-carboxy-2-methylphenyl)-7-(dimethylamino)-5,5-dimethyldibenzo[*b*,*e*]silin-3(5*H*)-ylidene)-*N*-methylmethanaminium 2,2,2-trifluoroacetate[30] (SiR precursor to compound **7**, 105 mg, 0.24 mmol) and benzotriazol-1-yl-oxytripyrrolidinophosphonium hexafluorophosphate (PyBOP, 307 mg, 0.59 mmol) were mixed in a dry Schlenk flask under nitrogen. Dry DMF (1.0 mL) containing triethylamine NEt_3 (0.2 mL) was added to the flask and the mixture was stirred at 20 °C for 10 min. *tert*-Butyl (2-aminoethyl)carbamate (95 mg, 0.59 mmol) was dissolved in dry DMF (1.0 mL) and added to the solution of the activated acid. The mixture was stirred at 20 °C for 12 h. The solvent was evaporated under reduced pressure, and the residue was purified by silica gel chromatography (CH_2Cl_2 to 98:2 CH_2Cl_2/CH_3OH) to give a dark blue solid (135 mg, 78%). R_f (SiO_2, 9:1 CH_2Cl_2/CH_3OH) = 0.38. ^1H NMR (400 MHz, $CDCl_3$) δ (ppm): 7.82 (s, 1H, H8), 7.78 (d, *J* = 10 Hz, 1H, H7), 7.56 (br. s, 1H, H10), 7.14 (overlapped signals, 3H, H2, H6), 7.00 (d, *J* = 10 Hz, 2H, H5), 6.58 (dd, *J* = 10, 1.0 Hz, 2H, H4), 5.23 (br. s, 1H, H13), 3.58 (br. m, 2H, H12), 3.42 (br. m, 2H, H11), 3.32 (s, 12H, H3), 2.05 (s, 3H, H9), 1.42 (s, 9H, H14), 0.58 (s, 3H, H1), 0.57 (s, 3H, H1'). $^{13}C\{^1H\}$ NMR (101 MHz, $CDCl_3$) δ (ppm): 167.8, 157.6, 154.3, 148.5, 141.6, 141.4, 136.4, 135.1, 129.2, 129.1, 127.1, 124.5, 120.9, 114.1, 79.8, 42.0, 40.9, 40.2, 28.5, 19.4, −1.0, −1.2. HRMS (ESI +ve) *m/z*: 585.32503, ($[M\text{-}PF_6]^+$, $C_{34}H_{45}O_3N_4Si$ requires 585.32554). UV-vis (H_2O): λ_{max} / nm (ε / M^{-1} cm^{-1}): 311 (1.3×10^4), 422 (5.2×10^3), 607 (2.8×10^4), 659 (1.0×10^5).

N-(7-(Dimethylamino)-5,5-dimethyl-10-(2-methyl-4-((2-(1',3',3'-trimethyl-6-nitrospiro[benzo[*h*]thiochromene-2,2'-indoline]-5'-carboxamido)ethyl)carbamoyl)phenyl) dibenzo[*b,e*]silin-3(5*H*)-ylidene)-*N*-methylmethanaminium 2,2,2-trifluoroacetate (Dyad 1)

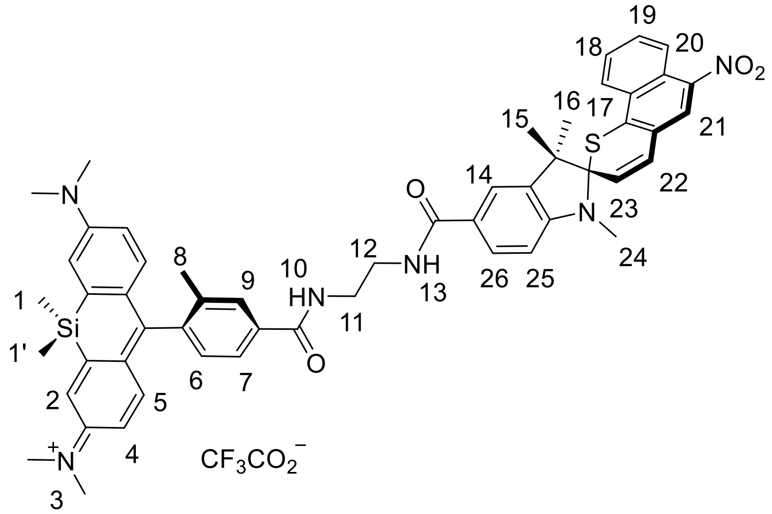

N-(10-(4-((2-((*tert*-Butoxycarbonyl)amino)ethyl)carbamoyl)-2-methylphenyl)-7-(dimethylamino)-5,5-dimethyldibenzo[*b*,*e*]silin-3(5*H*)-ylidene)-*N*-methyl-methanaminium hexafluorophosphate (**7**) (17 mg, 23 μmol) was added to a dry Schlenk flask that was evacuated and refilled with nitrogen three times. Dry CH_2Cl_2 (2.0 mL) was added and the solution cooled to 0 °C in an ice bath. TFA (1.0 mL, 13 mmol) was added dropwise and the mixture was stirred at 20 °C for 1 h. The solution was evaporated under reduced pressure. The residue was dissolved in CH_2Cl_2 and washed with an aqueous solution of K_2CO_3 (10 mL, 2 M), dried over $MgSO_4$, and the solvent was removed under reduced pressure. The residue was mixed with 1',3',3'-trimethyl-6-nitrospiro[benzo[*h*]thiochromene-2,2'-indoline]-5'-carboxylic acid (**6**) (10 mg, 23 μmol), EDC·HCl (8.8 mg, 46 μmol) and DMAP (0.78 mg, 0.25 mmol) in a dry Schlenk flask that was evacuated and refilled with nitrogen three times. Dry CH_2Cl_2 (2.0 mL) was added and the reaction was stirred for 2 h before the solvent was evaporated. The crude product was purified by silica gel chromatography (CH_2Cl_2, 97:3 to 9:1 CH_2Cl_2/CH_3OH) to yield a dark green solid (15 mg, 64%). R_f (SiO_2, 9:1 CH_2Cl_2/CH_3OH) = 0.16. ^{1}H NMR (500 MHz, $CDCl_3$) δ (ppm): 9.51 (br. s, 1H, H10), 8.97 (br. s, 1H, H13), 8.62 (d, *J* = 8.6 Hz, 1H, H17), 8.32–8.03 (overlapped peaks, 6H, H7, H9, H14, H20, H21, H26), 7.62 (dd, *J* = 7.7, 7.7 Hz, 1H, H18), 7.47 (dd, *J* = 7.6, 7.6 Hz, 1H, H19), 7.12–7.03 (overlapped peaks, 5H, H2, H5, H6), 6.99 (d, *J* = 10.8 Hz, 1H, H22), 6.56 (dd, *J* = 9.3, 2.3 Hz, 2H, H4), 6.47

(d, *J* = 8.2 Hz, 1H, H25), 5.99 (d, *J* = 10.8 Hz, 1H, H23), 3.80 (s, 4H, H11, H12), 3.32 (s, 12H, H3), 2.64 (s, 3H, H24), 2.03 (s, 3H, H8), 1.49 (s, 3H, H16), 1.28 (s, 3H, H15), 0.59 (s, 3H, H1), 0.56 (s, 3H, H1'). $^{13}C\{^1H\}$ NMR (126 MHz, $CDCl_3$) δ (ppm): 171.1, 168.1, 167.6, 154.3, 149.6, 148.4, 142.6, 142.2, 141.0, 140.5, 136.3, 135.8, 135.7, 131.6, 131.0, 130.2, 129.8, 129.1, 128.8, 127.6, 127.5, 126.4, 125.5, 125.1, 124.9, 124.8, 124.6, 124.0, 122.4, 122.3, 120.5, 114.3, 106.9, 89.7, 52.3, 41.0, 40.8, 40.5, 30.5, 24.9, 22.5, 19.5, 1.1, -0.5, -0.9. HRMS (ESI +ve) *m/z*: 899.3756, ($[M-CF_3CO_2]^+$, $C_{53}H_{55}N_6O_4SSi$ requires 899.3769). UV-vis (H_2O) λ_{max} / nm (ε / M^{-1} cm^{-1}) 302 (2.6×10^4), 420 (9.8×10^3), 613 (2.4×10^4), 654 (6.5×10^4); UV-vis (CH_3CN) λ_{max} / nm (ε / M^{-1} cm^{-1}) 283 (6.2×10^4), 419 (2.3×10^4), 602 (3.5×10^4), 653 (1.4×10^5); UV-vis (1,4-dioxane) λ_{max} / nm (ε / M^{-1} cm^{-1}) 290 (3.0×10^4), 418 (9.7×10^3), 608 (2.3×10^4), 652 (6.8×10^4).

2.9 References

[1] V. I. Minkin, *Chem. Rev.* **2004**, *104*, 2751–2776.

[2] V. A. Lokshin, A. Samat, A. V. Metelitsa, *Russ. Chem. Rev.* **2002**, *71*, 893–916.

[3] R. Klajn, *Chem. Soc. Rev.* **2013**, *43*, 148–184.

[4] G. Marriott, S. Mao, T. Sakata, J. Ran, D. K. Jackson, C. Petchprayoon, T. J. Gomez, E. Warp, O. Tulyathan, H. L. Aaron, et al., *Proc. Natl. Acad. Sci.* **2008**, *105*, 17789–17794.

[5] E. Fischer, Y. Hirshberg, *J. Chem. Soc.* **1952**, *5*, 4522–4524.

[6] W. Szymański, J. M. Beierle, H. A. V. Kistemaker, W. A. Velema, B. L. Feringa, *Chem. Rev.* **2013**, *113*, 6114–6178.

[7] M. Natali, S. Giordani, *Chem. Soc. Rev.* **2012**, *41*, 4010–4029.

[8] R. C. Bertelson, in *Org. Photochromic Thermochromic Compd. Vol. 1 Main Photochromic Fam.* (Eds.: J.C. Crano, R.J. Guglielmetti), Kluwer Academic Publishers, **2002**, pp. 11–83.

[9] G. Berkovic, V. Krongauz, V. Weiss, *Chem. Rev.* **2000**, *100*, 1741–1754.

[10] G. Lukinavičius, K. Umezawa, N. Olivier, A. Honigmann, G. Yang, T. Plass, V. Mueller, L. Reymond, I. R. Corrêa Jr, Z.-G. Luo, et al., *Nat. Chem.* **2013**, *5*, 132–139.

[11] Y. Koide, Y. Urano, K. Hanaoka, T. Terai, T. Nagano, *ACS Chem. Biol.* **2011**, *6*, 600–608.

[12] P. Rivera-Fuentes, A. T. Wrobel, M. L. Zastrow, M. Khan, J. Georgiou, T. T. Luyben, J. C. Roder, K. Okamoto, S. J. Lippard, *Chem. Sci.* **2015**, *6*, 1944–1948.

[13] C. Özçoban, T. Halbritter, S. Steinwand, L.-M. Herzig, J. Kohl-Landgraf, N. Askari, F. Groher, B. Fürtig, C. Richter, H. Schwalbe, et al., *Org. Lett.* **2015**, *17*, 1517–1520.

[14] W. Li, Z. Chen, L. Zhou, Z. Li, J. Ren, X. Qu, *J. Am. Chem. Soc.* **2015**, *137*, 8199–8205.

[15] Y. Xiong, P. Rivera-Fuentes, E. Sezgin, A. Vargas Jentzsch, C. Eggeling, H. L. Anderson, *Org. Lett.* **2016**, *18*, 3666–3669.

[16] M. Hammarson, J. R. Nilsson, S. Li, T. Beke-Somfai, J. Andréasson, *J. Phys. Chem. B* **2013**, *117*, 13561–13571.

[17] J. Whelan, D. Abdallah, K. Piskorz, J. T. C. Wojtyk, J. M. Dust, J.-M. Nunzi, S. Hoz, E. Buncel, *Phys. Chem. Chem. Phys.* **2012**, *14*, 13684–13691.

[18] V. Malatesta, in *Org. Photochromic Thermochromic Compd. Vol. 2 Physicochem. Stud. Biol. Appl. Thermochromism* (Eds.: J.C. Crano, R.J. Guglielmetti), Kluwer Academic Publishers, **2002**, pp. 65–166.

[19] S. Wu, Y. Luo, F. Zeng, J. Chen, Y. Chen, Z. Tong, *Angew. Chem. Int. Ed.* **2007**, *46*, 7015–7018.

[20] F. May, M. Peter, A. Hütten, L. Prodi, J. Mattay, *Chem. – Eur. J.* **2012**, *18*, 814–821.

[21] M. Hofmann, C. Eggeling, S. Jakobs, S. W. Hell, *Proc. Natl. Acad. Sci.* **2005**, *102*, 17565–17569.

[22] T. Grotjohann, I. Testa, M. Reuss, T. Brakemann, C. Eggeling, S. W. Hell, S. Jakobs, *eLife* **2012**, *1*, e00248.

[23] A. T. R. Williams, S. A. Winfield, J. N. Miller, *Analyst* **1983**, *108*, 1067–1071.

[24] H. J. Kuhn, S. E. Braslavsky, R. Schmidt, *Pure Appl. Chem.* **1989**, *61*, 187–210.

[25] M. Montalti, A. Credi, L. Prodi, M. Teresa Gandolfi, *Handbook of Photochemistry*, CRC Press, **2006**.

[26] A. E. Alegria, C. M. Krishna, R. K. Elespuru, P. Riesz, *Photochem. Photobiol.* **1989**, *49*, 257–265.

[27] M. Sobieraj, K. A. Krzyśko, A. Jarmuła, M. W. Kalinowski, B. Lesyng, M. Prokopowicz, J. Cieśla, A. Gojdź, B. Kierdaszuk, *J. Mol. Model.* **2015**, *21*, 1–14.

[28] J. R. Lakowicz, *Principles of Fluorescence Spectroscopy*, Springer Science & Business Media, **2007**.

[29] M. Tomasulo, S. L. Kaanumal, S. Sortino, F. M. Raymo, *J. Org. Chem.* **2007**, *72*, 595–605.

[30] T. Egawa, K. Hanaoka, Y. Koide, S. Ujita, N. Takahashi, Y. Ikegaya, N. Matsuki, T. Terai, T. Ueno, T. Komatsu, et al., *J. Am. Chem. Soc.* **2011**, *133*, 14157–14159.

Chapter 3

Spirooxazines

3 Spirooxazines

3.1 Introduction

This chapter describes another spiroheterocyclic photoswitch family of T-type (thermal), i.e. spirooxazines. Despite similarities in the structures and switching mechanisms of spiropyrans and spirooxazines, the latter exhibit significantly stronger fatigue resistance,[1–3] which is a crucial factor for RESOLFT microscopy. Additionally, spiropyrans are widely studied by the academic community, while spirooxazines are more commonly used for industrial applications such as photo-responsive sunglasses and ophthalmic lenses.[4] We initially investigated spiropyrans since a simple structural modification allowed a red shift of the absorption into the visible region, whereas the closed forms of most spirooxazines are only responsive to phototoxic UV light.[5,6] Nevertheless, we later were inspired by a few spironaphthoxazines reported in patents for various applications.[7,8] In particular, spironaphthoxazines bearing an indolinyl substituent, known commercially as palatinate purple, typically show strong absorption for the closed isomer at 405 nm. As the closely related spiropyran family described in Chapter 2, spirooxainzes also undergo reversible photoisomerisation between a closed spirooxazine form that is colourless or slightly yellow, and an open merocyanine form that is intensely coloured (example of palatinate purple see **Figure 3-1**).

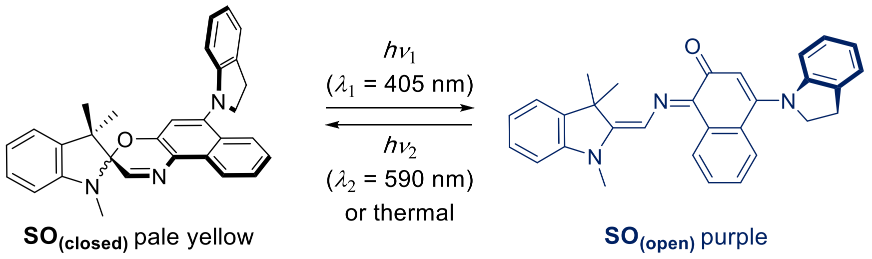

Figure 3-1 Example of an indolinyl substituted spironaphthoxazine and the switching mechanism.

Here we report a spironaphthoxazine that fulfills the design guidelines necessary to be utilised as a tunable fluorescence quencher in our modular molecular design. We first describe its synthesis, crystal structure and basic photophysical characterisation. The photochemistry and switching kinetics for both photo-processes are then elucidated by the means of ultrafast time-resolved spectroscopy. Following this Chapter, Chapter 4 continues to report on the possibility of such a switch to act as photochromic fluorescence quencher in our dyad molecular design for the purpose of RESOLFT imaging. The majority of the work in this Chapter has been published.[9] The work started with a Master's research project conducted by Johannes Osterrieth under the supervision of Dr Andreas Vargas Jentzsch and me.

3.2 Synthesis

The synthesis of molecular switch **SO** started with the preparation of indole **8**,[10] which was converted to the *t*-butyl ester **9**, then methylated using methyl iodide and deprotonated by KOH to yield Fischer's base **10**. Compound **SO** was prepared using chemistry developed by Pang, Meng and coworkers,[11] by the one-pot condensation of the zinc-chelated nitrosonaphthol **12**, indoline **13**, and Fischer's base **10**. Switch **SO** is soluble in many solvents, and was characterised using ultrafast time-resolved spectroscopy (see Section 3.5). As **SO** decomposed under conventional deprotection conditions, e.g. TFA or HCO_2H, deprotection was performed using silica in refluxing toluene[12] to afford acid **14**. Alternatively, acid **14** was prepared from compound **11**[13] by a similar one-pot method. Acid **14** was used to conjugate to a linker *via* an amide coupling and subsequently produce a dyad (see Chapter 4).

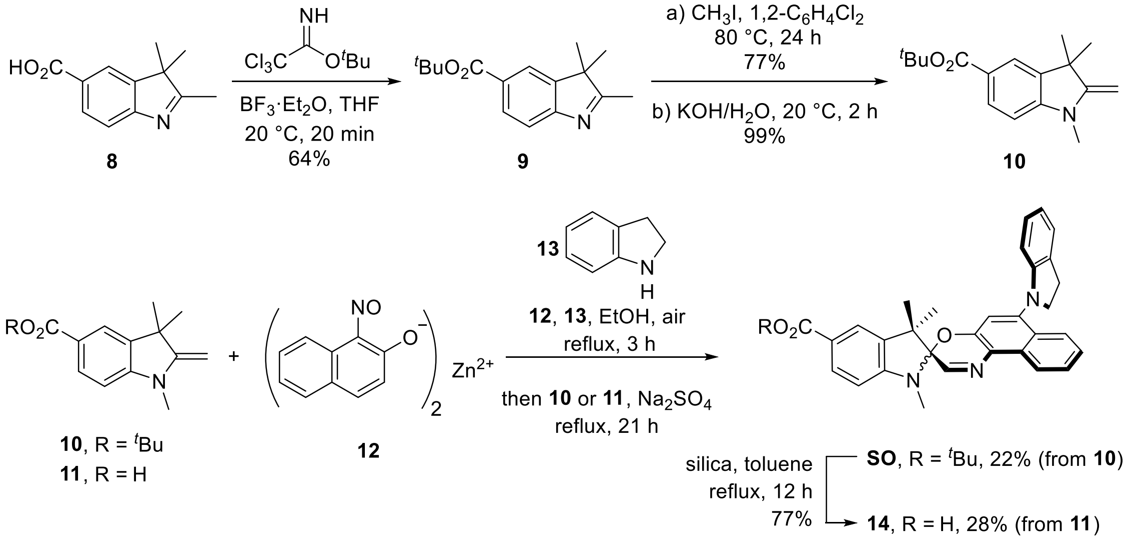

Scheme 3-1 Syntheses of switches **SO** and **14**.

3.3 X-ray crystallography and DFT calculations

Crystals of compound **14** (deprotected **SO**) suitable for X-ray analysis were obtained by slow evaporation of a solution in $CHCl_3$/CH_3OH at 25 °C. As in the structures of related spironaphthoxazines,[14–16] the naphthoxazine and indoline halves of the molecule are oriented orthogonally around the spiro sp^3 carbon center (**Figure 3-2**). This lack of π-conjugation implies that electronic transitions are mainly localised in each half of the molecule, giving rise to discrete absorption bands in the UV spectrum.[17] Thus, the bathochromic shift into the visible region shown by this switch, compared to analogues with different substituents, is attributed to the indoline-containing naphthoxazine component.[5]

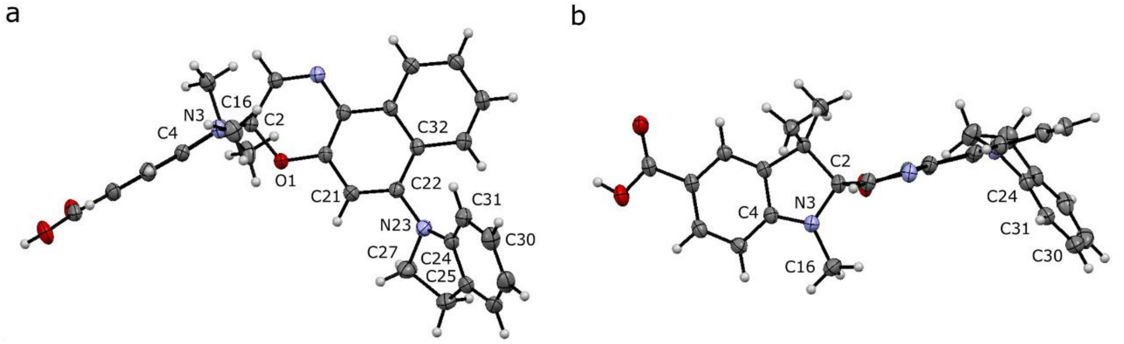

Figure 3-2 Crystal structure of **14** (deprotected **SO**)**.** Side (a) and axial (b) views are shown with thermal ellipsoids at 50% probability.

In the naphthoxazine moiety, the nitrogen atom (N23) on the indoline substitute is slightly pyramidal; it is 0.28 Å above the plane of its three connected carbon atoms (C22/C24/C27) shown in **Figure 3-3**a. As expected, the indoline unit is almost flat and the lone pair of this nitrogen interacts mainly with the indoline π-system; the C22/C24/C27 and C25/C24/C31 planes are almost parallel (angle: 14.3°) (**Figure 3-3**c). There is a significant twist between the indoline and naphthalene units; the angle between the C22/C24/C27 and C21/C22/C32 planes is 52.3° (**Figure 3-3**c), indicating weak overlap between the indoline nitrogen lone pair and the naphthalene π-system.

In the indoline moiety, the N3 nitrogen atom is pyramidalised (**Figure 3-3**e) so as to align its lone pair anti-parallel to the C$_{(spiro)}$–O bond; $n_N \rightarrow \sigma^*_{C\text{–}O}$ donation appears to weaken this bond, reducing the barrier to ring-opening. The C$_{(spiro)}$–O bond length (1.449 Å) in **14** is similar to that in other spirooxazines (mean = 1.46 Å, CCDC), and slightly longer than a typical C–O single bond (about 1.43 Å). The extent of pyramidalisation at N3 is similar to that at N23; N3 is displaced from the C2/C4/C16 plane by 0.22 Å.

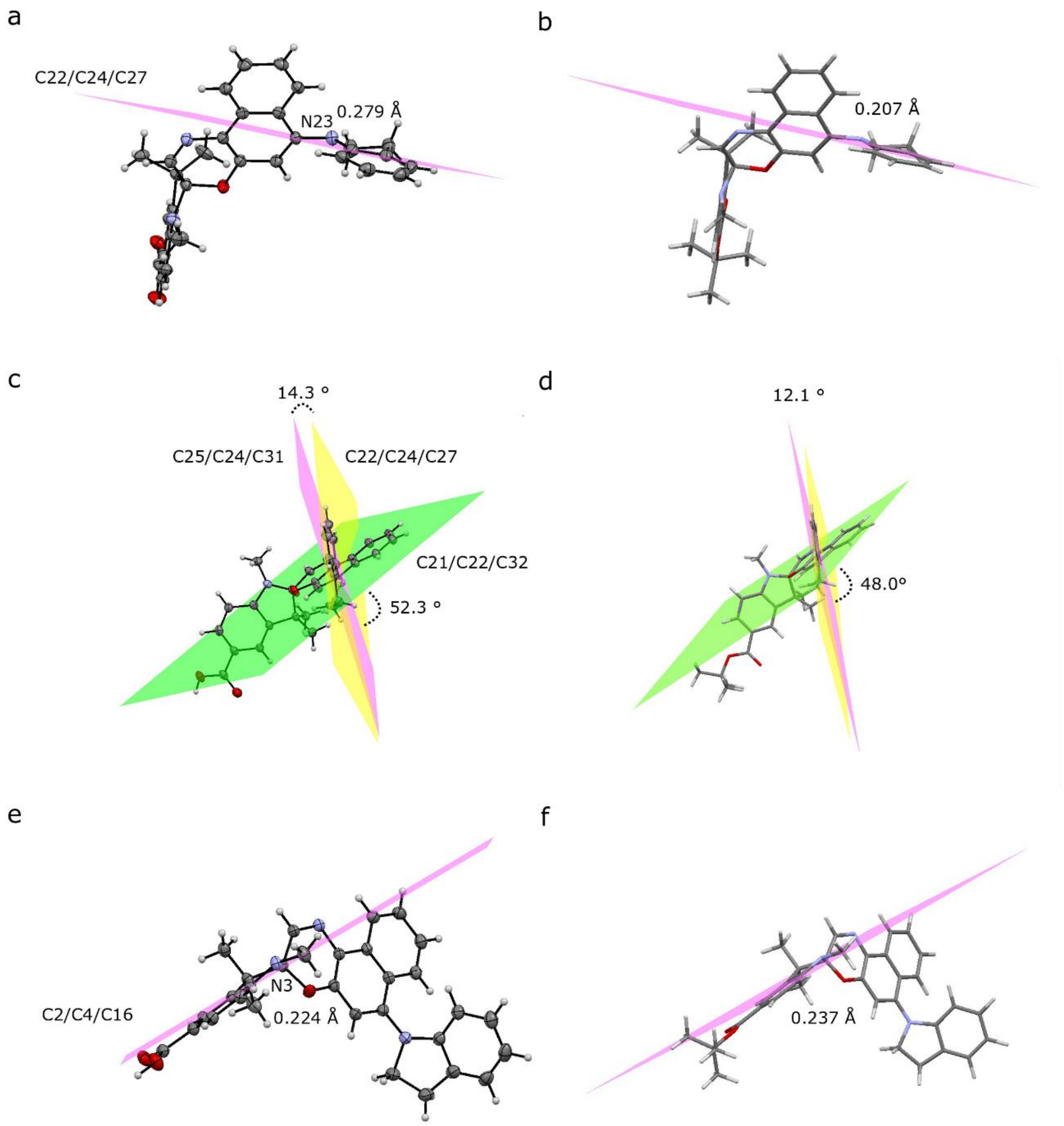

Figure 3-3 Comparison of the crystal structure (a, c, e) of compound **14** and the DFT-optimised structure (b, d, f) of **SO$_{(closed)}$**. Distorted trigonal configuration adopted by N23 on the naphthoxazine moiety a) in the crystal structure; b) from DFT calculations. Intersection angles between the planes C21/C22/C32, C22/C24/C27 and C25/C24/C31 c) in the crystal structure; d) from DFT calculations. Distorted trigonal configuration adopted by N3 on the indoline moiety e) in the crystal structure; f) from DFT calculations.

Density functional theory (DFT) calculations of **SO$_{(closed)}$** were performed by Dr Andreas Vargas Jentzsch using previously optimised methods (B3LYP/6-31+G(d,p) with the polarisable continuum model for solvation by CH_2Cl_2).[18,19] The DFT-optimised structure matches well with the crystal structure of **14**, indicating that the molecular geometry is not strongly influenced by crystal packing. The values of the parameters discussed above in this calculated stucture are shown in **Figure 3-3**b,d,f: displacement of N23 from C22/C24/C27 plane: 0.21 Å; angle between planes C22/C24/C27 and C25/C24/C31: 12.1°; angle between planes C22/C24/C27 and C21/C22/C32: 48.0°; displacement of N3 from C2/C4/C16 plane: 0.24 Å. TD-DFT calculations (cam-B3LYP/6-311+G(2d,p)) were used to predict the UV-vis absorption spectrum of **SO$_{\mathbf{(closed)}}$**, correctly reproducing the red-shifted absorption of indoline-substituted spirooxazines: λ_{max}(exp.) = 388 nm *vs.* λ_{max}(calc.) = 365 nm. These calculations predict an energy difference of 3701 cm^{-1} between the relaxed singlet excited state and the singlet excited state generated by vertical excitation from the ground state (i.e. a shift from 365 nm to 422 nm; **Figure 3-4**), suggesting significant geometry changes. Comparison of the optimised geometries of the ground state and singlet excited state (**Figure 3-5**) does not reveal a specific change leading to this energy difference but points toward minor changes across the whole molecule.

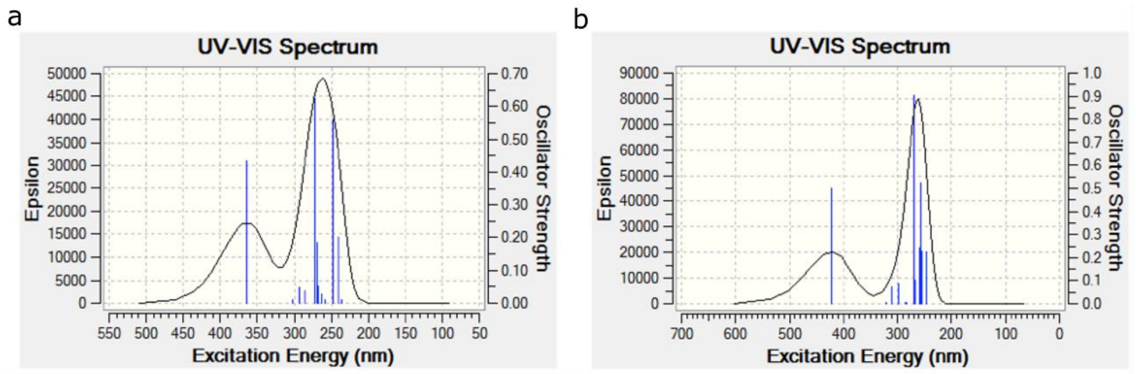

Figure 3-4 Comparison between the predicted absorption spectra of the vertical electronic transition for the ground-state (a) and singlet-excited state (b) optimised geometries of **SO$_{\mathbf{(closed)}}$**.

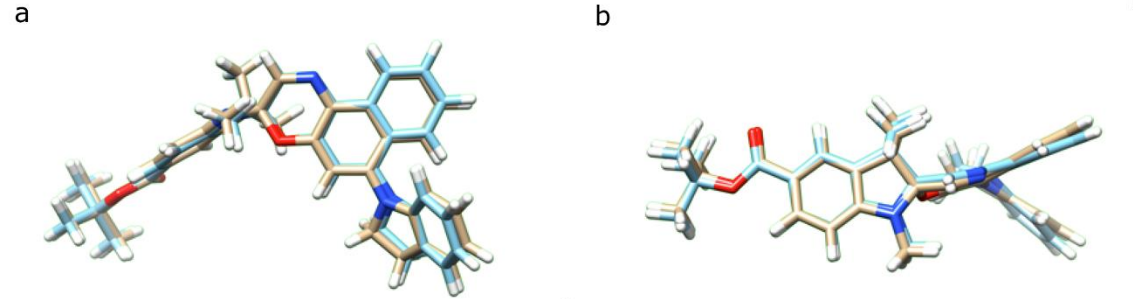

Figure 3-5 Comparison between the ground-state (light grey) and singlet-excited state (light blue) optimised geometries of **SO$_{\mathbf{(closed)}}$** from the side (a) and axial (b) views. Structures were aligned to the best match using Chimera.

DFT calculations were used to elucidate the stuctures of the open isomers of **SO**, which are not accessible by X-ray crystallography due to the fast thermal back reaction (<10 s). In theory, **SO$_{\mathbf{(open)}}$** can exist as eight stereoisomers depending on the geometry of the three consecutitve bonds that connect the naphthoxazine and indoline moieties. The calculations indicate that the most stable is TTC (*trans*-

trans-cis, 91.3%) followed by CTC (*cis-trans-cis*, 8.6%), with the other isomers accounting for less that 0.1% of the total speciation at thermodynamic equilibrium (**Figure 3-6**; **Table 3-1**), in agreement with results for similar systems.[18]

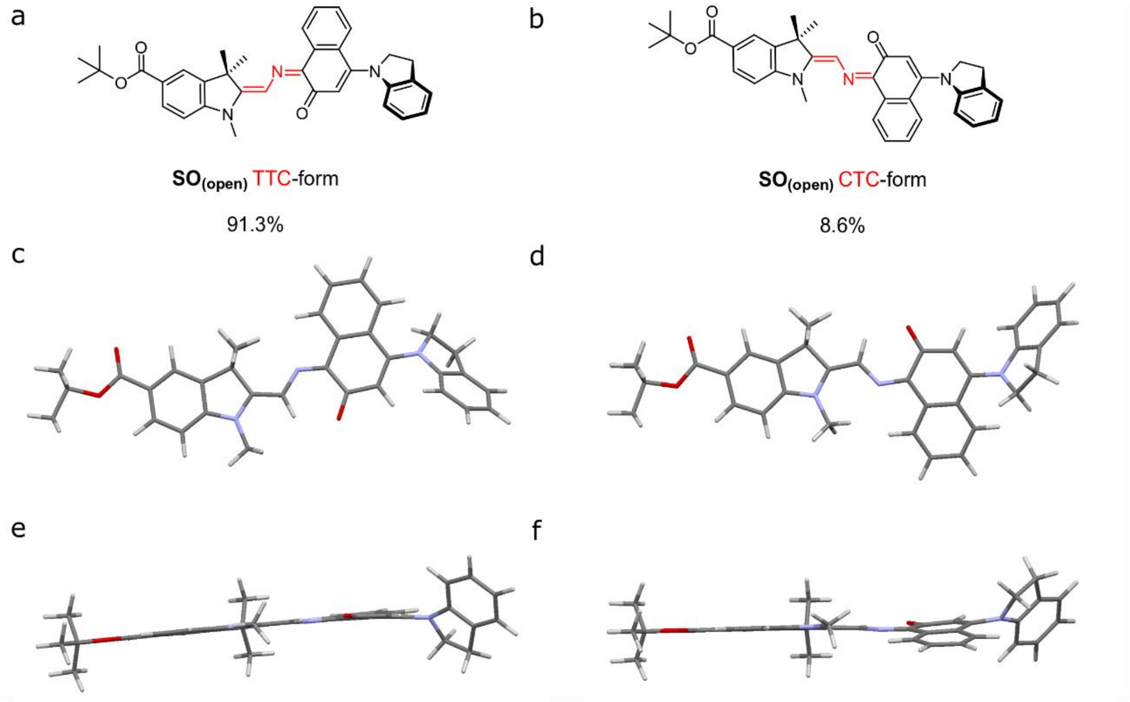

Figure 3-6 a,b) Molecular structures of major isomers of **$SO_{(open)}$** as predicted by DFT (B3LYP/6-31+G(d,p)). c–f) Side (c,d) and top (e,f) views of the predicted structure of the major **$SO_{(open)}$** isomers (TTC: c and e; CTC: d and f). Populations were calculated for thermodynamic equilibrium.

Table 3-1 Relative stabilities and species distributions of **$SO_{(open)}$** stereoisomers.

$SO_{(open)}$ isomer	relative stability (kcal mol^{-1})	speciation (%)
TTC	0	91.3
CTC	1.40	8.6
TTT	6.45	< 0.1
CTT	6.66	<0.1

3.4 Photophysical and photochemical characterisation

As discussed in Chapter 1, numerous criteria must be satisfied for a photochromic switch to be suitable for application in RESOLFT microscopy. Several of these properties, e.g. photoconversion and fatigue resistance, can be tested directly in dilute solution at an early stage. The photophysical characteristics of our switch of choice, **SO**, are presented here.

3.4.1 Photophysical and solvatochromic properties

The absorption spectrum of **SO$_{(closed)}$** displays two main bands (291 nm, $\varepsilon = 3.4 \times 10^4$ M^{-1} cm^{-1} and 390 nm, $\varepsilon = 1.4 \times 10^4$ M^{-1} cm^{-1} in CH_2Cl_2, **Figure 3-7**) as reported for similar spironaphthoxazines.[5,6,20] Significant absorption is observed at 405 nm ($\varepsilon = 1.2 \times 10^4$ M^{-1} cm^{-1}), indicating that it is possible to drive the photoswitching reaction using readily available 405 nm blue light. Compared to analogues with different substituents, spirooxazines incorporating an indoline substituent display a bathochromic shift in the UV-vis absorbance.[5,20] **SO$_{(closed)}$** exhibits weak fluorescence (541 nm, Φ_f = 5.1% in CH_2Cl_2; **Figure 3-7**, Experimental 3.7.6); similar fluorescence has been reported before for closely related spironaphthoxazines,[5,20–22] whereas most spirooxazines show no detectable fluorescence.[23] The large Stokes shift (151 nm, 7157 cm^{-1}) suggests that significant relaxation takes place in the singlet excited state; as discussed above, our TD-DFT calculations also predict a relatively large Stokes shift (3701 cm^{-1}).

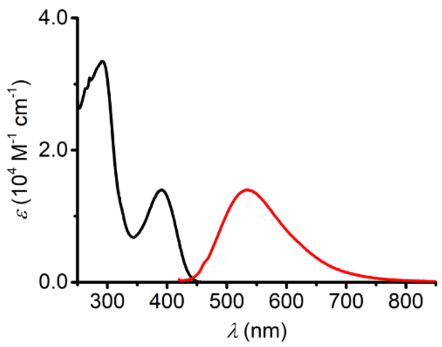

Figure 3-7 UV-vis absorption (black) and normalised fluorescence spectrum (red) of **SO$_{(closed)}$** in CH_2Cl_2 at 25 °C. The fluorescence spectrum was recorded using excitation at 405 nm.

Moreover, solvatochromic behaviour of **SO** was detected (**Figure 3-8**). While the absorption spectra remain unchanged, significant bathochromic shifts of the emission wavelength are observed with increasing solvent polarity, with exceptions of solvents of hydrogen bonding capacity, *e.g.* ^{i}PrOH. This is because **SO**, as a polar compound, has a larger dipole moment in the excited state relative to the ground state, and the interaction with polar solvents lowers the energy of the excited state, thus resulting in a red shifted emission wavelength. In addition to solvent polarity, other interactions between compounds and solvents, *e.g.* hydrogen bonding, can also give rise to spectral shifts.

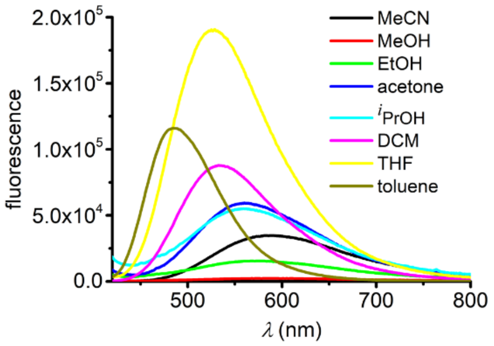

Solvent	**$\lambda_{abs,\ max}$ (nm)** ε (M^{-1} cm^{-1})	**$\varepsilon_{abs,\ 405nm}$ (M^{-1} cm^{-1})**	**$\lambda_{em,\ max}$ (nm)**
MeCN	**387** 1.3×10^4	9.8×10^3	592
MeOH	**389** 1.2×10^4	9.3×10^3	574[a]
EtOH	**389** 1.5×10^4	1.2×10^4	570
acetone	**389** 1.3×10^4	1.0×10^4	560
^{i}PrOH	**388** 1.5×10^4	1.2×10^4	562
CH_2Cl_2	**390** 1.4×10^4	1.2×10^4	533
THF	**389** 1.5×10^4	1.2×10^4	528
toluene	**391** 1.4×10^4	1.2×10^4	485

[a] The emission is very weak.

Figure 3-8 Solvatochromic behaviour of **SO**. Top: emission spectra of **SO** in different solvents. The measurements were taken of a 3.3 μM solution at 25 °C using excitation at 405 nm. Bottom: table of the values for the photophysical properties in different solvents.

3.4.2 Photochromic behaviour

The photoisomerisation reaction using 405 nm light was explored next. The open forms of spiro(naphth)oxazines are typically short-lived (less than 10 s),[5,6,20,21,24] which makes them difficult to characterise. We measured the decay of **SO$_{(open)}$** to estimate the rate of the thermal back reaction, which occurs in less than 100 ms in MeOH, while in apolar media lifetimes of a few seconds are observed (**Figure 3-9**). The results indicate that dielectric constants of solvents have an important effect on the rate of thermal ring closure. Accelerated thermal ring closure in polar solvents has been reported previously for spironaphthoxazines,[25–27] although some other spiropyrans display the opposite behaviour.[28]

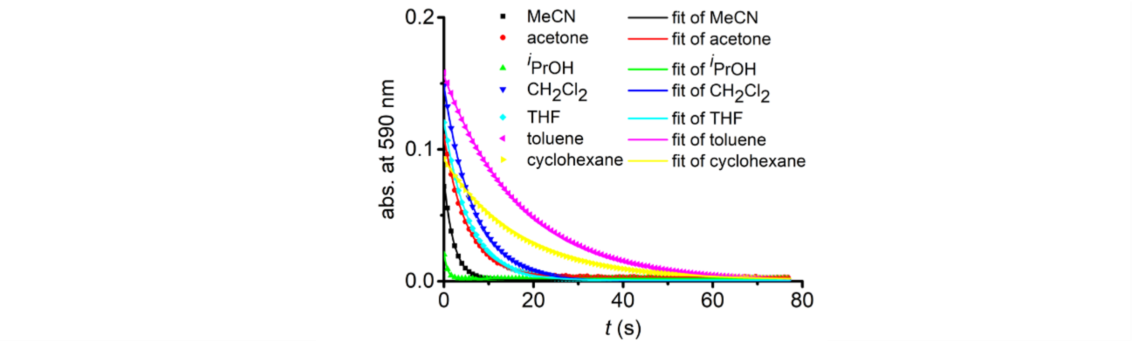

Solvent	Dielectric constant κ[a]	$t_{1/2}$ (s)[b]
MeCN	36.6 (20 °C)	1.55
MeOH	32.6	–[c]
EtOH	24.6	–[c]
acetone	20.7	3.62
^{i}PrOH	18.3	0.53
CH$_2$Cl$_2$	8.9	4.69
THF	7.5 (22 °C)	3.99
toluene	2.4	11.91
cyclohexane	2.0	11.51

Figure 3-9 Kinetic traces of thermal ring closure of **SO**$_{(\mathrm{open})}$ in different solvents (scatters) at 25 °C and corresponding mono-exponential fits (lines), and table of the calculated half lifetimes. [a]The values at 25 °C (unless otherwise stated in parentheses) are extracted from reference.[29] [b]All R^2 values for the mono-exponential fits are > 0.98. [c]The process was too fast to be recorded.

To explore the spectroscopic properties of **SO**, we used a custom-modified UV-vis spectrophotometer equipped with a pulsed LED light source (see Experimental 3.7.1) to generate **SO**$_{(\mathrm{open})}$ *in situ*. Under pulsed blue-light irradiation (405 nm, FWHM 15 nm, 80 mW, 100 ms pulse, 200 ms interval), **SO**$_{(\mathrm{open})}$ could be generated and observed in various solvents (**Figure 3-10**). Given the fast kinetics of ring closing, it is not possible to directly calculate the spectrum of **SO**$_{(\mathrm{open})}$ using standard methods, e.g. NMR or HPLC. Instead, the spectrum is estimated based on the observed photostationary state (PSS) (see later), and shows a very strong absorption band from 450 to 650 nm in cyclohexane (λ_{max}: 561 nm, ε: 8.9×10^4 M^{-1} cm^{-1}; **Figure 3-10**a) which is in line with similar spironaphthoxazines.[5,6,30] Remarkably, the **SO**$_{(\mathrm{closed})}$ band centered at 388 nm almost completely disappears in **SO**$_{(\mathrm{open})}$ implying that high degrees of conversion can be achieved using 405 nm light (85–95%; see below). This is important for the potential application in RESOLFT microscopy because most commercial microscopes are optimised for the use of visible light illumination rather than UV light, and visible light produces low photobleaching and phototoxicity. A similar feature centred at ca. 350 nm would limit the use of such a switch to custom-made microscopes.

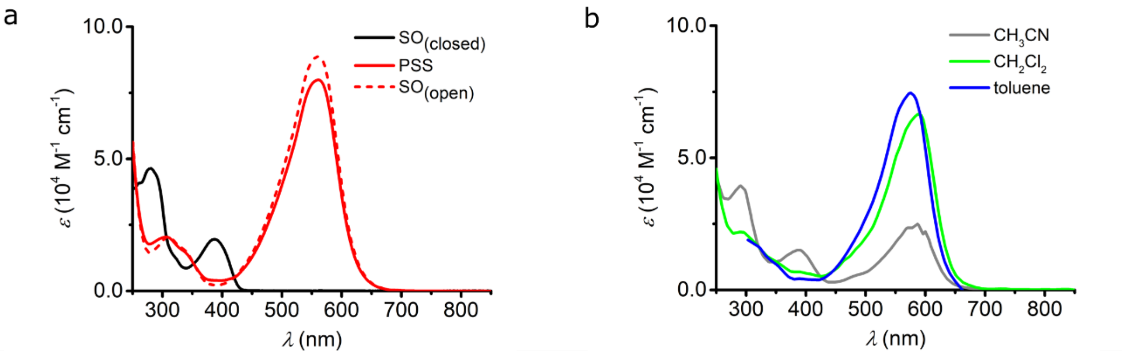

Figure 3-10 a) UV-vis absorption spectra of switch **SO$_{(closed)}$**, photostationary state (PSS), and calculated **SO$_{(open)}$** in cyclohexane at 10 °C. The PSS was obtained by irradiation with blue (405 nm) light, and the **SO$_{(open)}$** was reconstructed mathematically using custom written Matlab scripts. b) The PSS spectra of **SO** in different solvents after irradiation at 405 nm.

Specifically, the estimation of **SO$_{(open)}$** was based on three considerations: (a) Assume that the PSS is 100% **SO$_{(open)}$** and 0% **SO$_{(closed)}$**. In this case the absorption spectrum of the PSS would be the same as that of **SO$_{(open)}$**; (b) Assume that **SO$_{(open)}$** has no absorption at 390 nm, i.e. any absorption at 390 nm is from the remaining **SO$_{(closed)}$**. In this case the composition of the PSS can be easily calculated as 20% **SO$_{(closed)}$** because the ratio of the absorption of the PSS at 390 nm divided by the initial absorption of **SO$_{(closed)}$** at 390 nm is 0.2; (c) Assume that the fraction of **SO$_{(closed)}$** in the PSS is *x*, where *x* is in the range 0–20% from the extreme cases in (a) and (b). Using the equation PSS = (1-*x*)***SO$_{(open)}$** + *x****SO$_{(closed)}$**, the absorption spectrum of **SO$_{(open)}$** can be derived from subtracting a fraction *x* of the absorption spectrum of **SO$_{(closed)}$** from the absorption of the PSS (**Figure 3-11**a). Assuming that the absorption spectrum of **SO$_{(open)}$** has non-zero absorption at 390 nm but no obvious humps, the figures (**Figure 3-11**b) imply that the composition of the PSS is 15%–5% **SO$_{(closed)}$**, i.e. 85–95% **SO$_{(open)}$**. The assumption of no humps at around 390 nm is supported by the results of the TD-DFT calculations (see Section 3.5).

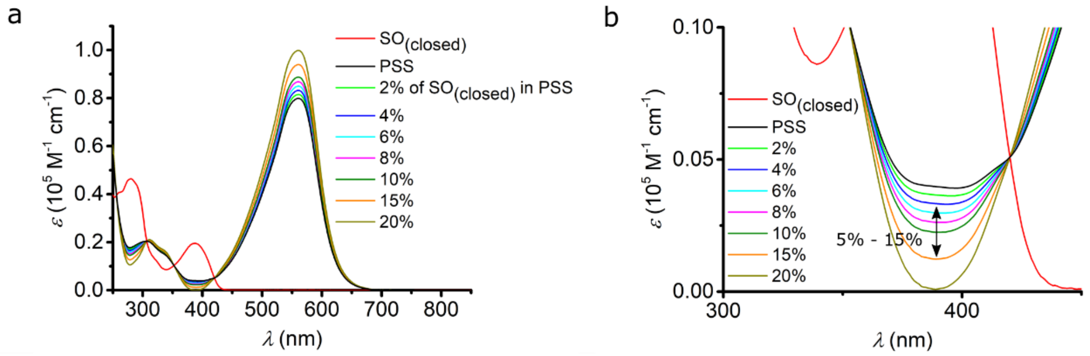

Figure 3-11 Analysis of the evolution of the spectral shape based on different contributions (%) of **SO$_{(closed)}$** to the PSS spectrum. Assuming **SO$_{(open)}$** absorbs at 390 nm but has no obvious humps, the composition of the PSS is 15%–5% **SO$_{(closed)}$**, i.e. 85–95% **SO$_{(open)}$**.

The quantum yield of ring opening was measured by analysing the changes in UV-vis absorption during excitation,[5,31,32] but due to the rapid back-reaction it was necessary to use time-resolved absorption (down to 200 ms; **Figure 3-12**). To minimise the interference of the back reaction, the photochemical quantum yield for ring opening ($\Phi_{c\rightarrow o}$) was measured in cyclohexane at 10 °C. The calculation was based on the equation,[31] $\Phi_o = \frac{mVN_Ahc}{P\lambda(1-10^{-A})\varepsilon_{\mathrm{prod}}d}$, where m is the slope of the linear fit at the initial rise stage, V is the sample volume, N_A, h, and c are Avogadro, Planck and speed of light constants, P is the power intensity, λ is the excitation wavelength, A is the absorbance at the excitation wavelength, $\varepsilon_{\mathrm{prod}}$ is the estimated molar absorption coefficient of **SO(open)** at 560 nm, d is the path length of the cuvette (see Experimental 3.7.7). The calculation gives the quantum yield of ring opening, $\Phi_o = 8.0 \pm 0.7\%$ in cyclohexane at 10 °C and $\Phi_o = 7.7 \pm 0.6\%$ in CH_2Cl_2 at 10 °C. The similar quantum yields imply that the solvent has little influence on the photochemistry of **SO**. These quantum yields are 2–4 times smaller than the values reported previously for related palatinate purple spironaphthoxazines.[5,20,32]

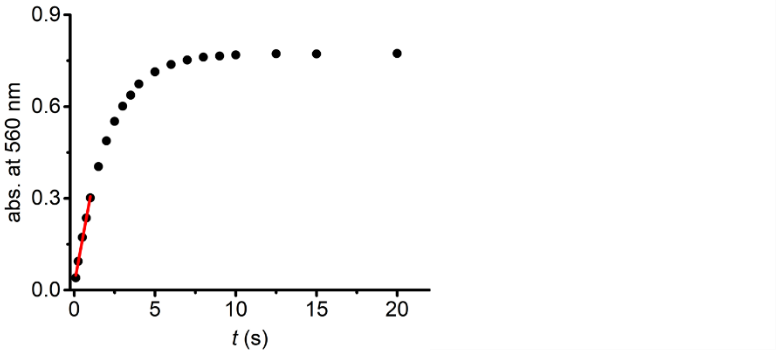

Figure 3-12 The initial part of the reconstructed ring opening kinetics of **SO** in cyclohexane at 10 °C, and the linear fit. The slope $m = 0.329 \pm 0.012$ (used in the calculation of the quantum yield of ring opening), $R^2 = 0.998$.

An important feature of spironaphthoxazines is that the thermal back reaction can be accelerated using light.[33,34] We explored the photo-reversion reaction using the same set-up described above by starting with blue (405 nm) irradiation followed by several short pulses of green light (525 nm, FWHM 60 nm, 69 mW, 100 ms pulse, 400 ms interval). **Figure 3-13** shows the acceleration of the thermal back reaction under green illumination. Using similar methods as for the ring opening reaction (see Experimental 3.7.7), we calculated the quantum yield of ring closing to be $\Phi_{o\rightarrow c} = 1.1 \pm 0.1\%$ in cyclohexane at 10 °C, in agreement with studies on related compounds.[5]

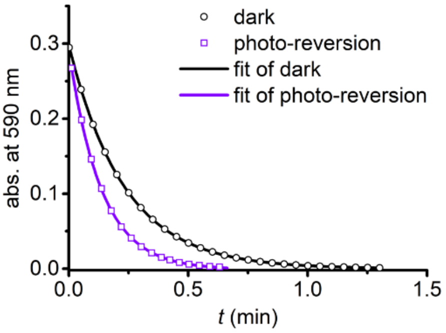

Figure 3-13 Kinetic traces for the ring-closure reaction **SO(open)** → **SO(closed)** after blue-light irradiation in cyclohexane at 10 °C. Both the thermal (black circles; fit, black line) and combined thermal and photochemical using green light (525 nm, 0.97 W/cm^2, 100 ms irradiation, 400 ms interval, violet squares; fit, violet line) are shown. Exponential fit of the thermal decay: $t_{1/2}$ = 0.17 min, R^2 = 1.000. Exponential fit of the photo-reversion decay: $t_{1/2}$ = 0.094 min, R^2 = 1.000.

The changes in the absorption spectra, together with the quantum yields of ring opening and closing, result in a high PSS (ca. 85–95% open, as calculated from the absorption spectra)[35–37] using 405 nm irradiation, which is a critical requirement for high contrast in microscopy applications.

3.4.3 Fatigue resistance

A crucial property of a molecular switch is its fatigue resistance (i.e. number of switching cycles the molecule can undergo before irreversible degradation), and this is most important in the context of RESOLFT, as mentioned in Chapter 1.

We investigated the fatigue resistance of **SO** in cyclohexane and CH_2Cl_2 by time-resolved absorption, alternating blue (405 nm) light irradiation and thermal relaxation (**Figure 3-14**a,b). Analogous experiments in polar solvents, e.g. MeOH, were not possible because the **SO(open)** does not persist long enough to be reliably detected. With less than 10% photo-degradation after 100 photo-cycles (in CH_2Cl_2), the fatigue resistance of **SO** is most promising compared to published dyes.[38,39] We also investigated the fatigue resistance under photo-reversion conditions (i.e. by alternating blue and green irradiations during the measurements, **Figure 3-14**c), and confirmed that over 100 cycles can be achieved with less than 20% photo-degradation in cyclohexane. This result confirms that spirooxazines are remarkably fatigue-resistant switches.[3,24,40]

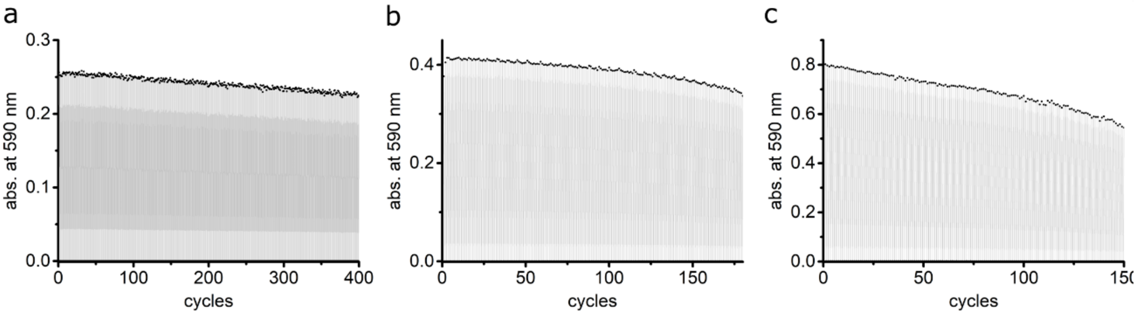

Figure 3-14 Fatigue resistance of **SO** in the cuvette. a) Fatigue resistance of **SO** in cyclohexane at 25 °C. Each cycle consists of blue irradiation (405 nm, 2.5 s, 2.1 W cm^{-2}), and thermal relaxation. b) Fatigue resistance of **SO** in CH_2Cl_2 at 25 °C. Each cycle consists of blue irradiation (405 nm, 2.5 s, 2.1 W cm^{-2}), and thermal relaxation. c) Photochemical fatigue resistance of **SO** in cyclohexane at 10 °C. Each cycle consists of excitation at 405 nm (2.5 s, 2.1 W cm^{-2}), 500 ms interval, excitation at 525 nm (30 s, 0.97 W cm^{-2}) and further 5 s waiting until the absorbance returned to ~0. The maximum and minimum absorbance of each cycle after 405 nm excitation were extracted using custom written Matlab scripts (see Appendices) to generate the graphs.

3.5 Ultrafast photochemistry: time-resolved infrared (TRIR) and transient absorption (TA) spectroscopy

The experiments described above provide valuable insights into the most important properties of **SO**, such as a strongly coloured open form, high fatigue resistance, and almost complete photoisomerisation using blue light. Further improvements to the molecular design require a thorough understanding of the underlying photochemistry. For instance, the photoisomerisation of structurally related spiropyrans can occur *via* either singlet or triplet pathways, or a combination of both,[32,41,42] and the reactions of triplet excited states, for example with oxygen, can lead to photo-degradation.[43–45]

A number of photophysical studies have been reported on different spirooxazines,[30,41–48] complemented by computational work.[18,19] Photoisomerisation is thought to proceed *via* dissociation of the C_{spiro}–O bond in the singlet electronic excited state, followed by the formation of a short-lived (ca. 10–100 ps) cisoid intermediate,[6] sometimes identified as the CCC merocyanine (the so-called "X-intermediate"; **Figure 3-15**).[49–51] This intermediate either relaxes back to the closed spirooxazine or transforms to one of the stable open merocyanine forms on a timescale of a few ps to ns. These isomers are thought to be in equilibrium, with the TTC and CTC forms predominating (**Figure 3-15**).[6] The kinetics of these processes and the distribution of the species are strongly dependent on the chemical structure.[3,40]

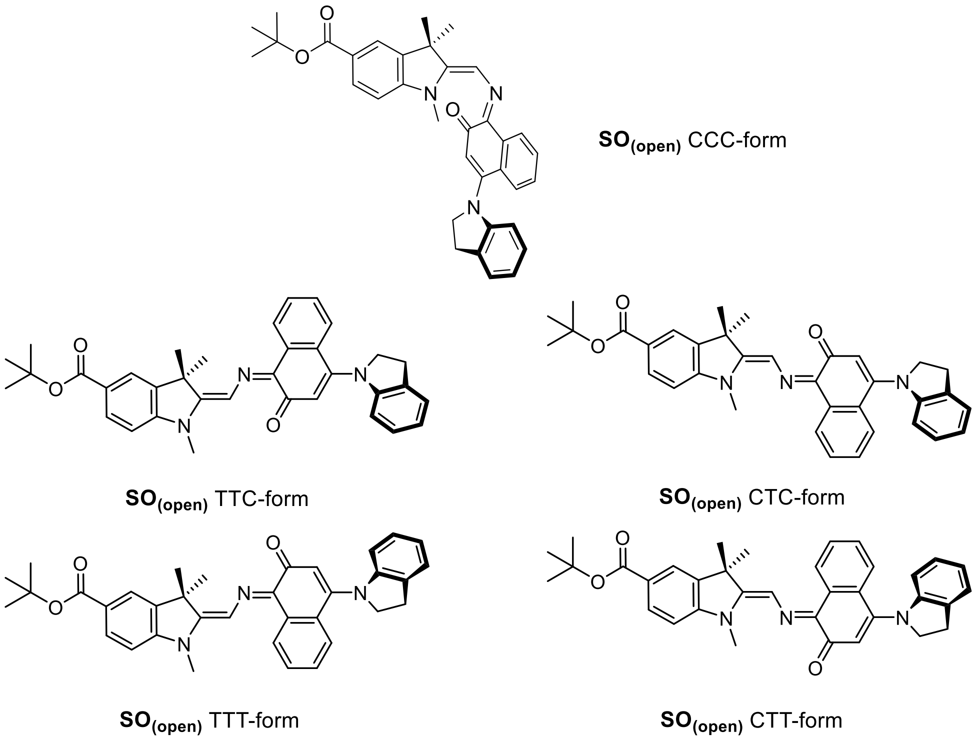

Figure 3-15 Structures of **SO(open)** isomers.

To date, the majority of studies of spirooxazines have been performed using transient absorption (TA) or time-resolved fluorescence,[52] and often the results observed for spiropyrans are extrapolated to spiro(naphth)oxazines. To gather a more reliable understanding of the structures of the various intermediates and their kinetics, ultrafast time-resolved infrared (TRIR) appears to be attractive, because our DFT calculations suggest that the different open merocyanine isomers have significantly different IR signatures (**Figure 3-17**), while being virtually indistinguishable by UV-vis spectroscopy (**Figure 3-16**). While the relative stabilities of the **SO(open)** isomers are predicted to favour the TTC (91.3%) at thermodynamic equilibrium, whether the other isomers represent reaction intermediates is an open question that can be addressed using TRIR.

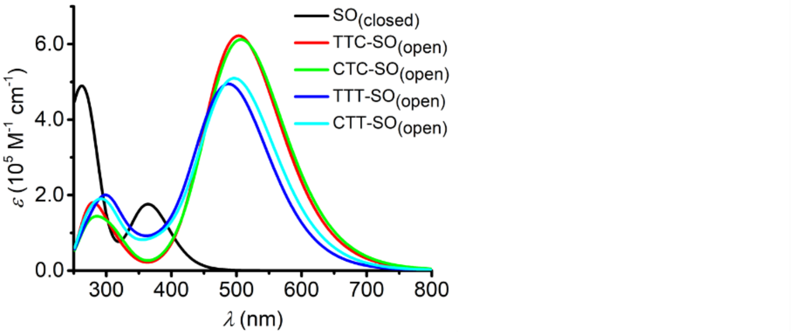

Figure 3-16 Predicted UV-vis spectra of **SO** in the closed form and the open form (all four isomers). Calculation was performed at the DFT B3LYP/6-31+G(d,p) level of theory with the polarisable continuum model for solvation by CH_2Cl_2.

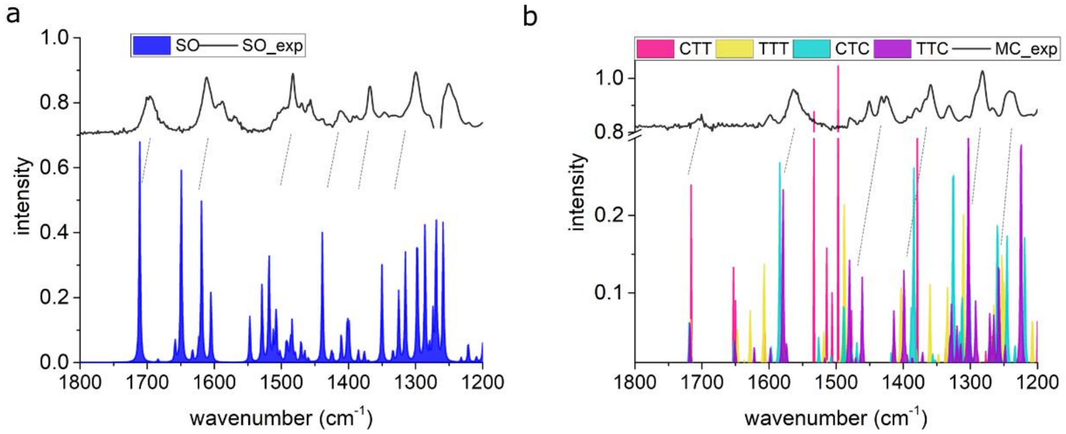

Figure 3-17 Predicted IR spectra for **SO** in the closed form (a) and the open form of all four isomers (b). Frequencies calculated at the DFT B3LYP/6-31+G(d,p) level of theory. Notice that the different isomers, notably those that are calculated to be unstable, have very different IR signatures (e.g. the strong CTT band ca. 1500 cm^{-1}). The experimental spectra are shown at the top.

Both the transient absorption (TA) and time-resolved IR (TRIR) techniques are based on pump-probe spectroscopy, where a sample is excited by a pump (excitation) pulse, and a time-delayed probe pulse detects the absorption difference of the sample with and without the pump excitation. With varied time delays of the probe pulse with respect to the pump pulse, absorption changes and thus dynamic information of typically femtosecond temporal resolution over microsecond timescales can be obtained. Along with the high temporal resolution of standard TA and TRIR spectroscopy, a unique advantage of the extended monitoring time up to 1 ms is granted by the use of our collaborator's (Prof. Anthony Parker) specialised instrumentation and techniques, i.e. TRIR and TA in time-resolved multiple probe spectroscopy at the STFC Rutherford Appleton Laboratory.[53,54] Technical details are provided in Experimental 3.7.10. In essence, absorption-based pump-probe spectroscopy measures absorbance changes that are caused by pump excitation as a function of time and wavelength, i.e. Δ(abs. at λ) = abs. (t, λ) – abs. (0, λ). The simplest and most common contributions to absorbance changes are (**Figure 3-18**):

a) ground state bleach, detected as negative peaks because electrons in the ground state at $t = 0$ are now in the excited state at $t > 0$, and absorbance by the ground state electrons is reduced; b) stimulated emission, detected as negative peaks because electrons in the excited state decay to the ground state by photon emission, i.e. ‘negative’ absorbance; c) absorption, detected as positive peaks because the newly formed excited state absorbs at a different wavelength. There are many more other processes that molecules undergo and that can be observed by the pump-probe technique, including vibrational relaxation and conformational changes of molecules, e.g. the photoswitching behaviour of photoswitches.

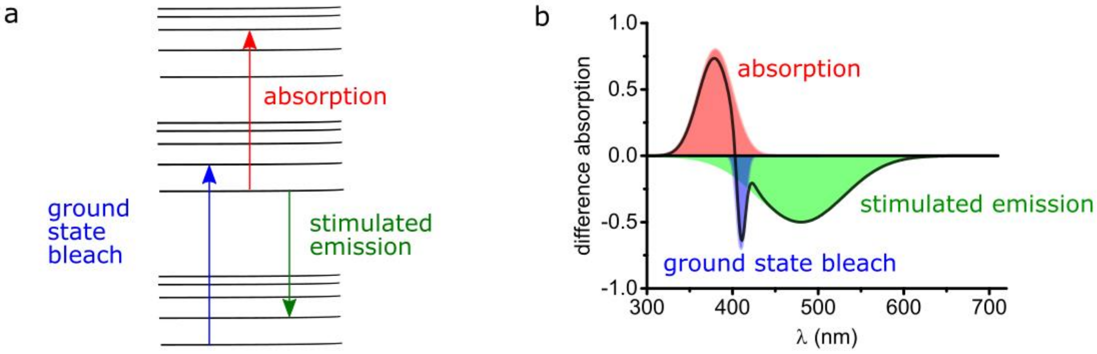

Figure 3-18 Common causes of absorbance changes in pump-probe spectroscopy, e.g. transient absorption spectroscopy. a) Schematic representation of energy levels and common transitions induced by a pump pulse. b) The corresponding difference absorption spectrum (black line) caused by the processes in a), with different contributions (coloured shades).

For photoswitching of **SO**, both TRIR and TA spectra in dichloromethane (CD_2Cl_2 for TRIR and CH_2Cl_2 for TA) show the presence of two clear transient species (**Figure 3-19**a,b, **Figure 3-20**a,b), indicated by distinct spectral features (e.g. in TA the absorptions at 440 nm and 590 nm). Upon close inspection, a third intermediate can be identified and is necessary to correctly describe the system. Such an intermediate (D in **Figure 3-21**, later **Scheme 3-2**) has been described previously for similar spirooxazines.[30,46–48]

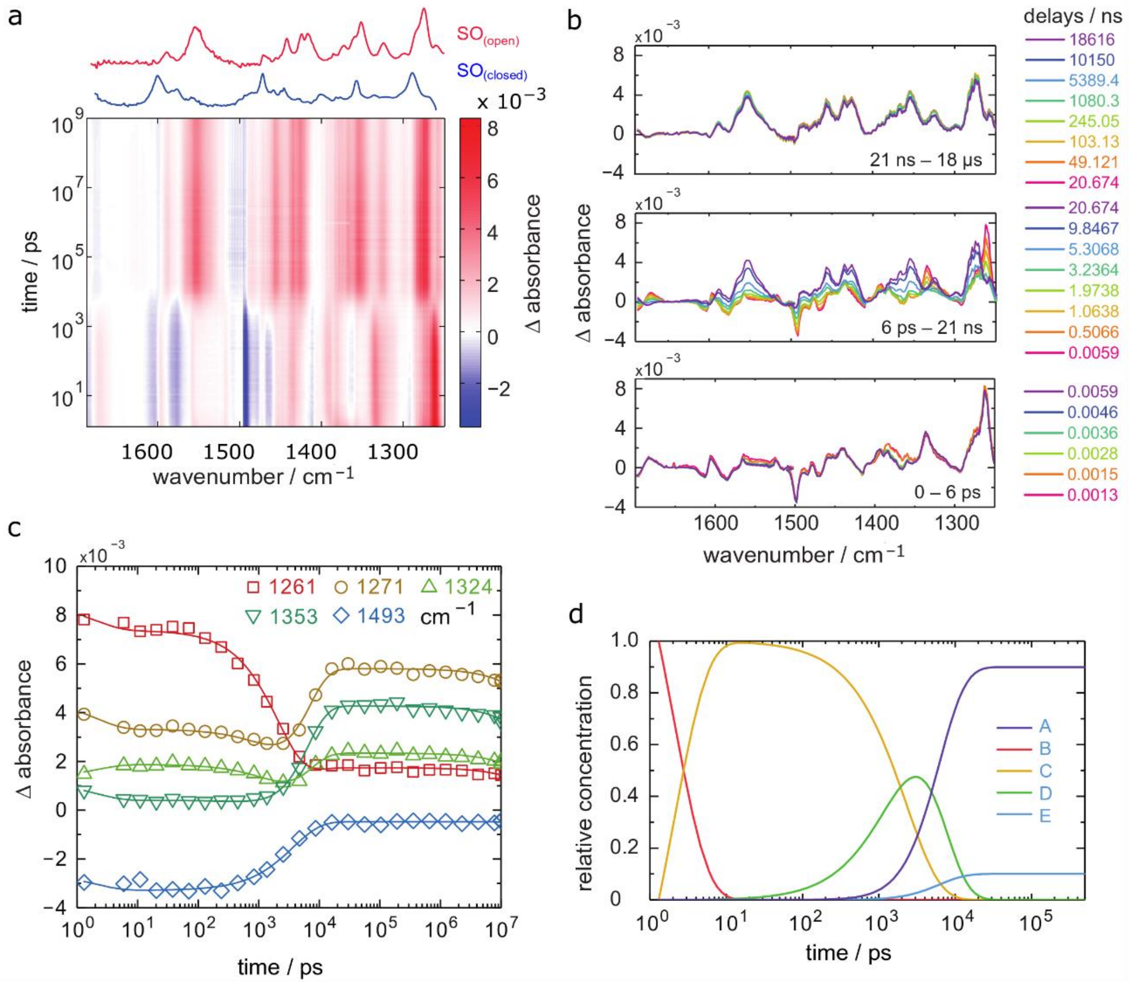

Figure 3-19 TRIR spectra in CD_2Cl_2, and excited-state kinetics of the ring-opening process of **SO(closed)**. a) TRIR contour spectrum; the steady-state spectra are shown for reference. b) TRIR spectra for selected probe times. c) TRIR kinetic traces for selected wavenumbers (scatter) and fitted kinetics (solid lines) using the values obtained from target analysis. d) Speciation plot for the ring-opening reaction using the values obtained by target analysis for TRIR. Laser details: 405 nm pump, 800 nJ.

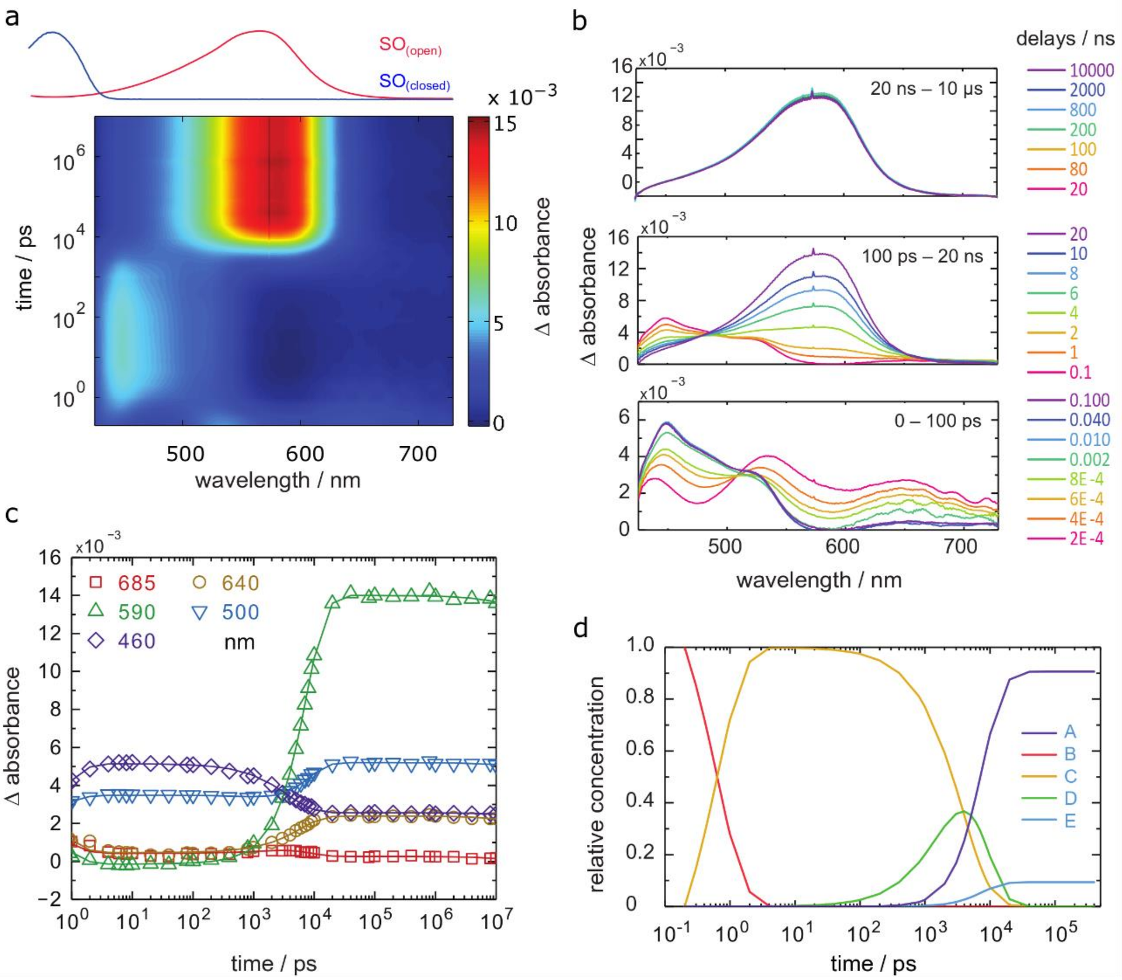

Figure 3-20 TA spectra in CH_2Cl_2, and excited-state kinetics of the ring-opening process of **SO(closed)**. a) TA contour spectrum; the steady-state spectra are shown for reference. b) TA spectra for selected probe times. c) TA kinetic traces for selected wavelengths (scatter) and fitted kinetics (solid lines) using the values obtained from target analysis. d) Speciation plot for the ring-opening reaction using the values obtained by target analysis for TA. Laser details: 400 nm pump, 200 nJ.

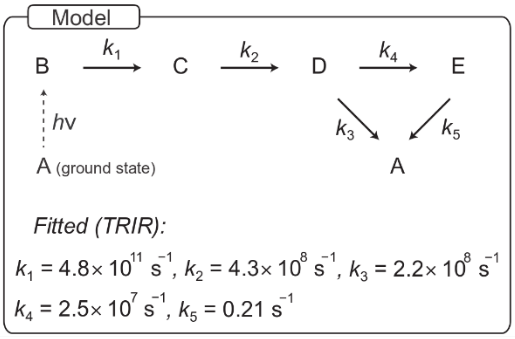

Figure 3-21 Model used to fit the TRIR and TA data presented in **Figure 3-19** and **Figure 3-20**.

In TRIR, the singlet excited state is formed within the first ps (i.e. the time resolution of the instrument), as indicated by the ground-state bleach 1493 cm^{-1}, and decays with a lifetime of 2 ps to a second transient species (**Figure 3-19**). The IR signatures of both transient species are strikingly similar but distinct, suggesting only minor structural changes and opposing a putative vibrational cooling (**Figure 3-19**b, lower panel). The generated singlet excited state displays a lifetime of ca. 3–9 ns (**Figure 3-19**b, middle panel) and transforms either to the final **SO$_{\mathbf{(open)}}$** isomer or back to the **SO$_{\mathbf{(closed)}}$** ground state. The identity of **SO$_{\mathbf{(open)}}$** can be confirmed both by its long lifetime (> 1 ms, **Figure 3-19**b, upper panel) and comparison to the FT-IR spectrum of **SO$_{\mathbf{(open)}}$**, recorded under constant 405 nm illumination (**Figure 3-19**a, top).

The TA spectra of **SO** could be easily related to the TRIR data, and both show similar kinetics. The first transformation (first 5 ps), characterised by a shift from $\lambda_{\max} = 534$ to $\lambda_{\max} = 450$ nm, is better observed in TA, suggesting a large change in the electronic structure relative to the ground state (**Figure 3-20**b, lower panel). Excitation to the S_2 state can be dismissed based on the excitation energy (i.e. too low for the predicted transition) and the calculated intensity of the transition (from DFT). Therefore, we assign this transition to a conformational relaxation of the singlet excited state. The large Stokes shift observed experimentally and predicted by TD-DFT supports this assignment. Next, a clear transformation to the **SO$_{\mathbf{(open)}}$** form is evidenced by the presence of a well-defined isosbestic point at 478 nm. The identity of **SO$_{\mathbf{(open)}}$** is confirmed by its characteristic UV-vis spectrum ($\lambda_{\max} =$ 590 nm). Nevertheless, relatively poor fits to exponential decays (see Experimental 3.7.10.4) and discrepancies regarding the accepted photo-conversion mechanism of spirooxazines[30,46–48] implied that the data required a more detailed analysis.

Target analysis, i.e. globally fitting the data assuming a putative kinetic model, was applied to gain further insights into the photoreaction and its associated kinetics. The selected model (**Figure 3-21**) is based on the literature regarding the inclusion of an intermediate between the singlet excited state and the photo-product. The data exclude significant formation of a triplet-excited state, based on the fact that we do not observe any transient species with lifetimes in the range 100 ns–100 µs typical for triplets. The Matlab script for the target analysis was written by Dr Andreas Vargas Jentzsch.

To reduce the number of fitted variables, certain assumptions were made and constraints applied: conformational relaxation was restricted to less than 3 ps, the thermal back reaction from **SO$_{\mathbf{(open)}}$** to **SO$_{\mathbf{(closed)}}$** was set to be longer than 1 ms;

under our flow measuring conditions, the renewal of the solution happens within 1 ms, and it is this process that was observed instead of the thermal back reaction. In addition, only solutions close to the experimental quantum yield for ring-opening were considered ($\Phi_{\mathrm{c}\rightarrow\mathrm{o}} < 20\%$). Using these constraints, it is possible to fit both TRIR and TA data (**Figure 3-19**c, **Figure 3-20**c) to the model depicted in **Figure 3-21** and **Scheme 3-2**. The use of a simpler model excluding species C results in a poor fit to the TA data, and completely fails to describe the TRIR data. For simplicity, radiative and nonradiative relaxation of the singlet excited state (C → A) was not included in this model; this is expected to be < 10% given that fluorescence occurs with a quantum yield of only 5.1%.

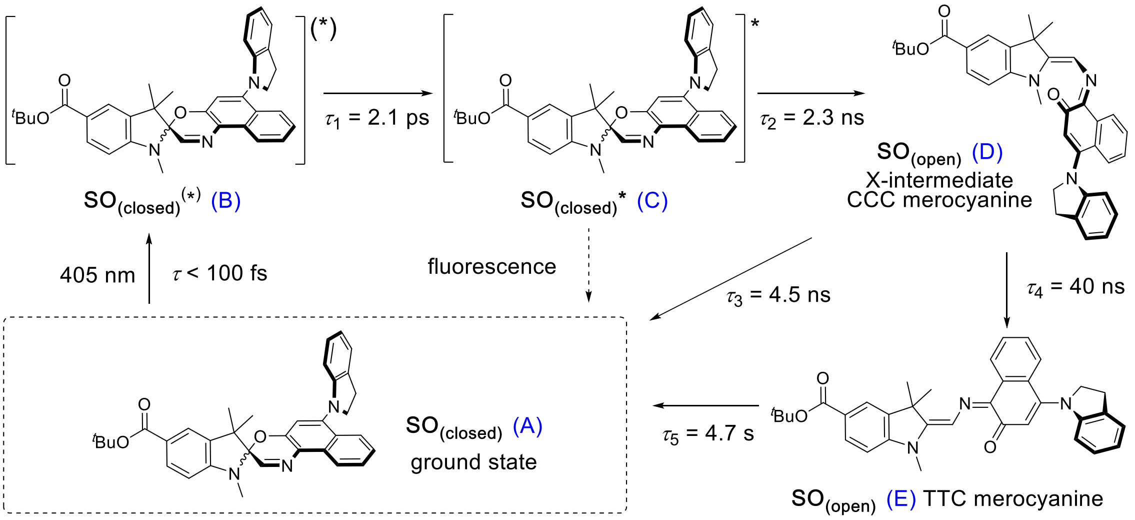

Scheme 3-2 Proposed reaction mechanism for the ring opening process of **SO**. The indicated lifetimes correspond to the values determined by target analysis of the TRIR data in CD_2Cl_2; τ_5 was determined separately. For simplicity, only the major isomer calculated by DFT is shown as photo-product. **SO$_{(closed)}$**$^{(*)}$ corresponds to the non-relaxed singlet excited state. The structure of the reaction intermediate **SO$_{(open)}$** X-intermediate (CCC-form) is shown for illustrative purposes and is based on previous literature.[6]

The overall model is as follows: photo-excitation happens during the pump pulse. Intermediate B corresponds to the singlet excited state, and C to the relaxed singlet excited state. Bond breaking leads to D, which is described in the literature as the "X intermediate"[49–51] and is postulated to be the CCC-form of **SO$_{(open)}$**.[6] E corresponds to the final form **SO$_{(open)}$** and A to the ground-state **SO$_{(closed)}$**.

Based on this model, following conformational relaxation, the singlet excited state is transformed to the "X intermediate" (τ = 2.3 ns), which proceeds either back to the ground-state (τ = 4.5 ns) or to the final photo-product **SO$_{(open)}$** (τ = 40 ns). The thermal back reaction occurs within seconds (τ = 4.7 s). The evolution of the different species is depicted in **Figure 3-19**d and **Figure 3-20**d. Our data do not show evidence of multiple, discernible, isomers of **SO(open)** (e.g. TTT, CTC forms etc.), implying that if these isomers are intermediates, they must be short-lived or not resolvable.

The TRIR data enable us to estimate the quantum yield for ring-opening $\Phi_{c\rightarrow o}$ using two different approaches: from the recovery of the ground-state bleach (eqn (**3.1**); e.g. at 1488 cm^{-1} **Figure 3-19**a), or from the rate constants deduced from the target analysis (eqn (**3.2**)). Both methods give similar results (eqn (**3.1**): $\Phi_{c\rightarrow o}$ = 7.4%; eqn (**3.2**): $\Phi_{c\rightarrow o}$ = 10%, in CD_2Cl_2 at 20 °C) and match well with the value from steady state measurements ($\Phi_{c\rightarrow o}$ = 7.7% in CH_2Cl_2 at 10 °C). Eqn (**3.2**) will over-estimate $\Phi_{c\rightarrow o}$ because it ignores direct relaxation of the singlet excited state (C → A); if 10% of C relaxes directly to A, this would reduce $\Phi_{c\rightarrow o}$ by 10%.

$$\Phi_{\mathrm{c}\,\rightarrow\,\mathrm{o}} \approx \frac{\Delta\ \mathrm{abs}_{(\mathrm{GS\ bleach})}(t \sim 1\ \mathrm{ms})}{\Delta\ \mathrm{abs}_{(\mathrm{GS\ bleach})}(t \sim 0)} \qquad \textbf{(3.1)}$$

$$\Phi_{\mathrm{c}\,\rightarrow\,\mathrm{o}} \approx \frac{k_4}{k_4 + k_3} \qquad \textbf{(3.2)}$$

To further explore the ring-closing photo-reaction, a photostationary state was generated *in situ* within the time-resolved set-up using continuous irradiation with blue light (405 nm). Since **SO(closed)** has no absorption above 500 nm, only the photo-generated species is excited by the pump pulse at 590 nm and any transient species observed correspond to the ring-closing process. We opted to use TRIR to avoid visible light scattering problems that would be introduced in TA, and because it should be better able to discern the different **SO(open)** isomers.

TRIR spectroscopy shows that photochemical ring-closure is about 1000 times faster than photochemical ring-opening (**Figure 3-22**). Target analysis of the TRIR data indicates that the formation of the transient intermediate occurs almost instantaneously after photo-excitation (an additional lifetime of 1–2 ps can be fitted using single wavenumber analysis, potentially indicating that the excited state and the intermediate are different species, but such a model did not yield satisfactory results using target analysis due to the proximity of time zero). It then decays back to **SO(open)** (τ_2 = 12 ps) or is transformed into **SO(closed)** (τ_1 = 280 ps). As before, the quantum yield of this photo-reaction can be estimated from the TRIR using two different approaches, eqn (**3.3**) and eqn (**3.4**). Again, the two methods give similar results (eqn (**3.3**): $\Phi_{o\rightarrow c}$ = 1.4–2.0%; eqn (**3.4**): $\Phi_{o\rightarrow c}$ = 4%, in CD_2Cl_2 at 20 °C), which are comparable to the value from steady state measurements ($\Phi_{o\rightarrow c}$ = 1.1% in cyclohexane at 10 °C).

$$\Phi_{\mathrm{o}\rightarrow\mathrm{c}} \approx \frac{\Delta\,\mathrm{abs}_{(\mathrm{GS\ bleach})}(t\sim 1\ \mu\mathrm{s})}{\Delta\,\mathrm{abs}_{(\mathrm{GS\ bleach})}(t\sim 0)} \qquad \textbf{(3.3)}$$

$$\Phi_{\mathrm{o}\rightarrow\mathrm{c}} \approx \frac{k_1}{k_1+k_2} \qquad \textbf{(3.4)}$$

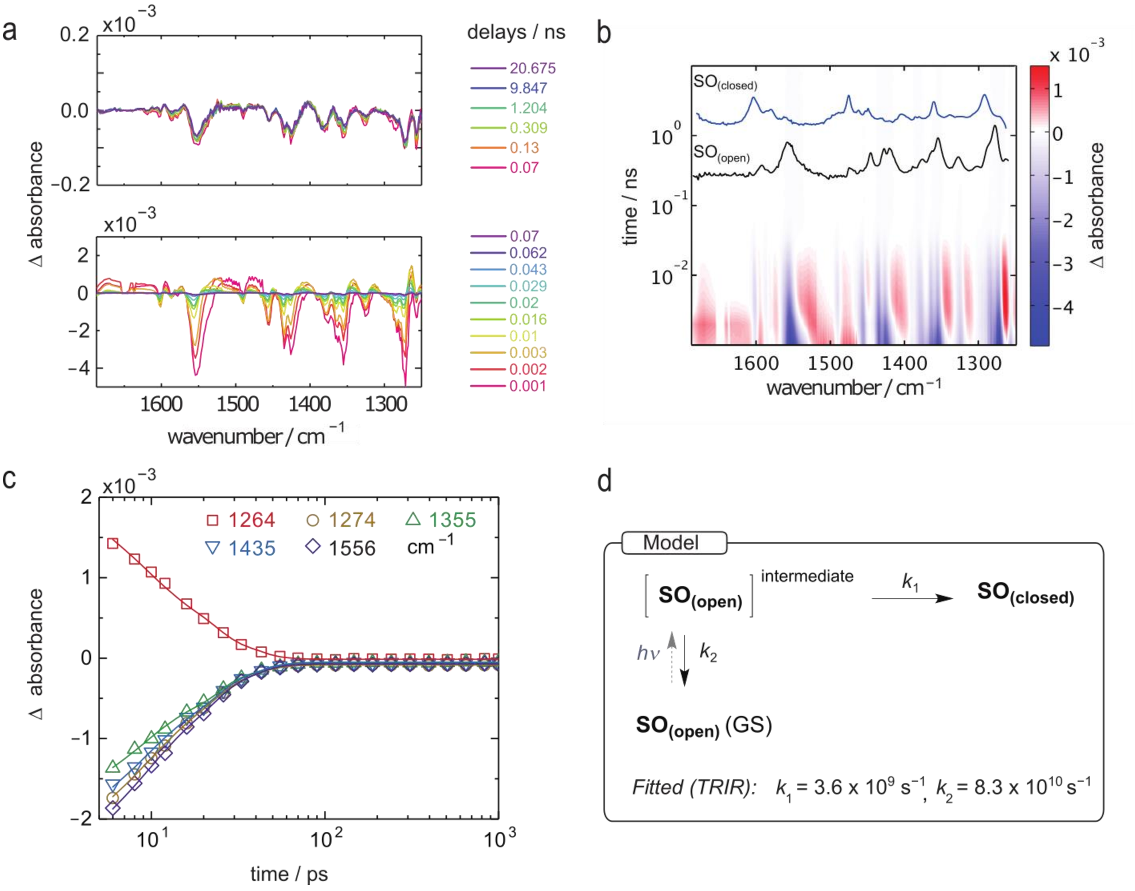

Figure 3-22 TRIR spectra and excited-state kinetics of the ring-closing process of **SO(open)** in CD_2Cl_2 by excitation at 590 nm. a) TRIR spectra for selected probe times. b) TRIR contour spectra; the steady-state spectra are shown for reference. c) Kinetic traces for selected wavenumbers (points) and fitted kinetics (solid lines) using the values obtained from target analysis. D) Model used to fit the TRIR. Laser energy: 800 nJ.

The ring-opening kinetics observed for **SO** are significantly different from those previously reported from studies of the ultrafast photochemistry of spirooxazines.[30,47–51] For instance, in the absence of the ester substituent, the corresponding spirooxazine converts to its open form with τ = 1 ns, and was shown by time-resolved resonance Raman to proceed through multiple open-form intermediates.[6] The substitution of the *N*-methyl by an *N*-isopropyl group resulted in a highly solvent-dependent photoisomerisation reaction.[30] In general, the photoisomerisation process occurs within a maximum timescale of a few ns. In our case, **SO** shows remarkably little solvent dependence (additional TA traces in acetone, DMSO, THF, and toluene can be found in Experimental 3.7.10.5), and the second step of photoisomerisation is much slower (τ = 40 ns) than the previously reported cases. This difference may be attributed to the ester substitution on the indoline moiety. The long-lived excited state of **SO$_{\mathbf{(closed)}}$** is also apparent from its steady-state properties: while most spirooxazines are non-emissive,[23] **SO$_{\mathbf{(closed)}}$** shows detectable fluorescence (Φ_f = 5.1%).

3.6 Conclusions

This chapter describes the synthesis and characterisation of a spironaphthoxazine switch that displays promising features required for application in RESOLFT microscopy. The photochromic switch shows a strong absorbance at 405 nm, which is almost completely absent in the active, coloured form. Due to the favourable quantum yield of ring-opening and a comparatively poor quantum yield of ring closing, an uncommonly high photoconversion can be achieved. The possibility to achieve high photochromic conversions using readily accessible non-UV light sources is of great interest in microscopy.

The ultrafast photochemistry of this spironaphthoxazine molecular switch is shown to be simpler than other reported spiro-photoswitches, and no evidence of a triplet-excited state was observed. Moreover, the kinetic traces show no evidence of multiple merocyanine isomers. The results indicate that **SO** has relatively simple photochemistry and good fatigue resistance. Given the desirable properties of **SO**, dyads formed by conjugating this switch to a commercial dye were synthesised and are described in Chapter 4. Subsequent live-cell confocal imaging of such dyads is reported, followed by discussion of their possible application in RESOLFT microscopy.

3.7 Experimental

3.7.1 General procedures

For general experimental methods (NMR, mass spectrometry, UV-vis spectroscopy), please see Chapter 2 Experimental section, with the following additions and modifications:

Anhydrous solvents were obtained from an MBraun solvent purification system. Column chromatography was carried out using SiO_2 60 (particle size 40–63 μm, Merck, UK) as the stationary phase.

Fluorescence and excitation spectra were recorded on a FS5 fluorescence spectrophotometer (Edinburgh Instruments). Absolute fluorescence quantum yields (see later) were obtained on an integrating sphere (Edinburgh Instruments).

The LED setup in the UV-vis spectrometer was the same as described in Chapter 2 Experimental section. The irradiation sources were mic-LED-405 (from Prizmatix Ltd.; centered at 405 nm, FWHM = 15 nm) up to 360 mW, and mic-LED-525 (from Prizmatix Ltd; centered at 525 nm, FWHM = 60 nm) up to 69 mW. The measurement of the LED power is described in Chapter 2.[39]

3.7.2 UV-vis absorption and fluorescence

The UV-vis absorption spectrum of **SO** was compared with the excitation spectrum of the same sample with detection at 560 nm. The emission spectrum was recorded with excitation at 405 nm, and fluorescence emission was measured between 420 and 800 nm.

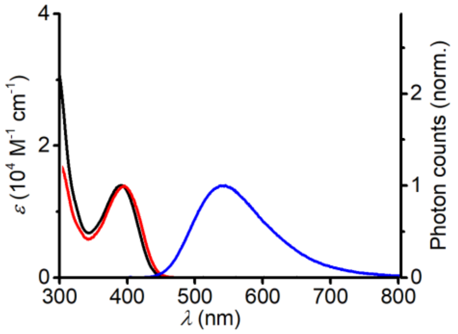

Figure 3-23 Absorption (black), excitation (red) and emission spectra (blue) of **SO** in CH_2Cl_2. The measurements were taken of a 10 μM solution at 25 °C. The excitation spectrum was monitored at 560 nm, and the emission spectrum was recorded once excited at 405 nm.

3.7.3 Solvatochromism of SO

Please see **Figure 3-8**. In each solvent, the sample was prepared to have the maximum absorbance between 0.04 and 0.07, and the UV-vis absorption spectrum was recorded. For the emission spectrum, the same sample was excited at 405 nm, and fluorescence emission in the region 420–850 nm was measured.

3.7.4 Acquisition of the photostationary state (PSS) spectra

See **Figure 3-10**. A typical experiment is as follows: a solution of **SO** in cyclohexane (10 μM, 2.0 mL) at 10 °C was irradiated with pulses of 405 nm LED (2.1 W/cm^2, 100 ms irradiation, 200 ms interval), during which the PSS spectrum was recorded by the UV-vis spectrometer. The raw spectrum was processed in Matlab to remove the negative spikes due to scattering of the excitation light. In addition, conversion from the closed to open form was estimated to be about 85–95% to give a smooth **SO$_{\text{(open)}}$** spectrum (**Figure 3-11**). The **SO$_{\text{(open)}}$** spectrum was used to calculate the FRET efficiency.

3.7.5 Rates of thermal ring closure

See **Figure 3-9**. In the UV-vis spectrometer, a vigorously stirred solution of **SO** (3.3 μM, 3.0 mL) at 25 °C was irradiated by 405 nm LED (2.1 W/cm^2, 2.5 s) to establish the PSS, then the irradiation was stopped and the absorbance changes at 590 nm were monitored over time. The decay was fitted to a mono-exponential function.

3.7.6 Absolute fluorescence quantum yields

The absolute fluorescence quantum yields were measured using a SC-30 integrating sphere module (Edinburgh Instruments). Due to the low fluorescence quantum yields of **SO,** the scattering spectrum was measured with a neutral density filter behind the excitation monochromator to protect the detector, and the emission spectrum was obtained separately in a standard way. Excitation wavelength was set at 405 nm. Once the scattering region was scaled accordingly to match the overlapped region with the emission, the scattering region between 392 and 420 nm and emission between 460 and 850 nm were used to calculate the observed quantum yield, 5.1%.

3.7.7 Quantum yields of photochemical reactions

3.7.7.1 Quantum yield of ring opening

Please see Section 3.4.2. A cyclohexane solution of **SO** (10.0 μM, 2.0 mL) was placed in the sample holder of a UV-vis spectrometer and stirred at 10 °C. While it was irradiated with pulses of mic-LED-405 (28.1 mW, 100 ms pulse, 200 ms interval), a kinetic trace of absorption intensity at 560 nm was recorded and processed in Matlab to give the time-dependent absorbance change (see **Figure 3-12**).

3.7.7.2 Quantum yield of ring closure

The photoreversion traces of ring closure monitored at 560 nm were obtained using the same conditions as those of thermal ring closure, except that the sample was given pulses of mic-LED-525 (68.5 mW, 100 ms irradiation, 400 ms interval) while recording the spectrum (**Figure 3-13**). The monitoring of 560 nm absorbance is based on the assumption that the closed form does not absorb at this wavelength, and upon exposure to the 525 nm LED, the ring closing reaction is accelerated without significant side-reactions. Thus, the disappearance of the starting material/open isomer is at the same rate as the appearance of the product/closed isomer. The trace was reconstructed in Matlab.

To calculate the ring closing quantum yield of **SO**, the measurements were carried out as follows: after irradiation with mic-LED-405 (150 mW, 2.5 s) to generate the open form, the sample solution was exposed to a pulse of mic-LED-525 (68.5 mW, 100 ms) to initiate photochemical reversion. After the pulse, the sample was allowed to continue to ring close thermally. During the experiment, the absorbance at 560 nm was recorded as a function of time, giving a kinetic trace. The above procedure was repeated using increasing duration of 525 nm irradiation (200 ms, 400 ms etc.). Each photochemical trace was subtracted from the thermal trace, and the first value (to be accurate, the average of the first few values to minimise random fluctuations) after the light scattering region in each processed photochemical trace gave the difference caused by irradiation of 525 nm of a specified period. By using the equation,[7] $\Phi_\mathrm{c} = \frac{mVN_Ahc}{P\lambda(1-10^{-A})\varepsilon_{\mathbf{SO(open)}}d}$, where m is the linear fit for the disappearance of **SO$_{\mathbf{(open)}}$** by monitoring at 560 nm (m = 0.108 ± 0.002 s^{-1} in **Figure 3-24**), P is the power intensity (68.5 ± 1.7 mW), λ is the excitation wavelength (525 nm), *A* is the absorbance at excitation wavelength (0.60), and $\varepsilon_{\mathbf{SO(open)}}$ is the molar absorption coefficient of **SO**$_{\mathbf{(open)}}$ at 560 nm (8.9 ± 0.5 × 10^4 M^{-1} cm^{-1}). The calculation gave $\Phi_\mathrm{C} = 1.1 \pm 0.1$ %. This value agrees with that obtained from the TR-IR measurements, i.e. 1.4–2.3%.

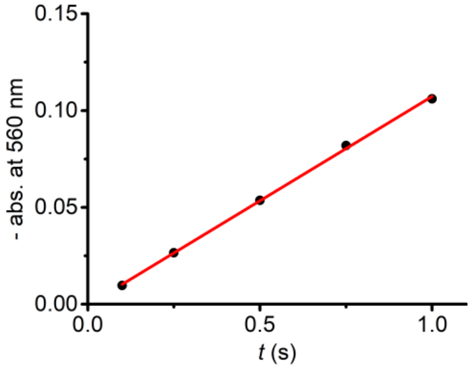

Figure 3-24 The initial part of the reconstructed photochemical ring closing kinetics of **SO**, and the linear fit. The slope $m = 0.108 \pm 0.002$ (used in the calculation of the quantum yield of ring closing), $R^2 = 0.999$.

3.7.8 Fatigue resistance in the cuvette

See **Figure 3-14**. The fatigue resistance by thermal reversion is measured as follows: a cyclohexane solution of **SO** (10 μM, 2.0 mL) was placed in the sample holder of a UV-vis spectrometer and stirred at 25 °C. The samples were irradiated using mic-LED-405 (2.1 W/cm^2) for 2.5 s at the beginning of each cycle. Immediately after irradiation, a kinetic trace of absorption intensity at 590 nm was recorded until the ring closure was completed. The above procedure was repeated for > 100 cycles. The raw data were treated in Matlab to extract the maximal and minimal absorbance after 405 nm excitation for each cycle.

3.7.9 DFT calculations

DFT calculations, including predicted IR and UV-vis transitions, were carried out by Dr Andreas Vargas Jentzsch and followed the literature procedure.[55] Briefly, the molecular structures were optimised at the DFT B3LYP/6-31+G(d,p) level of theory using the software package Gaussian 16.[56] Solvation in CH_2Cl_2 was applied using the polarisable continuum model (PCM).[57] All structures are confirmed ground-state minima according to the analysis of their analytical frequencies computed at the same level, which show no imaginary frequencies. On these minima, the vertical transition energies were calculated by time-dependent density functional theory (TD-DFT) at DFT cam-B3LYP/6-311+G(2d,p) level of theory with the PCM solvation in CH_2Cl_2. The choice of functionals and basis sets are based on the results in the literature.[18]

The calculated geometries for switch **SO** in the closed and all four open isomers CTT, CTT, TTT, and TTC are presented at the Appendices together with the Cartesian coordinates. All structures are optimised at the DFT B3LYP/6-31+G(d,p) level.

3.7.10 Ultrafast time-resolved spectroscopy

3.7.10.1 Experimental procedures

The sample of **SO** used for time-resolved IR had an absorbance of about 1.3 at 405 nm in CD_2Cl_2. TA samples were prepared with a typical absorbance of 0.5 at 405 nm in CH_2Cl_2. The UV-vis absorption and FT-IR spectra were measured before and after the experiments to check for any noticeable decomposition. A flow system, along with cell raster scanning, was set up to minimise the interference from the long-lived **SO$_{\textbf{(open)}}$** form and effects of photodegradation.

The LIFETime (TRIR in Time-Resolved Multiple Probe Spectroscopy mode, time resolution 1 ps up to 1 ms) and ULTRA (TA in Time-Resolved Multiple Probe Spectroscopy mode, time resolution 100 fs up to 10 μs) instruments at the STFC Rutherford Appleton Laboratory were used, and are described in detail elsewhere.[53,58] The equipment was set up and maintained by the group of Prof. Anthony Parker. The support and help from Prof. Anthony Parker and Dr Igor Sazanovich is much appreciated.

3.7.10.2 ULTRA (TR^{M}PS-TA)

The TA measurements were performed on the ULTRA[54] setup in the Time-Resolved Multiple Probe Spectroscopy mode[58] (hereafter TR^{M}PS) at the Central Laser Facility (STFC Rutherford Appleton Laboratories, Oxfordshire, UK). The TA experiments were driven by a 10 kHz repetition rate Ti:Sapph amplifier (Thales) as a probe source, producing 40 fs pulses at 800 nm. A fraction of the Ti:Sapph laser output was used to generate a white light continuum (WLC) in a CaF_2 plate to probe the sample transient absorption. The WLC was passed through the photoexcited spot on the sample (probe spot size approx. 80 μm) and dispersed through the 0.25 m (f/4) grating spectrograph and detected using a silicon diode array (Quantum Detectors). The long-pass filter was used in front of the spectrograph to block the scattered excitation radiation. No referencing was required for the TA experiments thanks to sufficiently stable white light. The excitation source for the TA experiments was the second harmonic (400 nm) of the 1 kHz titanium sapphire amplifier (Spectra Physics Spitfire XP, 100 fs pulse length), pulse energy at sample attenuated down to 0.2–1 μJ and focused down to 150 × 150 μm^2 spot). Both ULTRA amplifier and Spitfire amplifier were optically synchronized by sharing the same seed from 68 MHz Ti:Sapph oscillator. The seed beam was delayed with an optical delay line before the 1 kHz amplifier to accommodate for the 100 fs–14.7 ns time delays between pump and probe. To go beyond 14.7 ns and up to 100 μs, subsequent seed pulses are selected from the 68 MHz seed pulse train accompanied by the appropriate setting of the optical delay line. The polarisation of the excitation beam at sample was set to be at 54.7° with respect to the probe in TA experiments.

3.7.10.3 LIFETime (TR^{M}PS-TRIR)

The TRIR experiments were performed in TR^{M}PS mode on LIFEtime setup at the Central Laser Facility STFC.[53] The LIFEtime setup is based on a dual-amplifier 100 kHz Yb:KGW laser system (Pharos & Pharos SP, Light Conversion Ltd.). The two Yb:KGW amplifiers are optically synchronized through sharing the same oscillator seed beam. The output beam of Pharos amplifier is split 50/50 and used to pump the two identical OPAs (Orpheus ONE, Light Conversion Ltd.) followed with GaSe DFG stages. The two identical OPA+DFG systems produce two independently tunable mid-IR probe beams for TRIR experiments, each covering > 200 cm^{-1} useable bandwidth. The Pharos SP amplifier is used to pump Orpheus HP OPA generating the excitation beam for the TRIR experiments tunable from UV to mid-IR. In the current study the excitation wavelength was set at 320, 405, and 590 nm. The repetition rate of the output beam of Pharos SP amplifier was divided down programmatically by an internal pulse picker to excitation repetition rate of 0.1–1 kHz to enable Time-Resolved Multiple Probe Spectroscopy (TR^{M}PS) mode. Relative pump–probe timing control between the two Yb:KGW amplifiers is programmable from 100 fs to 10 ms, using a combination of oscillator roundtrip timing to achieve steps of 12 ns and translation stage optical delay of the pump similar to our previous work.[13] Here, we opted for optical delay of the OPA output but not of the amplifier seed beam. The excitation beam was focused to approx.

100 μm spot at the sample and overlapped at the sample with the two mid-IR probe beams (each probe beam is approx. 100 μm in size). The excitation pulse energy at sample was set to 0.4–1.0 μJ. The polarisation of the excitation beam at the sample was at 54.7° with respect to the probe beams. After the sample, the two probe beams enter independently tunable homemade spectrographs (0.15 m, f/6) and spectra are measured on two 128-element MCT detector arrays (IR Associates). The spectrum acquired by each MCT detector is integrated and digitised by an FPAS system (Infrared Systems Development Corporation). Thanks to the excellent stability of the mid-IR probe beams, no referencing has been applied in the measurements shown here.

For the TR-IR measurements, the sample solution was excited using 405 nm of 0.7 μJ (or 590 nm, 0.6 μJ) at the frequency of 100 Hz (or 1 kHz), and probed in the ca. 1200–1600 and 1400–1800 cm^{-1} regions at 100 KHz. For TA measurements, the sample was pumped at 400 nm (0.2 μJ, 1 KHz repetition rate), and probed in the visible region (10 KHz probe repetition rate).

3.7.10.4 Data treatment

All data sets were initially corrected for time zero and group velocity dispersion (i.e. chirp correction) prior to analysis of the data. The TR-IR data were preliminarily analysed using the software Surface Xplorer Pro and home-made UltraView.

Single wavenumber/wavelength traces were fitted using OriginLab to multiexponential functions as in the following equation:

$$y = \sum A_i e^{-x/t_i} + y_0$$

where i is either 1 or 2, x is the time, t_i is the lifetime, A_i is the pre-exponential factor. Figures **Figure 3-25** and **Figure 3-26** show some examples of TRIR and TA single-wavenumber/wavelength data at selected time ranges where the data can be roughly fitted to exponential decays. The data were further analysed by target analysis using a custom written Matlab script.[59]

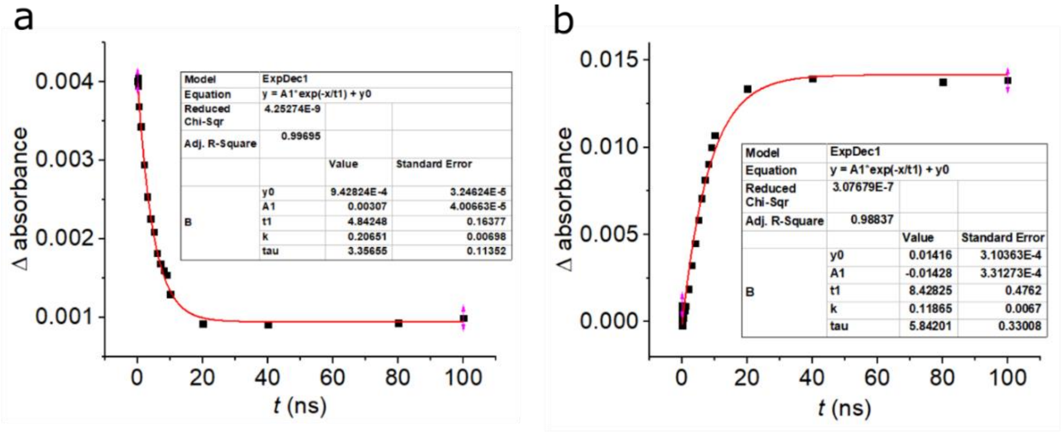

a

Model	ExpDec1		
Equation	y = A1*exp(-x/t1) + y0		
Reduced Chi-Sqr	4.25274E-9		
Adj. R-Square	0.99695		
		Value	Standard Error
B	y0	9.42824E-4	3.24624E-5
	A1	0.00307	4.00663E-5
	t1	4.84248	0.16377
	k	0.20651	0.00698
	tau	3.35655	0.11352

b

Model	ExpDec1		
Equation	y = A1*exp(-x/t1) + y0		
Reduced Chi-Sqr	3.07679E-7		
Adj. R-Square	0.98837		
		Value	Standard Error
B	y0	0.01416	3.10363E-4
	A1	-0.01428	3.31273E-4
	t1	8.42825	0.4762
	k	0.11865	0.0067
	tau	5.84201	0.33008

Figure 3-25 Fitting of TA ring opening kinetics at selected single wavelengths to exponential decays, over a selected time range of 0–100 ns. a) Kinetics at 432 nm. b) Kinetics at 591 nm. The lifetimes from this simple analysis are slightly different from the values obtained from target analysis.

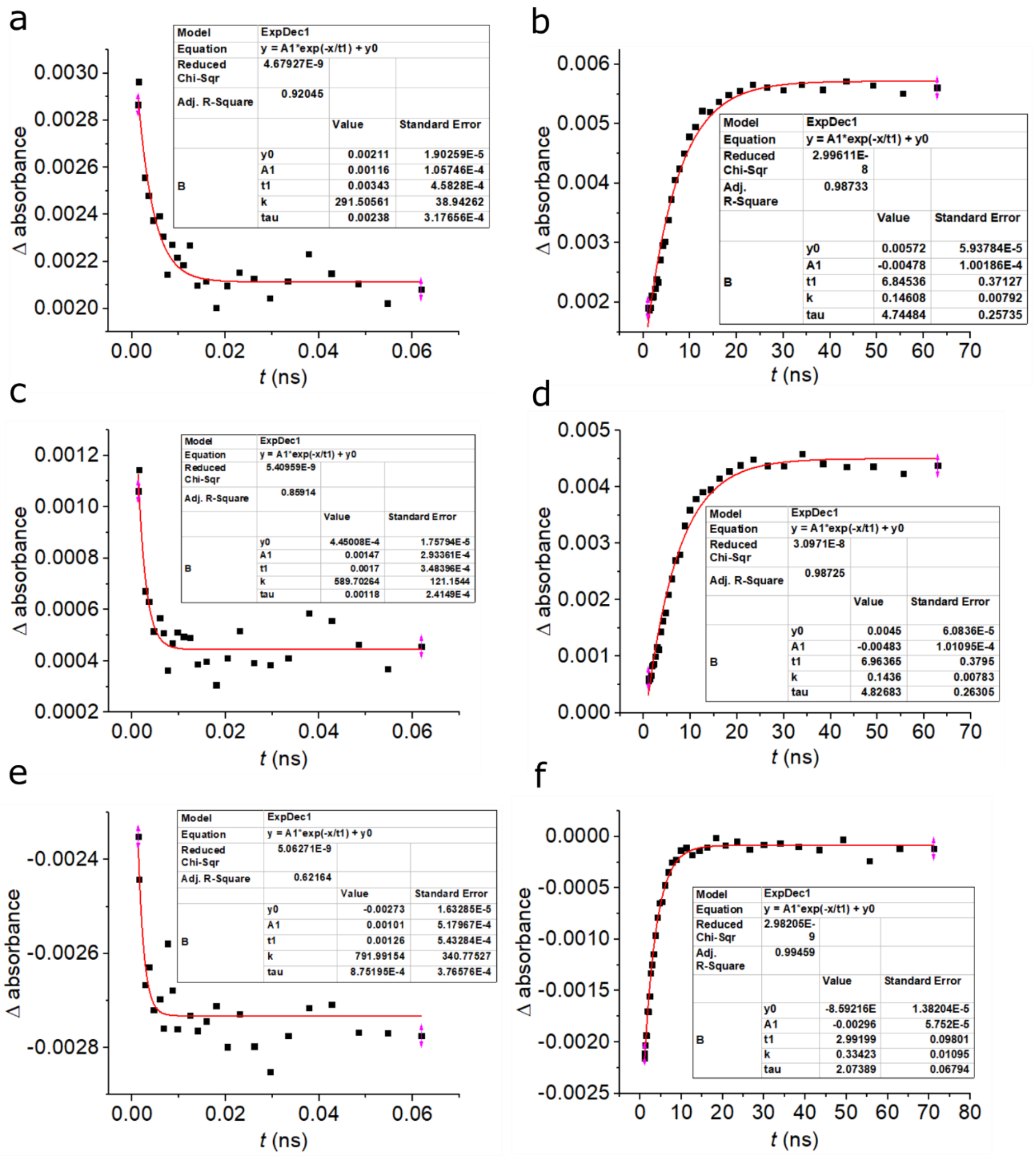

a

Model	ExpDec1		
Equation	y = A1*exp(-x/t1) + y0		
Reduced Chi-Sqr	4.67927E-9		
Adj. R-Square	0.92045		
		Value	Standard Error
B	y0	0.00211	1.90259E-5
	A1	0.00116	1.05746E-4
	t1	0.00343	4.5828E-4
	k	291.50561	38.94262
	tau	0.00238	3.17656E-4

b

Model	ExpDec1		
Equation	y = A1*exp(-x/t1) + y0		
Reduced Chi-Sqr	2.99611E-8		
Adj. R-Square	0.98733		
		Value	Standard Error
B	y0	0.00572	5.93784E-5
	A1	-0.00478	1.00186E-4
	t1	6.84536	0.37127
	k	0.14608	0.00792
	tau	4.74484	0.25735

c

Model	ExpDec1		
Equation	y = A1*exp(-x/t1) + y0		
Reduced Chi-Sqr	5.40959E-9		
Adj. R-Square	0.85914		
		Value	Standard Error
B	y0	4.45008E-4	1.75794E-5
	A1	0.00147	2.93361E-4
	t1	0.0017	3.48396E-4
	k	589.70264	121.1544
	tau	0.00118	2.4149E-4

d

Model	ExpDec1		
Equation	y = A1*exp(-x/t1) + y0		
Reduced Chi-Sqr	3.0971E-8		
Adj. R-Square	0.98725		
		Value	Standard Error
B	y0	0.0045	6.0836E-5
	A1	-0.00483	1.01095E-4
	t1	6.96365	0.3795
	k	0.1436	0.00783
	tau	4.82683	0.26305

e

Model	ExpDec1		
Equation	y = A1*exp(-x/t1) + y0		
Reduced Chi-Sqr	5.06271E-9		
Adj. R-Square	0.62164		
		Value	Standard Error
B	y0	-0.00273	1.63285E-5
	A1	0.00101	5.17967E-4
	t1	0.00126	5.43284E-4
	k	791.99154	340.77527
	tau	8.75195E-4	3.76576E-4

f

Model	ExpDec1		
Equation	y = A1*exp(-x/t1) + y0		
Reduced Chi-Sqr	2.98205E-9		
Adj. R-Square	0.99459		
		Value	Standard Error
B	y0	-8.59216E	1.38204E-5
	A1	-0.00296	5.752E-5
	t1	2.99199	0.09801
	k	0.33423	0.01095
	tau	2.07389	0.06794

Figure 3-26 Fitting of TRIR ring opening kinetics at selected single wavenumbers to exponential decays, over selected time ranges. a,b) Kinetics at 1279 cm^{-1}. c,d) Kinetics at 1355 cm^{-1}. e,f) Kinetics at 1488 cm^{-1}. Some data fit well and the lifetimes agree with those obtained from target analysis, but some do not.

3.7.10.5 Additional results

While TRIR could only be carried out in CD_2Cl_2 because of intense absorptions from the non-deuterated solvent, TA allowed us to study the influence of different solvents in the ring-opening photochemistry of **SO**. The photo-induced ring-opening of **SO** was additionally measured in acetone, DMSO, THF, and toluene and the resulting TA spectra are presented in **Figure 3-27**. Qualitatively, the TA spectra look strikingly similar in terms of intermediate species and timescales. The main outlier is DMSO, which appears to hamper the formation of the photo-product. Additionally, the shape of the excited state absorption is less defined as compared to other solvents, notably CH_2Cl_2 and toluene. In fact, the difference of the spectrum in DMSO is marked enough for the proposed model (see main text) to fail when attempting to simulate the data in DMSO, suggesting a different reaction pathway. Moreover, when considering that acetone also induces the same features to a lesser extent and one can tentatively suggest that photoconversion may undergo a different reaction pathway in polar solvents. From steady state measurements we know that the thermal back reaction is slower (more than 50 times slower cyclohexane to MeOH) and that the fatigue resistance is best in apolar solvents.

Target analysis of the TA spectra in acetone, THF and toluene reveals similar values for the kinetic constants (see **Figure 3-28**). Minor differences can be observed on the speciation plots, with the notable difference in accumulation of the X-intermediate for the acetone and toluene cases. Nevertheless, these differences are minor and it can be concluded that solvent has only a minor influence on the photoisomerisation reaction of **SO**.

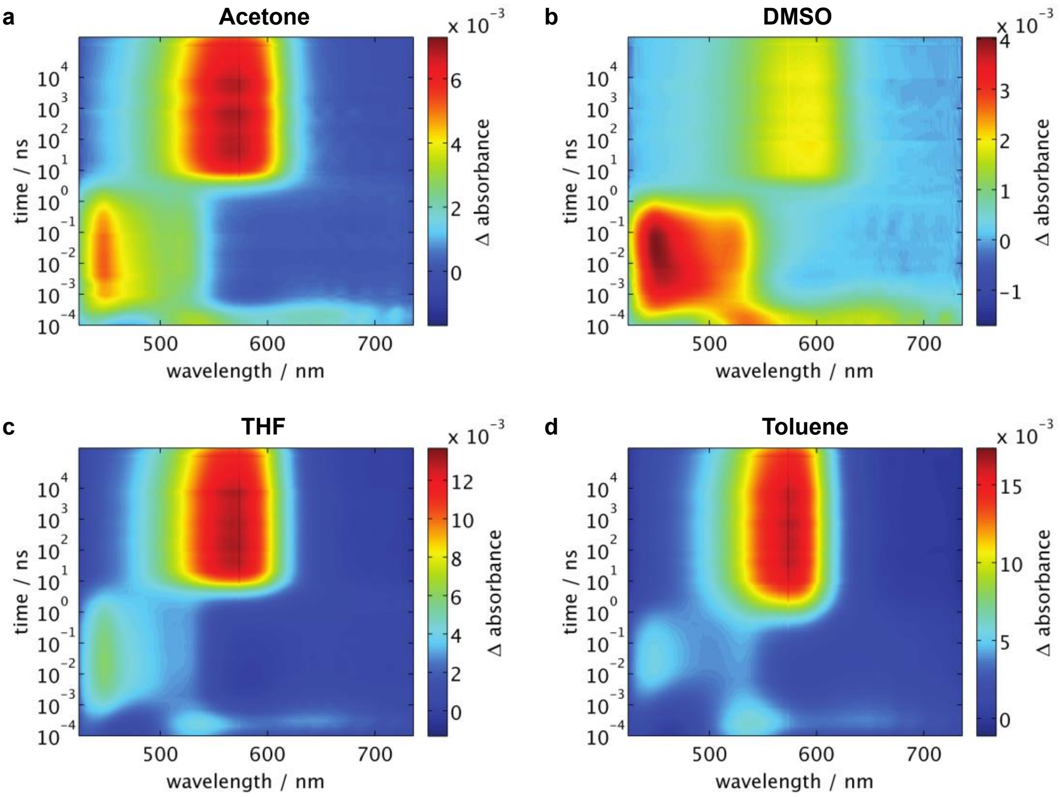

Figure 3-27 TA ring opening spectra of **SO** in different solvents.

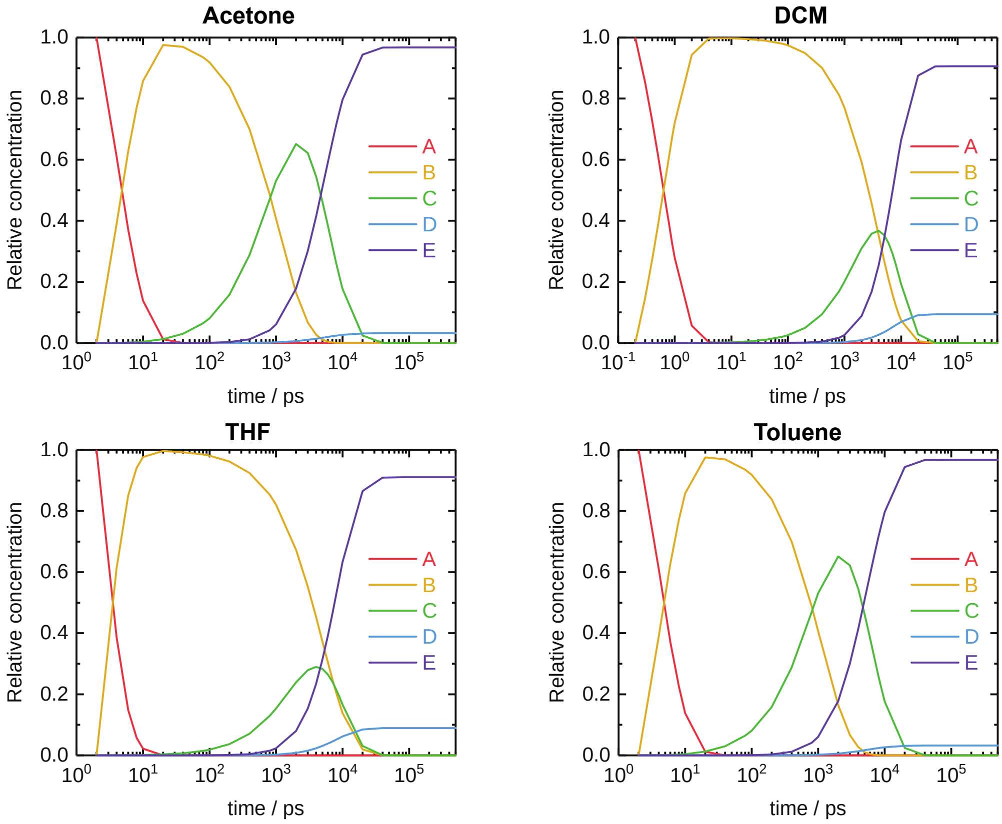

Figure 3-28 Speciation plots for ring opening processes of **SO** in different solvents. Fitted parameters: τ_1 = 1.3; 2.8; 2.1; 4.0 ps. τ_2 = 1.9; 2.3; 5.0; 1.1 ns. τ_3 = 4.2; 4.5; 3.6; 5.2 ns. and τ_4 = 37; 40; 36; 160 ns for acetone, CH_2Cl_2, THF, and toluene respectively.

3.7.11 Crystallographic and structural analysis

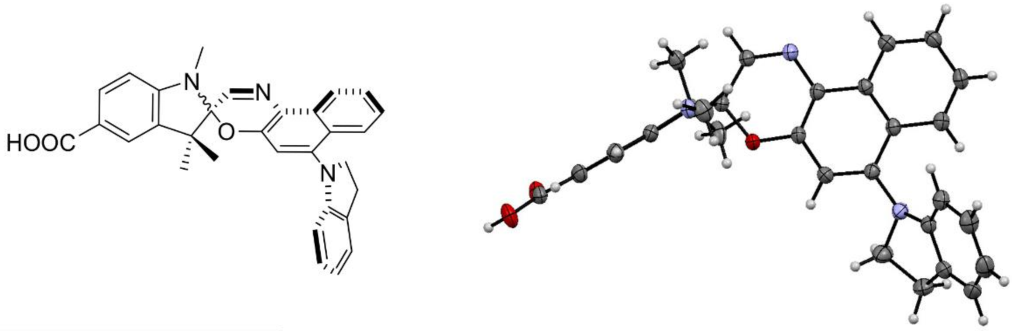

Figure 3-29 Crystal structure of compound **14**. The crystals suitable for X-ray diffraction studies were grown from slow evaporation of a solution of compound **14** in a solvent mixture of CH_3OH and $CHCl_3$ at 20 °C. Single crystal data: $C_{31}H_{27}N_3O_3$, $M_r = 489.57$, triclinic, **P** –1, $a = 7.6914(3)$ Å, $b = 8.8535(4)$ Å, $c = 18.0798(9)$ Å, $\alpha = 91.235(4)°$, $\beta = 97.2.1(3)°$, $\gamma = 92.431(3)°$, $V = 1218.20(10)$ Å, data/restraints/parameters: 5026/0/334, $R_{\text{int}} = 3.4\%$, final $R_1 = 4.07\%$, $wR_2 = 10.51\%$ ($I > 2\sigma(I)$), $\Delta\rho_{\text{min,max}} = -0.24,+0.29$ e Å^3.

Single crystal X-ray diffraction data were collected at 150 K using an Oxford Diffraction/Agilent SuperNovae A (Cu) X-ray source. The raw frame data were integrated and reduced using CrysAlisPro (Agilent Technologies, 2010). The structure was solved using charge flipping[60,61] with SuperFlip method.[62] It was refined by full-matrix least-squares on F^2 in CRYSTALS.[63–65] The crystallographic data have been deposited with the Cambridge Crystallographic Data Centre (CCDC 1812758), and copies of these data can be obtained free of charge *via* www.ccdc.cam.ac.uk/data_request/cif.

3.8 Synthetic procedures

1,3,3-Trimethyl-2-methyleneindoline-5-carboxylic acid (**11**) was prepared according to the reported procedure.[10]

tert-Butyl 2,3,3-trimethyl-3*H*-indole-5-carboxylate (9)

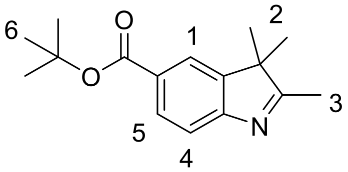

tert-Butyl 2,2,2-trichloroacetimidate (2.20 g, 10 mmol) was dried in a flask under high vacuum and subsequently dissolved in cyclohexane (10 mL). Meanwhile, 2,3,3-trimethyl-3*H*-indole-5-carboxylic acid (**8**) (1.00 g, 4.9 mmol) was dissolved in THF (5.0 mL). The first solution was added dropwise to the second solution under nitrogen. $BF_3{\cdot}OEt_2$ (0.18 mL, 1.6 mmol) was added and the mixture was stirred for 20 min at room temperature. After stirring, the mixture was diluted with 5% aqueous $NaHCO_3$ solution (200 mL) and the product was extracted with EtOAc (200 mL). The organic phase was washed with brine and dried using Na_2SO_4. The residue was purified by silica gel chromatography (95:5 to 8:2 40–60 °C petroleum ether/EtOAc), yielding the product as a white solid (817 mg, 64%). ^1H NMR (400 MHz, $CDCl_3$) δ (ppm): 7.98 (dd, J = 8.1, 1.7 Hz, 1H, H5), 7.91 (d, J = 1.7 Hz, 1H, H1), 7.53 (d, J = 8.1 Hz, 1H, H4), 2.31 (s, 3H, H3), 1.60 (s, 9H, H6), 1.33 (s, 6H, H2). ^{13}C {^1H} NMR (101 MHz, $CDCl_3$) δ (ppm): 191.4, 166.1, 157.3, 145.6, 129.9, 128.8, 122.5, 119.4, 81.0, 53.8, 28.3, 23.0, 15.7.

5-(*tert*-Butoxycarbonyl)-1,2,3,3-tetramethyl-3*H*-indol-1-ium iodide

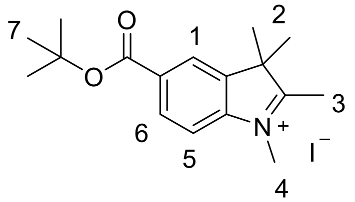

tert-Butyl 2,3,3-trimethyl-3*H*-indole-5-carboxylate (**9**) (817 mg, 3.15 mmol) was dissolved in 1,2-dichlorobenzene (12 mL) and CH_3I was added (3.92 mL, 63.1 mmol). The tube was sealed and heated to 80 °C for 24 h. After cooling to room temperature, the mixture was washed with cold Et_2O and filtered, yielding the product as a beige solid (978 mg, 77%). R_f (SiO_2, 9:1 CH_2Cl_2/CH_3OH) = 0.7. ^1H NMR (400 MHz, $CDCl_3$) δ (ppm): 8.21 (d, J = 8.4 Hz, 1H, H6), 8.11 (s, 1H, H1), 7.76 (d, J = 8.4 Hz, 1H, H5), 4.31 (s, 3H, H4), 3.13 (s, 3H, H3), 1.70 (s, 6H, H2), 1.62 (s, 9H, H7). $^{13}C\{^1H\}$ (101 MHz, $CDCl_3$) δ (ppm): 164.1, 144.7, 141.4, 134.0, 131.3, 124.2, 115.3, 82.8, 55.0, 38.0, 28.3, 23.3, 17.9. HRMS (ESI +ve) *m*/*z*: 274.18004, ($[M-I]^+$, $C_{17}H_{24}O_2N$ requires 274.18016).

***tert*-Butyl 1,3,3-trimethyl-2-methyleneindoline-5-carboxylate (10)**

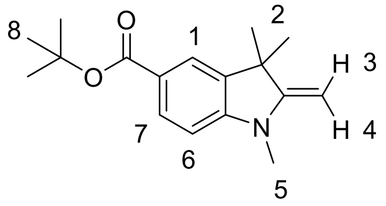

5-(*tert*-Butoxycarbonyl)-1,2,3,3-tetramethyl-3*H*-indol-1-ium iodide (190 mg, 0.49 mmol) was dissolved in aqueous KOH solution (0.3 M, 4.9 mL) and isopropyl alcohol (5.0 mL). After stirring at room temperature for 2 h, the mixture was concentrated *in vacuo* and extracted with CH_2Cl_2. Evaporation of the solvent afforded a white solid (132 mg, 99%). The product is highly light sensitive, turning pink upon exposure to ambient light. ^1H NMR (400 MHz, $CDCl_3$) δ (ppm): 7.83 (dd, J = 8.3, 1.8 Hz, 1H, H7), 7.68 (d, J = 1.7 Hz, 1H, H1), 6.50 (d, J = 8.3 Hz, 1H, H6), 3.95 (2nd order m, 2H, H3, H4), 3.07 (s, 3H, H5), 1.58 (s, 9H, H8), 1.35 (s, 6H, H2). $^{13}C\{^1H\}$ (101 MHz, $CDCl_3$) δ (ppm): 166.3, 162.3, 149.9, 137.3, 130.7, 123.0, 122.0, 104.0, 80.0, 75.6, 43.7, 29.8, 28.8, 28.3.

***tert*-Butyl 6'-(indolin-1-yl)-1,3,3-trimethylspiro[indoline-2,3'-naphtho[2,1-*b*][1,4]oxazine]-5-carboxylate (SO)**

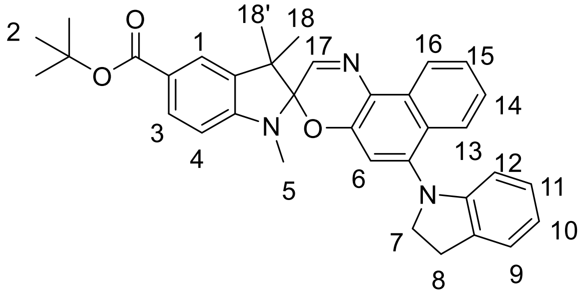

Zinc salt of 1-nitrosonaphthalen-2-olate (**12**) was prepared by following the reported procedure.[11] The zinc complex (500 mg, 1.22 mmol) was dissolved in EtOH (25 mL) and indoline (**13**) (0.48 mL, 4.3 mmol) was added. The mixture was heated under reflux for 3 h under aerobic conditions. *tert*-Butyl 1,3,3-trimethyl-2-methyleneindoline-5-carboxylate (**10**) (534 mg, 1.95 mmol) in EtOH (28 mL) and Na_2SO_4 (800 mg) were added. The system was purged with argon and heated under reflux for 21 h. The mixture was cooled to room temperature, and the precipitate was collected by filtration, and washed with cold acetone (5 mL). The residue was purified by silica gel chromatography (3:7 to 7:3 CH_2Cl_2/40–60 °C petroleum ether) to afford the product as a pale yellow solid (203 mg, 22%). R_f (SiO_2, CH_2Cl_2) = 0.4. ^{1}H NMR (400 MHz, $CDCl_3$) δ (ppm): 8.61 (d, J = 8.6 Hz, 1H, H16), 7.96 (d, J = 8.3 Hz, 1H, H13), 7.92 (dd, J = 8.4, 1.7 Hz, 1H, H3), 7.69 (d, J = 1.7 Hz, 1H, H1), 7.67 (s, 1H, H17), 7.60 (dd, J = 8.4, 6.8 Hz, 1H, H15), 7.35 (dd, J = 8.4, 6.8 Hz, 1H, H14), 7.20 (d, J = 6.7 Hz, 1H, H9), 6.94 (dd, J = 7.4, 7.4 Hz, 1H, H11), 6.91 (s, 1H, H6), 6.74 (dd, J = 7.4, 7.4 Hz, 1H, H10), 6.53 (d, J = 8.2 Hz, 1H, H4), 6.30 (d, J = 7.8 Hz, 1H, H12), 3.93 (br. s, 2H, H7), 3.18 (br. s, 2H, H8), 2.83 (s, 3H, H5), 1.58 (s, 9H, H2), 1.40–1.36 (2 x s overlapped, 6 H, H18, H18’). ^{13}C{^{1}H} (101 MHz, $CDCl_3$) δ (ppm): 166.2, 151.3, 150.0, 148.6, 144.6, 144.4, 135.9, 131.8, 131.0, 127.7, 127.0, 125.50, 125.48, 124.8, 123.9, 123.6, 123.1, 122.0, 120.6, 119.3, 110.0, 108.6, 106.2, 98.9, 80.4, 55.3, 51.5, 29.7, 29.0, 28.5, 25.5, 20.9. HRMS (ESI +ve) *m/z*: 546.27533, ($[M+H]^+$, $C_{35}H_{36}O_3N_3$ requires 546.27512). UV-vis (CH_3CN) λ_{max} / nm (ε / M^{-1} cm^{-1}) 291 (2.8×10^4), 387 (1.3×10^4); UV-vis (CH_2Cl_2) λ_{max} / nm (ε / M^{-1} cm^{-1}) 292 (2.5×10^4), 390 (1.4×10^4); UV-vis (toluene) λ_{max} / nm (ε / M^{-1} cm^{-1}) 391 (1.4×10^4); UV-vis (cyclohexane) λ_{max} / nm (ε / M^{-1} cm^{-1}) 279 (3.3×10^4), 387 (1.5×10^4).

Synthesis of **14** by de-protection of switch **SO**:

6'-(Indolin-1-yl)-1,3,3-trimethylspiro[indoline-2,3'-naphtho[2,1-*b*][1,4]oxazine]-5-carboxylic acid (14)

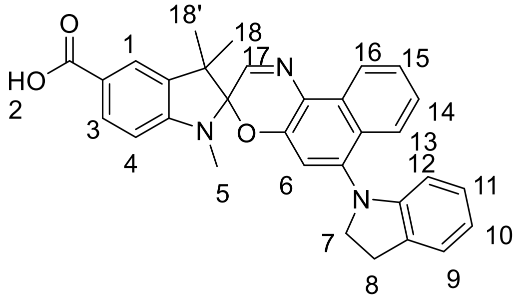

tert-Butyl 6'-(indolin-1-yl)-1,3,3-trimethylspiro[indoline-2,3'-naphtho[2,1-*b*][1,4]oxazine]-5-carboxylate (**SO**) (94 mg, 0.17 mmol) was dried with silica gel (1.0 g) under high vacuum at room temperature. Dry toluene (20 mL) was added and the resulting mixture was heated under reflux overnight. The silica was filtered off and the filtrate was concentrated *in vacuo*. The residue was purified by silica gel chromatography (CH_2Cl_2 to 9:1 CH_2Cl_2/CH_3OH) to yield the product as a pale yellow solid (65 mg, 77%). R_f (SiO_2, 9:1 CH_2Cl_2/CH_3OH) = 0.5. ^{1}H NMR (400 MHz, 1:1 $CD_3OD/CDCl_3$) δ (ppm): 8.54 (dt, *J* = 8.5, 0.9 Hz, 1H, H16), 7.98–7.89 (overlapped, 2H, H3, H13), 7.72 (d, *J* = 1.6 Hz, 1H, H1), 7.67 (s, 1H, H17), 7.62–7.56 (m overlapped with solvent, 1H, H15), 7.34 (ddd, *J* = 8.3, 6.8, 1.3 Hz, 1H, H14), 7.16 (dd, *J* = 7.3, 1.3 Hz, 1H, H9), 6.92 (s, 1H, H6), 6.89 (ddd, *J* = 7.8, 7.8, 1.3 Hz, 1H, H11), 6.70 (ddd, *J* = 7.4, 7.4, 1.0 Hz, 1H, H10), 6.58 (d, *J* = 8.3 Hz, 1H, H4), 6.25 (d, *J* = 7.9 Hz, 1H, H12), 3.91 (br. s, 2H, H7), 3.15 (br. s, 2H, H8), 2.84 (s, 3H, H5), 1.37 (s, 3H, H18), 1.36 (s, 3H, H18'). ^{13}C{^{1}H} NMR (101 MHz, 1:1 $CD_3OD/CDCl_3$) δ (ppm): 151.5, 149.8, 148.7, 144.3, 135.8, 131.6, 131.5, 130.9, 127.5, 127.5, 126.7, 125.5, 124.6, 124.5, 123.6, 123.3, 121.6, 120.4, 119.1, 109.7, 108.4, 106.1, 98.7, 55.2, 51.2, 29.1, 28.7, 25.0, 20.5. HRMS (ESI +ve) *m*/*z*: 490.21262 ($[M+H]^+$, $C_{31}H_{28}O_3N_3$ requires 490.21252). UV-vis (cyclohexane) of the closed form λ_{max} / nm (ε / M^{-1} cm^{-1}) 281 (4.6×10^4), 388 (2.0×10^4); UV-vis (cyclohexane) of the PSS λ_{max} / nm (ε / M^{-1} cm^{-1}) 560 (8.0×10^4).

Synthesis of **14** using one-pot reaction involving a zinc-chelate complex[11]:

6'-(Indolin-1-yl)-1,3,3-trimethylspiro[indoline-2,3'-naphtho[2,1-*b*][1,4]oxazine]-5-carboxylic acid (14)

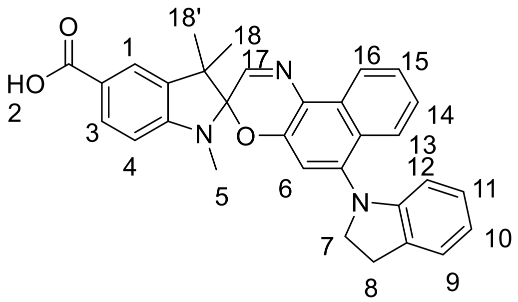

Zinc salt of 1-nitrosonaphthalen-2-olate (**12**) (1.45 g, 3.53 mmol) was dissolved in EtOH (74 mL) and indoline (**13**) (1.38 mL, 12.4 mmol) added. The mixture was heated at 78 °C for 3 h under aerobic conditions. 1,3,3-Trimethyl-2-methyleneindoline-5-carboxylic acid (**11**) (1.15 g, 5.29 mmol) in EtOH (74 mL) and Na_2SO_4 (4.6 g) were added. The system was purged with argon and left to be heated at 78 °C for 27 h. The mixture was cooled to room temperature, and Na_2SO_4 was removed by filtration. After solvent removal of the filtrate, the crude was purified by silica gel chromatography (CH_2Cl_2, 99.5:0.5 to 9:1 CH_2Cl_2/CH_3OH), and recrystallised from CH_2Cl_2 and then CH_3OH several times to get a pale yellow solid (737 mg, 28%). Characterisation data match those given above.

3.9 References

[1] J. C. Crano, R. J. Guglielmetti, Eds. , *Organic Photochromic and Thermochromic Compounds: Volume 1: Main Photochromic Families*, Kluwer Academic Publishers, **2002**.

[2] J. C. Crano, R. J. Guglielmetti, Eds. , *Organic Photochromic and Thermochromic Compounds: Volume 2: Physicochemical Studies, Biological Applications, and Thermochromism*, Kluwer Academic Publishers, **2002**.

[3] V. I. Minkin, *Chem. Rev.* **2004**, *104*, 2751–2776.

[4] S. N. Corns, S. M. Partington, A. D. Towns, *Color. Technol.* **2009**, *125*, 249–261.

[5] F. Wilkinson, J. Hobley, M. Naftaly, *J. Chem. Soc. Faraday Trans.* **1992**, *88*, 1511–1517.

[6] F. Wilkinson, D. R. Worrall, J. Hobley, L. Jansen, S. L. Williams, A. J. Langley, P. Matousek, *J. Chem. Soc. Faraday Trans.* **1996**, *92*, 1331–1336.

[7] I. Calderara, V. Neyrat, D. Baude, **2001**, WO0109645 (A1).

[8] M. Suzuki, **2015**, WO2015060227 (A1).

[9] Y. Xiong, A. Vargas Jentzsch, J. W. M. Osterrieth, E. Sezgin, I. V. Sazanovich, K. Reglinski, S. Galiani, A. W. Parker, C. Eggeling, H. L. Anderson, *Chem. Sci.* **2018**, *9*, 3029–3040.

[10] S. Wan, Y. Zheng, J. Shen, W. Yang, M. Yin, *ACS Appl. Mater. Interfaces* **2014**, *6*, 19515–19519.

[11] M.-L. Pang, H.-J. Zhang, P.-P. Liu, Z.-H. Zou, J. Han, J.-B. Meng, *Synthesis* **2010**, *20*, 3418–3422.

[12] R. W. Jackson, *Tetrahedron Lett.* **2001**, *42*, 5163–5165.

[13] M. Tomasulo, S. L. Kaanumal, S. Sortino, F. M. Raymo, *J. Org. Chem.* **2007**, *72*, 595–605.
[14] T.-F. Tan, *Chin. J. Struct. Chem.* **2007**, *26*, 572–574.
[15] M. York, R. A. Evans, *Tetrahedron Lett.* **2010**, *51*, 2195–2197.
[16] H. Guo, Y.-B. Gao, Y.-X. Li, J. Han, J.-B. Meng, *Acta Crystallogr. Sect. E Struct. Rep. Online* **2005**, *61*, o988–o989.
[17] N. W. Tyer, R. S. Becker, *J. Am. Chem. Soc.* **1970**, *92*, 1289–1294.
[18] A. Perrier, F. Maurel, E. A. Perpète, V. Wathelet, D. Jacquemin, *J. Phys. Chem. A* **2009**, *113*, 13004–13012.
[19] P. J. Castro, I. Gómez, M. Cossi, M. Reguero, *J. Phys. Chem. A* **2012**, *116*, 8148–8158.
[20] M. R. di Nunzio, P. L. Gentili, A. Romani, G. Favaro, *ChemPhysChem* **2008**, *9*, 768–775.
[21] T. Tan, P. Chen, H. Huang, J. Meng, *Tetrahedron* **2005**, *61*, 8192–8198.
[22] M. R. di Nunzio, A. Romani, G. Favaro, *J. Phys. Chem. A* **2009**, *113*, 9424–9433.
[23] N. Y. C. Chu, *Can. J. Chem.* **1983**, *61*, 300–305.
[24] R. Klajn, *Chem. Soc. Rev.* **2013**, *43*, 148–184.
[25] G. Favaro, F. Masetti, U. Mazzucato, G. Ottavi, P. Allegrini, V. Malatesta, *J. Chem. Soc. Faraday Trans.* **1994**, *90*, 333–338.
[26] V. G. Luchina, I. Y. Sychev, A. I. Shienok, N. L. Zaichenko, V. S. Marevtsev, *J. Photochem. Photobiol. Chem.* **1996**, *93*, 173–178.
[27] A. V. Metelitsa, V. Lokshin, J. C. Micheau, A. Samat, R. Guglielmetti, V. I. Minkin, *Phys. Chem. Chem. Phys.* **2002**, *4*, 4340–4345.
[28] J. B. Flannery, *J. Am. Chem. Soc.* **1968**, *90*, 5660–5671.
[29] J. L. Dean, *Lange's Handbook of Chemistry*, McGraw Hill, **1999**.
[30] M. R. di Nunzio, E. O. Danilov, M. A. J. Rodgers, G. Favaro, *Photochem. Photobiol. Sci.* **2010**, *9*, 1391–1399.
[31] C. Özçoban, T. Halbritter, S. Steinwand, L.-M. Herzig, J. Kohl-Landgraf, N. Askari, F. Groher, B. Fürtig, C. Richter, H. Schwalbe, et al., *Org. Lett.* **2015**, *17*, 1517–1520.
[32] J. Hobley, F. Wilkinson, *J. Chem. Soc. Faraday Trans.* **1996**, *92*, 1323–1330.
[33] D. Bléger, S. Hecht, *Angew. Chem. Int. Ed.* **2015**, *54*, 11338–11349.
[34] C. Li, H. Yan, L.-X. Zhao, G.-F. Zhang, Z. Hu, Z.-L. Huang, M.-Q. Zhu, *Nat. Commun.* **2014**, *5*, 5709.
[35] P. Remón, M. Hammarson, S. Li, A. Kahnt, U. Pischel, J. Andréasson, *Chem. – Eur. J.* **2011**, *17*, 6492–6500.
[36] H. Sell, C. Näther, R. Herges, *Beilstein J. Org. Chem.* **2013**, *9*, 1–7.
[37] S. Fredrich, R. Göstl, M. Herder, L. Grubert, S. Hecht, *Angew. Chem. Int. Ed.* **2016**, *55*, 1208–1212.
[38] B. Roubinet, M. L. Bossi, P. Alt, M. Leutenegger, H. Shojaei, S. Schnorrenberg, S. Nizamov, M. Irie, V. N. Belov, S. W. Hell, *Angew. Chem. Int. Ed.* **2016**, *55*, 15429–15433.
[39] Y. Xiong, P. Rivera-Fuentes, E. Sezgin, A. Vargas Jentzsch, C. Eggeling, H. L. Anderson, *Org. Lett.* **2016**, *18*, 3666–3669.
[40] V. A. Lokshin, A. Samat, A. V. Metelitsa, *Russ. Chem. Rev.* **2002**, *71*, 893–916.
[41] C. Kaiser, T. Halbritter, A. Heckel, J. Wachtveitl, *ChemistrySelect* **2017**, *2*, 4111–4123.
[42] Y. Sheng, J. Leszczynski, A. A. Garcia, R. Rosario, D. Gust, J. Springer, *J. Phys. Chem. B* **2004**, *108*, 16233–16243.

[43] M. Sakuragi, K. Aoki, T. Tamaki, K. Ichimura, *Bull. Chem. Soc. Jpn.* **1990**, *63*, 74–79.

[44] H. Görner, *Phys. Chem. Chem. Phys.* **2001**, *3*, 416–423.

[45] A. K. Chibisov, H. Görner, *Phys. Chem. Chem. Phys.* **2001**, *3*, 424–431.

[46] L. Kong, H.-L. Wong, A. Y.-Y. Tam, W. H. Lam, L. Wu, V. W.-W. Yam, *ACS Appl. Mater. Interfaces* **2014**, *6*, 1550–1562.

[47] M. Suzuki, T. Asahi, H. Masuhara, *ChemPhysChem* **2005**, *6*, 2396–2403.

[48] K. M. Siddiqui, G. Corthey, S. A. Hayes, A. Rossos, D. S. Badali, R. Xian, R. S. Murphy, B. J. Whitaker, R. J. D. Miller, *CrystEngComm* **2016**, *18*, 7212–7216.

[49] S. Aramaki, G. H. Atkinson, *Chem. Phys. Lett.* **1990**, *170*, 181–186.

[50] N. Tamai, H. Masuhara, *Chem. Phys. Lett.* **1992**, *191*, 189–194.

[51] G. Buntinx, O. Poizat, S. Foley, M. Sliwa, S. Aloïse, V. Lokshin, A. Samat, *Dyes Pigments* **2011**, *89*, 305–312.

[52] J. L. Bahr, G. Kodis, L. de la Garza, S. Lin, A. L. Moore, T. A. Moore, D. Gust, *J. Am. Chem. Soc.* **2001**, *123*, 7124–7133.

[53] G. M. Greetham, P. M. Donaldson, C. Nation, I. V. Sazanovich, I. P. Clark, D. J. Shaw, A. W. Parker, M. Towrie, *Appl. Spectrosc.* **2016**, *70*, 645–653.

[54] G. M. Greetham, P. Burgos, Q. Cao, I. P. Clark, P. S. Codd, R. C. Farrow, M. W. George, M. Kogimtzis, P. Matousek, A. W. Parker, et al., *Appl. Spectrosc.* **2010**, *64*, 1311–1319.

[55] A. Khadria, Y. de Coene, P. Gawel, C. Roche, K. Clays, H. L. Anderson, *Org. Biomol. Chem.* **2017**, *15*, 947–956.

[56] M. J. Frisch, G. W. Trucks, H. B. Schlegel, G. E. Scuseria, M. A. Robb, J. R. Cheeseman, G. Scalmani, V. Barone, G. A. Petersson, H. Nakatsuji, et al., *Gaussian 16*, Wallingford, CT, **2016**.

[57] J. Tomasi, B. Mennucci, R. Cammi, *Chem. Rev.* **2005**, *105*, 2999–3094.

[58] G. M. Greetham, D. Sole, I. P. Clark, A. W. Parker, M. R. Pollard, M. Towrie, *Rev. Sci. Instrum.* **2012**, *83*, 103107.

[59] I. H. M. van Stokkum, D. S. Larsen, R. van Grondelle, *Biochim. Biophys. Acta BBA - Bioenerg.* **2004**, *1657*, 82–104.

[60] L. Palatinus, A. van der Lee, *J. Appl. Crystallogr.* **2008**, *41*, 975–984.

[61] L. Palatinus, *Acta Crystallogr. Sect. B Struct. Sci. Cryst. Eng. Mater.* **2013**, *69*, 1–16.

[62] L. Palatinus, G. Chapuis, *J. Appl. Crystallogr.* **2007**, *40*, 786–790.

[63] P. W. Betteridge, J. R. Carruthers, R. I. Cooper, K. Prout, D. J. Watkin, *J. Appl. Crystallogr.* **2003**, *36*, 1487–1487.

[64] R. I. Cooper, A. L. Thompson, D. J. Watkin, *J. Appl. Crystallogr.* **2010**, *43*, 1100–1107.

[65] P. Parois, R. I. Cooper, A. L. Thompson, *Chem. Cent. J.* **2015**, *9*, 30–43.

Chapter 4

Spirooxazine-Based Dyads

4 Spirooxazine-Based Dyads

Here we demonstrate that spirooxazine **SO** (**Figure 4-1**; detailed in Chapter 3) can be used to modulate the fluorescence of a covalently-linked fluorophore. Such dyads display remarkable fatigue resistance and bright/dark contrast ratio in live cells. The application of the dyads in RESOLFT imaging is then explored, and some related systems are compared. Part of the work in this Chapter has been published.[1]

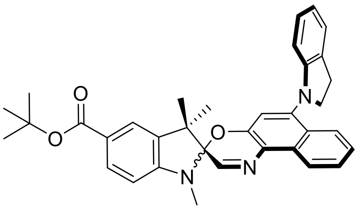

SO

Figure 4-1 Molecular structure of the spirooxazine switch **SO** that possesses promising features as a tuneable fluorescence quencher in our dyad design (detailed in Chapter 3).

4.1 Rationale

It is apparent from the results presented in Chapter 3 that **SO** possesses many of the required photophysical properties to function as a fluorescence quencher in our proposed molecular design of a FRET-based switchable dyad. Nevertheless, properties such as membrane permeability, photostability in cellular media, and fluorescence quenching efficiency of an attached dye (*via* FRET) can only be assessed in real systems.

Based on the absorption spectrum of **SO$_{\mathbf{(open)}}$**, we chose a robust fluorescent dye, **Atto565**,[2] to be part of the dyad. A model structure is shown in **Figure 4-2**, where the ^{t}Bu deprotected **SO** is linked to an **Atto565** dye by a simple ethylenediamine linker. The two extreme geometries, i.e. folded and extended conformers, suggest a donor-acceptor distance between 6.8 and 15.4 Å (**Figure 4-2**).

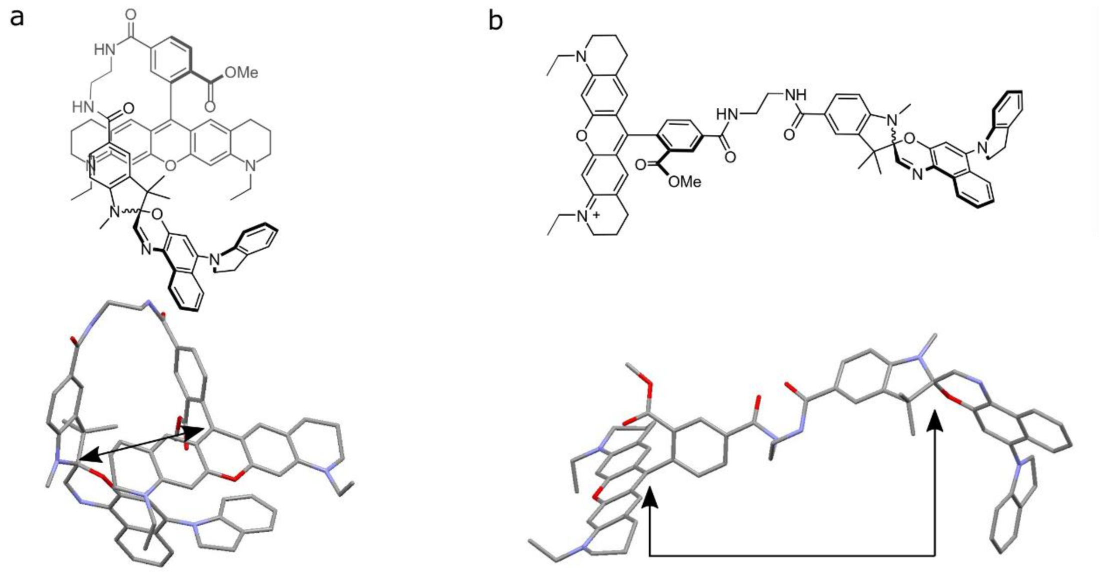

Figure 4-2 Conformers and the corresponding modelled structures of a dyad, which comprises the spirooxazine switch and **5'-Atto565** dye that are linked by an ethylenediamine linker. The distance between the C atoms marked in black was used to calculate FRET efficiency. a) Folded conformer, distance: 6.8 Å. b) Unfolded conformer, distance: 15.4 Å. The modelling was carried out in the molecular mechanics mode of HyperChem.

Our calculations based on the spectral overlap (**Figure 4-3**) give a Förster radius of 66.4 Å and hence, quenching efficiency above 99% for such a dyad system (for calculation details see Experimental 4.8.4). Moreover, given the broad absorption of $\mathbf{SO_{(open)}}$, other dyes such as AlexaFluor488® are expected to be quenched with similar efficiencies, which creates the possibility of multi-colour imaging.

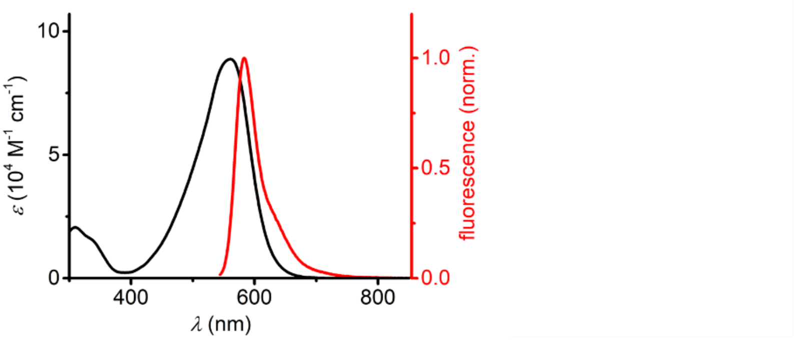

Figure 4-3 Overlap of the reconstructed spectrum of $\mathbf{SO_{(open)}}$ in cyclohexane (black) and normalised emission spectrum of **5'-Atto565** in PBS buffer (red). Based on the spectral overlap, a Förster radius of 66.4 Å was obtained using PBS as the medium. This indicates that FRET efficiencies of ~100% are expected for interchromophore distances smaller than 16 Å. The spectrum of $\mathbf{SO_{(open)}}$ cannot be acquired in PBS buffer due to the fast thermal recovery.

4.2 Synthesis

We prepared two model dyads: **Dyad 2** and **Dyad 3**, both consisting of the spirooxazine switch and **Atto565** dye (**Scheme 4-1**). The syntheses of both dyads follow a similar sequence (**Scheme 4-1**). The fluorescent dye **5'-Atto565** was coupled to Boc-protected ethylenediamine using HBTU as a coupling reagent. The free amine was unmasked by acid promoted Boc-deprotection using TFA. Acid **14** was then coupled to the amine and quenched with MeOH to afford **Dyad 2** in 21% overall yield. A similar procedure was used to prepare **Dyad 3** from the 6'-isomer of **Atto565** without protecting the acid at the 3'-position, and the overall yield was 16%. The main difference between the dyads is the permanent cationic form of **Dyad 2**, while **Dyad 3** can exist as a zwitterion.

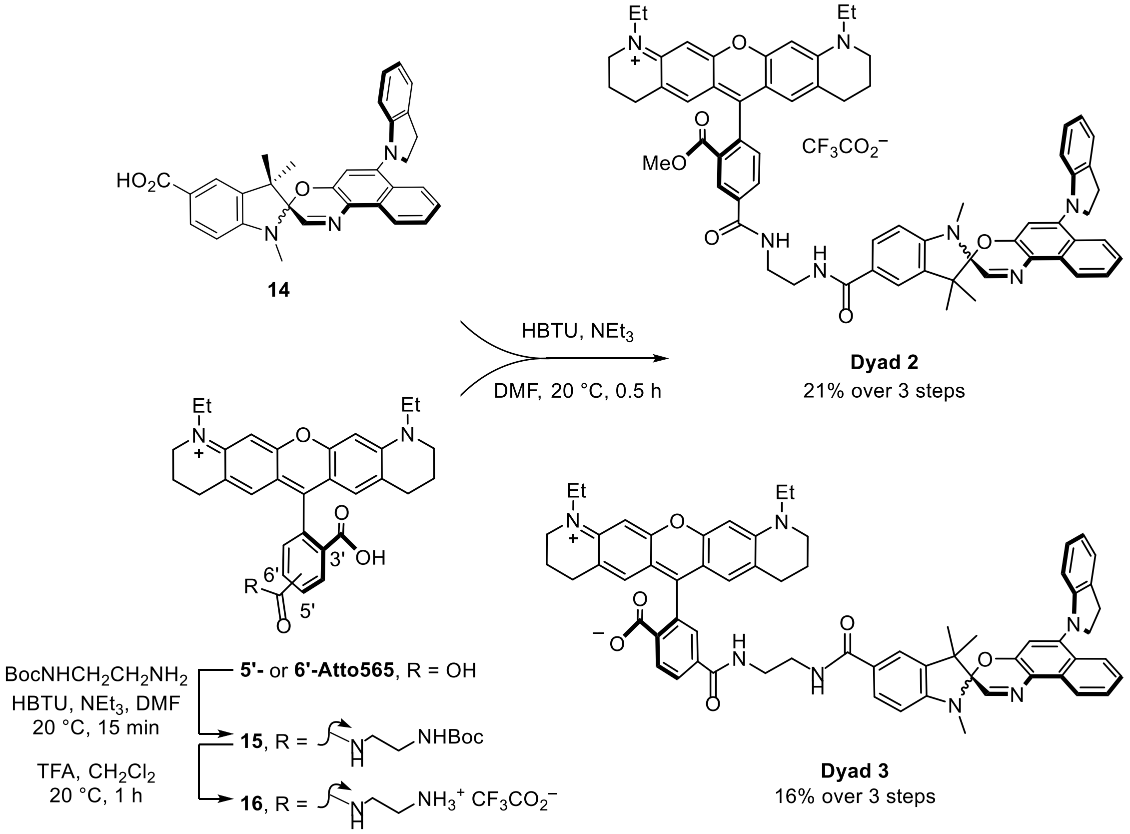

Scheme 4-1 Syntheses of **Dyad 2** and **Dyad 3**.

4.3 Photophysical characterisation

The photophysical properties of both dyads were investigated. In methanol solution, the absorption spectra of the dyads are close to the sum of those of their components (**Figure 4-4**).

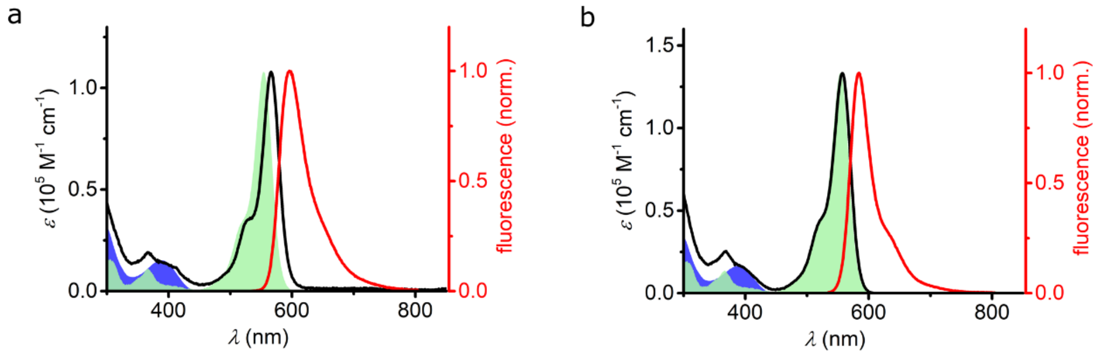

Figure 4-4 UV-vis absorption (black) and emission spectra (red) for **Dyad 2** (a) and **Dyad 3** (b) in CH_3OH. The normalised absorption spectra of **SO$_{\text{(closed)}}$** and **Atto565** are shown in blue and green respectively for reference.

As seen before (**Figure 4-3**), the observed absorption of **SO$_{\text{(open)}}$** overlaps substantially with the emission of **Atto565** and the fluorescence lifetimes are identical within the error of the measurement (e.g. **5'-Atto565** and **Dyad 2** have fluorescence lifetimes of τ = 4.05 ns and τ = 3.88 ns respectively; **Table 4-1**). Curiously, the fluorescence quantum yields of the dyads show a marked decrease in PBS compared to those in organic solvents (e.g. for **Dyad 2**, Φ_f = 33% in CH_3OH and Φ_f = 3.6% in PBS; **Table 4-1**) which, taken together with the virtually unchanged fluorescence lifetime, suggests a static quenching mechanism. That is, a population of molecules has a very short fluorescence lifetime and is not observed in emission. The decrease in fluorescence quantum yield is attributed to aggregation because it is accompanied by marked changes of the absorption spectrum in PBS, such as appearance of a shoulder, relative to those in organic solvents (**Figure 4-5**). The fact that Φ_f of the dyads remains lower than that of **Atto565** even in solvents such as CH_2Cl_2 (<50% against 80%; **Table 4-1**) indicates that other quenching mechanisms are involved, which will be discussed in detail later.

Table 4-1 Photophysical properties of selected compounds in various solvents.

compound (solvent)	$\lambda_{\text{abs, max}}$ (nm) ε (M^{-1} cm^{-1})	$\varepsilon_{570}/\varepsilon_{405}$	$\lambda_{\text{em, max}}$ (nm)	fluorescence lifetime τ (ns)	Φ_f (%)
SO (CH_2Cl_2)	**390**	0	533	–	5.1%
5’-Atto565 (PBS)	**564** 1.8 × 10^5	22.5	589	4.05	79%, 80%[a]
5’-Atto565 (CH_3OH)	**554** 1.7 × 10^5	19.6	578	4.16	85%; 85%[a]
5’- & 6’-Atto565[3] (PBS)	**564**	–	590	4.0	90%
Dyad 2 (PBS)	**576** 6.8 × 10^4	3.6	598	3.88	3.6%
Dyad 2 (CH_3OH)	**566** 1.1 × 10^5	8.4	591	1.68, 3.70	33%; 33%[a]
Dyad 2 (CH_2Cl_2)	**567** 1.2 × 10^5	10.5	587	1.19, 3.18	47%; 48%[a]
Dyad 2 (DMSO)	**578** 1.0 × 10^5	9.6	605	0.24, 3.39	65%; 66%[a]
Dyad 3 (PBS)	**571** 5.5 × 10^4	5.5	589	4.00	5.1%
Dyad 3 (CH_3OH)	**557** 1.3 × 10^5	6.3	580	1.43, 3.55	39%; 40%[a]

[a] The values are re-absorption corrected (see Experimental 4.8.3).

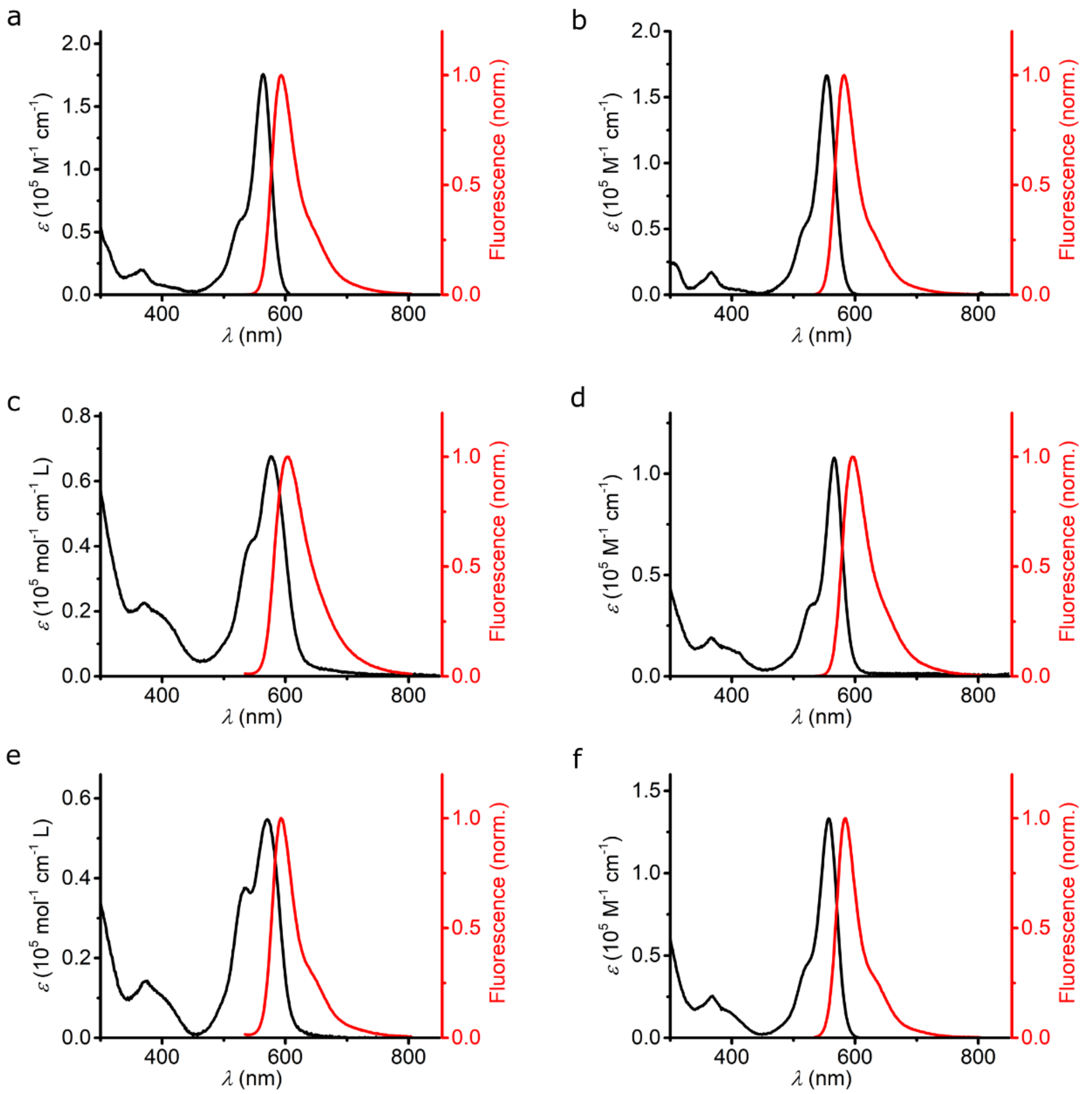

Figure 4-5 Absorption and normalised emission spectra at μM concentrations of a) **5'-Atto565** in PBS. b) **5'-Atto565** in CH_3OH. c) **Dyad 2** in PBS. d) **Dyad 2** in CH_3OH. e) **Dyad 3** in PBS. f) **Dyad 3** in CH_3OH.

4.4 Live-cell imaging

A critical factor in the application of spironaphthoxazines is whether they function in biological media. Indeed, there are no examples of this family of photochromic switches being used in cells, and very few examples in aqueous media have been reported, typically in vesicles[3] or nanoparticles.[4]

To investigate the switching and fluorescence quenching of the two dyads in biological media, we added solutions of the dyads in DMSO directly to live human embryonic kidney cells (HEK 293 cells from ATCC, Manassas, VA, USA) in cell culture medium. After 15 min incubation, we removed the excess dyad and recorded confocal images of the stained cells. Cellular uptake was confirmed for both dyads by the observation of fluorescence from inside the cell (λ_{ex} = 561 nm, 5 μW, λ_{em} = 570–650 nm). In spite of the similarity of the dyads, their localisation within the cell is significantly different: while **Dyad 2** accumulates in the membrane-bound intracellular compartments, **Dyad 3** appears to be dispersed in the cytosol. This is important because it suggests that cellular uptake and intracellular localisation can be affected by the choice of dye, rather than being dominated by the hydrophobicity of **SO**.

The photoswitching behaviour of the spironaphthoxazine and the concomitant fluorescence quenching using **Dyads 2** and **3** was explored in cells using a commercial confocal microscope (Zeiss LSM780 inverted confocal microscope). Important properties like fatigue resistance and quenching efficiencies were analysed. As described in Chapter 1, fatigue resistance is defined as how many switching cycles a dyad (as an entire dyad of the switch and dye) can survive before photo-degradation. This property is calculated as the normalised fluorescence of the same field of view over consecutive cycles, relative to the fluorescence readout in the first bright state. The quenching efficiency, on the other hand, describes the performance of the switch *without* considering the effects from factors such as motion of cells and decomposition of the dye. This presents the extent to which the switch depletes the fluorescence in a single cycle, and is defined as

$$\mathrm{QE} = 1 - I_{\mathrm{dark}} / I_{\mathrm{bright}}$$

where I_{dark} and I_{bright} refer to the average photon counts in the dark and bright states respectively of the same switching cycle.

The imaging was performed as follows: the field of view was scanned first with a green laser (561 nm, 5 µW), to acquire the "bright" image, and then sequentially with a blue laser (405 nm, 30 µW) to activate the switch, followed immediately by the image acquisition using the green laser to obtain the "dark" image (**Figure 4-6**a and **Figure 4-7**a). Following this procedure, quenching efficiency values of 75–85% for **Dyad 2** and 70–80% for **Dyad 3** could be consistently recorded. Under the same conditions, the fatigue resistance in cellular media was measured by repeating the photoswitching sequence described above. **Dyad 2** loses 15% of its quenching efficiency after 23 cycles (**Figure 4-6**b,c). It is important to notice that while the pixel size is set to 80 nm × 80 nm, the actual illumination spot size is larger (ca. 300 nm/200 nm because of the diffraction-limited illumination) implying that every switching cycle effectively involves multiple switching events. Assuming that a minimum contrast of 50% is necessary to discern both states, an increase in resolution of 10 times is to be expected using a RESOLFT set-up.[5] A similar fatigue resistance is measured for **Dyad 3** (**Figure 4-7**b,c).

Overall, both dyads showed remarkable fatigue resistance and high fluorescence modulation using visible light, which led us to explore the possibility of RESOLFT imaging.

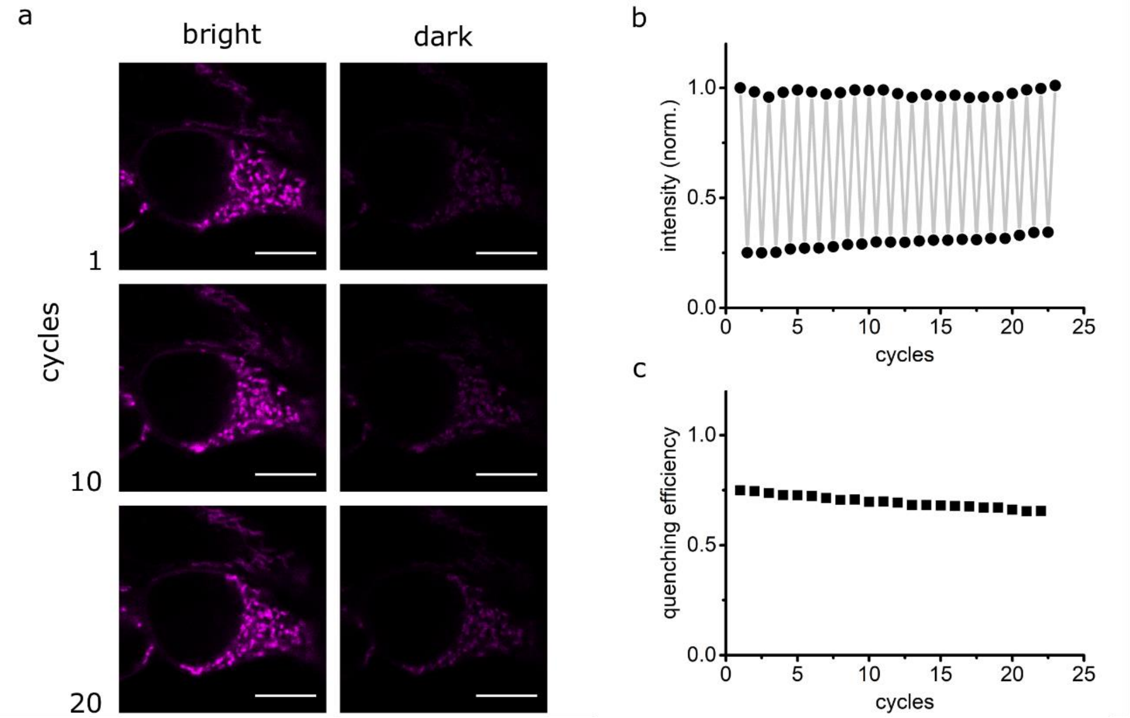

Figure 4-6 a) Confocal image in live HEK cells stained with **Dyad 2** in the bright state and dark state after a number of cycles. The bright state was obtained by excitation at 561 nm. The dark state was obtained by irradiation at 405 nm followed by excitation at 561 nm. b) and c) Fluorescence quantification of **Dyad 2** over several switching cycles. Quenching efficiency refers to the effective quenching of fluorescence per cycle. Scale bar: 10 μm.

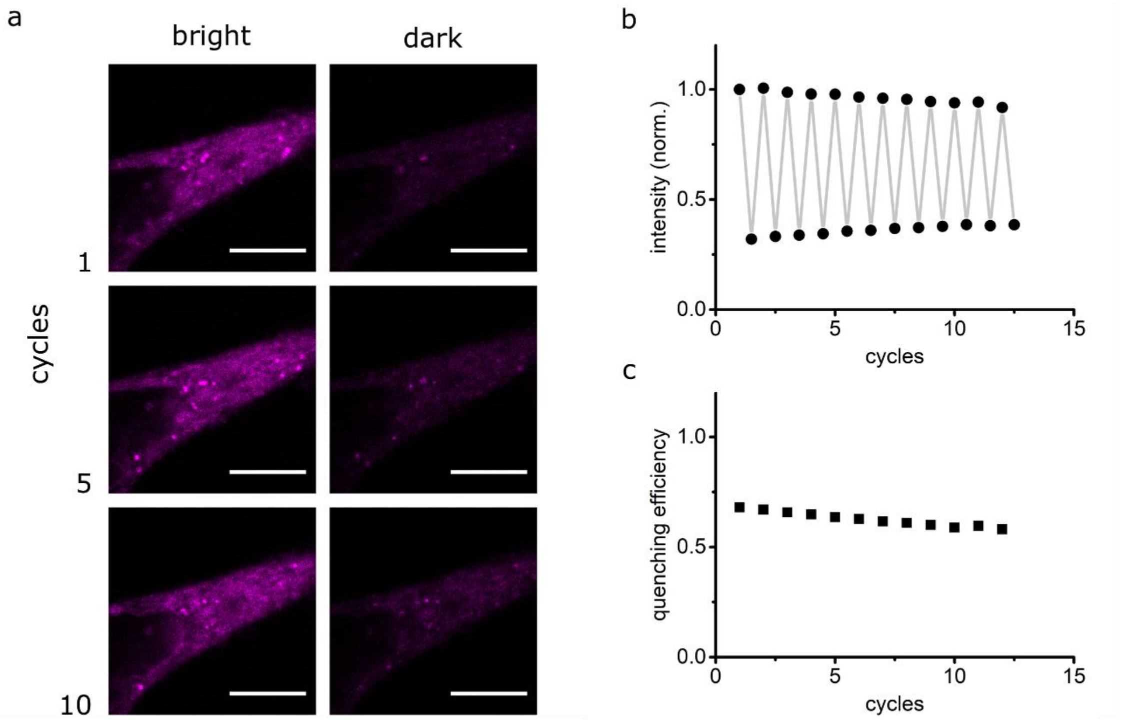

Figure 4-7 a) Confocal image in live HEK cells stained with **Dyad 3** in the bright state and dark state after a number of cycles. The bright state was obtained by excitation at 561 nm. The dark state was obtained by irradiation at 405 nm followed by excitation at 561 nm. b) and c) Fluorescence quantification of **Dyad 3** over several switching cycles. Quenching efficiency refers to the effective quenching of fluorescence per cycle. Scale bar: 10 μm.

4.5 Preliminary RESOLFT imaging

4.5.1 Rationale

Confocal imaging of **Dyad 2** in live cells suggested that the dyad accumulated in membrane-bound intracellular compartments, with particularly pronounced localisation after 4 h (**Figure 4-8**). In addition, the fatigue resistance of the dyad was maintained for such incubation times, but was poorer after longer incubation, e.g. after 28 h (**Figure 4-8**h,i).

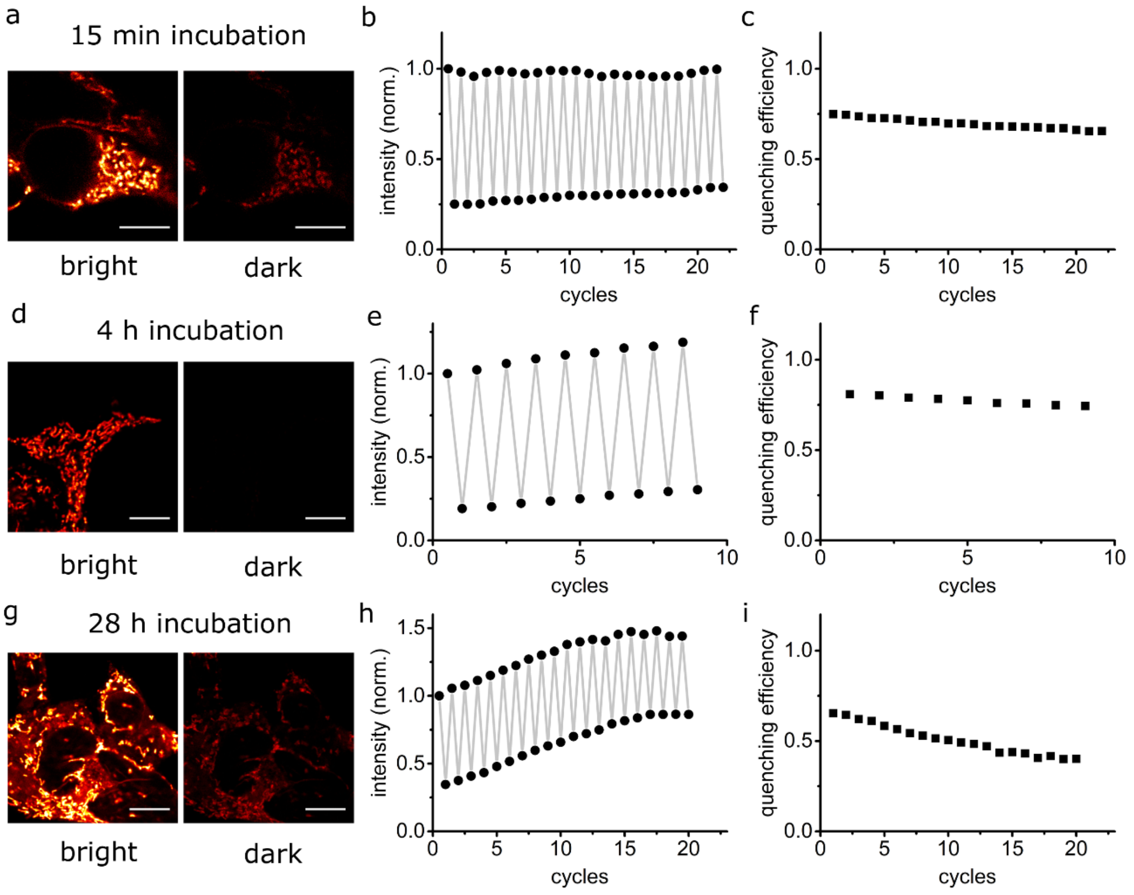

Figure 4-8 Confocal images of HEK cells after incubation with **Dyad 2** for the indicated time period. Scale bar: 10 µm. The dyad in DMSO was added to live HEK cells at the final concentration of 2.5 µM, and incubated for the specified time. The cells were washed with dye-free medium, and incubated for another 1 h before imaging. The images were recorded on a Zeiss LSM780 inverted confocal microscope, 4.6 µW of 561 nm laser, 33 µW of 405 nm, dwell time 1.58 µs/pixel (speed 9), pixel size 80 nm × 80 nm.

We then devoted efforts to imaging the dyad under RESOLFT microscopy in the hope that such localisation would provide an opportunity to visualise particular structures at sub-diffraction resolution. To begin with, we needed to obtain reference performance of **Dyad 2** on a confocal microscope. We optimised imaging conditions: 2.5 µM of the dyad, 4 h incubation time, 4.6 µW of 561 nm laser, 33 µW of 405 nm. These parameters consistently led to 81% quenching efficiency and 15% photo-degradation after 23 cycles.

4.5.2 Initial attempts at live-cell RESOLFT imaging

Once the reference performance on the confocal microscope was completed, we wanted to test the dyad performance on a RESOLFT microscope. The RESOLFT microscope was custom modified from a commercial Abberior STED microscope, housed at Weatherall Institute of Molecular Medicine (WIMM), University of Oxford. While 561 nm excitation was ideal for our dyad, the only available relevant wavelengths were 405 nm (diode, CW, Cobolt), 485 nm (diode, pulsed, PicoQuant), 594 nm (diode, pulsed, Abberior), and 640 nm (diode, pulsed, PicoQuant). Despite the similar absorbance at 485 nm and 594 nm by the **6'-Atto565** dye, we chose 594 nm as the excitation source due to less photobleaching and photodamage associated with longer wavelengths.

To start with, in the confocal mode of the RESOLFT microscope, we tried to reproduce the results from the Zeiss confocal microscope. We first used line-by-line scanning and then pixel-by-pixel scanning. The only available scanning mode on the Zeiss confocal microscope is line-by-line, i.e. to acquire the dark state, the first line of the field of view (FOV) is scanned by the depletion light, immediately followed by the excitation light, and this process is repeated for the second, third line etc., until it is completed for the entire FOV. This line-by-line scanning is different from what is required for RESOLFT microscopy, i.e. pixel-by-pixel scanning, where the depletion and excitation is performed on one pixel before moving to the next. Therefore, we needed to check whether the promising results from line-by-line scanning were reproducible on a different microscope, and to optimise pixel-by-pixel scanning parameters for RESOLFT imaging. A typical imaging sequence for each pixel in the pixel-by-pixel scanning process is shown in **Figure 4-9**.

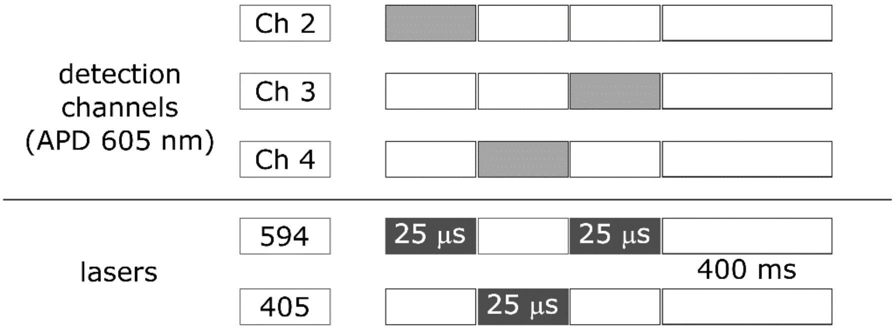

Figure 4-9 Imaging sequence for pixel-by-pixel scanning in the confocal mode of a RESOLFT microscope, WIMM, Oxford. Detection at Channel 2 gives the image of the bright state, and Channel 3 gives the image of the dark state. Channel 4 collected emission signals resulting from the 405 nm excitation. However, these data were not required for construction of images. This sequence was repeated for each pixel before moving to the next pixel. APD (605 nm) = avalanche photodiode (detected at 605–625 nm), Ch = channel.

Both the line-by-line and pixel-by-pixel scanning processes in the confocal mode of the Abberior RESOLFT microscope gave similar results, and the switching properties were poorer than those acquired on the Zeiss confocal microscope (**Figure 4-10**). Firstly, the quenching efficiency was significantly lower (60% on Abberior *vs.* 81% on Zeiss). It is possible that the use of different excitation lasers (594 nm pulsed diode laser on Abberior and 561 nm CW diode laser on Zeiss) could explain this change. Despite attempts to optimise the imaging parameters, further improvements in contrast could not be achieved.

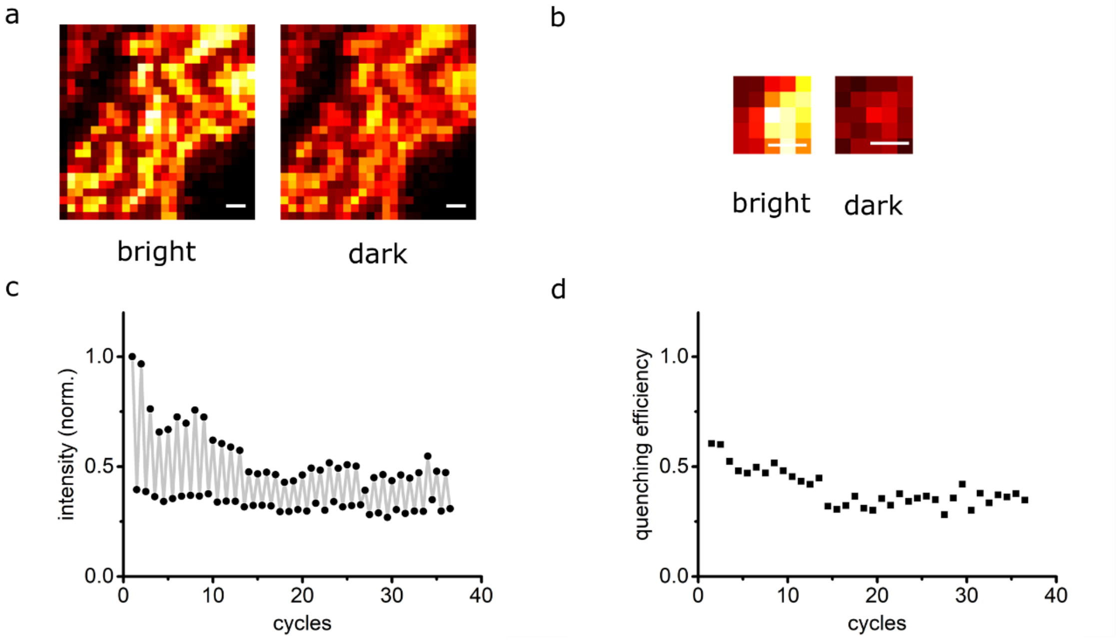

Figure 4-10 Live-cell images of **Dyad 2** in the confocal mode of the Abberior RESOLFT microscope using pixel-by-pixel scanning process. a) Confocal images of a 10 µm × 10 µm field of view in live HEK cells stained with **Dyad 2**. The bright state was obtained by excitation at 594 nm. The dark state was obtained by irradiation at 405 nm followed by excitation at 594 nm by following the pixel-by-pixel scanning sequence in **Figure 4-9**. b) Expanded view in bright and dark states, similar to that in a). c) and d) Fluorescence quantification of the field of view in b) over switching cycles. Quenching efficiency refers to the effective quenching of fluorescence per cycle. Scale bar: 1 µm.

Another problem was that fluorescent objects, i.e. organelles stained with the dyad or the freely moving dyad, move fast relative to the image acquisition speed, which has been previously reported for fluorescent proteins.[6] This problem became more pronounced when the pixel size was set below the diffraction limit, which is necessary for sub-diffraction imaging. From pixel to pixel, thermal relaxation of at least hundreds of milliseconds was required for the dyad in the neighbouring pixel to recover from the exposure to the diffraction-limited depletion light. This mismatch of fast dyad movement and slow image acquisition prevents acquisition of RESOLFT images. One potential solution would be to use photochemical acceleration of the back reaction using the 594 nm laser, rather than waiting for slow thermal relaxation. We have demonstrated this is possible in the photochemical recovery of the switch (alone) in organic solvents (see Chapter 3). However, in the case of live-cell imaging using **Dyad 2**, significant photobleaching was observed on photochemical reversion (**Figure 4-11**).

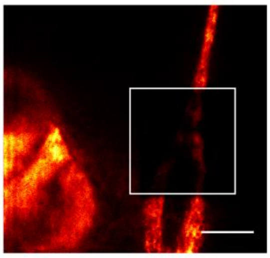

Figure 4-11 Photobleaching (highlighted) was observed when photochemical reversion by 594 nm laser was applied. The image was taken of live HEK cells stained with **Dyad 2** after two photoswitching cycles, in the confocal mode of the RESOLFT microscope. Scale bar: 10 μm.

The second possible solution would be to image fixed cells rather than live cells, although clearly this is a compromise. Initially, we used the common mounting medium Mowiol, which is a water-soluble polymer solution derived from polyvinyl alcohol, to preserve the sample, but no switching behaviour was detected under these conditions. We then resorted to PBS buffer as the imaging medium, and the quenching efficiency was recovered to 65% (**Figure 4-12**a). However, it was clear that the previous localisation in the intracellular compartments of **Dyad 2** was disrupted, and the dyad was found scattered randomly in the cytoplasm (**Figure 4-12**b). In addition, the brightness decreased by a factor of ca. 5 compared to that observed in live cells.

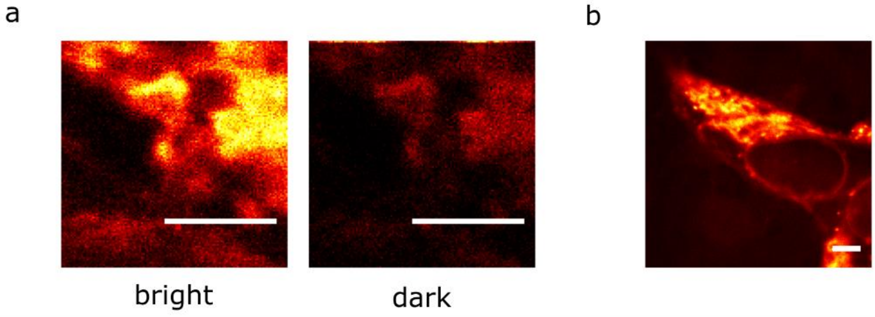

Figure 4-12 Confocal images of fixed HEK cells stained with **Dyad 2** mounted in PBS buffer. a) The bright state was obtained by excitation at 594 nm. The dark state was obtained by irradiation at 405 nm followed by excitation at 594 nm in the pixel-by-pixel scanning manner as in **Figure 4-9**. b) The previous localisation in the intracellular compartments was lost, with the dyad randomly scattered in the cytoplasm. Scale bar: 5 μm.

A third potential solution that may solve the problem from a different perspective is to modify the microscope operating protocol (**Figure 4-13**).[7] Instead of waiting at one pixel for the nearby fluorescence to recover, the laser beams could be programmed to move to a location outside the diffraction-limited region, and start to acquire the bright image and deplete the fluorescence there. Such a remote location is chosen so that the dyad could revert to the bright state before undergoing another switching cycle. This modification would require input from the instrument manufacturer Abberior, which is unavailable at the time of writing. Such a strategy is generalisable to any switchable dyes that require relatively long waiting times to recover either from the bright or dark state.

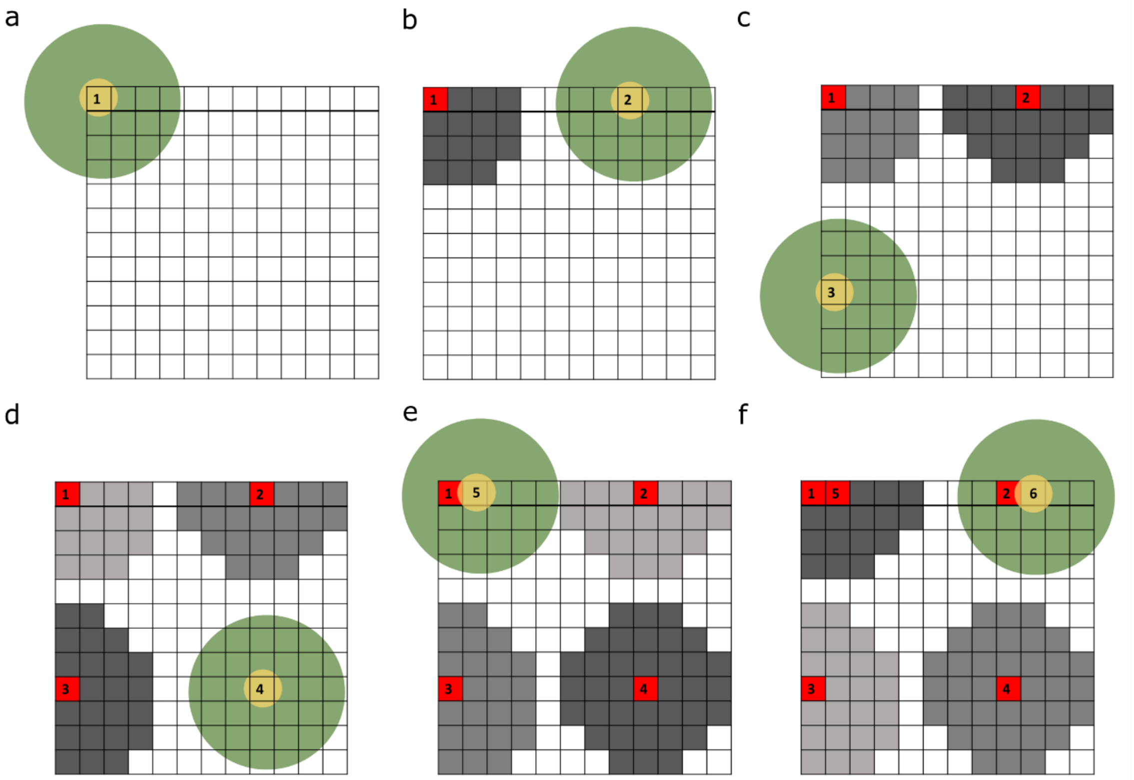

Figure 4-13 Potential solution to resolve the slow recovery of the switch by programming the scanning in a 'random' way. Instead of waiting at the spot for the nearby fluorescence to recover, the laser beams are targeted at a location outside the diffraction-limited region, and start to acquire the bright image and deplete the fluorescence there. Such a remote location is chosen so that the dyad could revert to the bright state before undergoing another switching cycle.[7] Green = donut-shaped depletion beam, yellow = effective excitation spot as a result of superimposition of the excitation and donut-shaped depletion beams, red = pixel of which the fluorescence readout is recorded, dark grey to light grey = pixels at which dyads gradually recover from dark to bright states to different extents.

In conclusion, the preliminary results indicate that future work such as modification of the microscope scanning scheme is required to perform RESOLFT imaging of dyads with slow switching kinetics, e.g. **Dyad 2**.

4.6 Investigation of photophysical properties of dyads

4.6.1 Low fluorescence quantum yields

We have demonstrated that the dyads show remarkable fatigue resistance and contrast of bright/dark states in live cells, confirming the potential of our modular molecular design for super-resolution microscopy. Nevertheless, as described above, the application of such dyads in RESOLFT imaging was challenging, and there were several aspects that could be improved. One was to selectively label proteins of interest and this will be addressed in Chapter 5. Another potential issue was the poor fluorescence quantum yields of the dyads in PBS buffer, which could result in low brightness and contrast ratio of bright and dark states in cell imaging. For example, as briefly mentioned earlier, the quantum yield of **Dyad 2** is 3.6% in PBS and 33% in CH_3OH, whereas the values for the parent dye **5’-Atto565** are 80% and 85% respectively (**Table 4-1**). Additional analyses show that while the fluorescence lifetimes are similar for **5’-Atto565** (τ = 4.05 ns) and **Dyad 2** (τ = 3.88 ns) in PBS, the UV-vis absorption spectrum of **Dyad 2** shows a shoulder at a shorter wavelength compared to the absorption peak expected for **5’-Atto565** (**Figure 4-5**). On account of the above information, the hypothesis was that the dyad aggregates in PBS buffer to form weakly fluorescent or non-fluorescent species. Aggregation, like any other static quenching, occurs when molecules form non-fluorescent complexes in the ground state rather than excited state as in dynamic quenching. This essentially reduces the concentration of fluorophores in the solution while the remaining fluorophores fluoresce in the usual way. The effects are lower quantum yields, unchanged lifetimes (of the fluorophores), and different UV-vis absorption spectra due to the presence of the non-fluorescent species. In our dyads, the static quenching may occur both intramolecularly and intermolecularly since both the switch and dye are hydrophobic aromatic moieties.

4.6.2 Analysis of fluorescence quenching mechanisms

One way to test the above hypothesis is to vary the linker length in the dyad. It might be expected that longer linkers would give more spatial freedom between the two components of the dyad, which would, in turn, reduce aggregation. Hence, **Dyad 4** was prepared by following a similar synthetic route as **Dyads 2** and **3** (**Figure 4-14**), using a polyethylene glycol (PEG) linker to increase hydrophilicity. Analyses were performed by comparing properties of **6’-Atto565**, **6’-Atto565-C2linker**, **Dyad 3** and **Dyad 4** (**Figure 4-14**).

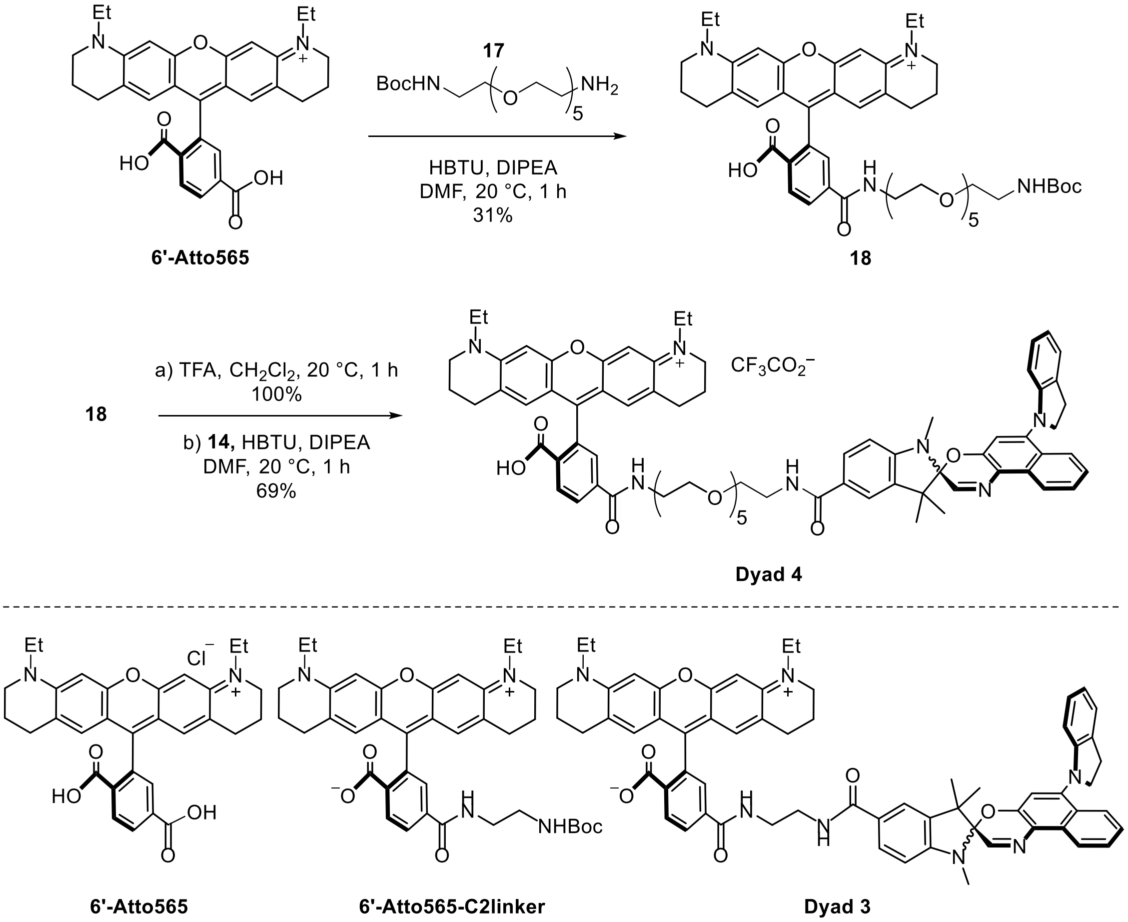

Figure 4-14 Synthesis of **Dyad 4**, and structures of **6’-Atto565**, **6’-Atto565-C2linker** and **Dyad 3**.

Firstly, because the dyads were obtained only in very small quantities, it was difficult to know the accurate masses by directly weighting them on the balance. The typical process is as follows: a vial was pre-weighed, a compound in a mixture of MeOH and DCM was transferred to the vial, the solvents were removed under N_2 flow, the compound was further dried under high vacuum, and the vial was weighed to get the mass of the compound. During this process, dust, grease left on the vial wall (from fingers) and error margins of balance reading caused by e.g. air drafts could influence the mass.

Therefore, NMR calibration experiments were carried out to measure the actual quantities of these compounds, to identify the counter-ions and to calculate molar absorption coefficients. The procedure is as follows: 1. A stock solution of 10 mM anhydrous toluene in CD_3OD (10 mL) was freshly prepared. 2. Each compound was dissolved in 0.6 mL of the stock deuterated solution. 3. ^1H NMR spectra were obtained, with relaxation time set at 20 seconds to allow reliable proton integrals. 4. By comparing the integrals for toluene and the compound, the quantity of that compound was calculated based on the known amount of toluene. 5. ^{19}F NMR spectra were recorded to identify the counter-ion. The results are summarised in **Table 4-2**. It is shown that for a small quantity of a sample (< 3 mg), the NMR derived amount may be quite different from the mass read from a balance because of the reasons mentioned earlier. Hence, NMR calibration is necessary to calculate reliable and reproducible molar absorption coefficients, which is an important factor in brightness (the product of molar absorption coefficient and fluorescence quantum yield).

Table 4-2 NMR calibration experiments to determine the quantities of the dyes and dyads.

compound	presence of ^{19}F signals	integral ratio of compound:toluene	qty derived from NMR	qty from weighing
6'-Atto565	No	0.62:1.0	2.04 mg	3.32 mg
6'-Atto565-C2linker	No	0.26:1.0	1.02 mg	4.21 mg
Dyad 3	No	0.14:1.0	0.86 mg	3.40 mg
Dyad 4	Yes	0.17:1.0	1.39 mg	2.75 mg

Secondly, measurements of photophysical properties, i.e. fluorescence lifetime, quantum yield, UV-vis absorbance and excitation, were carried out for the four compounds in three solvents, and each measurement in triplicate. The results are shown in **Table 4-3, Table 4-4**, and **Figure 4-15** until **Figure 4-18**. Overlay of spectra for different compounds in the same solvent, and overlay of spectra for the same compound in different solvents can be found in Appendices.

Table 4-3 Fluorescence lifetimes (τ) of the dyes and dyads.

	6'-Atto 565	6'-Atto565-C2linker	Dyad 3	Dyad 4
PBS	4.04 ns	3.71 ns	4.07 ns	4.09 ns
MeOH	4.14 ns	4.26 ns	1.12 ns (18%), 3.59 ns (82%)	1.58 ns (28%), 3.58 ns (72%)
DCM	3.87 ns	3.76 ns	1.09 ns (48%), 3.45 ns (52%)	1.19 ns (35%), 3.32 ns (65%)

[a] The values were obtained by fitting the data to either a mono-exponential or bi-exponential decay. The values in brackets are the pre-exponential factors, which represent the fractions of fluorescent species with different lifetimes.

Table 4-4 Fluorescence quantum yields of the dyes and dyads.

	6’-Atto 565	6’-Atto565-C2linker	Dyad 3	Dyad 4
PBS	79%	61%	5.1%	6.3%
MeOH	83%	76%	39%	30%
DCM	73%	73%	38%	28%

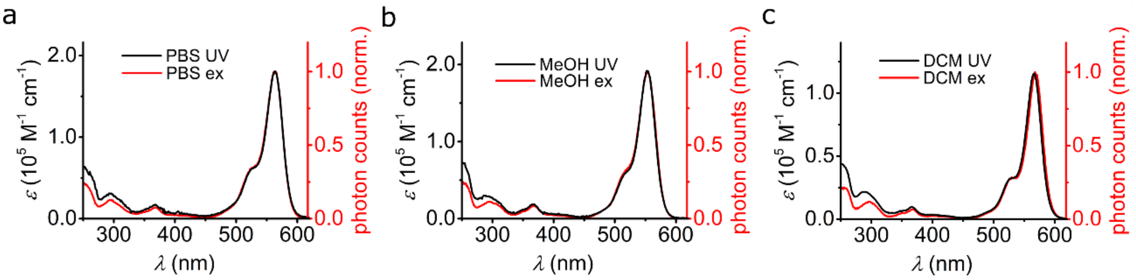

Figure 4-15 UV-vis absorption and excitation spectra of **6’-Atto565** in a) PBS buffer, b) MeOH, c) DCM.

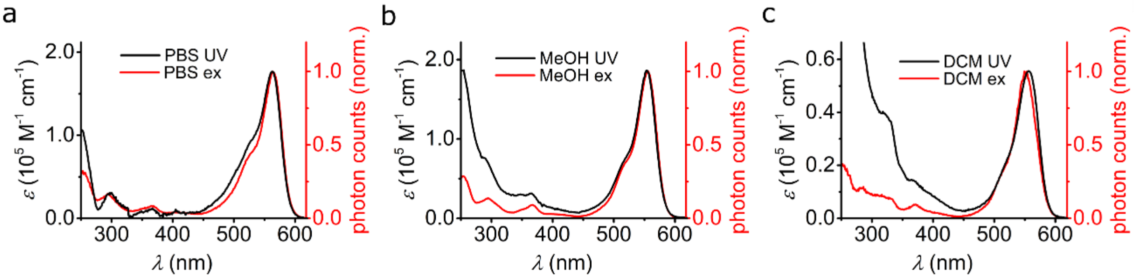

Figure 4-16 UV-vis absorption and excitation spectra of **6’-Atto565-C2linker** in a) PBS buffer, b) MeOH, c) DCM.

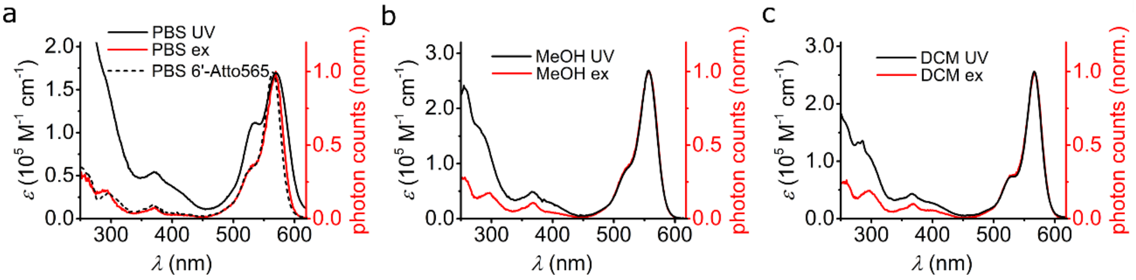

Figure 4-17 UV-vis absorption and excitation spectra of **Dyad 3** in a) PBS buffer, with normalised UV-vis absorption of **6’-Atto565**, b) MeOH, c) DCM.

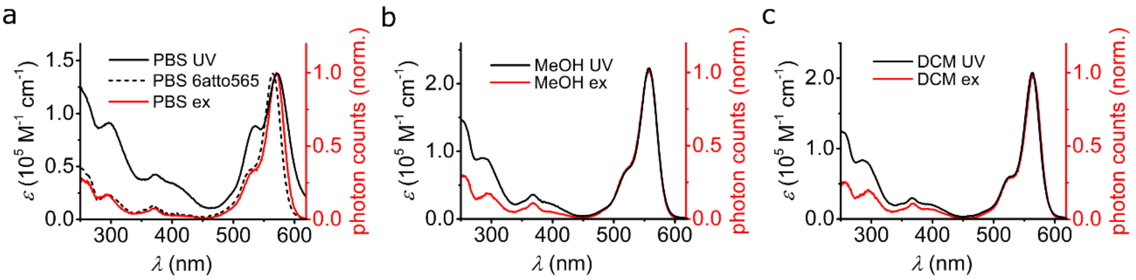

Figure 4-18 UV-vis absorption and excitation spectra of **Dyad 4** in a) PBS buffer, with normalised UV-vis absorption of **6’-Atto565**, b) MeOH, c) DCM.

4.6.2.1 Important conclusions from the analysis

These measurements reveal important points that could lead to the design of improved dyads:

1. In agreement with the initial analysis, the quenching mechanism in PBS buffer for the dyads involves static quenching, i.e. aggregation. Firstly, while **6'-Atto565** and **6'-Atto-C2linker** have the same UV-vis absorption and excitation spectra (**Figure 4-15**, **Figure 4-16**), for **Dyads 3** and **4**, the UV-vis spectra show an extra shoulder compared to the excitation spectra, and the excitation spectra are the same as the UV-vis absorbance of **6'-Atto565** (**Figure 4-17**a, **Figure 4-18**a). The shoulder is unique to the dyads in PBS buffer, not observed for these compounds in organic solvents, and not observed for the free dyes in any solvents. Such behaviour is characteristic of an aggregation phenomenon, and the shoulder arises from aggregates that are formed either intermolecularly or intramolecularly. The broadening of the absorbance peak leads to reduced molar absorption coefficients. Secondly, from **6'-Atto565** to the dyads, the observed fluorescence lifetimes remain unchanged (4.04 ns *vs* 4.07 ns & 4.09 ns) (**Table 4-3**) and the quantum yields dramatically decrease (79% *vs* 5.1% & 6.1%; **Table 4-4**). These comparisons strongly support the existence of a static quenching process. Dynamic quenching may also play a key role, as shown in the calculations later.

2. Dynamic quenching is observed in organic solvents for **Dyads 3** and **4**, accounting for their lower quantum yields (39%, 30% in MeOH; 38%, 28% in DCM) relative to those of **6'-Atto565** (83% in MeOH; 73% in DCM) and **6'-Atto565-C2linker** (76% in MeOH; 73% in DCM) (**Table 4-4**). Unlike static quenching, dynamic quenching takes place in the excited state, with common examples being Förster resonance energy transfer (FRET) and photoinduced electron transfer (PET). Dynamic quenching does not change the UV-vis absorbance, but changes the fluorescence lifetime, because it provides an additional nonradiative pathway for the excited state. These match our observations for the dyads in organic solvents (**Table 4-3**, e.g. **Figure 4-17**b). At the resting state, the switch is in the closed form and thus, the FRET process is unlikely to happen due to insufficient spectral overlap. On the other hand, PET from the electron-rich spirooxazine to the cationic **Atto565**, may be responsible. Similar findings have been reported previously.[8,9] In addition, the fact

that increasing the linker length in **Dyad 4** did not improve the quantum yield suggests the quenching is through space rather than through bond.

3. Quantitative analyses can be performed to calculate the population percentage of different species in the sample solution. From the ^{1}H NMR spectra, we know that the aryl regions for the dyads are void of impurities, and the quantity differences from the NMR calibration and balance reading methods probably arise from aliphatic impurities e.g. grease, solvents or dust. These are unlikely to absorb at the excitation wavelength for lifetime and quantum yield measurements (473 nm, 520 nm), and therefore, the following calculations should be considered only for fluorophores (fluorescent or non-fluorescent). In general, the lifetime is calculated as $\tau = 1/(k_{\mathrm{NR}} + k_{\mathrm{R}})$, where k_{NR} is the combined rate constants of all nonradiative pathways, and k_{R} is the rate constant of radiative emission. The fluorescence quantum yield is calculated as $\Phi_{\mathrm{f}} = \sum_1^{\mathrm{n}}[D_{\mathrm{n}} \times k_{\mathrm{Rn}}/(k_{\mathrm{NRn}} + k_{\mathrm{Rn}})]$, where D_{n} is the population percentage of the n$^{\mathrm{th}}$ species, k_{NRn} and k_{Rn} are the nonradiative and radiative rate constants for the n$^{\mathrm{th}}$ species, respectively.

   Taking **Dyad 3** in PBS buffer as an example, the reasonable assumptions are that: (a) there is one fluorescent and one or more non-fluorescent species in the sample because of a single lifetime and a low quantum yield (**Table 4-3**, **Table 4-4**); (b) the radiative rate constant is the same for **6’-Atto565** and the fluorescent species in the sample of **Dyad 3**, because the fluorescent component is the same. Firstly, we calculate the radiative rate constant. For **6’-Atto565** in PBS, $\tau = 1/(k_{\mathrm{NR'}} + k_{\mathrm{R}}) = 4.04$ ns, $\Phi_{\mathrm{f}} = k_{\mathrm{R}}/(k_{\mathrm{NR'}} + k_{\mathrm{R}}) = 0.79$ and thus, $k_{\mathrm{R}} = 0.20$ ns^{-1}. For **Dyad 3**, $\tau_1 = 1/(k_{\mathrm{NR1}} + k_{\mathrm{R}}) = 4.07$ ns, $\tau_2 = \tau_3 = \tau_{\mathrm{n}} = 1/(k_{\mathrm{NRn}} + k_{\mathrm{Rn}}) \approx 0$ (not detected or unresolved by the fluorometer), $\Phi_{\mathrm{f}} = D_1 \times k_{\mathrm{R}}/(k_{\mathrm{NR1}} + k_{\mathrm{R}}) + \sum_2^{\mathrm{n}}[D_{\mathrm{n}} \times k_{\mathrm{Rn}}/(k_{\mathrm{NRn}} + k_{\mathrm{Rn}})] = 0.051$, where D_1 is the population percentage of the fluorescent species and D_{n} of the non-fluorescent species, $D_1 + \sum_2^{\mathrm{n}} D_{\mathrm{n}} = 100\%$. With the values plugged in, $0.051 = D_1 \times 0.18 \times 4.07$; thus, $D_1 = 6\%$ population is the fluorescent species, and $\sum_2^{\mathrm{n}} D_{\mathrm{n}} = 94\%$ non-fluorescent species which could be due to weakly or non-fluorescent complexes formed in the ground state and/or quenching by PET in the excited state.

   Now examining **Dyad 3** in organic solvents, e.g. MeOH, the same assumptions hold except that there must be two fluorescent species *I* and *II* from the observed lifetimes. The radiative rate constant of **6’-Atto565** in MeOH changes little relative to that in

PBS: $k_R = \Phi_f/\tau = 0.83/4.14 = 0.20$ ns^{-1}. The calculations are then: $\tau_1 = 1/(k_{NR1} + k_R) = 1.12$ ns, $\tau_2 = 1/(k_{NR2} + k_R) = 3.59$ ns, $\tau_3 = \tau_n = 1/(k_{NRn} + k_{Rn}) \approx 0$. $\Phi_f = D_1 \times k_R/(k_{NR1} + k_R) + D_2 \times k_R/(k_{NR2} + k_R) = 0.39$, where D_1: D_2 = 18:82 from the pre-exponential factors of the lifetime measurement (**Table 4-3**), D_n of the non-fluorescent species, $D_1 + D_2 + \sum_3^n D_n = 100\%$. Thus, 11% fluorescent species *I* ($\tau_1 = 1.12$ ns), 51% fluorescent *II* ($\tau_2 = 3.59$ ns), 38% non-fluorescent species. These three species may come from different spatial isomers that have different through-space distances between the switch and dye, and hence have different electron transfer rates.

4. Aggregation in PBS buffer and the undesired photoinduced electron transfer process in the dyads contribute to lower brightness in contrast to that of the dyes. This is because both the processes decrease the fluorescence quantum yield, and the formation of aggregates also reduces the absorbance. It indicates that significantly stronger laser powers are needed, potentially causing photodamage (to cells or to the switch) and photobleaching (to the dye). Moreover, with less emission from the dyad, non-switchable autofluorescent noise is proportionally higher in cellular imaging, resulting in a poorer contrast between bright and dark states during switching cycles.

5. The preliminary modification using a longer linker and comparison with other compounds made clear the problem of the undesired PET process and aggregation in PBS buffer. For further improvement, we could synthesise a dyad with a rigid linker of length between 20–30 Å. FRET efficiency needs to be high for effective switching, and it is inversely proportional to the 6th–power of the transition dipole separation between the donor and acceptor.[10] Our current system allows separation distance up to 30 Å for > 99% FRET efficiency. For example, the separation is calculated to be max. 15.4 Å in **Dyad 2**, which leaves much flexibility to modify the linker. On the other hand, PET is more distance dependent (usually exponentially), making it much less effective at a longer distance (ca. 20 Å).[9,10] That is why the donor-acceptor distance should be designed with this 20–30 Å range to have high FRET and low PET efficiencies. Additionally, the linker should be rigid, perhaps composed of fused/spiro rings, to eliminate the possibility of the dye and switch approaching close to each other. Such a design could improve the quantum yield, but may not restore the value to that of **6’-Atto565**, because it does not eliminate the problem of *intermolecular* aggregation in PBS buffer.

4.6.2.2 Molar absorption coefficients

It may be noticed that the molar absorption coefficients are peculiar by comparison of the dyes and dyads in organic solvents. As expected, the molar absorption coefficients of **Dyads 3** and **4** in PBS buffer are lower than those for **6’-Atto565** and **6’-Atto565-C2linker**, due to the aggregation of the dyads in aqueous media. However, the observation is reversed in organic solvents, particularly noticeable in DCM. Further investigation was performed. Firstly, triplicate measurements were carried out, and consistent molar absorption coefficients were derived based on the quantities derived from the NMR calibration experiments. Secondly, the pH dependence was checked. When TFA was added, **6’-Atto565-C2linker** and **Dyad 4** showed an increased absorbance at $\lambda_{\max}$. In **Dyad 4**, an additional peak centred at 700 nm appeared, which does not correspond to the open form of the switch (**Figure 4-19**). We do not have an explanation for this. Moreover, the UV-vis absorption spectra of **6’-Atto565** and **Dyad 4** remain unchanged in the pH range 4.8–8.1 in PBS buffer (**Figure 4-20**), suggesting that they may not change in cellular environments. Thirdly, even with the addition of excess TFA, the molar absorption coefficients of **6’-Atto565-C2linker** are lower than those of the dyads (**Figure 4-19**a), suggesting other factors in addition to pH effect. The speculation is that given the more hydrophilic nature of **6’-Atto565**, it might form a colloid rather than a solution given that the dye is not very soluble in DCM. The size of the dispersed particles in the colloid could be very small because no apparent suspension was observed. This discussion does not change the conclusions in Section 4.6.2.1.

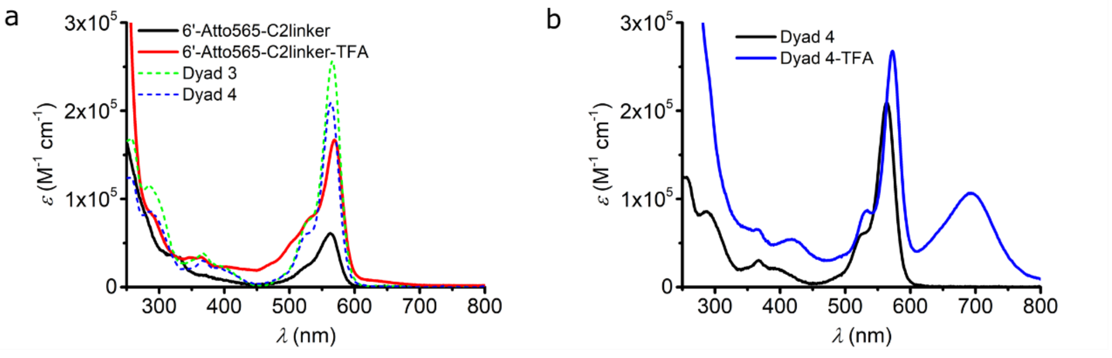

Figure 4-19 Variance of UV-vis absorption spectra of a) **6’-Atto565-C2linker**, b) **Dyad 4** in DCM before and after addition of excess TFA. After the addition of TFA, the molar absorption coefficients of **6’-Atto565** are still lower than the dyads, suggesting other factors in addition to pH.

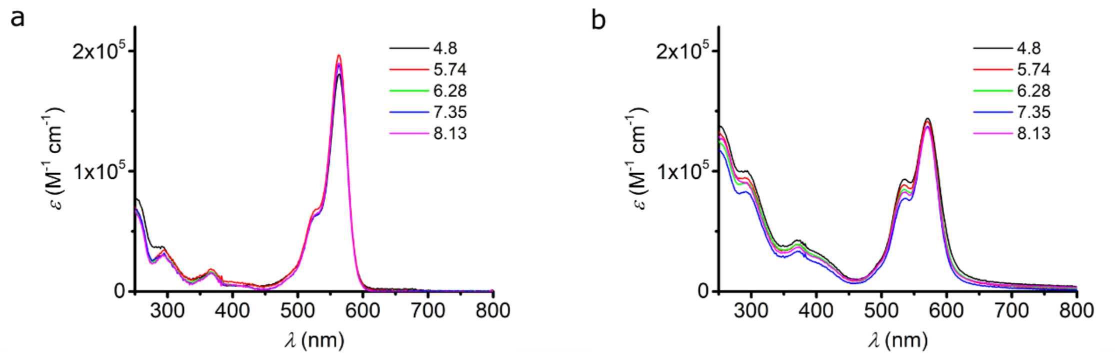

Figure 4-20 Analysis of pH dependence of a) of **6'-Atto565**, b) **Dyad 4** in PBS buffer in the pH range 4.8–8.1.

4.7 Conclusions and future work

We report spironaphthoxazine based dyads that display high fluorescence modulation using visible light and outstanding fatigue resistance in cellular environments, which are critical requirements for switchable dyes to be used in super-resolution microscopy. Nevertheless, the direct application of such dyads in RESOLFT imaging was unsuccessful mainly due to the relatively fast movement of cellular organelles and diffusing dyads compared to the slow image acquisition speed. Several potential solutions were pursued but hindered by different reasons like photobleaching under photoreversion conditions. On the other hand, efforts were devoted to improving the fluorescence quantum yield, and comprehensive characterisation of similar systems pointed to promising further directions. Prospective work may include use of a relatively rigid linker, the length of which permits high FRET efficiency, but prevents undesired PET process.

4.8 Experimental

4.8.1 General procedures

General procedures for NMR and mass spectrometry are described in Chapter 2 Experimental section, and those for reagents, UV-vis and excitation spectroscopies and fluorescence emission are described in Chapter 3 Experimental section, with the following additions and modifications:

For amide coupling reactions, DMF and DIPEA (over KOH) were freshly distilled, the glassware was dried with a heat gun, and all the solid reactants dried under high vacuum before use. Unless otherwise stated, reactions were carried out under an atmosphere of argon. MALDI mass spectra were obtained on a Waters MALDI Micro MX instrument.

4.8.1.1 HPLC

HPLC was performed on an Agilent 1100 system equipped with an autosampler, degasser, multi-channel pump, column oven, UV-vis diode array detector and fraction collector.

Analytical HPLC was performed using an Agilent Eclipse XDB-C18 column (5 µm particle size, 4.6 × 150 mm) at a rate of 1 mL/min at 298 K, monitoring at 254 nm, 405 nm, and 565 nm, using the following method:

Method A: CH_3OH and H_2O (with 0.1% TFA additive) as eluents. 5% CH_3OH to 100% CH_3OH over 20 min, 100% CH_3OH for 15 min.

Semi-preparative HPLC was performed using an Agilent Eclipse XDB-C18 column (5 µm particle size, 9.4 × 250 mm) at a rate of 3 mL/min at 298 K, using the following method:

Method B: CH_3OH and H_2O (with 0.1% TFA additive) as eluents. 5% CH_3OH to 100% CH_3OH over 20 min, 100% CH_3OH for 20 min.

4.8.2 Fluorescence lifetime measurements

Fluorescence lifetimes were determined by time correlated single photon counting (TCSPC) using the FS5-TCSPC unit (Edinburgh Instruments) with a picosecond pulsed diode laser (473.4 nm ± 0.5 nm). Once a time-resolved fluorescence decay and the instrument response function were measured, a reconvolution fit analysis was carried out using the software Fluoracle (Edinburgh Instruments) by fitting a mono-exponential or bi-exponential function: Fit = $A + \sum_{1}^{\mathrm{n}} B_{\mathrm{n}} e^{(-t/\tau_{\mathrm{n}})}$ (n = 1 or 2), where A is the calculated background, B is the calculated pre-exponential factor, and the goodness of fit is given as χ^2. For our compounds, all χ^2 values approach 1, indicating the good fit to a mono-exponential or bi-exponential decay. The following are the examples of **5'-Atto565** that shows mono-exponential decays in both PBS buffer and CH_3OH, and **Dyad 3** that shows a mono-exponential decay in PBS buffer and a bi-exponential decay in CH_3OH.

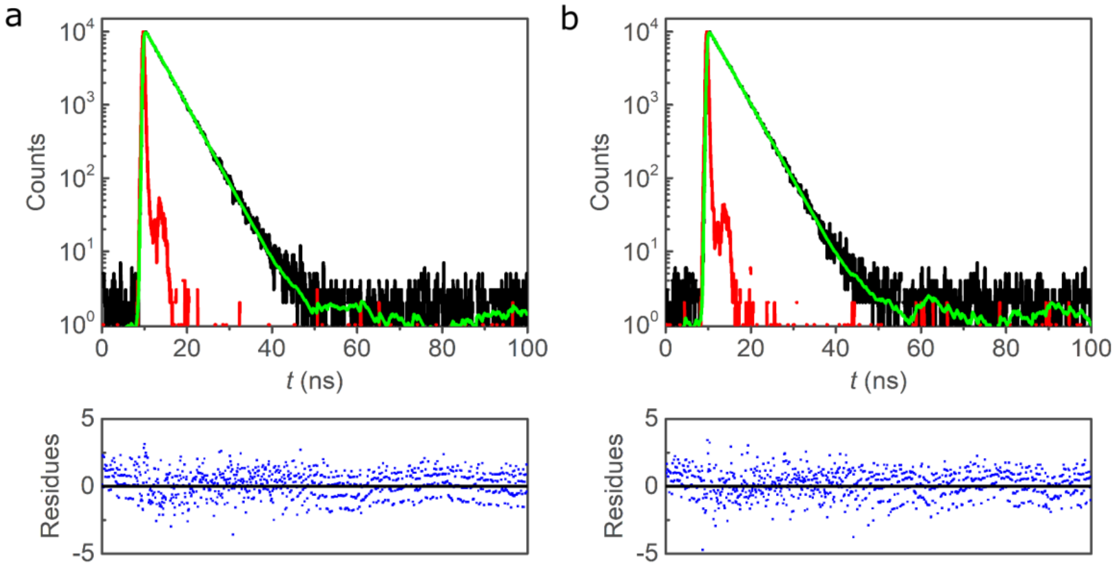

Figure 4-21 The fluorescence decays of **5'-Atto565** in different solvents and the corresponding exponential fits. a) Top: fluorescence decay of **5'-Atto565** in PBS buffer, black; instrument response function, red; mono-exponential fit, green. Bottom: residues after the fit. The residues for each of the compounds are randomly scattered around the axis *y* = 0 without an apparent pattern, indicating the presence of a single fluorescence decay. b) Fluorescence decay of **5'-Atto565** in CH_3OH, mono-exponential fit and residues after the fit.

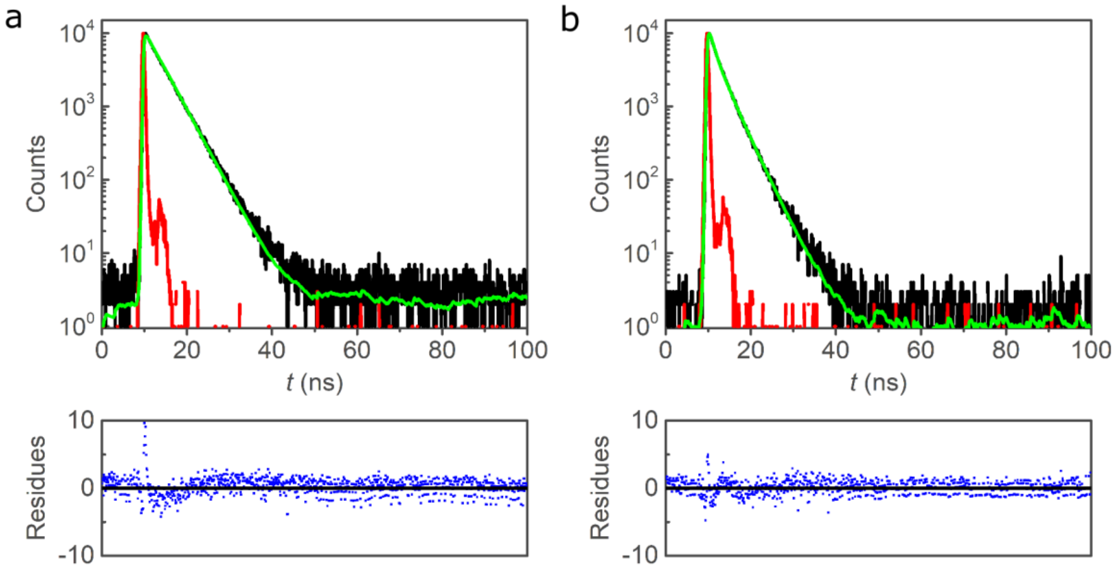

Figure 4-22 The fluorescence decays of **Dyad 3** in different solvents and the corresponding exponential fits. a) Top: fluorescence decay of **Dyad 2** in PBS buffer, black; instrument response function, red; mono-exponential fit, green. Bottom: residues after the fit. The residues for each of the compounds are randomly scattered around the axis *y* = 0 without an apparent pattern, indicating the presence of a single fluorescence decay. b) Fluorescence decay of **Dyad 2** in CH_3OH, bi-exponential fit and residues after the fit.

4.8.3 Re-absorption corrected absolute fluorescence quantum yields

The absolute fluorescence quantum yields were measured using a SC-30 integrating sphere module (Edinburgh Instruments) and the re-absorption effect was corrected when possible. For the dyes and dyads with fluorescence quantum yields above 10%, the excitation wavelength was 520 nm, the wavelength step size 0.1 nm, and integration time

0.2 s. Three scans were repeated for both the sample solution and the solvent (example see **Figure 4-23**a). The scattering region between 512 and 528 nm, and emission region between 540 and 770 nm were chosen for the calculation of the observed quantum yields.

Due to the low fluorescence quantum yields of **SO** and **Dyads 2-4** in PBS, the scattering spectra centred around the maximum absorbance were measured with a neutral density filter behind the excitation monochromator to protect the detector, and the emission spectra were obtained separately in a standard way.

The above procedures give the observed quantum yields, but the true fluorescence quantum yields might be higher due to re-absorption of dyes with a significant spectral overlap between absorption and emission. Practically, the emission spectrum of the sample is measured in both the standard fluorescence module and the integrating sphere. Once the tails of the two spectra are normalised (**Figure 4-23**b), the difference in the areas is calculated, denoted as *a* = (true em./obs. em. – 1), the fraction reduced by re-absorption. The re-absorption corrected fluorescence quantum yield is then calculated using the formula, $\mathrm{QY}^{\mathrm{true}} = \frac{\mathrm{QY}^{\mathrm{obs}}}{1-a+a*\mathrm{QY}^{\mathrm{obs}}/100}$. For highly fluorescent dyes, e.g. **Atto565** and the dyads in organic solvents, the re-absorption corrected fluorescence absolute quantum yields are only slightly higher than the uncorrected values. In contrast, it was impossible to acquire the values for other weakly fluorescent compounds like the dyads in PBS because of difficulties in getting sensible *a* values due to their weak emission.

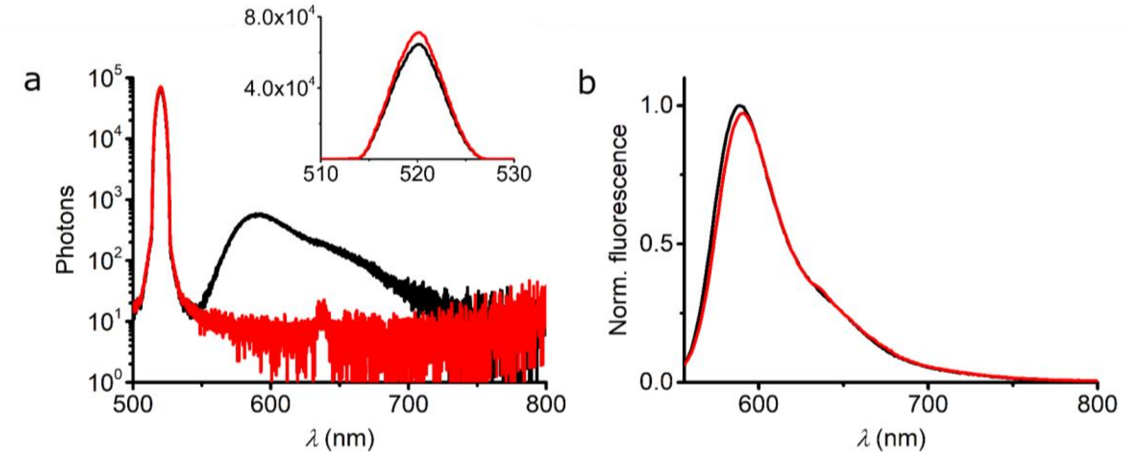

Figure 4-23 Representative spectra used in the calculation of the absolute fluorescence quantum yield. a) Spectra used in the calculation of the observed quantum yield using an integrating sphere, *y*-axis displayed on a logarithmic scale. PBS solution of **5'-Atto565**, black; PBS blank solvent, red. The inset is the zoom-in in the scattering region, *y*-axis displayed in the linear scale for clarity. b) Normalised fluorescence spectra using a standard fluorescence module (black) and an integrating sphere (red), and the percentage of the area difference *a*, caused by re-absorption, was used to calculate the absorption-corrected absolute quantum yield.

4.8.4 FRET efficiency (E) calculations

The following equations were used:[11]

$$E = \frac{1}{1 + (^{r}/_{R_0})^6} \qquad (1)$$

$$R_0 = 0.2108\left[\frac{\kappa^2 \Phi_{\mathrm{D}} J(\lambda)}{n^4}\right]^{\frac{1}{6}} \qquad (2)$$

$$J(\lambda) = \int F_{\mathrm{D}}(\lambda)\varepsilon_{\mathrm{A}}(\lambda)\lambda^4 d\lambda \qquad (3)$$

where r is the distance between the donor and acceptor, R_0 is the Förster radius (distance at which the energy transfer efficiency is 50%), κ^2 is the dipole orientation factor (assumed to be 2/3 given free rotation between the donor and acceptor),[12] Φ_{D} is the fluorescence quantum yield of the donor in the absence of the acceptor (80%), n is the refractive index of the solvent (1.34 for PBS buffer), $J(\lambda)$ is the spectral overlap integral based on the data of **Figure 4-3**, F_{D} is the fluorescence intensity of the donor (in PBS) after the total intensity is normalised to 1, ε_{A} is the acceptor molar absorption coefficient (in cyclohexane), and λ is the wavelength. Because the spectrum of **SO(open)** in PBS is unavailable due to the rapid thermal recovery, we choose the **SO(open)** form in cyclohexane instead to calculate the spectral overlap (**Figure 4-3**). The calculated Förster radius is 66.4 Å for the dyads.

The distance between the switch and dye in **Dyad 2** was simulated by optimising the molecular geometry in HyperChem with a molecular mechanics calculation in an MM$^+$ force field (**Figure 4-2**). With a distance of max. 15.4 Å and min. 6.8 Å, the FRET efficiency is ca. 100% for both the cases.

4.8.5 Cell culture and staining procedures

4.8.5.1 Live-cell imaging

Human embryonic kidney cells (HEK 293 from ATCC, Manassas, VA, USA) were cultured and stained with the dyad in the same way as described in Chapter 2 Experimental section. The cells were imaged at 37 °C.

4.8.5.2 Fixed-cell imaging

Live HEK cells were fixed using either MeOH or 3% aqueous PFA solution. The fixed cells were mounted in either Mowiol or PBS buffer. The cells were imaged at ambient temperature.

4.8.6 Optical microscopy

4.8.6.1 Confocal imaging on Zeiss microscope

Confocal images were acquired on a Zeiss confocal laser scanning microscope (Zeiss LSM 780 inverted confocal microscope), using a 63x/1.4 numerical aperture oil immersion objective lens (Plan-Apochromat 63x/1.4 Oil, Zeiss, Germany). The microscope was operated with Zen software. The light sources were 594 nm (HeNe, 84 μW at 100%), 561 nm (diode, 920 μW at 100%) and 405 nm (diode, 815 μW at 100%).

4.8.6.2 Confocal imaging on RESOLFT microscope

The imaging was performed in the confocal mode of a RESOLFT microscope that was modified from a commercial Abberior STED microscope (Eggeling group, Weatherall Institute of Molecular Medicine, University of Oxford). A 100 x/1.4 numerical aperture oil immersion objective lens (UPlanSApo 100x/1.4 oil, Olympus, Japan) was used. The light sources were 405 nm (Cobolt diode laser, CW), and 594 nm (PDL594, Abberior, pulsed). The microscope was operated with Imspector software (Abberior Instruments).

The data were processed in ImageJ (Fiji software).

4.9 Synthetic procedures

3-Carboxy-4-(1,11-diethyl-3,4,8,9,10,11-hexahydro-2*H*-pyrano[3,2-*g*:5,6-*g'*]diquinolin-1-ium-6-yl)benzoate, chloride salt (5'-Atto565) and 4-carboxy-3-(1,11-diethyl-3,4,8,9,10,11-hexahydro-2*H*-pyrano[3,2-*g*:5,6-*g'*]diquinolin-1-ium-6-yl)benzoate (6'-Atto565), chloride salt[13] (synthesis modified from[14])

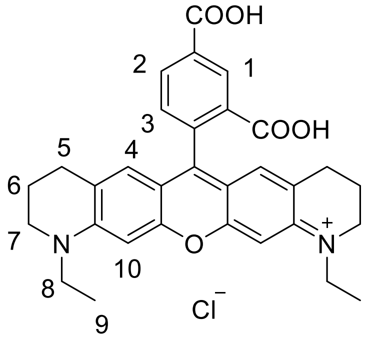

5'-Atto 565

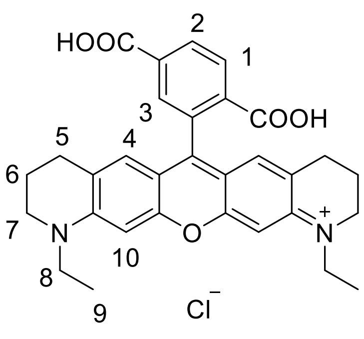

6'-Atto 565

1-Ethyl-1,2,3,4-tetrahydroquinolin-7-ol[15] (2.32 g, 13.1 mmol) and trimellitic anhydride (1.26 g, 6.54 mmol) were dissolved in butyric acid (100 mL), and conc. H_2SO_4 (50 μL) was added. The mixture was heated to 164 °C for 28 h, and the solvents were removed by vacuum distillation to generate a dark purple gum. Separation of the regioisomers was achieved by silica gel chromatography (1.5:5:93.5 to 3:15:82 $NEt_3/CH_3OH/CH_2Cl_2$).

Each of the resulting bands was dissolved in 10% ^{i}PrOH/CHCl$_3$, washed with 3 M aqueous HCl solution and H$_2$O, dried over Na$_2$SO$_4$, and the solvents were removed *in vacuo*. The solids were further purified by recrystallisation from warm CHCl$_3$.

5'-Atto565, 706 mg, yield: 20%.

R_f (SiO$_2$, 3:10:87 NEt$_3$/CH$_3$OH/CH$_2$Cl$_2$) = 0.15. ^{1}H NMR (400 MHz, CD$_3$OD) δ (ppm): 8.91 (d, *J* = 1.6 Hz, 1H, H1), 8.42 (dd, *J* = 7.6, 1.6 Hz, 1H, H2), 7.49 (d, *J* = 7.6 Hz, 1H, H3), 6.93 (s, 2H, H10), 6.74 (s, 2H, H4), 3.67 (q, *J* = 7.1 Hz, 4H, H8), 3.58 (t, *J* = 5.6 Hz, 4H, H7), 2.69 (t, *J* = 6.2 Hz, 4H, H5), 1.99–1.89 (m, 4H, H6), 1.33 (t, *J* = 7.2 Hz, 6H, H9). HRMS (ESI +ve) *m*/*z*: 511.22287 ([M-Cl]$^+$, C$_{31}$H$_{31}$O$_5$N$_2$ requires 511.22275). UV-vis (PBS) λ_{max} / nm (ε / M^{-1} cm^{-1}) 564 (1.8 × 10^5). Fluorescence emission (PBS) λ_{max} / nm (Φ_f): 589 (80%). UV-vis (CH$_3$OH) λ_{max} / nm (ε / M^{-1} cm^{-1}) 554 (1.7 × 10^5). Fluorescence emission (CH$_3$OH) λ_{max} / nm (Φ_f): 578 (85%).

6'- Atto565, 1.00 g, yield: 28%.

R_f (SiO$_2$, 3:10:87 NEt$_3$/CH$_3$OH/CH$_2$Cl$_2$) = 0.25. ^{1}H NMR (400 MHz, CD$_3$OD) δ (ppm): 8.44–8.37 (2nd order, 12H, H1, H2), 7.93 (d, *J* = 0.9 Hz, 1H, H3), 6.93 (s, 2H, H10), 6.75 (s, 2H, H4), 3.67 (q, *J* = 7.1 Hz, 4H, H8), 3.58 (t, *J* = 5.6 Hz, 4H, H7), 2.70 (t, *J* = 6.2 Hz, 4H, H5), 1.99–1.89 (m, 4H, H6), 1.34 (t, *J* = 7.2 Hz, 6H, H9). HRMS (ESI +ve) *m*/*z*: 511.22260 ([M-Cl]$^+$, C$_{31}$H$_{31}$O$_5$N$_2$ requires 511.22275). UV-vis (PBS) λ_{max} / nm (ε / M^{-1} cm^{-1}) 564 (1.8 × 10^5). Fluorescence emission (PBS) λ_{max} / nm (Φ_f): 586 (79%). UV-vis (CH$_3$OH) λ_{max} / nm (ε / M^{-1} cm^{-1}) 552 (1.9 × 10^5). Fluorescence emission (CH$_3$OH) λ_{max} / nm (Φ_f): 575 (83%). UV-vis (CH$_2$Cl$_2$) λ_{max} / nm (ε / M^{-1} cm^{-1}) 566 (1.2 × 10^5). Fluorescence emission (CH$_2$Cl$_2$) λ_{max} / nm (Φ_f): 584 (73%).

1,11-Diethyl-6-(4-((2-(6'-(indolin-1-yl)-1,3,3-trimethylspiro[indoline-2,3'-naphtho[2,1-*b*][1,4]oxazine]-5-carboxamido)ethyl)carbamoyl)-2-(methoxycarbonyl)phenyl)-3,4,8,9,10,11-hexahydro-2*H*-pyrano[3,2-*g*:5,6-*g'*]diquinolin-1-ium trifluoroacetate (Dyad 2)

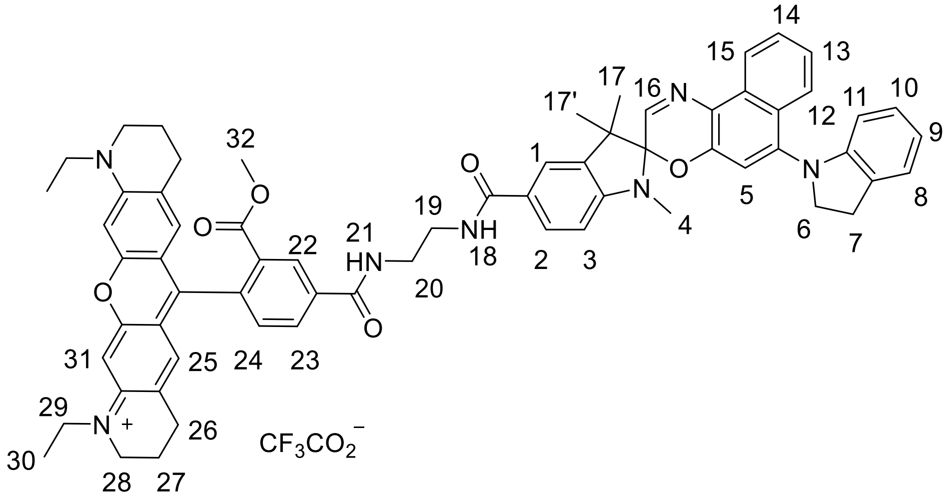

6-(2,4-Dicarboxyphenyl)-1,11-diethyl-3,4,8,9,10,11-hexahydro-2*H*-pyrano[3,2-*g*:5,6-*g'*]diquinolin-1-ium chloride (**5'-Atto565**) (12 mg, 23 μmol) was dissolved in dry DMF (2.0 mL) and HBTU (17 mg, 45 μmol) was added. After stirring for 2 min at room temperature, *N*-Boc-ethylenediamine (0.19 mL, 58 μmol) and triethylamine (40 μL, 0.29 mmol) were added. The mixture was stirred for another 10 min, and the reaction was monitored by TLC. After consumption of the starting material, the solvent was distilled off *in vacuo* using a short path distillation setup. The crude product was purified by silica gel chromatography (3:10:87 $NEt_3/CH_3OH/CH_2Cl_2$). The compound (16 mg) was slightly impure and consequently the yield was later reported over 3 steps.

The compound above (8.0 mg, 11 μmol) was stirred in a 1:1 mixture of CH_2Cl_2 and TFA for 2 h at room temperature. A crude NMR confirmed the Boc-deprotected compound. In the meanwhile, 6'-(indolin-1-yl)-1,3,3-trimethylspiro[indoline-2,3'-naphtho[2,1-*b*][1,4]oxazine]-5-carboxylic acid (**14**) (3.5 mg, 7.2 μmol) was dissolved in dry DMF (1.0 mL) and HBTU (6.3 mg, 17 μmol) was added. After 5 min of stirring, the amine solution was added followed by addition of triethylamine (40 μL, 0.29 mmol). The reaction was monitored by TLC (3:17 CH_3OH/CH_2Cl_2). CH_3OH was added and after complete consumption of the starting material, the solvent was distilled off *in vacuo* using a distillation apparatus, and the crude product was purified by silica gel chromatography (3:10:87 $NEt_3/CH_3OH/CH_2Cl_2$). Further purification was carried out using RP-HPLC (method B) to afford the product as a pink solid (1.2 mg, 16%). ^{1}H NMR (500 MHz, $CDCl_3$) δ (ppm): 8.73 (d, *J* = 1.8 Hz, 1H, H22), 8.53 (d, *J* = 8.4 Hz, 1H, H15), 8.19 (dd, *J* = 7.9, 1.8 Hz, 1H, H23), 7.87 (d, *J* = 8.5 Hz, 1H, H12), 7.82 (dd, *J* = 8.3, 1.8 Hz, 1H, H2), 7.65 (d, *J* = 1.8 Hz, 1H, H1), 7.60 (s, 1H, H16), 7.57 (br. s, 1H, H21), 7.54–7.49 (m, 1H, H14), 7.30–7.25 (m, 1H, H13), 7.23 (d, *J* = 7.8 Hz, 1H, H24), 7.18 (overlapped with solvent, 1H, H18), 7.10 (d, *J* = 7.1 Hz, 1H, H8), 6.83 (t and s overlapped, 2H, H5, H10), 6.65 (m and s overlapped, 3H, H9, H31), 6.60 (s, 2H, H25), 6.51 (d, *J* = 8.2 Hz, 1H, H3), 6.20 (d, *J* = 8.0 Hz, 1H, H11), 3.85 (br. s, 2H, H6), 3.79–3.70 (m, 5H, H19, H20), 3.64 (s, 3H, H32), 3.54–3.45 (m, 4H, H29), 3.45–3.49 (m, 5H, H28), 3.12 (br. s, 4H, H7), 2.72 (s, 3H, H4), 2.67–2.57 (m, 4H, H26), 1.91–1.83 (m, 4H, H27), 1.29–1.13(overlapped, 38 H, H17, H17’, H30). LRMS (MALDI) *m*/*z*: 1038.85, ($[M-CF_3CO_2]^+$, $C_{65}H_{64}O_6N_7$ requires 1038.85). Analytical HPLC (method A), t_R = 20.7 min. UV-vis (PBS) λ_{max} / nm (ε / M^{-1} cm^{-1}) 576 (6.8×10^4). Fluorescence emission (PBS) λ_{max} / nm (Φ_f): 598 (3.6%). UV-vis (CH_3OH) λ_{max} / nm (ε / M^{-1} cm^{-1}) 566 (1.1×10^5). Fluorescence emission (CH_3OH) λ_{max} / nm (Φ_f): 591 (33%). UV-vis (CH_2Cl_2) λ_{max} / nm (ε / M^{-1} cm^{-1}) 567 (1.2×10^5). Fluorescence emission (CH_2Cl_2) λ_{max} / nm (Φ_f): 587 (48%).

6-(5-((2-((*tert*-Butoxycarbonyl)amino)ethyl)carbamoyl)-2-carboxyphenyl)-1,11-diethyl-3,4,8,9,10,11-hexahydro-2*H*-pyrano[3,2-g:5,6-*g'*]diquinolin-1-ium chloride (6’-Atto565-C2linker)

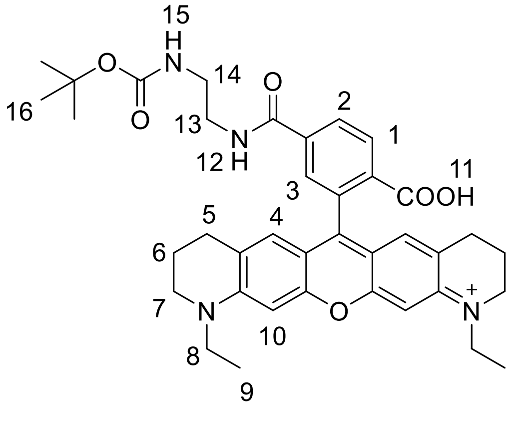

6-(2,5-Dicarboxyphenyl)-1,11-diethyl-3,4,8,9,10,11-hexahydro-2*H*-pyrano[3,2-g:5,6-*g'*]diquinolin-1-ium chloride (**6’-Atto565**) (130 mg, 0.24 mmol) was dissolved in dry DMF (5.0 mL), and triethylamine (83 µL, 0.6 mmol) and HBTU (99 mg, 0.26 mmol) were added. After stirring for 2 min at room temperature, a DMF (5.0 mL) solution of *N*-Boc-ethylenediamine (38 µL, 0.24 mmol) and triethylamine (83 µL, 0.6 mmol) was added. The reaction mixture was stirred for 30 min before being quenched with H_2O (1 mL). The solvents were removed under strong N_2 flow at 40 °C. The crude product was purified by silica gel chromatography (1:9 CH_3OH/CH_2Cl_2) to yield a pink solid (82 mg, 32%). ^{1}H NMR (500 MHz, $CDCl_3$) δ (ppm): 8.19 (d, *J* = 8.1 Hz, 1H, H1), 7.96 (d, *J* = 8.0 Hz, 1H, H2), 7.72 (br. s, 1H, H15), 7.63 (s, 1H, H3), 6.66 (s, 2H, H10), 6.50 (s, 2H, H4), 5.26 (t, *J* = 6.0 Hz, 1H, H12), 3.55–3.27 (overlapped, 13H, H7, H8, H13, H14), 2.70–2.51 (m, 4H, H5), 1.96–1.81 (m, 4H, H6), 1.38 (s, 9H, H16), 1.25 (t, *J* = 7.0 Hz, 8H, H9). HRMS (ESI +ve) *m*/*z*: 653.33307 ([M-anion]$^+$, $C_{38}H_{45}O_6N_4$ requires 653.33336).

6-(2-Carboxy-4-((2-(6'-(indolin-1-yl)-1,3,3-trimethylspiro[indoline-2,3'-naphtho[2,1-*b*][1,4]oxazine]-5-carboxamido)ethyl)carbamoyl)phenyl)-1,11-diethyl-3,4,8,9,10,11-hexahydro-2*H*-pyrano[3,2-*g*:5,6-*g'*]diquinolin-1-ium acetate (Dyad 3)

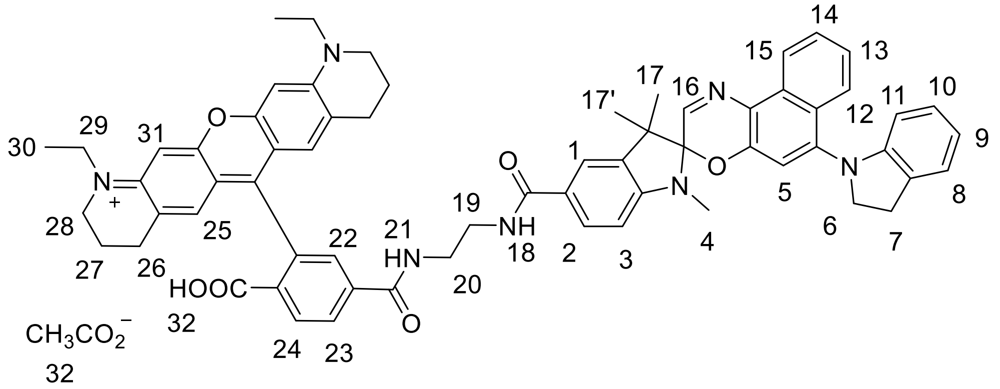

6-(5-((2-((*tert*-Butoxycarbonyl)amino)ethyl)carbamoyl)-2-carboxyphenyl)-1,11-diethyl-3,4,8,9,10,11-hexahydro-2*H*-pyrano[3,2-*g*:5,6-*g'*]diquinolin-1-ium chloride (**6'-Atto565-C2linker**) (7.7 mg, 14 μmol) was stirred in a 1:1 mixture of CH_2Cl_2 and TFA for 2 h at room temperature. A crude NMR confirmed the Boc-deprotected compound. At the same time, 6'-(indolin-1-yl)-1,3,3-trimethylspiro[indoline-2,3'-naphtho[2,1-*b*][1,4]oxazine]-5-carboxylic acid (**14**) (5.0 mg, 10 μmol) was dissolved in dry DMF (2.0 mL), DIPEA (2.7 μL, 15 μmol) and HBTU (3.9 mg, 10 μmol) was added. After 5 min of stirring, the amine solution was added with DIPEA (2.7 μL, 15 μmol). The reaction was stirred for 30 min before being quenched with H_2O (1 mL). The solvents were removed under strong N_2 flow at 40 °C. The crude product was purified by silica gel chromatography (1:10:89 $CH_3COOH/CH_3OH/CH_2Cl_2$) to yield a pink solid (5.3 mg, 51%). ^{1}H NMR (500 MHz, $CDCl_3$) δ (ppm): 8.53 (br. s and d overlapped, *J* = 8.3 Hz, 2H, H15, NH or CO_2H), 8.23 (s, 1H, NH or CO_2H), 8.02 (d, *J* = 7.7 Hz, 1H, H24), 7.93–7.86 (overlapped, 2H, H12, H23), 7.72 (d, *J* = 8.3 Hz, 1H, H2), 7.68 (s, 1H, H22), 7.59 (s, 1H, H1), 7.57–7.50 (s and ddd overlapped, *J* = 8.3, 7.0, 1.2 Hz, 2H, H14, H16), 7.28 (ddd, *J* = 8.3, 6.8, 1.3 Hz, 1H, H13), 7.12 (d, *J* = 7.3 Hz, 1H, H8), 6.89–6.83 (m, 1H, H10), 6.82 6.77 (overlapped s, 3H, H5, H31), 6.66 (ddd, *J* = 7.4, 7.4, 1.0, 1H, H9), 6.47 (d, *J* = 1.9 Hz, 2H, H25), 6.35 (d, *J* = 8.1 Hz, 1H, H3), 6.21 (d, *J* = 7.9 Hz, 1H, H11), 3.85 (br. s, 2H, H6), 3.57–3.44 (m, 4H, H19, H20), 3.38 (q, *J* = 7.2 Hz, 3H, H29), 3.29 (t, *J* = 5.1 Hz, 2H, H28), 3.10 (br. s, 2H, H7), 2.68 (s, 3H, H4), 2.60–2.42 (m, 4H, H26), 2.07 (s, 13H, H32 and CH_3CO_2H residue), 1.86–1.66 (m, 4H, H27), 1.25–1.14 (overlapped, 25H, H17, H17’, H30). HRMS (ESI +ve) *m*/*z*: 1024.47485 ([M-anion]$^+$, $C_{64}H_{62}O_6N_7$ requires 1024.47561). Analytical HPLC (method A), t_R = 20.3 min. UV-vis (PBS) λ_{max} / nm (ε / M^{-1} cm^{-1}) 571 (1.7×10^5). Fluorescence emission (PBS) λ_{max} / nm (Φ_f): 586 (5.1%). UV-vis (CH_3OH) λ_{max} / nm (ε / M^{-1} cm^{-1}) 557 (2.7×10^5). Fluorescence emission (CH_3OH) λ_{max} / nm (Φ_f): 579 (39%). UV-vis (CH_2Cl_2) λ_{max} / nm (ε / M^{-1} cm^{-1}) 566 (2.6×10^5). Fluorescence emission (CH_2Cl_2) λ_{max} / nm (Φ_f): 583 (38%).

4-((17-Amino-3,6,9,12,15-pentaoxaheptadecyl)carbamoyl)-2-(1,11-diethyl-3,4,8,9,10,11-hexahydro-2*H*-pyrano[3,2-*g*:5,6-*g*′]diquinolin-1-ium-6-yl)benzoate (18)

To a mixture of **6’-Atto565** (100 mg, 18 μmol) and HBTU (83 mg, 22 μmol) under argon was added dry DMF (3.0 mL). *tert*-Butyl (17-amino-3,6,9,12,15-pentaoxaheptadecyl)carbamate (**17**, 70 mg, 18 μmol) and DIPEA (0.29 mL, 1.6 mmol) in dry DMF (4.0 mL) was added to the above solution. The reaction mixture was stirred for 1 h before being quenched with H_2O (2 mL). The solvents were removed under N_2 flow at 40 °C. The crude product was purified by silica gel chromatography (0:1:99 to 1:10:89 $NEt_3/CH_3OH/CH_2Cl_2$) to yield a pink solid (44 mg, 31%). R_f (SiO_2, 17:3 CH_2Cl_2/CH_3OH) = 0.25. ^1H NMR (500 MHz, $CDCl_3$) δ (ppm): 8.15 (d, *J* = 8.1 Hz, 1H, H18), 8.00 (dd, *J* = 8.1, 1.7 Hz, 1H, H17), 7.65–7.56 (overlapped peaks, 2H, H16, H15), 6.59 (s, 2H, H25), 6.45 (s, 2H, H19), 3.69–3.52 (m, 22H), 3.51–3.38 (m, 8H), 3.34 (m, 4H, H22), 3.28–3.21 (m, 3H), 2.65–2.47 (m, 10H, 1 eq. NEt_3, H20), 1.94–1.79 (m, 5H, H21), 1.40 (s, 10H, H1), 1.21 (t, *J* = 7.1 Hz, 7H, H24), 1.02 (t, *J* = 7.2 Hz, 9H, NEt_3). $^{13}C\{^1H\}$ NMR (101 MHz, $CDCl_3$) δ (ppm): 169.1, 166.5, 156.1, 154.5, 150.1, 137.9, 137.0, 128.5, 128.1, 127.7, 126.0, 121.7, 109.7, 95.2, 79.1, 77.3, 70.48, 70.45, 70.3, 70.1, 70.0, 69.7, 52.7, 48.8, 46.2, 46.1, 40.3, 39.9, 28.4, 27.5, 21.4, 11.2, 10.9. HRMS (ESI +ve) *m/z*: 873.46436, ($[M+H]^+$, $C_{48}H_{65}N_4O_{11}$ requires 873.46553).

2-(1,11-Diethyl-3,4,8,9,10,11-hexahydro-2*H*-pyrano[3,2-*g*:5,6-*g'*]diquinolin-1-ium-6-yl)-4-((1-(6'-(indolin-1-yl)-1,3,3-trimethylspiro[indoline-2,3'-naphtho[2,1-*b*][1,4]oxazin]-5-yl)-1-oxo-5,8,11,14,17-pentaoxa-2-azanonadecan-19-yl)carbamoyl)benzoate (Dyad 4)

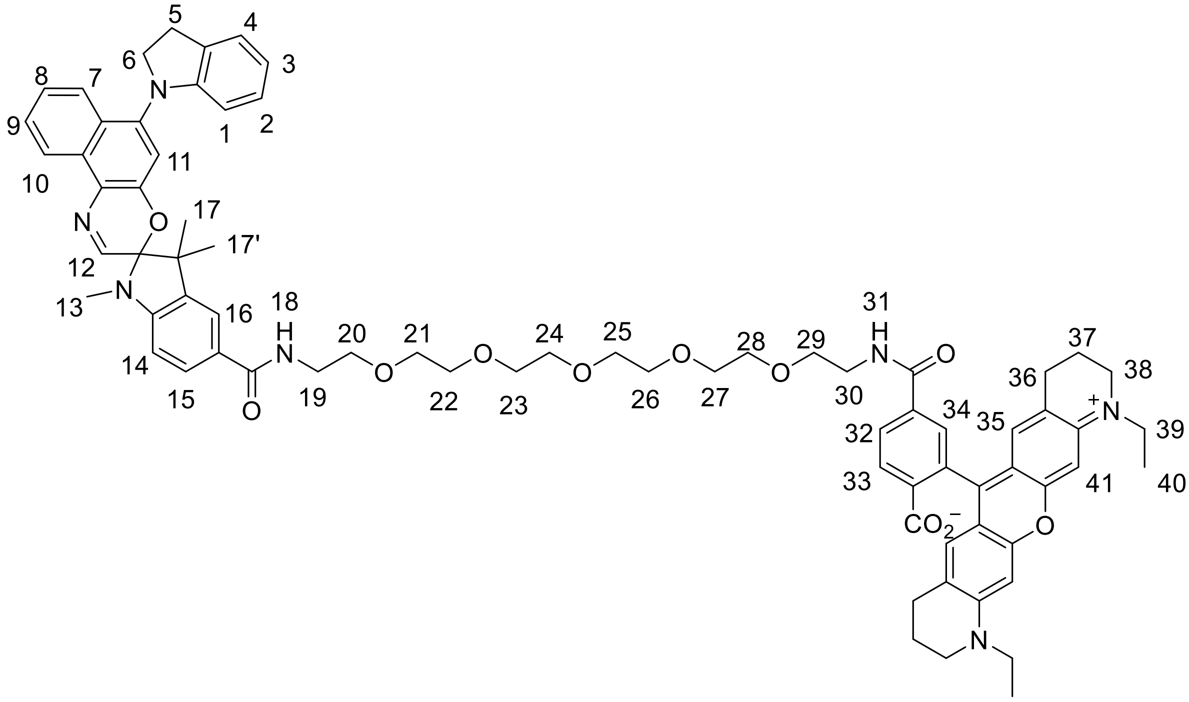

To a CH_2Cl_2 (1.0 mL) solution of 5-((2-((*tert*-butoxycarbonyl)amino)ethyl)(24-chloro-3,6,9,12,15,18-hexaoxatetracosyl)carbamoyl)-2-(1,11-diethyl-3,4,8,9,10,11-hexahydro-2*H*-pyrano[3,2-*g*:5,6-*g'*]diquinolin-1-ium-6-yl)benzoate (**18**) was added TFA (0.10 mL). The reaction was left stirring for 1 h. The solvent was removed *in vacuo*, and the deprotected product was obtained in quantitative yield.

To a mixture of 6'-(indolin-1-yl)-1,3,3-trimethylspiro[indoline-2,3'-naphtho[2,1-*b*][1,4]oxazine]-5-carboxylic acid (**14**; 3.1 mg, 6.3 μmol) and HBTU (2.4 mg, 6.3 μmol) under argon was added dry DMF (0.50 mL). Mono(6-(5-((17-ammonio-3,6,9,12,15-pentaoxaheptadecyl)carbamoyl)-2-carboxyphenyl)-1,11-diethyl-3,4,8,9,10,11-hexahydro-2*H*-pyrano[3,2-*g*:5,6-*g'*]diquinolin-1-ium) mono(2,2,2-trifluoroacetate) (deprotected **18**; 5.1 mg, 5.7 μmol) and DIPEA (9.0 μL, 52 μmol) in dry DMF (1.0 mL) were added to the above solution. The reaction mixture was stirred for 1 h before being quenched with H_2O (1 mL). The solvents were removed under N_2 flow at 40 °C. The crude product was purified by RP-HPLC (method B) to yield a pink solid (4.9 mg, 69%). ^{1}H NMR (500 MHz, $CDCl_3$) δ (ppm): 8.59 (d, J = 8.1 Hz, 1H, H10), 8.36 (overlapped d and br. s, 2H, H33, NH), 8.16 (d, J = 8.1 Hz, 1H, H32), 7.95 (d, J = 8.4 Hz, 1H, H7), 7.80 (s, 1H, H34), 7.74 (d, J = 8.1 Hz, 1H, H15), 7.68–7.64 (overlapped peaks, 2H, H12, H16), 7.60 (ddd, J = 8.4, 6.8, 1.2 Hz, 1H, H9), 7.49 (br. s, 1H, NH), 7.35 (ddd, J = 8.3, 6.8, 1.3 Hz, 1H, H8), 7.18 (d, J = 7.2 Hz, 1H, H4), 6.95–6.88 (overlapped peaks, 2H, H2, H11), 6.77–6.68 (overlapped peaks, 3H, H3, H41), 6.61 (s, 2H, H35), 6.51 (d, J = 8.2 Hz, 1H, H14), 6.29 (d, J = 8.0 Hz, 1H, H1), 3.92 (s, 2H, H6), 3.72–3.40 (m, 37H), 3.28–3.12 (m, 2H, H5), 2.79 (s, 3H, H13), 2.64 (m, 4H, H36), 2.03–1.84 (m, 4H, H37), 1.43–1.16 (overlapped peaks, 15H, H17, H17', H40). HRMS (ESI +ve) m/z: 1244.60559, ([M+H]$^+$, $C_{74}H_{82}N_7O_{11}$ requires 1244.60668). Analytical HPLC (method A), t_R = 20.5 min. UV-vis (PBS) λ_{max} / nm (ε / M^{-1} cm^{-1}) 571 (1.4×10^5). Fluorescence emission (PBS) λ_{max} / nm (Φ_f): 591 (6.3%). UV-vis (CH_3OH) λ_{max} / nm (ε / M^{-1} cm^{-1}) 558 (2.2×10^5). Fluorescence emission (CH_3OH) λ_{max} / nm (Φ_f): 580 (30%). UV-vis (CH_2Cl_2) λ_{max} / nm (ε / M^{-1} cm^{-1}) 563 (2.1×10^5). Fluorescence emission (CH_2Cl_2) λ_{max} / nm (Φ_f): 582 (28%).

4.10 References

[1] Y. Xiong, A. Vargas Jentzsch, J. W. M. Osterrieth, E. Sezgin, I. V. Sazanovich, K. Reglinski, S. Galiani, A. W. Parker, C. Eggeling, H. L. Anderson, *Chem. Sci.* **2018**, *9*, 3029–3040.

[2] E. K. L. Yeow, S. M. Melnikov, T. D. M. Bell, F. C. De Schryver, J. Hofkens, *J. Phys. Chem. A* **2006**, *110*, 1726–1734.

[3] A. V. Metelitsa, C. Coudret, J. C. Micheau, N. A. Voloshin, *RSC Adv.* **2014**, *4*, 20974–20983.

[4] X. Li, C. Li, S. Wang, H. Dong, X. Ma, D. Cao, *Dyes Pigments* **2017**, *142*, 481–490.

[5] B. Roubinet, M. L. Bossi, P. Alt, M. Leutenegger, H. Shojaei, S. Schnorrenberg, S. Nizamov, M. Irie, V. N. Belov, S. W. Hell, *Angew. Chem. Int. Ed.* **2016**, *55*, 15429–15433.

[6] M. Hofmann, C. Eggeling, S. Jakobs, S. W. Hell, *Proc. Natl. Acad. Sci.* **2005**, *102*, 17565–17569.

[7] T. Grotjohann, I. Testa, M. Leutenegger, H. Bock, N. T. Urban, F. Lavoie-Cardinal, K. I. Willig, C. Eggeling, S. Jakobs, S. W. Hell, *Nature* **2011**, *478*, 204–208.

[8] N. Marmé, J.-P. Knemeyer, M. Sauer, J. Wolfrum, *Bioconjug. Chem.* **2003**, *14*, 1133–1139.

[9] T. Heinlein, J.-P. Knemeyer, O. Piestert, M. Sauer, *J. Phys. Chem. B* **2003**, *107*, 7957–7964.

[10] S. Speiser, *Chem. Rev.* **1996**, *96*, 1953–1976.

[11] M. Sobieraj, K. A. Krzyśko, A. Jarmuła, M. W. Kalinowski, B. Lesyng, M. Prokopowicz, J. Cieśla, A. Gojdź, B. Kierdaszuk, *J. Mol. Model.* **2015**, *21*, 1–14.

[12] J. R. Lakowicz, *Principles of Fluorescence Spectroscopy*, Springer Science & Business Media, **2007**.

[13] “ATTO-TEC GmbH - ATTO 565,” can be found under https://www.atto-tec.com/attotecshop/product_info.php?language=en&info=p104_atto-565.html&, **2016**.
[14] M. J. Uddin, L. J. Marnett, *Org. Lett.* **2008**, *10*, 4799–4801.
[15] A. V. Anzalone, T. Y. Wang, Z. Chen, V. W. Cornish, *Angew. Chem. Int. Ed.* **2013**, *52*, 650–654.

Chapter 5

Labelling of Biomolecules

5 Labelling of Biomolecules

5.1 Introduction

In Chapter 4, we demonstrated the promising properties of spirooxazine-based dyads, e.g. strong contrast and fatigue resistance, and their potential in live cell imaging. However, these dyads did not show selective staining of a particular cellular structure. In this chapter, we address this limitation by exploiting bioconjugation techniques.

Selectively introducing probes to proteins of interest (POIs) is important for protein visualisation and manipulation in a complex cellular environment, e.g. studying protein organisation, dynamics and functions. As discussed in Chapter 1, fluorescent fusion proteins achieve absolute specificity by genetic encoding, whereas small-molecule synthetic fluorophores commonly lack specificity for a particular protein.[1,2] In recent decades, large families of fluorescent proteins have been developed, which have become indispensable and widely used tools in biological studies. Nevertheless, drawbacks such as difficult rational design, particularly of photoswitchable fluorescent proteins, and a small number of available colours, limit the use of this type of probe.[3,4] On the other hand, given the advantages of high brightness, photostability and versatility of synthetic dyes, considerable research has been devoted to developing strategies for attaching them to POIs.

The earliest approach is immunolabelling, where a synthetic dye is attached to POIs by relying on interactions of high specificity and affinity between antigens and antibodies.[5] The antigen is the target protein, to which an antigen-specific antibody has distinct recognition and binding affinity, while fluorescence comes from the antibody-conjugated dye.[6] The conjugation usually involves an electrophilic functional group on the dye, which reacts with primary amines present on the *N*-terminus and in the side-chains of lysine amino acid residues in the antibody.[7] One of the most popular electrophilic functional groups is the *N*-hydroxysuccinimide ester (NHS ester), which readily reacts with primary amines under physiological or slightly alkaline conditions to form an amide bond (**Scheme 5-1**).[7]

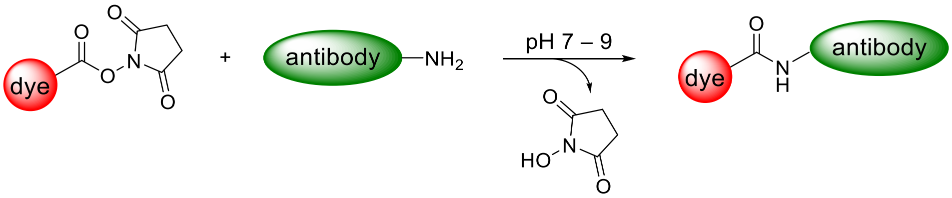

Scheme 5-1 Reaction of an *N*-hydroxysuccinimide ester (NHS ester) and a primary amine as a common means of conjugating a dye to an antibody.

Immunolabelling can be classified as either 'direct' or 'indirect' (**Figure 5-1**). The direct method conjugates a fluorescent dye directly to a primary antibody that selectively binds to an antigen, whereas the indirect method uses a dye-conjugated secondary antibody which exhibits specific binding to primary antibodies from a particular animal species, and the primary antibody binds to a specific target antigen.[6]

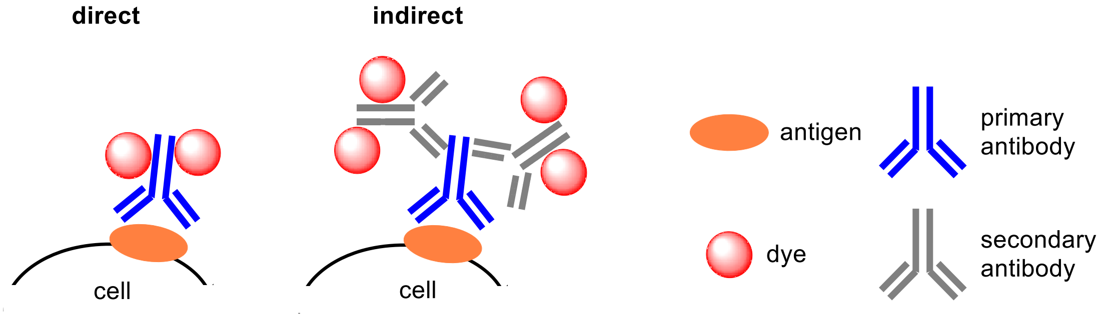

Figure 5-1 Schematic representation of direct and indirect immunolabelling methods. In the direct method, a dye-containing antibody directly binds to an antigen. In the indirect method, a dye is conjugated to a secondary antibody, the secondary antibody binds to a primary antibody and the primary antibody binds to the target antigen. Specificity of immunolabelling arises from interactions between antigens and antigen-specific antibodies.

Indirect immunolabelling is more widely used due to two main advantages: firstly, it is more sensitive because fluorescence signals amplify as multiple dye-decorated secondary antibodies can bind to one primary antibody; secondly, it is more flexible because the same secondary antibody can be used to detect different primary antibodies (from the same species) and thus different POIs.[8] While immunolabelling is a widespread technique, it is generally restricted to fixed and permeabilised cells or extracellular proteins due to the large size of antibodies (ca. 150 kDa) which often cannot be internalised by a living cell.[1,9]

For live-cell labelling of POIs with a small-molecule synthetic dye, the general strategy is to genetically express a protein tag fused to a target protein. Specific labelling is achieved by interactions (covalent or non-covalent) of the fusion protein tag and a tag-binding ligand that is appended to the dye.[4] This combines specificity inherited from genetic encoding of protein tags, and diversity of properties and functionalities provided by synthetic chemistry.[10,11] A variety of approaches have been developed and reviewed elsewhere.[4,10–14] Here we focus on what is categorised as the self-labelling tag strategy, where protein tags show unique reactivities towards electrophilic ligands to form covalent bonds.[10] The most common examples include a) FlAsH[15] and ReAsH,[16] in which a biarsenical containing fluorescein, i.e. FlAsH-EDT$_2$ (fluorescein arsenical helix binder, bis-EDT adduct), reacts specifically with a tetracysteine-containing peptide and becomes fluorescent once the adduct is formed (example of FlAsH in **Figure 5-2**a); b) hAGT-tag[17] and its variants, SNAP-tag[18] and CLIP-tag,[19] which are human O^6-alkylguanine-DNA alkyltransferases (hAGT) and react with benzylguanine derivatives (hAGT, SNAP-tag ligands; **Figure 5-2**b) or benzylcytosine derivatives (CLIP-tag ligands); c) Halo-tag,[20] which is a dehalogenase fusion protein and reacts with ligands containing a chloroalkane unit (**Figure 5-2**c).

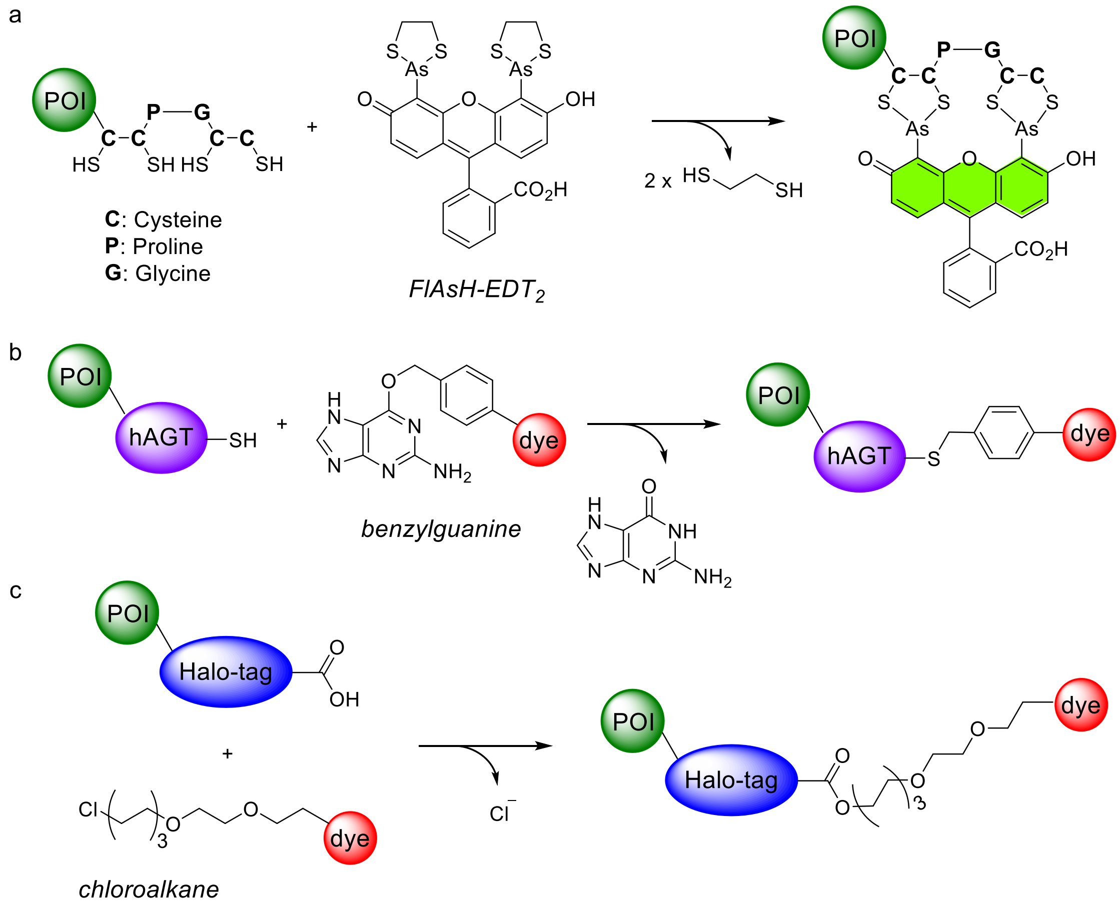

Figure 5-2 Self-labelling tag strategies by covalent attachment of a small-molecule dye to a genetically expressed protein tag that is fused to proteins of interest (POIs). a) FlAsH technique. A tetracysteine motif in the protein reacts with a biarsenical compound, e.g. FlAsH-EDT$_2$, and the latter becomes fluorescent once the adduct is formed. FlAsH-EDT$_2$ stands for fluorescein arsenical helix binder, bis-EDT adduct. b) hAGT, SNAP and CLIP-tag techniques. A human O^6-alkylguanine-DNA alkyltransferase (hAGT) that is fused to POIs reacts with benzylguanine derivatives (hAGT, SNAP-tag ligands) or benzylcytosine derivatives (CLIP-tag ligands; not shown). c) Halo-tag technique. A dehalogenase fusion protein reacts with a chloroalkyl-functionalised dye.

In this chapter, several Halo-tag ligand triads were synthesised, and initial results of live-cell imaging were compared. Following this, we prepared an NHS ester-containing triad, and preliminary immunolabelling in fixed cells was explored.

5.2 Halo-tag ligand triads

5.2.1 Molecular design

We first considered the self-labelling tag strategies because of their capacity to label live cells. Our collaborators, the Eggeling group, were able to provide cells that are genetically encoded (i.e. transfected) to express the Halo-tag protein. Synthetically, it appeared to be simpler to incorporate a chloroalkane unit in the design, rather than more reactive biarsenical or benzylguanine/benzylcytosine units. Thus, we initially focused on the application of the Halo-tag technique. The Halo-tag is a mutated bacterial haloalkane dehalogenase which undergoes an irreversible S_N2 reaction specifically with chloroalkanes to form a stable covalent bond.[20] To incorporate this in our molecular design, we proposed a triad model, where the tag-binding ligand, i.e. the chloroalkane unit, is appended to a photoswitchable dyad that consists of a photoswitch and fluorescent dye (**Figure 5-3**).

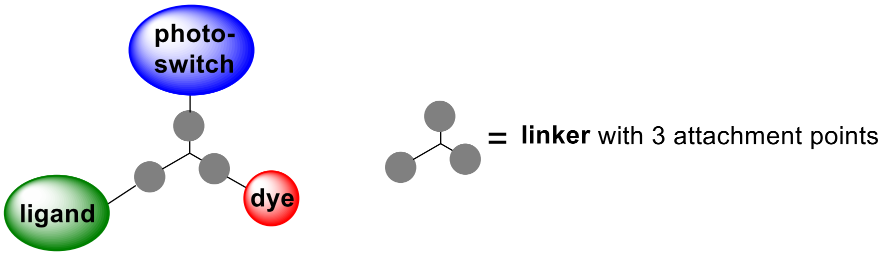

Figure 5-3 Design of a triad for live-cell imaging based on self-labelling tag strategies. The triad comprises a photoswitch, a fluorescent dye and a tag-binding ligand, e.g. a chloroalkane unit as a Halo-tag ligand. The components are connected by a linker with 3 attachment points.

5.2.2 Synthesis of Triad 1

In Chapter 4, we demonstrated the potential of the spirooxazine-**Atto565** dyads in cell imaging, and hence the target **Triad 1** (**Figure 5-4**) would combine the same components with the Halo-tag ligand. In addition, we chose a commercially available lysine-derived linker, which has orthogonally protected amines to allow sequential addition of the triad components.

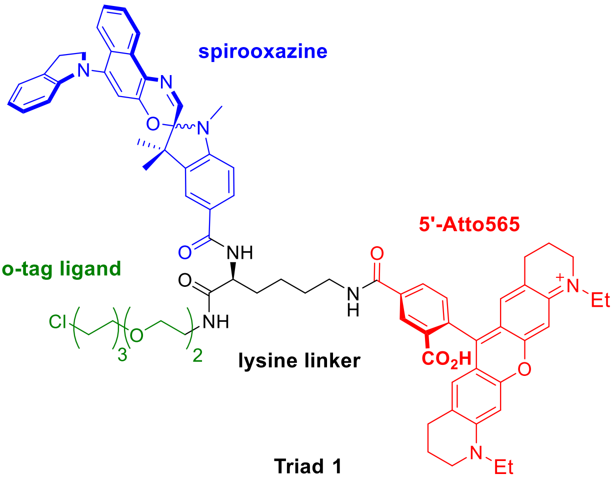

Figure 5-4 Molecular structure of **Triad 1**, which comprises a spirooxazine photoswitch, **5'-Atto565** dye, Halo-tag ligand and a lysine-derived linker.

Models of various conformations of **Triad 1** suggest a separation distance between 9.4 Å and 17.3 Å for the **Atto565** dye and the spirooxazine switch (**Figure 5-5**). Similar to the calculation of FRET efficiency in Chapter 4, the Förster radius for this pair is calculated to be 67.5 Å in CH_3OH. Thus, quantitative FRET efficiency is expected for the triad.

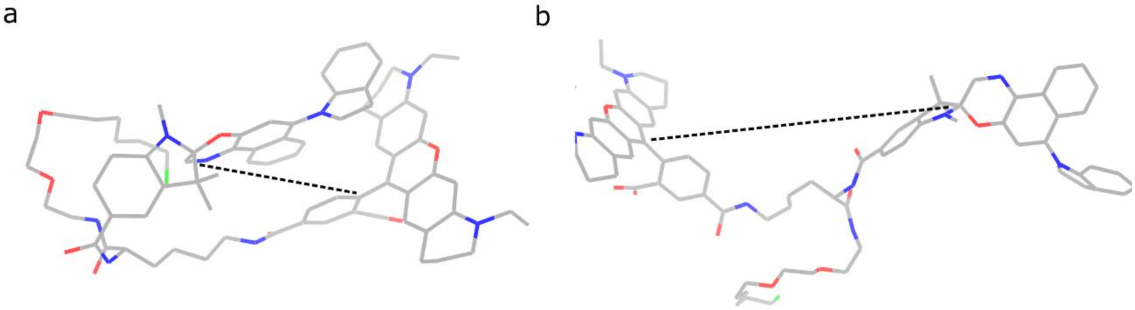

Figure 5-5 Simulated geometries for **Triad 1**. The distance between the **5'-Atto565** dye and the spirooxazine switch (dashed lines) is a) 9.4 Å, in the folded conformer. b) 17.3 Å, in the unfolded conformer. Grey, C; red, O; blue, N; green, Cl. The simulations were carried out in HyperChem using the molecular mechanics MM^+ force field.

We first prepared **Triad 1** in a total of 16 steps using a lysine-derived linker with orthogonal amine protecting groups (**Scheme 5-2**). The synthesis starts with an HBTU-promoted amide coupling of compound **20**[21–23] and commercial lysine-based linker **19** bearing Boc and Cbz protected amines to provide product **21** in 85% yield. The Cbz-protected amine in **21** was revealed by hydrogenolysis, and was then coupled to the dye **5'-Atto565** under similar HBTU-assisted coupling conditions. Analytical HPLC suggested that the desired compound **22** was the dominant product. However, the reaction mixture could not be purified using standard techniques such as silica gel chromatography and recrystallisation. Pure product **22** was eventually afforded in small quantities by subjecting a small amount of the mixture to semi-preparative RP-HPLC. The major side-product has the same *m*/*z* value to that of compound **22** by ESI mass spectrometry, and has an identical UV-vis absorption spectrum, which suggests it is the other regioisomer formed from the coupling between 3’-COOH of **5’-Atto565** and the amine. It may seem peculiar because one would expect the 3’-COOH to be more sterically hindered. This type of side-reaction has been frequently observed in our syntheses when common commercial dyes containing two carboxylic acids are used for amide couplings. With the isolation of compound **22**, Boc deprotection was carried out using TFA, and the unmasked amine was coupled to spirooxazine **14** (see Chapter 3) to afford **Triad 1** in 21% yield after semi-preparative RP-HPLC purification.

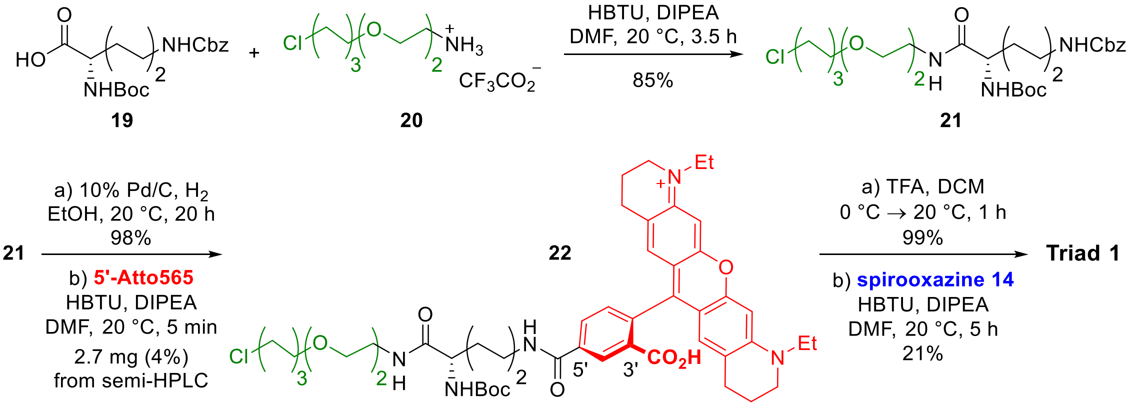

Scheme 5-2 Synthesis of **Triad 1**, during which consecutive HBTU-mediated amide coupling reactions were carried out using orthogonally-deprotected amines.

The photophysical properties of **Triad 1** in CH_3OH were analysed with reference to the starting materials. The UV-vis absorbance of **Triad 1** resembles the sum of those for the **5’-Atto565** dye and photoswitch **SO**, and the fluorescence spectrum is similar to that of **5’-Atto565** as expected (**Figure 5-6**).

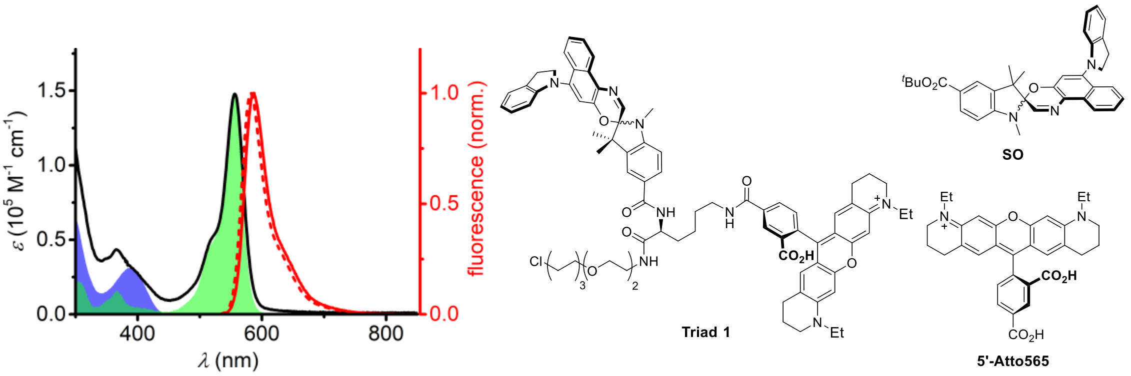

Figure 5-6 UV-vis absorption (black) and emission (red, solid line) spectra of **Triad 1** in CH_3OH. The normalised absorption of **SO** (blue) and **5'-Atto565** (green), and the emission of **5'-Atto565** (red, dotted line) in CH_3OH are also shown for comparison.

5.2.3 Cell imaging of Triad 1

The specific labelling capacity and photoswitching behaviour of **Triad 1** were investigated in live transfected cells that had been genetically encoded to express the Halo-tag protein fused to target proteins in microtubules. Microtubules are tubular structures present in the cytoplasm of cells, which, along with actin filaments and intermediate filaments, form the cytoskeleton.[24] Microtubules and actin are usually among the first choice as target structures to validate labelling specificity. Labelling of microtubules by **Triad 1** was tested on three different cell lines, i.e. human embryonic kidney (HEK 293) cells, COS-7 (monkey kidney) cells, Chinese hamster ovary (CHO) cells. While the characteristic filaments could be noticed, a strong background was observed arising from unspecific binding. The microtubule structure was most recognisable in CHO cells, but unfortunately, the switching behaviour of **Triad 1** was poor, with fluorescence quantification showing only 7% quenching efficiency (**Figure 5-7**).

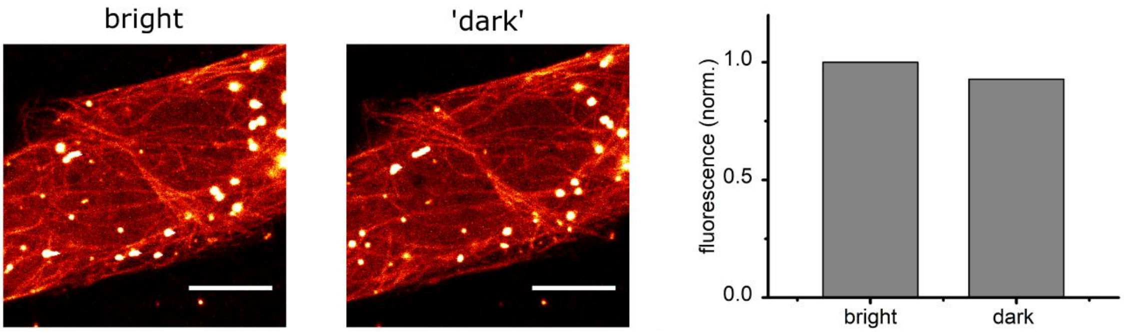

Figure 5-7 Confocal images of live transfected Chinese hamster ovary (CHO) cells stained with **Triad 1**. Target microtubules were observed, but only 7% fluorescence quenching was detected in the 'dark' state after exposure to the 405 nm laser. Scale bar: 10 μm. The images were recorded on a Zeiss LSM780 inverted confocal microscope.

In live COS-7 cells, **Triad 1** showed slightly improved fluorescence modulation upon exposure to the 405 nm laser (**Figure 5-8**). In the same field of view, bright blobs of unidentified intracellular compartments could be switched between bright and dark states with up to 28% quenching efficiency (**Figure 5-8**c), whereas the triad on the dimly labelled microtubules showed significantly worse quenching efficiency of 12% (**Figure 5-8**b).

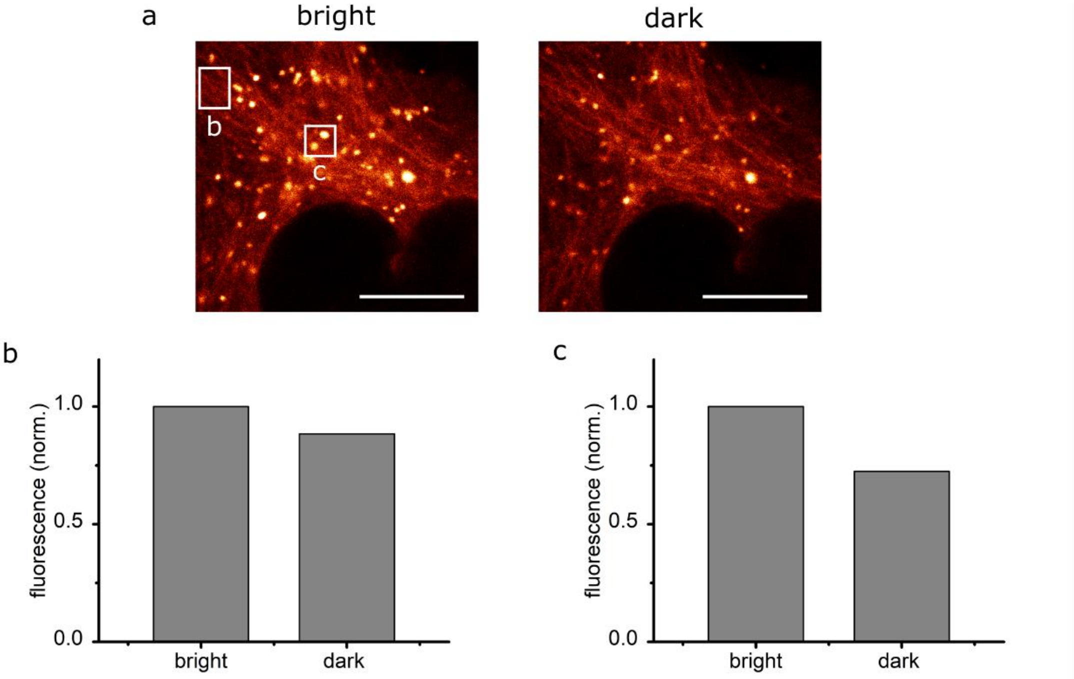

Figure 5-8 Confocal images of live transfected COS-7 cells stained with **Triad 1**. a) Target microtubules were observed. The bright state was obtained by excitation at 561 nm. The dark state was obtained by irradiation at 405 nm followed by excitation at 561 nm. Scale bar: 10 µm. b) Fluorescence quantification of **Triad 1** on target microtubules, highlighted in the box ‘b’ in a). The best quenching efficiency was 12%. c) Fluorescence quantification of **Triad 1** on blobs, highlighted in the box ‘c’ in a). The best quenching efficiency was 28%. The images were recorded on a Zeiss LSM780 inverted confocal microscope.

Among all the cell lines, the most promising imaging was recorded in live HEK 293 cells. Quantification of switching in labelled microtubules showed 25% quenching efficiency (**Figure 5-9**b), significantly higher than those observed in COS-7 and CHO cells. In the same image, bright blobs were also observed with a higher quenching efficiency (35%; **Figure 5-9**c). This result appears to be consistent with the result in COS-7 cells that **Triad 1** showed different quenching efficiencies in non-identical environments.

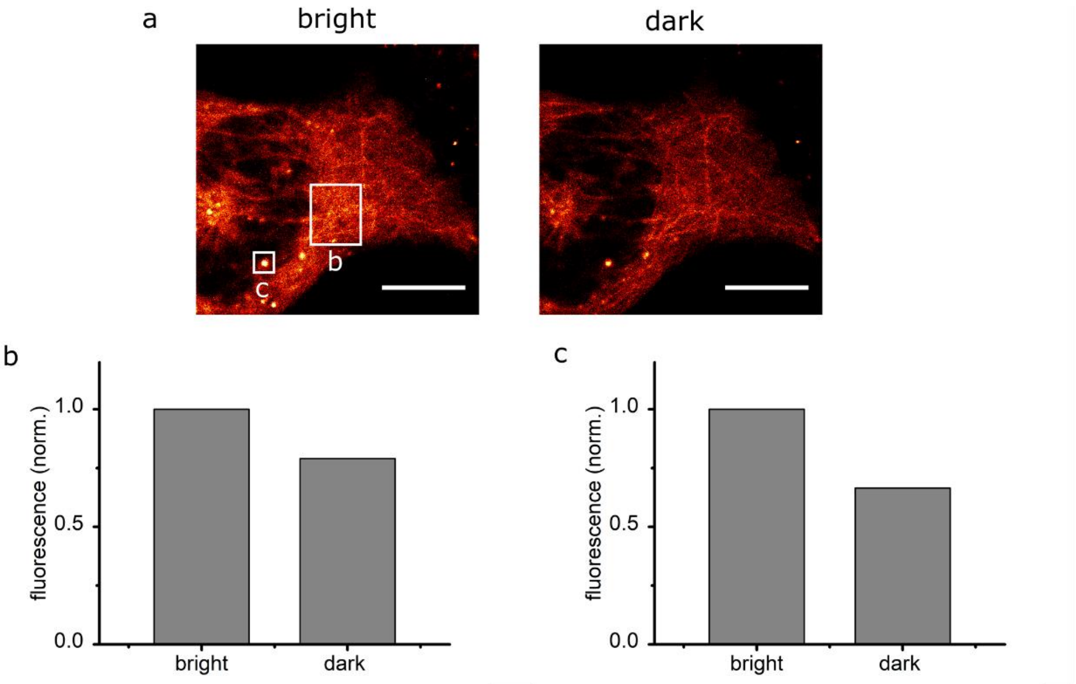

Figure 5-9 Confocal images of live transfected human embryonic kidney (HEK 293) cells stained with **Triad 1**. a) Target microtubules were observed. The bright state was obtained by excitation at 561 nm. The dark state was obtained by irradiation at 405 nm followed by excitation at 561 nm. Scale bar: 10 µm. b) Fluorescence quantification of **Triad 1** on target microtubules, highlighted in the box 'b' in a). The best quenching efficiency was 25%. c) Fluorescence quantification of **Triad 1** on blobs, highlighted in the box 'c' in a). The best quenching efficiency was 35%. The images were recorded on a Zeiss LSM780 inverted confocal microscope.

The reproducible and consistent results in different cell lines seem to suggest that once the triads are bound to the Halo-tag protein, their photoswitching behaviour deteriorates relative to that of unbound triads. One possible explanation is that the spacer between the Halo-tag ligand and the dyad is relatively short, and that once the ligand is bound, the photoswitch is located near the entrance of the binding site in a congested environment, which inhibits the photoisomerisation reaction. Furthermore, the generally poor quenching efficiencies associated with **Triad 1** are in sharp contrast to 75–85% for **Dyad 2** in live cells described in Chapter 3. One postulation is the different local environments that the dyad and the triad occupy possibly due to their hydrophobicity, and the environment for the latter impairs the performance of the switch in **Triad 1**.

5.2.4 Protein-ligand covalent docking

In order to investigate the potential issue of a short spacer, we first performed protein-ligand covalent docking simulations. The crystal structure of the Halo-tag protein (PDB: 1BN6)[25] shows that the binding pocket is narrow and deep, ca. 14–15 Å, from the surface to the reactive site where the nucleophilic substitution reaction takes place between the carboxylic acid of the *ASP106* amino acid residue and the chloroalkane unit. This suggests that the spacer length is important for the chloroalkane chain to reach the reactive site without steric hindrance from the remaining bulky group, which might explain the presence of strong background noise in the cell images of **Triad 1**, if the spacer is of an insufficient length to reach the reactive site of the Halo-tag protein.

Protein-ligand docking simulations of **Triad 1** and a hypothetical molecule with a longer spacer were performed using the GOLD programme (for details see Experimental 5.5.3). The two most likely binding arrangements for each molecule are presented in **Figure 5-10**, and the photoswitch is circled in each case. The simulations support the conjecture that with our current spacer, when the ligand successfully binds to the Halo-tag, the photoswitch is forced into a congested environment just outside the binding pocket, surrounded by amino acid side chains. By comparison, in the longer spacer analogue, the photoswitch is allowed more freedom to occupy a larger space away from the binding pocket, so is more likely to undergo the desired photoisomerisation upon exposure to illumination at 405 nm.

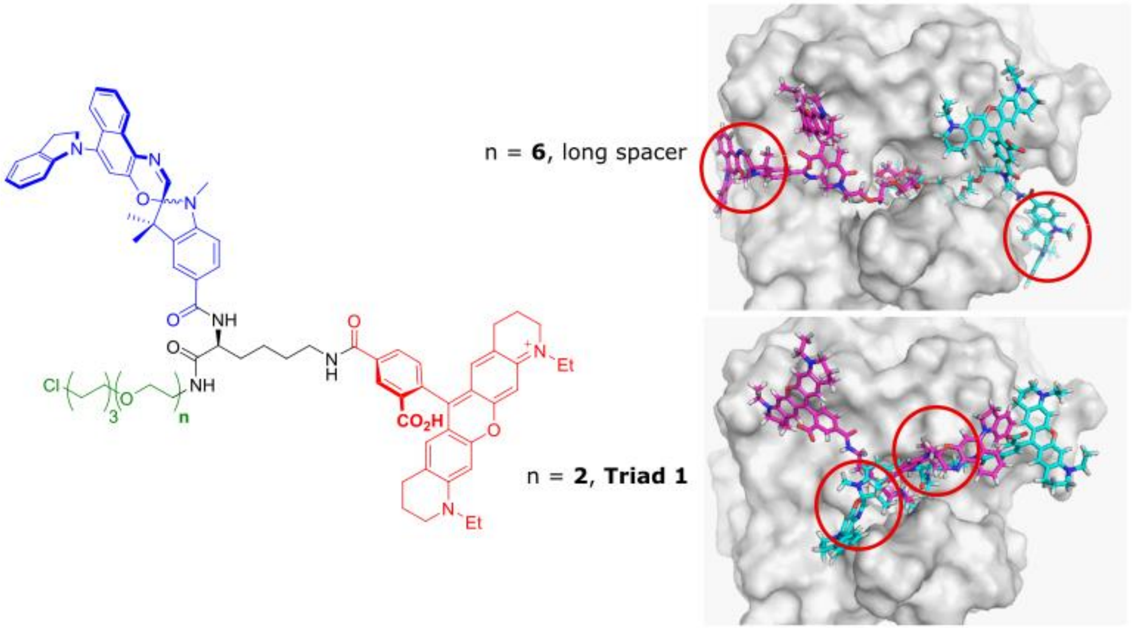

Figure 5-10 Docking simulations of **Triad 1** and a hypothetical triad with a longer spacer. Circled are photoreactive sites of the switch. On the right top are the two most likely positions that the longer-spacer triad would accommodate once the covalent bond is formed between the Halo-tag protein and the ligand. The right bottom shows the results for the short spacer analogue. The docking results imply that the ligand in the longer spacer triad may be more likely to reach the reactive site to form a covalent bond with the Halo-tag protein. Additionally, the longer spacer may allow the switch to be further away from the narrow entrance of the binding pocket, enabling the switch to photoisomerise more efficiently. The binding arrangements were simulated using protein-ligand covalent docking in the GOLD programme, and the images were generated in PyMOL.

5.2.5 Synthesis of Triad 2 with a longer spacer

Given the potential issue concerning **Triad 1**, we designed the analogous **Triad 2** with a longer spacer between the Halo-tag ligand and the dyad. The spacer is based on a polyethylene glycol (PEG) chain to increase the hydrophilicity. We expected ca. 100% FRET efficiency for **Triad 2** as for **Dyad 2** since their linkers between the **Atto565** dye and spirooxazine switch are almost the same.

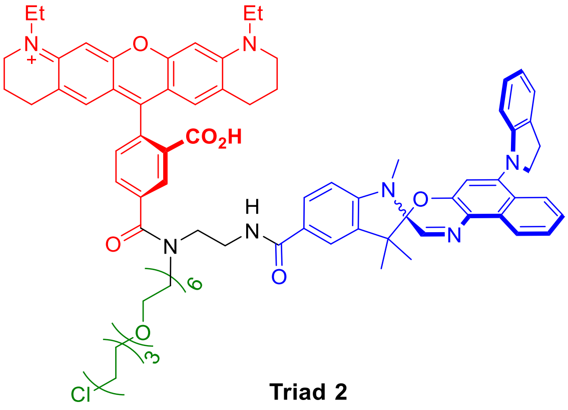

Figure 5-11 Molecular structure of **Triad 2**, an analogue of **Triad 1** with a longer spacer that is based on a polyethylene glycol (PEG) chain to separate the Halo-tag ligand and the dyad.

Triad 2 was prepared using a significantly shorter synthetic route of overall 7 steps compared to the 16-step synthesis of **Triad 1**. Starting material **24** was synthesised according to the literature procedure,[26,27] and after Boc-deprotection, it underwent reductive amination with aldehyde **23** to afford compound **25** in low yield. Subsequently, an amide coupling was carried out between the secondary amine in compound **25** and the acid in **5'-Atto565** to provide compound **26** in 51% yield. Unlike couplings with primary amines, this reaction did not proceed at room temperature, so it was carried out at 50 °C. Subsequent Boc deprotection and amide coupling with the photoswitch afforded **Triad 2** in 17% yield. The low yield may be due to the similar steric argument that 3'-COOH is accessible (though more hindered) as in the synthesis of **Triad 1**.

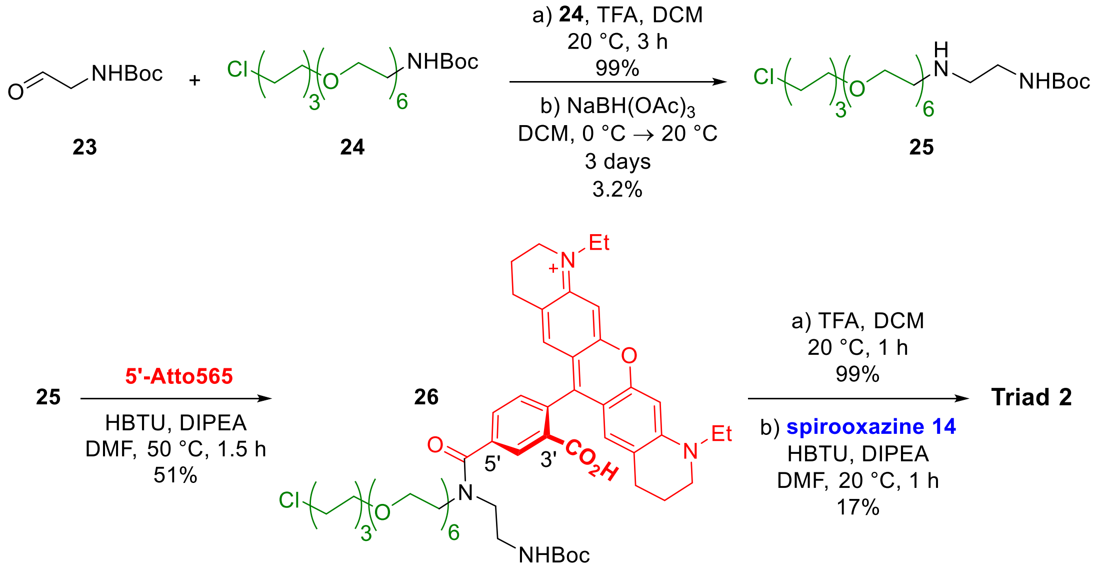

Scheme 5-3 Synthesis of **Triad 2**, in which amide couplings were carried out using primary amines and secondary amines at room temperature and elevated temperature respectively.

As expected, the photophysical properties of **Triad 2** are similar to those of **Triad 1**. In CH_3OH, the UV-vis absorption spectrum of **Triad 2** is close to the sum of those for **5'-Atto565** dye and photoswitch **SO**, and the fluorescence spectrum is similar to that of **5'-Atto565** (**Figure 5-12**).

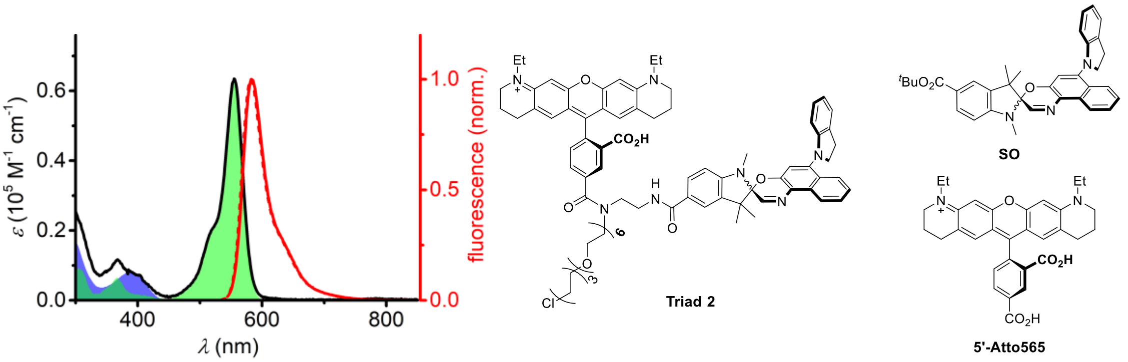

Figure 5-12 UV-vis absorption (black) and emission (red, solid line) spectra of **Triad 2** in CH_3OH. The normalised absorption of **SO** (blue) and **5'-Atto565** (green), and the emission of **5'-Atto565** (red, dotted line) in CH_3OH are also shown for comparison.

5.2.6 Cell imaging of Triad 2

As before, the properties of **Triad 2** were assessed in live transfected cells in which the Halo-tag protein fused to microtubules was expressed. Unfortunately, in both GM5756T (human fibroblast) and HEK 293 cell lines, only weak labelling of target microtubules was observed in the presence of high background noise. While **Triad 2** could hardly be switched in GM5756T cells (**Figure 5-13**), the triad underwent switching cycles in HEK 293 cells, with ca. 28% quenching efficiency (**Figure 5-14**). For **Triad 2**, we did not observe a difference in the quenching efficiency for triads in apparent microtubule structures or in bright blobs, which was different from the observation for **Triad 1**. It could be that the bright blobs stained with **Triad 1** and **Triad 2** were actually different intracellular compartments, which affect the switching in different ways.

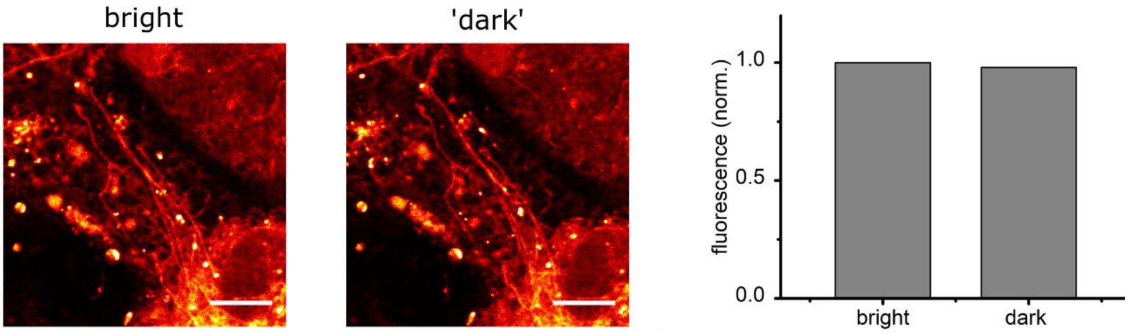

Figure 5-13 Confocal images of live GM5756T (human fibroblast) cells stained with **Triad 2**. Target microtubules were observed, but no switching behaviour was detected in the 'dark' state after exposure to the 405 nm laser. Scale bar: 10 µm. The images were recorded on a Zeiss LSM780 inverted confocal microscope.

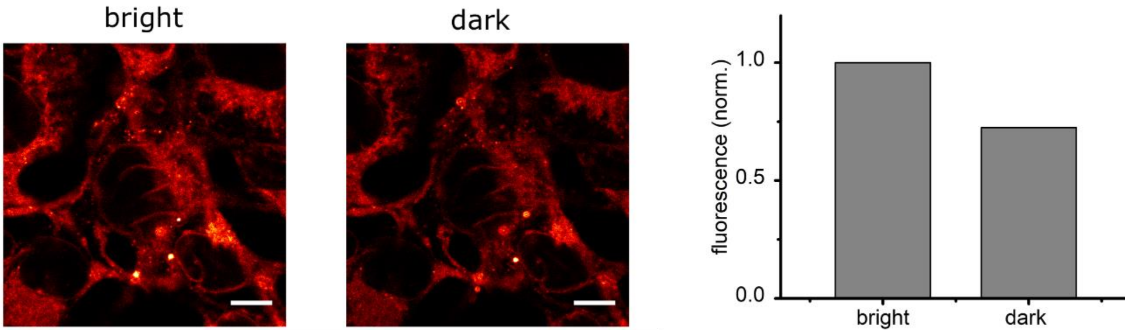

Figure 5-14 Confocal images of live HEK 293 cells stained with **Triad 2**. Target microtubules were observed, and ca. 28% quenching efficiency was detected in the dark state after exposure to the 405 nm laser. Scale bar: 10 µm. The images were recorded on a Zeiss LSM780 inverted confocal microscope.

5.2.7 Comparative analysis of Triads 1 and 2

Comparison of cell images for **Triads 1** and **2** leads to two possible conclusions. Firstly, in **Triad 2**, the PEG-based longer spacer may adopt a coiled conformation such that the effective length is similar to that in **Triad 1**. Thus, the same issue underlies the unsatisfactory outcome for both triads. It had been reported that PEG exists in coiled conformation in aqueous environments.[28,29] A second suggestion is that the hydrophobic nature of the dyad, i.e. **Atto565** dye and spirooxazine switch, dominates the localisation of the triad. For example, undesirable interactions with cellular proteins may prevent the triad from approaching and specifically binding to the Halo-tag. This probably explains the high background present in cell images for both triads. To solve the problem of an insufficiently long spacer, we may consider using a relatively rigid and long peptide chain, and manipulating hydrophilicity by different choices of amino acid residues. Regarding the second potential issue, it would be feasible to vary the choice of the fluorescent dye to counter-balance the overall hydrophilicity of the triad.

5.2.8 Synthesis of a more hydrophilic triad (Triad 3)

In order to improve hydrophilicity of our system, we prepared **Triad 3** (**Figure 5-15**), which includes a more hydrophilic dye, i.e. sulfonated Rhodamine110 (**sR110**), that is structurally closely related to commercial **Alexa488**. The **sR110** dye was prepared by Dr Andreas Vargas Jentzsch.

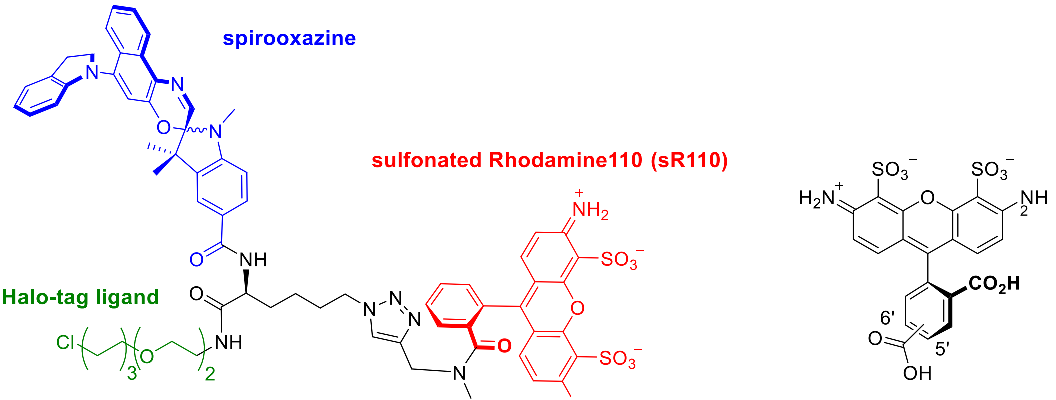

Triad 3 **Alexa488**

Figure 5-15 Molecular structure of **Triad 3**, which includes the same spirooxazine switch and Halo-tag ligand as **Triads 1** and **2**, but with a different dye, i.e. sulfonated Rhodamine 110 (**sR110**). **sR110** is our custom-made dye that is closely related to commercial **Alexa488**, and does not have a second carboxylic acid that may give side-products in amide coupling reactions.

This custom dye **sR110** was chosen based on three considerations. Firstly, it is obvious that the emission spectrum of **sR110** must have good spectral overlap with the open form of the spirooxazine switch to achieve high FRET efficiency (**Figure 5-16**). This spectral overlap is more significant than that for the **Atto565**–spirooxazine pair, but **sR110** (or **Alexa488**) has a shorter excitation wavelength, which might lead to more photodamage to cells. The fluorescence quantum yield of **sR110** was measured to be 91% in CH_3OH, and hence a Förster radius of 70.2 Å was calculated. Given the similar linkers in **Triad 1** and **Triad 3**, we assumed their dye–switch distances to be similar, i.e. < 20 Å. Hence, FRET efficiency is expected to be > 99% for **Triad 3**. In addition, the charged sulfonate groups in **sR110** impart water solubility to the triad, and they may also help to alleviate the aggregation problem previously associated with **Atto565**-based dyads (described in Chapter 4). Moreover, it does not have a second reactive carboxylic acid at the 5’ or 6’ position (as **Alexa488** and **Atto565** do) which would result in inefficient amide coupling reactions.

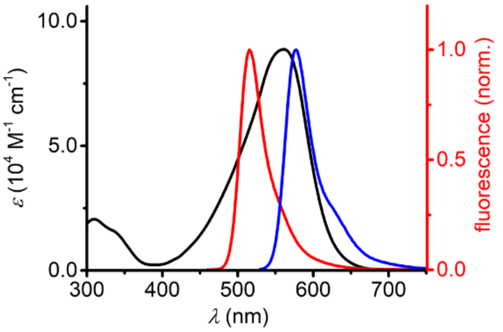

Figure 5-16 Overlap of the reconstructed absorption spectrum of **SO$_{(open)}$** in cyclohexane (black) and normalised emission spectrum of **sR110** in CH_3OH (red) and **5'-Atto565** in CH_3OH (blue). The spectrum of **SO$_{(open)}$** could be obtained only in apolar solvents like cyclohexane because of its fast thermal relaxation in polar solvents. No significant wavelength shifts are anticipated for the **SO$_{(open)}$** spectra in other solvents.

The synthesis of **Triad 3** (**Scheme 5-4**) started with sulfonation of **Rhodamine110** to form **sR110**, which was reacted with secondary amine **27** at 100 °C to form amide **28** that exists as *cis* and *trans* amide rotamers in 93% yield. The choice of a secondary amine was based on the consideration that the product from a primary amine may exist as a non-fluorescent spirolactam instead of the fluorescent open form,[30,31] which would complicate the cell images by introducing pH dependence. Meanwhile, commercial unnatural amino acid **29** underwent H^+/cation exchange, and the corresponding acid was coupled to compound **20** under HBTU-mediated amide coupling conditions. The resulting amide **30** underwent TFA-promoted Boc deprotection to reveal the amine, and another amide reaction generated a mixture of diastereomers of compound **31** that were distinguished by pure-shift ^{1}H (proton-proton decoupled) NMR spectroscopy (see Section 5.6) in 35% yield. A copper-catalysed alkyne-azide cycloaddition (CuAAC) reaction between compounds **28** and **31** afforded **Triad 3** in 37% yield.

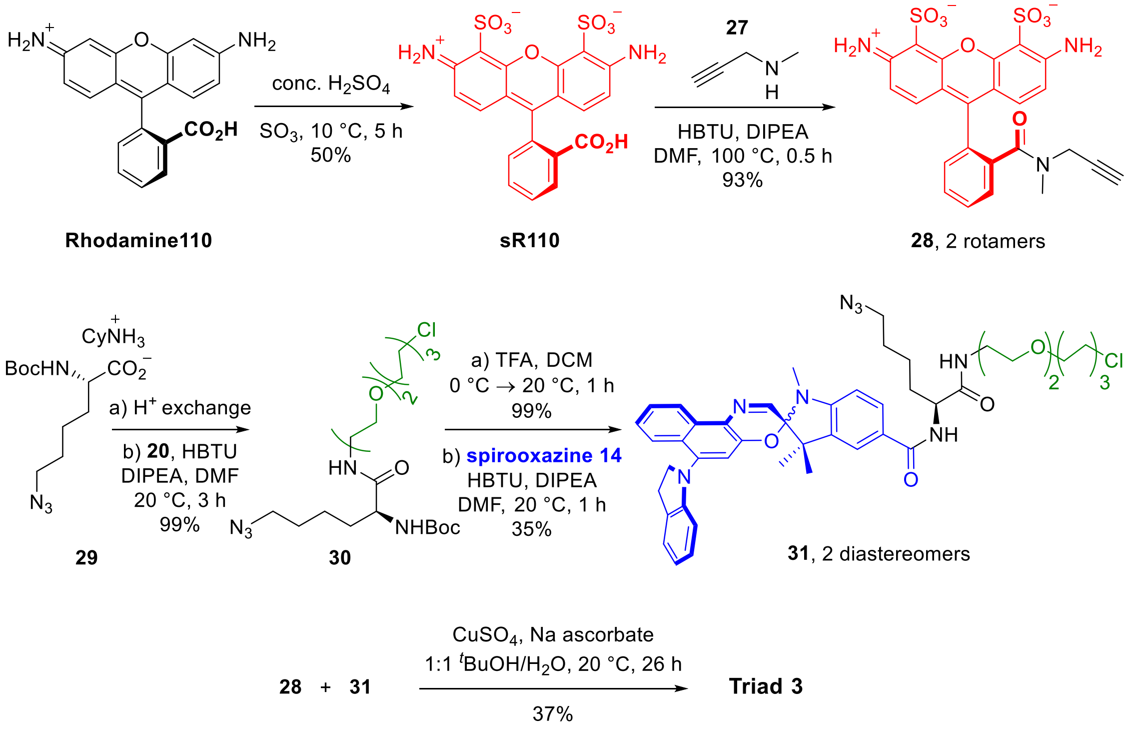

Scheme 5-4 Synthesis of **Triad 3**, in which amide couplings and a copper-catalysed alkyne-azide cycloaddition (CuAAC) reaction were carried out. Compound **27** with a secondary amine was chosen to form a product that could not exist in a non-fluorescent spirolactam form. Cy: cyclohexane.

The photophysical properties of **Triad 3** were characterised in CH_3OH (**Figure 5-17**). Compared to **sR110** dye, the maximum absorption band of **Triad 3** is slightly red shifted, and the spectrum also contains the absorption contribution from the spirooxazine switch around 400 nm. Similarly, the fluorescence emission spectrum of **Triad 3** shows a marginal red shift in the maximum emission wavelength compared to that of **sR110**.

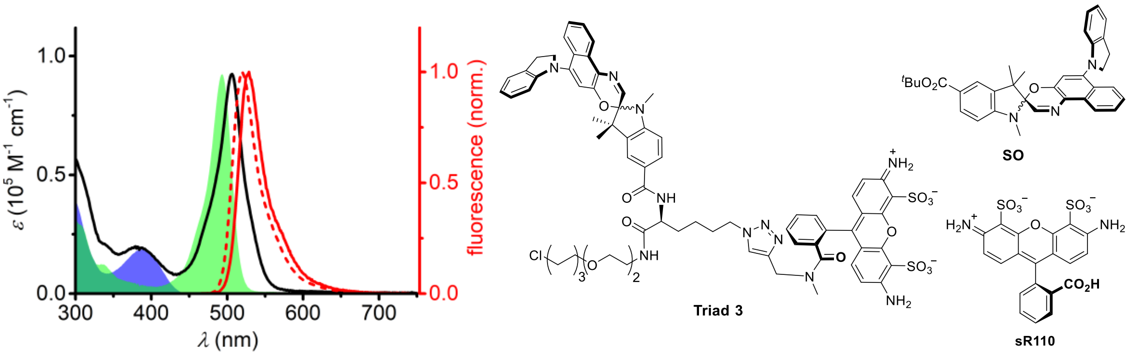

Figure 5-17 UV-vis absorption (black) and emission (red, solid line) spectra of **Triad 3** in CH_3OH. The normalised absorption of **SO** (blue) and **sR110** (green), and the emission of **sR110** (red, dotted line) in CH_3OH are also shown for comparison.

5.2.9 Cell imaging of Triad 3

The properties of **Triad 3** were tested in live transfected CHO cells. It was observed that very few healthy live cells were stained with the triad. This might be attributed to the presence of multiple charges in the molecule, making it difficult to cross the cellular membrane. On the other hand, fluorescence signals were detected from some ill-looking or dead cells. In these cells, the photoswitching behaviour of **Triad 3** was demonstrated (**Figure 5-18**), and the quenching efficiency 64% was significantly higher than the best (28%) observed for **Triad 1** on the structure-unspecific bright blobs, albeit lower than 81% for the dyads (see Chapter 4). **Triad 3** lost 7% quenching efficiency after 6 cycles, which is slightly poorer than that of **Dyad 2**, i.e. 15% loss after 23 cycles, if fatigue resistance is assumed to follow a first-order decay.

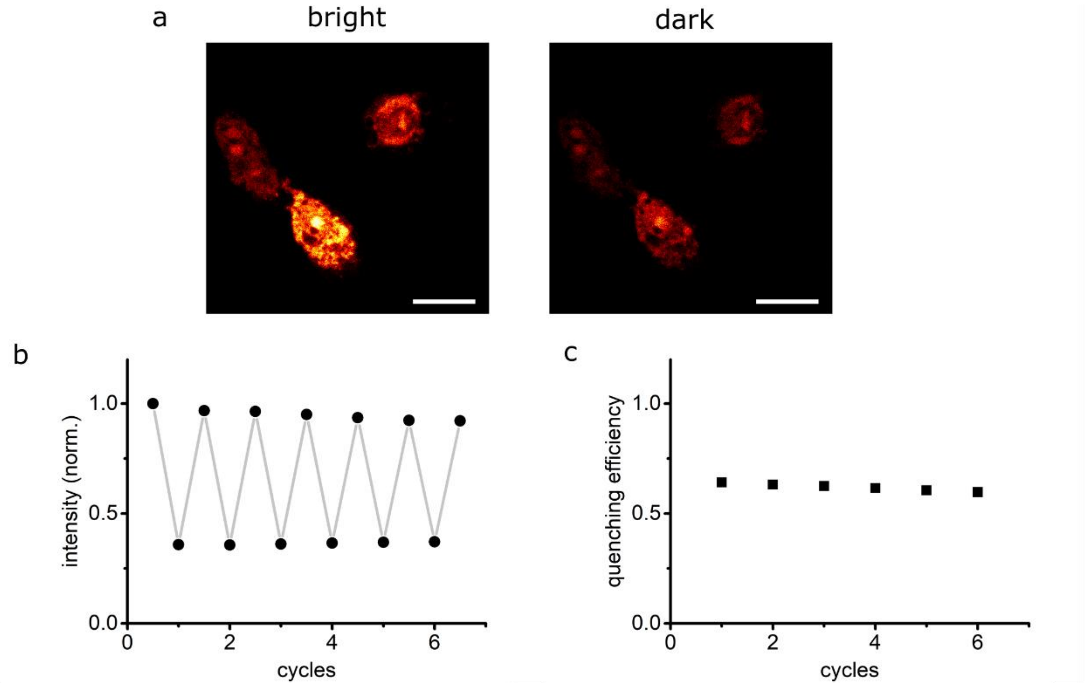

Figure 5-18 Confocal images of transfected CHO cells stained with **Triad 3**. a) Fluorescence signals were detected from ill-looking or dead cells rather than healthy live cells. The bright state was obtained by excitation at 485 nm. The dark state was obtained by irradiation at 405 nm followed by excitation at 485 nm. Scale bar: 10 µm. b,c) Fluorescence quantification of **Triad 3** over a few switching cycles. Quenching efficiency refers to the effective quenching of fluorescence per cycle. The images were recorded on a Zeiss LSM780 inverted confocal microscope.

5.2.10 Conclusions and future work

Comparison of the imaging results of the triads indicates that with the hydrophilic **sR110** dye, high fluorescence modulation could be realised in **Triad 3**, whereas **Triads 1** and **2** that include **Atto565** dye could be switched with only low quenching efficiencies. Nevertheless, no satisfactory specific labelling was achieved with any of the triads in live cells. Selective staining of POIs is challenging because there are a number of interdependent factors that require careful consideration. For example, the overall hydrophobicity of the molecule that may dominate the localisation could be counter-balanced by introduction of multiple charges, but this change may impair cellular permeability. Future work may include: (a) use of a different fluorescent dye that combines hydrophilicity with cellular permeability. An analogous dye to **sR110** with fewer charges may be possible. (b) Incorporation of a relatively long and rigid peptide spacer to ensure sufficient separation of the bulky dyad from the Halo-tag ligand. This work is based on our assumption that the short spacer prevents the Halo-tag ligand from approaching the deep binding site, and that even when the ligand is bound, the switch is forced to be in a congested environment which makes the photoisomerisation process difficult. The choice of amino acids in the peptide spacer could also help to alleviate the potential problem that the dyad dominates the localisation rather than the Halo-tag ligand.

5.3 Immunolabelling

Given that the self-labelling tag strategy proved to be challenging, we decided to turn to immunolabelling methods. Despite being a compromise due to the use of fixed cells, immunolabelling may open up opportunities to demonstrate the potential of our molecular design in achieving and advancing super-resolution microscopy. The indirect method using secondary antibodies was chosen on account of the advantages described in Section 5.1, such as signal amplification and versatility to target multiple structures.

5.3.1 Design of Triad 4

We decided to synthesise **Triad 4**, incorporating an NHS ester which is one of the most common functional groups used to conjugate emissive dyes to antibodies. **Triad 4** would contain the same spirooxazine switch as in **Triads 1** to **3**, but a new fluorescent dye **Atto590**. This change was made because its excitation wavelength (590 nm) is a better match to the lasers that are available on the RESOLFT microscope (405 nm, 485 nm, 594 nm, 640 nm), compared to **Atto565**. Meanwhile, **Atto590** is expected to be quenched efficiently by the open form of the spirooxazine, although the spectral overlap is less significant compared to the **Atto565**-spirooxazine pair (**Figure 5-19**). With the measured fluorescence quantum yield of 71% in CH_3OH, the Förster radius for the **Atto590-**spirooxazine pair is calculated to be 58.0 Å, significantly shorter than 67.5 Å for the **Atto565**-spirooxazine pair. Nevertheless, we would still expect > 99% FRET efficiency based on the reasonable assumption that the distance between **Atto590** and spirooxazine is similar to that in **Triad 1**, i.e. < 20 Å. Even with a donor–acceptor separation of 30 Å, > 98% FRET efficiency is anticipated. The **Atto590** dye was generously provided by Dr Andrew Frawley.

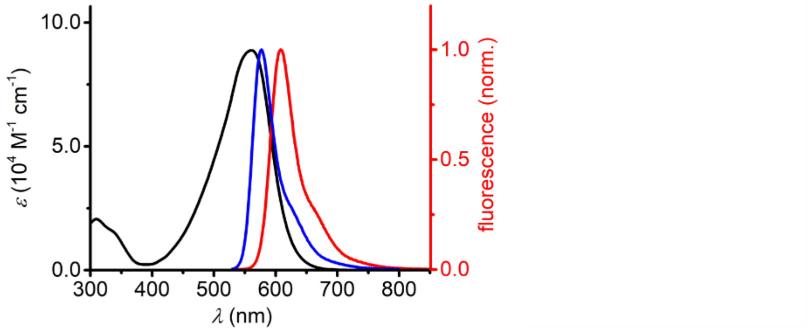

Figure 5-19 Overlap of the reconstructed absorption spectrum of **SO$_{(open)}$** in cyclohexane (black) and the normalised emission spectra of **5'-Atto590** in CH_3OH (red) and **5'-Atto565** in CH_3OH (blue). The spectrum of **SO$_{(open)}$** could be obtained only in apolar solvents like cyclohexane because of its fast thermal relaxation in polar solvents. No significant wavelength shifts are anticipated for the **SO$_{(open)}$** spectra in other solvents.

5.3.2 Synthesis of Triad 4

The synthesis of **Triad 4** (**Scheme 5-5**) started with an HBTU-mediated amide coupling of **5'-Atto590** and but-3-yn-1-amine (**32**) to generate functionalised dye **33** in 60% yield. In parallel, azide **34** was reacted with compound **35**[32] under similar amide coupling conditions to afford compound **36** in 80% yield. The conventional Fmoc deprotection method, i.e. 20% piperidine in DMF, unmasked the amine in compound **36**, but the residual piperidine was difficult to remove, and reacted as an undesired amine in the subsequent amide coupling. Instead, the Fmoc deprotection was carried out using 2% DBU in DMF in 99% yield. The unmasked amine reacted with spirooxazine **14** to form amide **37** in 38% yield. The CuAAC reaction of compounds **37** and **33** was performed to produce the desired compound **38** in 81% yield. The subsequent $CO_2{}^t$Bu deprotection did not employ TFA or HCO_2H because the switch decomposes under acidic conditions. As an alternative, $ZnBr_2$ in DCM[33,34] successfully hydrolysed the *tert*-butyl ester to provide the acid product. In the final step, the NHS ester was prepared using *N*-hydroxysuccinimide and DCC. **Triad 4** was generated as bis-NHS in 57% yield, rather than the expected mono-NHS analogue. The reaction was initially carried out at room temperature, and monitored by analytical HPLC and LC-MS. However, only the starting material appeared to be detected after two days. Retrospectively, it is possible that the mono-NHS product has an identical retention time as the starting material because even the bis-NHS **Triad 4** showed a very marginal difference in the HPLC retention time compared to the starting material, i.e. 15.35 min *vs* 15.14 min using 25 min long HPLC method F (see Experimental 5.5.1). Nevertheless, the specific labelling and switching properties of **Triad 4** should be the same as the mono-NHS analogue.

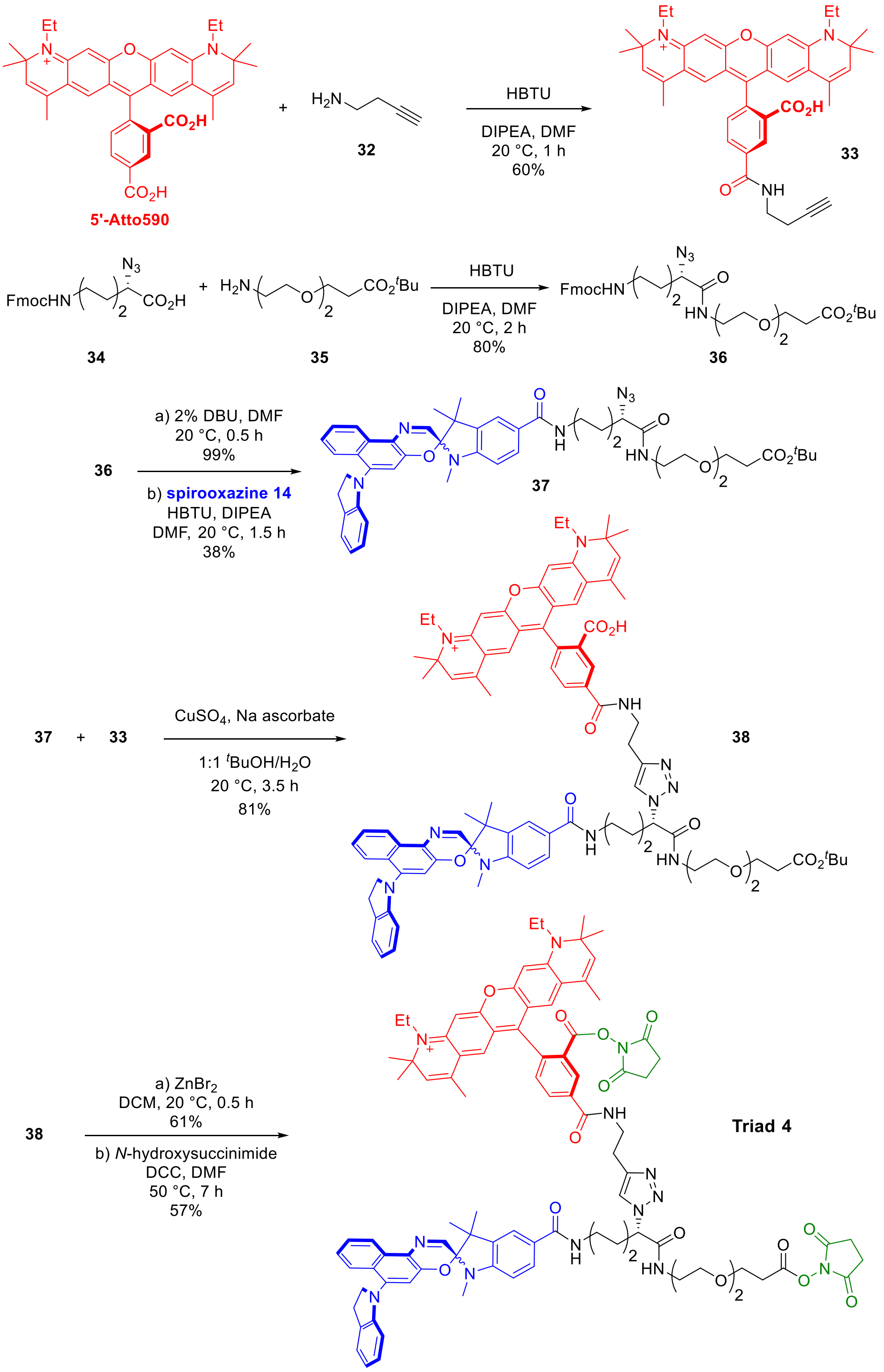

Scheme 5-5 Synthesis of **Triad 4**, during which HBTU-mediated amide coupling and CuAAC reactions were carried out to couple the **Atto590** dye, the spirooxazine switch and NHS esters.

The photophysical properties of **Triad 4** were characterised in CH_2Cl_2 (**Figure 5-17**) due to the concern that the NHS ester in the triad would gradually react with CH_3OH, which was the solvent of choice for other triads. The UV-vis absorption spectrum of **Triad 4** is the sum of those for **5'-Atto590** and the spirooxazine switch. The fluorescence emission of **Triad 4** is similar to that of **5'-Atto590**.

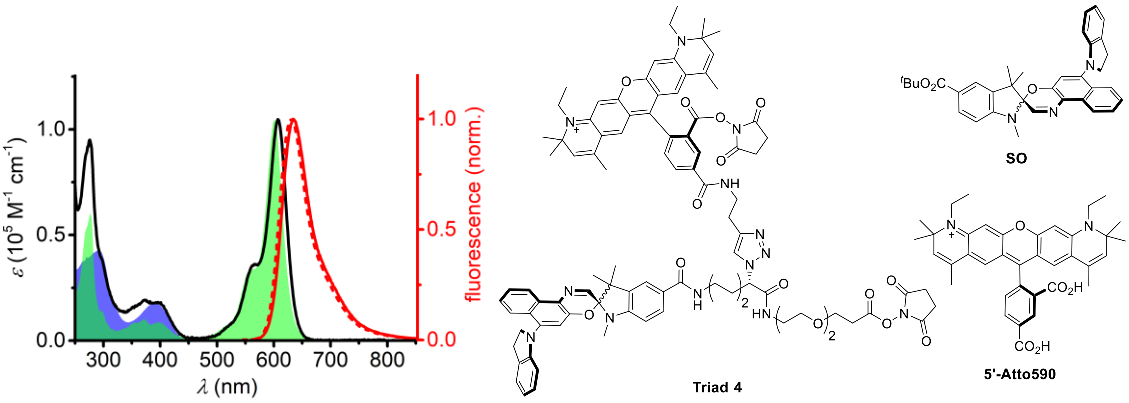

Figure 5-20 UV-vis absorption (black) and emission (red, solid line) spectra of **Triad 4** in CH_2Cl_2. The normalised absorption of **SO** (blue) and **5'-Atto590** (green), and the emission of **5'-Atto590** (red, dotted line) in CH_2Cl_2 are also shown for comparison.

5.3.3 Antibody labelling and cell imaging

We employed the indirect immunolabelling method, which involves the use of a primary antibody that specifically targets POIs, and a dye-conjugated secondary antibody that binds to the primary antibody. Specifically, **Triad 4** was reacted with secondary antibody 187.1,[35] which is derived from rats and recognises antigens present in mice. The resulting 187.1-**Triad 4** conjugate was used to target the mouse anti PEX5 primary antibody,[36] which specifically stains peroxisomes in fixed and permeabilised HEK 293 cells. Peroxisomes are small, membrane-enclosed organelles in almost all eukaryotic cells, and carry out a variety of metabolic reactions, e.g. oxidation of fats.[37]

The preliminary imaging result showed no specific labelling by **Triad 4** with reference to GFP-peroxisomes (**Figure 5-21**). It is possible that the **Triad 4**-antibody conjugate had denatured in storage, as precipitates appeared after 14 days, despite being stored at 2 °C in PBS buffer. In the near future, this procedure will be repeated, and the secondary antibody conjugate will be used immediately for staining the primary antibody. Following specific labelling of POIs, we will investigate the switching behaviour of **Triad 4** and test its applicability in RESOLFT imaging.

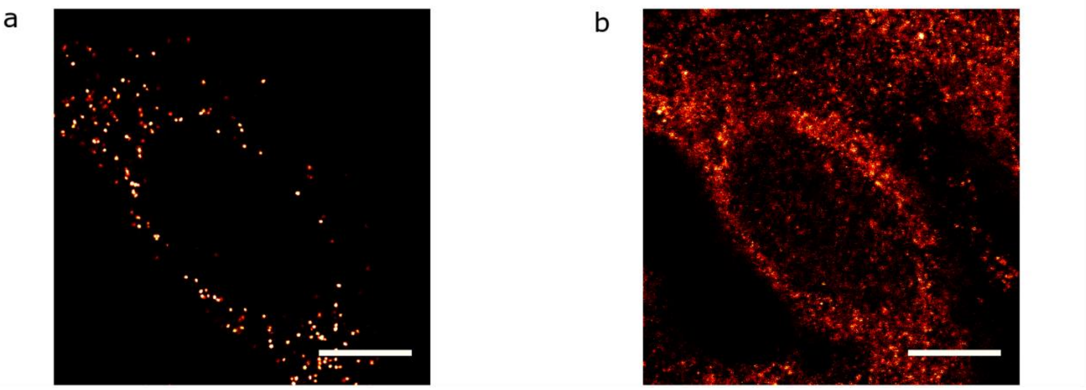

Figure 5-21 Confocal images of fixed HEK 293 cells that were transfected to express GFP against peroxisomes and that were stained with **Triad 4** using the indirect immunolabelling method. a) Fluorescence signals from GFP that were genetically expressed in peroxisomes. Excitation at 485 nm, detection range 500–570 nm. b) Weak fluorescence signals from **Triad 4**. No specific labelling was observed. Excitation at 594 nm, detection range 605–625 nm. The images were acquired in the confocal mode of the RESOLFT microscope. Scale bar: 10 µm.

5.4 Conclusions and future work

This chapter reports the initial attempts in advancing our molecular design by exploiting the Halo-tag technique for live cell imaging and the immunolabelling method for fixed cell imaging. Despite the failure of **Triads 1** to **3** to achieve specific labelling of POIs, these triads and NHS-based **Triad 4** validated several synthetic approaches towards such complex multi-functional molecules. Additionally, the cell imaging of the triads provoked thorough thinking into the molecular design by considering many interdependent properties, e.g. membrane permeability and aggregation/solubility in aqueous media.

Firstly, the yields of key steps in the syntheses of **Triads 3** and **4** (12%; 5.1%) are significantly improved compared to those for **Triads 1** and **2** (0.69%; 0.27%). It is mainly because the syntheses of **Triads 1** and **2** included amide couplings between the **Atto565** dye and an amine, which were low-yielding due to the formation of regioisomer side products that were difficult to separate. Additionally, purification of small amounts of crude materials by semi-preparative HPLC led to low yields of isolated products (4%; 3.2%). In contrast, preparation of **Triads 3** and **4** relied on CuAAC reactions to couple the dye with other components, and the yields were moderate to high (37%; 81%) without HPLC purification. Secondly, three different dyes were used, **sR110**, **Atto565** and **Atto590**. Compared to the other two dyes, **sR110** enhances the water solubility of **Triad 3**, but concomitantly, makes it difficult for the triad to cross the cellular membrane. On the other hand, **Atto590** has a better matched excitation wavelength than **Atto565** on the

RESOLFT microscope, which lowers required illumination intensities, potentially causing less photodamage to samples. Therefore, for future synthetic work, CuAAC reactions rather than amide couplings should be employed to minimise side reactions, and **Atto590** would be the preferred choice of dye. Efforts should also be devoted to realisation of site-specific labelling using **Triad 4,** and subsequent investigation of the photoswitching performance.

5.5 Experimental

Many of the general procedures in this chapter have been described in the previous chapters as follows:

NMR, mass spectrometry: Chapter 2 Experimental.

UV-vis absorption spectroscopy, fluorescence emission: Chapter 3 Experimental.

Reagents, absolute fluorescence quantum yields, optical microscopy: Chapter 4 Experimental.

5.5.1 HPLC

The HPLC system is described in Chapter 4 Experimental section. The HPLC traces were monitored at 254 nm, 405 nm, and 488 or 565 or 590 nm depending on the choice of fluorescent dyes.

For analytical HPLC, one of the following methods was used, and the method numbering is continued from Chapter 4:

Method A: CH_3OH and H_2O (with 0.1% TFA additive) as eluents. 5% CH_3OH to 100% CH_3OH over 20 min, 100% CH_3OH for 15 min.

Method C: CH_3CN and H_2O (with 0.1% TFA additive) as eluents. 5% CH_3CN to 100% CH_3CN over 20 min, 100% CH_3CN for 15 min.

Method D: ^{i}PrOH and H_2O (with 0.1% TFA additive) as eluents. 5% ^{i}PrOH to 100% ^{i}PrOH over 15 min, 100% ^{i}PrOH for 10 min.

Method E: CH_3OH and H_2O (with 0.1% TFA additive) as eluents. 5% CH_3OH to 100% CH_3OH over 15 min, 100% CH_3OH for 10 min.

Method F: CH_3CN and H_2O (with 0.1% TFA additive) as eluents. 5% CH_3CN to 100% CH_3CN over 15 min, 100% CH_3CN for 10 min.

Semi-preparative HPLC was performed using one of the following methods:

Method G: CH_3OH and H_2O (with 0.1% TFA additive) as eluents. 0% CH_3OH to 100% CH_3OH over 30 min, 100% CH_3OH for 10 min.

Method H: CH_3CN and H_2O (with 0.1% TFA additive) as eluents. 0% CH_3CN to 100% CH_3CN over 20 min, 100% CH_3CN for 20 min.

Method I: CH_3OH and H_2O (with 0.1% TFA additive) as eluents. 0% CH_3OH to 100% CH_3OH over 10 min, 100% CH_3OH for 20 min.

5.5.2 FRET efficiency (*E*) calculations

For the general calculation procedure, please refer to Experimental in Chapter 4. The absorption spectrum of the acceptor, i.e. **SO$_{\textbf{(open)}}$** in PBS is unavailable due to the rapid thermal recovery, so we choose the **SO$_{\textbf{(open)}}$** form in cyclohexane instead. Based on the spectral overlap between **SO$_{\textbf{(open)}}$** and **5’-Atto565**, the calculated Förster radius is 67.5 Å.

The distance between the dye and switch in **Triad 1** was simulated by optimising the molecular geometry in HyperChem with a molecular mechanics calculation in an MM^+ force field. With a distance of max. 17.3 Å and min. 9.4 Å, the FRET efficiency is ca. 100% for both the cases.

5.5.3 Protein-ligand covalent docking simulations

Ligands were covalently docked into the binding site of a Halo-tag crystal structure (site: *ASP106*, PDB: 5UXZ without covalently linked ligands) using the GOLD program.[38] The crystal structure PDB 5UXZ[39] instead of 1BN6[25] was used because the original 5UXZ was measured from a crystal of the Halo-tag that already had a covalently attached fluorophore to the *ASP106* amino acid residue. It is likely that PDB 5UXZ is better for docking simulations as it already accounts for conformational changes induced by ligand binding. Due to the large size and flexibility of our triads, the binding site was defined by a radius of 20 Å around the reactive site O-*ASP106*. Docking was performed with a search efficiency of 200% as recommended for flexible ligands, and the CHEMPLP (CHEM Piecewise Linear Potential) fitness scoring was used. Graphical representations were generated in PyMOL(TM) 1.7.4.5 Edu.

5.5.4 Live cell imaging of Triads 1–3

Transfected HEK 293 (human embryonic kidney), COS-7 (monkey kidney) and CHO (Chinese hamster ovary) cells were kindly provided by Dr Katharina Reglinski (WIMM, Oxford), and transfected GM5756T (human fibroblast) cells were generously provided by Dr Silvia Galiani (WIMM, Oxford). These cells were transiently transfected by DNA encoding to express the Halo-tag proteins fused to microtubules.

For the staining procedure, please see Chapter 2 Experimental section.

5.5.5 Antibody labelling

Live untransfected HEK 293 cells were used and they were provided by Dr Katharina Reglinski. Immunolabelling was carried out with assistance from Dr Dilip Shrestha and Dr Katharina Reglinski at WIMM, Oxford.

*5.5.5.1 Conjugation of **Triad 4** to secondary antibody*

1. The antibody 187.1 (rat, anti-mouse)[35] was dissolved to make a 1 μg/μL solution in PBS at pH = 7.4.

2. 0.1 M $NaHCO_3$ in PBS buffer was added to the above solution to raise the pH to ~8.3, which is the alkaline condition required for the reaction between the NHS ester in **Triad 4** and primary amines present in the antibody.

3. **Triad 4** was dissolved in PBS buffer to make a 1 mM stock solution. 6.3 μL of the stock solution was mixed with 220 μL of the solution from step 2. The reaction mixture was incubated at 20 °C for 1 h.

4. The reaction mixture was subjected to a size exclusion column (antibody conjugate purification kit from Thermo Fischer Scientific) to remove unbound triads.

5. The purified 187.1–**Triad 4** conjugate was stored in PBS buffer at 2 °C for 14 days before use in the next stage.

5.5.5.2 Labelling primary antibody

6. Untransfected live HEK 293 cells were fixed using a PBS solution of 3% formaldehyde, washed with PBS twice, and permeabilised with methanol at –20 °C for 6 min.

7. After washing with PBS twice, the cells were immersed in a blocking buffer, i.e. 2% BSA + 5% FCS in PBS for 1 h at 20 °C.

8. The cells were washed once with 1% BSA in PBS, and incubated with the anti PEX5 primary antibody (mouse, anti-peroxisomes)[36] in 1% BSA in PBS for 1 h at 20 °C.

9. After washing with 1% BSA in PBS five times, the cells were incubated with the 187.1–**Triad 4** conjugate for 30 min at 20 °C.

10. After washing with 1% BSA in PBS five times, the cells were mounted on a drop of Mowiol, or in PBS buffer.

11. The cell imaging was performed either on a Zeiss 780 confocal laser scanning microscope or in the confocal mode of a RESOLFT microscope (microscope details see Chapter 4 Experimental).

5.6 Synthetic procedures

Amino acid derivatives **19**, **29** and **34** were commercially available from Chem-Impex International. Compound **20**[21–23], compound **24**[26,27] and compound **35**[32] were prepared according to the literature.

Benzyl *tert*-butyl (6-((2-(2-((6-chlorohexyl)oxy)ethoxy)ethyl)amino)-6-oxohexane-1,5-diyl)(*S*)-dicarbamate (21)

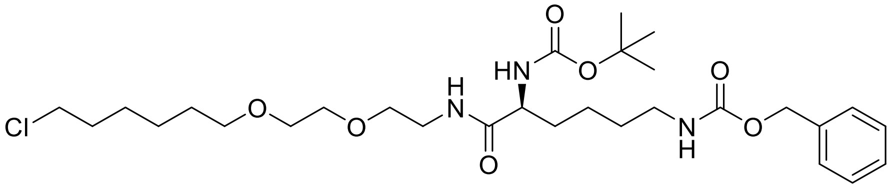

Dry DMF (13.8 mL) was added to a solid mixture of *N*^{6}-((benzyloxy)carbonyl)-*N*^{2}-(tert-butoxycarbonyl)-*L*-lysine (**19**) (647 mg, 2.04 mmol) and HBTU (967 mg, 2.55 mmol), and the colourless solution was stirred at room temperature for 30 min. A solution of 2-(2-((6-chlorohexyl)oxy)ethoxy)ethan-1-aminium 2,2,2-trifluoroacetate (**20**[21–23]; 629 mg, 1.70 mmol) in dry DMF (13.8 mL), and DIPEA (1.67 mL, 9.59 mmol) were added. The reaction was stirred for 3 h before being quenched with H_2O (1 mL). The solvents were removed using a distillation apparatus under 0.5 mBar at 40 °C. The residue was subjected to silica gel chromatography (CH_2Cl_2 to 97:3 CH_2Cl_2/CH_3OH) to yield a yellow oil. The impure product was dissolved in CH_2Cl_2 (100 mL), washed with 5% w/w LiCl (aq.) solution (4 × 50 mL) and H_2O (3 × 50 mL), dried over Na_2SO_4, and the solvent was removed to afford the product as a yellow oil (888 mg, 89%). R_f (SiO_2, 9:1 CH_2Cl_2/CH_3OH) = 0.57. ^1H NMR (400 MHz, $CDCl_3$) δ (ppm): 7.30–7.21 (overlapped m, 5H), 6.45 (br. s, 1H), 5.12 (br. s, 1H), 5.02 (s, 2H), 4.91 (br. s, 1H), 3.98 (m, 1H), 3.55–3.51 (m, 2H), 3.51–3.43 (overlapped m, 6H), 3.39 (m, 4H), 3.11 (m, 2H), 1.70 (m, 2H), 1.60–1.23 (overlapped m + s, 21H). $^{13}C\{^1H\}$ (101 MHz, $CDCl_3$) δ (ppm): 171.9, 156.5, 155.6, 136.6, 128.5, 128.11, 128.07, 71.28, 70.3, 70.0, 69.7, 66.6, 54.3, 45.0, 40.5, 38.2, 38.6 (impurity 1,1,3,3-tetramethylurea), 32.5, 32.4, 29.5, 29.4, 28.3, 26.7, 25.4, 22.5, Boc quaternary-C not observed. HRMS (ESI +ve) *m/z*: 586.32471, ($[M+H]^+$, $C_{29}H_{49}O_7N_3{}^{35}Cl$ requires 586.32535).

tert-Butyl (S)-(6-amino-1-((2-(2-((6-chlorohexyl)oxy)ethoxy)ethyl)amino)-1-oxohexan-2-yl)carbamate (Cbz-deprotected 21)

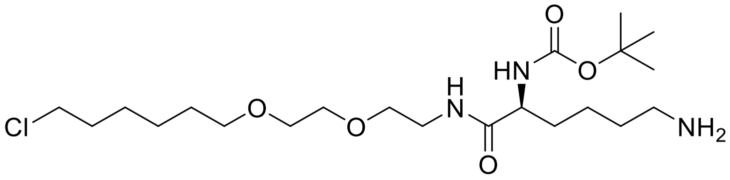

Benzyl *tert*-butyl (6-((2-(2-((6-chlorohexyl)oxy)ethoxy)ethyl)amino)-6-oxohexane-1,5-diyl)(*S*)-dicarbamate (**21**; 190 mg, 0.32 mmol) and 10% w/w Pd/C (8.0 mg, 0.2 mmol) were suspended in EtOH (25 mL). The mixture was subjected to three cycles of vacuum and H_2, and was stirred under a H_2 balloon for 20 h. The resulting mixture was filtered through a short pad of Celite, and the filtrate was concentrated to afford the product as a yellow oil (142 mg, 98%). ^1H NMR (400 MHz, $CDCl_3$) δ (ppm): 3.99 (m, 1H), 3.64–3.52 (overlapped peaks, 8 H), 3.49 (t, J = 6.6 Hz, 2H), 3.45–3.30 (m, 2H), 2.63 (t, J = 6.9 Hz, 2H), 1.82–1.69 (overlapped peaks, 4H), 1.66–1.56 (overlapped peaks, 4H), 1.54–1.32 (overlapped peaks, 22H). LRMS (ESI +ve) *m/z*: 452.3, ($[M+H]^+$, $C_{21}H_{43}N_3O_5Cl$ requires 452.3).

(*S*)-6-(4-((5-((*tert*-Butoxycarbonyl)amino)-6-((2-(2-((6-chlorohexyl)oxy)ethoxy)ethyl)amino)-6-oxohexyl)carbamoyl)-2-carboxyphenyl)-1,11-diethyl-3,4,8,9,10,11-hexahydro-2*H*-pyrano[3,2-*g*:5,6-*g*']diquinolin-1-ium 2,2,2-trifluoroacetate (22)

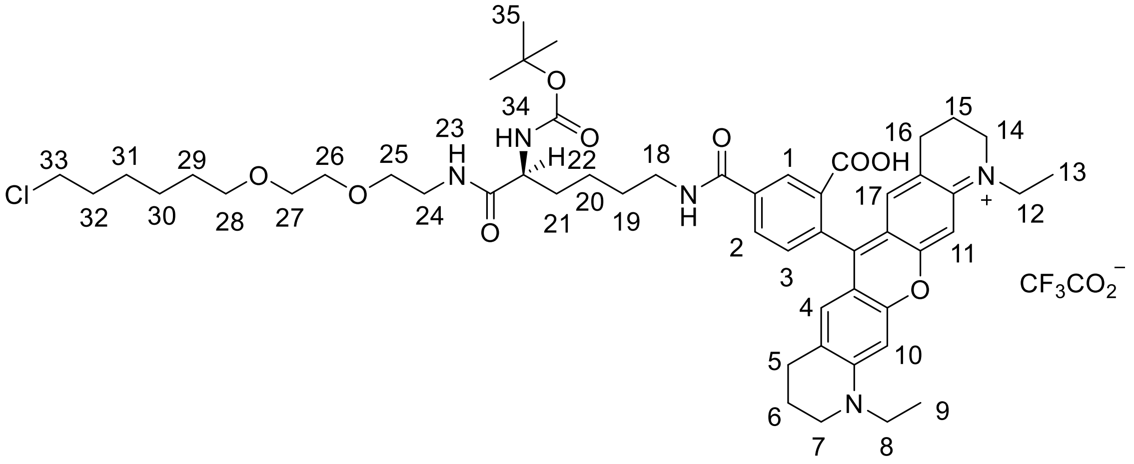

To a mixture of 6-(2,4-dicarboxyphenyl)-1,11-diethyl-3,4,8,9,10,11-hexahydro-2*H*-pyrano[3,2-*g*:5,6-*g'*]diquinolin-1-ium chloride (**5'-Atto565;** 32 mg, 71 µmol) and HBTU (40 mg, 0.11 mmol) under argon was added dry DMF (2.0 mL). *tert*-Butyl (*S*)-(6-amino-1-((2-(2-((6-chlorohexyl)oxy)ethoxy)ethyl)amino)-1-oxohexan-2-yl)carbamate (Cbz-deprotected **21**; 32 mg, 71 µmol) in dry DMF (6.0 mL) was added to the above solution. Dry DIPEA (37 mL, 0.21 mmol) was added and the reaction mixture was stirred for 5 min before being quenched with H_2O (8 mL). The solvents were removed using a distillation apparatus under 0.5 mBar at 40 °C. Several purification techniques were attempted but failed, and 2.7 mg (4%) of the pure product was finally obtained from RP-HPLC (method H). R_f (SiO_2, 3:10:87 $NEt_3/CH_3OH/CH_2Cl_2$) = 0.50. ^1H NMR (500 MHz, CD_3OD) δ (ppm): 8.76 (d, *J* = 1.8 Hz, 1H, H1), 8.25 (dd, *J* = 7.9, 1.9 Hz, 1H, H2), 7.48 (d, *J* = 7.9 Hz, 1H, H3), 6.93 (s, 2H, H10, H11), 6.74 (d, *J* = 1.3 Hz, 2H, H4, H17), 4.11–3.97 (m, 1H, H22), 3.66 (q, *J* = 7.2 Hz, 4H, H8, H12), 3.63–3.51 (m, 13H), 3.48 (td, *J* = 6.6, 1.7 Hz, 4H), 3.44–3.36 (m, 1H), 2.73–2.64 (m, 4H, H5, H16), 2.02–1.87 (m, 4H), 1.84–1.63 (m, 4H), 1.62–1.52 (m, 2H), 1.44 (overlapped s + m, 12H, H35 + m), 1.33 (t, *J* = 7.1 Hz, 6H, H9, H13). $^{13}C\{^1H\}$ NMR (126 MHz, CD_3OD) δ (ppm): 173.8, 166.8, 166.1, 157.0, 156.4, 156.2, 153.5, 136.9, 136.2, 131.5, 130.9, 130.6, 129.8, 127.1, 125.5, 113.1, 94.5, 79.2, 70.8, 69.8, 69.1, 54.7, 44.3, 39.5, 38.9, 32.3, 31.8, 29.7, 29.1, 28.7, 27.4, 27.1, 26.3, 25.1, 22.9, 22.8, 20.6, 9.9. $^{19}F\{^1H\}$ NMR (470 MHz, CD_3OD) δ (ppm): –77.0.

6-(2-Carboxy-4-(((5*S*)-6-((2-(2-(2-chloroethoxy)ethoxy)ethyl)amino)-5-(6'-(indolin-1-yl)-1,3,3-trimethylspiro[indoline-2,3'-naphtho[2,1-*b*][1,4]oxazine]-5-carboxamido)-6-oxohexyl)carbamoyl)phenyl)-1,11-diethyl-3,4,8,9,10,11-hexahydro-2*H*-pyrano[3,2-*g*:5,6-*g*']diquinolin-1-ium 2,2,2-trifluoroacetate (Triad 1)

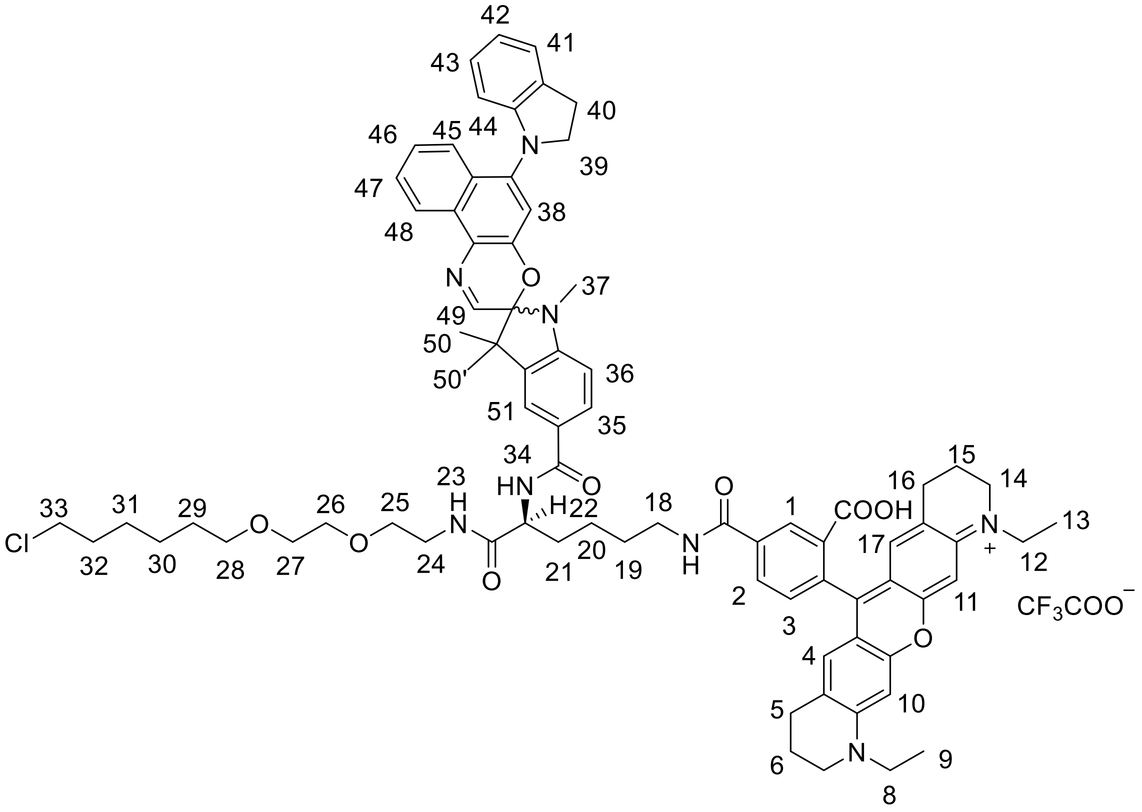

(*S*)-6-(4-((5-((*tert*-Butoxycarbonyl)amino)-6-((2-(2-((6-chlorohexyl)oxy)ethoxy)ethyl)amino)-6-oxohexyl)carbamoyl)-2-carboxyphenyl)-1,11-diethyl-3,4,8,9,10,11-hexahydro-2*H*-pyrano[3,2-*g*:5,6-*g*']diquinolin-1-ium 2,2,2-trifluoroacetate (**22**; 3.0 mg, 2.8 µmol) was dissolved in dry CH_2Cl_2 (2.0 mL), and the flask was purged with argon. TFA (0.20 mL) was added to the above solution, and the reaction was stirred for 1 h. The solvent was removed *in vacuo*, and Boc-deprotected **22** was obtained in 99% yield (3.0 mg). ^{1}H NMR and analytical HPLC indicated a single product. R_f (SiO_2, 3:10:87 $NEt_3/CH_3OH/CH_2Cl_2$) = 0.45. HRMS (ESI +ve) *m/z*: 844.43903, ($[M-CF_3CO_2]^+$, $C_{47}H_{63}N_5O_7{}^{35}Cl$ requires 844.44105).

To a mixture of 6'-(indolin-1-yl)-1,3,3-trimethylspiro[indoline-2,3'-naphtho[2,1-*b*][1,4]oxazine]-5-carboxylic acid (**14**; 2.0 mg, 4.1 µmol) and HBTU (1.6 mg, 4.2 µmol) under argon was added dry DMF (1.0 mL). Boc-deprotected **22** (2.7 mg, 2.8 µmol) and DIPEA (4.5 µL, 25 µmol) in dry DMF (1.0 mL) was added to the above solution. The reaction mixture was stirred for 5 h before being quenched with H_2O (6 mL). The solvents were removed using a distillation apparatus under 0.5 mBar at 40 °C. The HPLC trace of the mixture indicated ~50% conversion. Based on the assumption that the extinction coefficients of the product and **5'-Atto565** are the same at 555 nm in CH_3OH, 0.89 mg (21% yield; 42% based on recovered starting material) of the product was obtained from RP-HPLC (method H). R_f (SiO_2, 3:10:87 NEt_3/CH_3OH/CH_2Cl_2) = 0.53. HRMS (ESI +ve) *m/z*: 1315.63281, ($[M\text{-anion}]^+$, $C_{78}H_{88}N_8O_9{}^{35}Cl$ requires 1315.63573). Semi-preparative HPLC (method H), t_R = 31.4 min. UV-vis (CH_3OH) λ_{max} / nm (ε / M^{-1} cm^{-1}) 556 (1.5×10^5). Fluorescence emission (CH_3OH) λ_{max} / nm (Φ_f): 581 (47%).

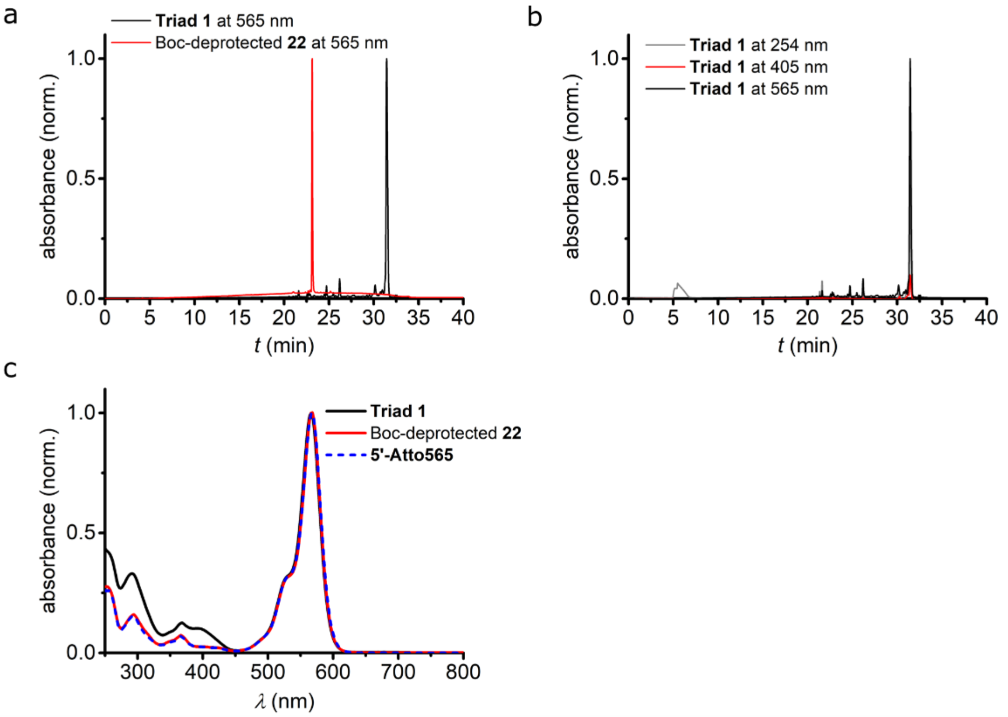

Figure 5-22 HPLC characterisation of **Triad 1** using method H. a) HPLC traces of **Triad 1** and Boc-deprotected **22** as one of the SMs, by monitoring at 565 nm. b) HPLC trace of **Triad 1** detected at 254, 405 and 565 nm. c) UV-vis absorption spectra obtained from the HPLC peaks of **Triad 1**, Boc-deprotected **22** and **5'-Atto565** dye.

***tert*-Butyl (27-chloro-6,9,12,15,18,21-hexaoxa-3-azaheptacosyl)carbamate (25)**

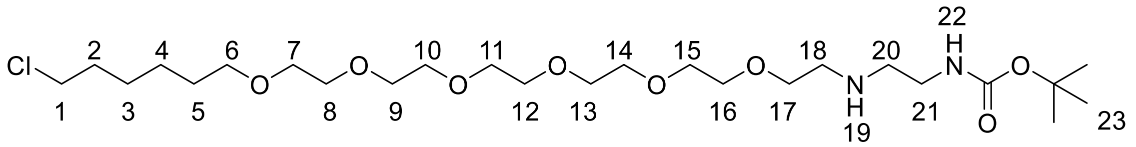

To a CH_2Cl_2 (5.0 mL) solution of *tert*-butyl (24-chloro-3,6,9,12,15,18-hexaoxatetracosyl)carbamate (**24**[26,27]; 600 mg, 1.2 mmol) was added TFA (0.50 mL, 6.5

mmol) dropwise. The reaction was left to stir for 1.5 h. The solvents were removed *in vacuo*, and the deprotected product was used without further purification.

To a suspension of deprotected **24** (612 mg, 1.2 mmol) and *tert*-butyl (2-oxoethyl)carbamate (**23**; 191 mg, 1.2 mmol) in CH_2Cl_2 (10 mL) at 0 °C was added $NaBH(OAc)_3$ (509 mg, 2.4 mmol). The reaction was slowly warmed to room temperature, and after stirring for 2 days, TLC analysis suggested incomplete conversion. The mixture was cooled to 0 °C again, and more *tert*-butyl (2-oxoethyl)carbamate (**23**; 96 mg, 0.6 mmol) and $NaBH(OAc)_3$ (254 mg, 1.2 mmol) were added. After stirring at room temperature for 15 h, DIPEA (0.63 mL, 3.6 mmol) was added to the reaction, and the solvents were removed. The crude product was purified by silica gel chromatography (1:0 to 1:1 petroleum ether/EtOAc, then 98:2 to 88:12 $CHCl_3/CH_3OH$) to obtain the product as a colourless oil (21 mg, 3.2%). The yield could potentially be improved by optimising reaction conditions, e.g. use of an alternative reductive amination reagent, e.g. $NaBH_3CN$, and pH control. R_f (SiO_2, 9:1 CH_2Cl_2/CH_3OH) = 0.15. ^1H NMR (500 MHz, $CDCl_3$) δ (ppm): 3.78 (t, *J* = 5.0 Hz, 1H, H22), 3.69–3.58 (overlapped peaks, 21H), 3.58–3.54 (m, 2H), 3.54–3.48 (overlapped peaks, 3H, H1 and others), 3.44 (t, *J* = 6.6 Hz, 4H, H6 and others), 3.18–3.03 (overlapped peaks, 4H, H18, H20), 1.83–1.71 (m, 3H), 1.62–1.52 (m, 2H), 1.49–1.30 (overlapped peaks, 15H). LRMS (ESI +ve) *m/z*: 543.4 ($[M+H]^+$), 565.4 ($[M+Na]^+$).

5-((2-((*tert*-Butoxycarbonyl)amino)ethyl)(24-chloro-3,6,9,12,15,18-hexaoxatetracosyl)carbamoyl)-2-(1,11-diethyl-3,4,8,9,10,11-hexahydro-2*H*-pyrano[3,2-*g*:5,6-*g'*]diquinolin-1-ium-6-yl)benzoate (26)

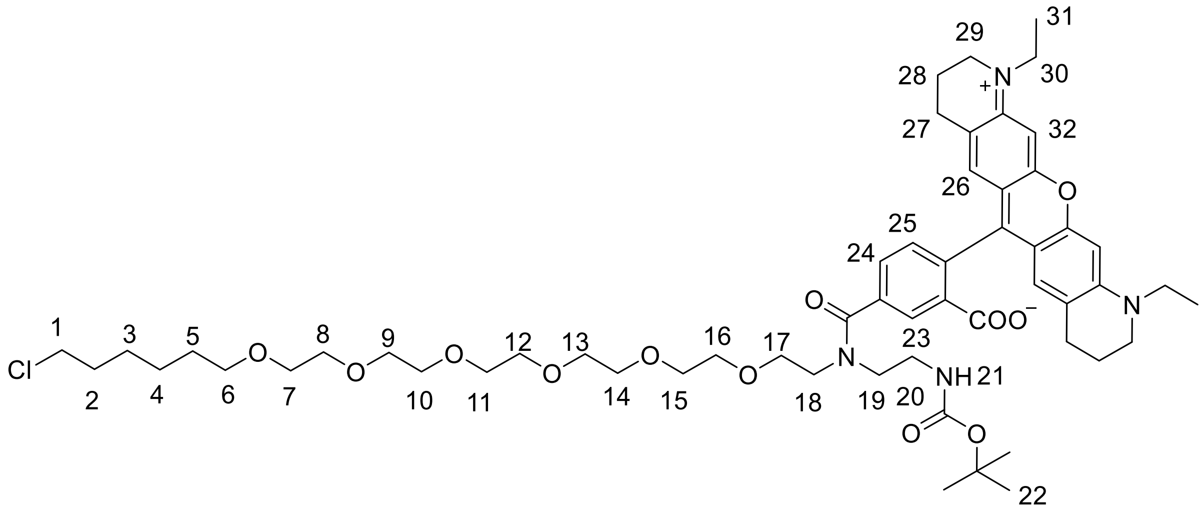

To a mixture of **5’-Atto565** (20 mg, 37 µmol) and HBTU (21 mg, 56 µmol) under argon was added dry DMF (0.50 mL). *tert*-Butyl (27-chloro-6,9,12,15,18,21-hexaoxa-3-azaheptacosyl)carbamate (**25**; 20 mg, 37 µmol) and DIPEA (4.5 µL, 25 µmol) in dry DMF (1.0 mL) was added to the above solution. The reaction mixture was heated to 50 °C and stirred for 1.5 h before being quenched with H_2O (2 mL). The solvents were removed under N_2 flow at 40 °C. The crude product was purified by silica gel (0:5:95 to 2:15:83 $NEt_3/CH_3OH/CH_2Cl_2$) and C18-reversed phase silica gel chromatography (1:1 to 0:1 H_2O/CH_3OH) to afford a pink solid (20 mg, 51%). R_f (RP-C18, CH_3OH) = 0.30. Despite the presence of a single peak in the HPLC trace, the two rotamers in 1:1 ratio are clear in the NMR spectrum. ^{1}H NMR (500 MHz, $CDCl_3$) δ (ppm): 8.18 (s, 1H, H23), 8.07 (s, 1H, H23’ in the other rotamer), 7.73 (d, *J* = 7.9 Hz, 1H, H24), 7.61 (d, *J* = 7.9 Hz, 1H, H24’), 7.2–7.15 (overlapped 2 x d, 2H, H25, H25’), 6.53–6.30 (overlapped peaks, 8H, H26, H26’, H32, H32’), 5.43 (br. s, 1H, H21), 5.37 (br. s, 1H, H21’), 3.87–3.34 (overlapped m, 77H), 3.22 (m, 8H, H29, H29’), 2.65–2.48 (overlapped peaks, 8H, H27, H27’), 1.87 (m, 8H, H28, H28’), 1.80–1.71 (m, 4H), 1.65–1.53 (m, 4H), 1.50–1.41 (m, 12H), 1.40–1.33 (m, 15H), 1.20 (t, *J* = 7.0 Hz, 12H), 0.93–0.83 (overlapped t, 11H, H31, H31’).^{13}C{^{1}H} NMR (126 MHz, $CDCl_3$) δ (ppm): 171.8, , 171.5, 169.0, 168.9, 156.3, 155.8, 152.8, 152.5, 150.9, 149.4, 148.1, 147.9, 147.8, 137.6, 137.5, 132.8, 131.8, 131.7, 131.3, 130.2, 127.99, 127.94, 127.8, 125.6, 125.2, 124.7, 124.6, 120.3, 120.0, 119.6, 108.7, 106.8, 106.2, 96.0, 95.9, 80.9, 79.3, 71.2, 70.62, 70.58, 70.45, 70.1, 69.1, 68.7, 51.0, 50.2, 50.0, 48.4, 46.6, 45.8, 45.1, 39.0, 33.3, 32.6, 31.9, 31.8, 29.88–29.28 (overlapped br. peaks), 28.5, 27.5, 26.7, 25.4, 23.0, 22.9, 22.7, 22.6, 21.8, 17.3, 16.9, 14.1, 13.0, 10.8. HRMS (ESI +ve) *m/z*: 1035.54504, ($[M+H]^+$, $C_{56}H_{80}N_4O_{12}{}^{35}Cl$ requires 1035.54558). Analytical HPLC (method A), t_R = 17.4 min.

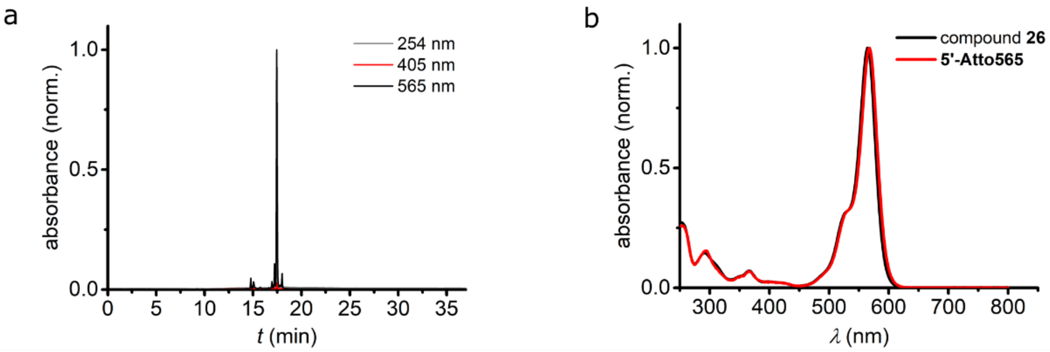

Figure 5-23 HPLC characterisation of compound **26** using method A. a) HPLC trace of compound **26** detected at 254, 405 and 565 nm. b) UV-vis absorption spectra obtained from the HPLC peaks of compound **26** and **5’-Atto565** dye.

5-((24-Chloro-3,6,9,12,15,18-hexaoxatetracosyl)(2-(6'-(indolin-1-yl)-1,3,3-trimethylspiro[indoline-2,3'-naphtho[2,1-*b*][1,4]oxazine]-5-carboxamido)ethyl)carbamoyl)-2-(1,11-diethyl-3,4,8,9,10,11-hexahydro-2*H*-pyrano[3,2-*g*:5,6-*g'*]diquinolin-1-ium-6-yl)benzoate (Triad 2)

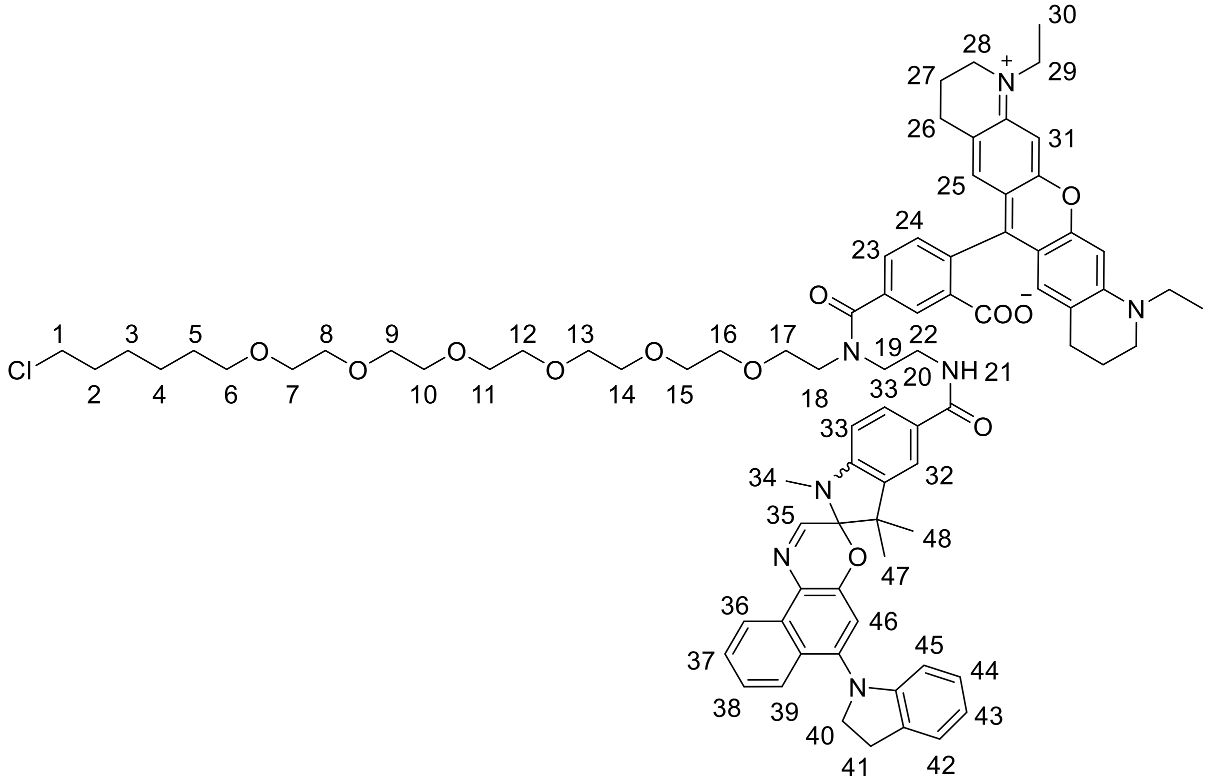

To a CH_2Cl_2 (1.0 mL) solution of 5-((2-((*tert*-butoxycarbonyl)amino)ethyl)(24-chloro-3,6,9,12,15,18-hexaoxatetracosyl)carbamoyl)-2-(1,11-diethyl-3,4,8,9,10,11-hexahydro-2*H*-pyrano[3,2-*g*:5,6-*g'*]diquinolin-1-ium-6-yl)benzoate (**26**; 9.8 mg, 9.4 μmol) was added TFA (0.10 mL). The reaction was stirred for 1 h. The solvent was removed *in vacuo*, and Boc-deprotected **26** was obtained in 99% yield (9.9 mg). ^{1}H NMR and analytical HPLC indicated a single compound.

To a mixture of 6'-(indolin-1-yl)-1,3,3-trimethylspiro[indoline-2,3'-naphtho[2,1-*b*][1,4]oxazine]-5-carboxylic acid (**14**; 5.0 mg, 11 μmol) and HBTU (4.3 mg, 11 μmol) under argon was added dry DMF (0.50 mL). Deprotected **26** (9.9 mg, 9.4 μmol) and DIPEA (15 μL, 85 μmol) in dry DMF (1.5 mL) were added to the above solution. The reaction mixture was stirred for 1 h before being quenched with H_2O (2 mL). The solvents were removed under N_2 flow at 40 °C. The crude product was purified by RP-HPLC (method I) to yield a pink solid (2.2 mg, 17%). Rotamers are present. ^{1}H NMR (500 MHz, $CDCl_3$) δ (ppm): 8.60–8.52 (overlapped peaks, 2H), 8.47 (s, 1H), 8.23 (s, 1H), 8.03–7.74

(overlapped peaks, 7H), 7.73–7.57 (overlapped peaks, 6H), 7.48–7.34 (overlapped peaks, 4H), 7.30 (d, *J* = 7.8 Hz, 1H), 7.21 (d, *J* = 7.3 Hz, 2H), 7.00 (s, 1H), 6.96–6.86 (overlapped peaks, 6H), 6.81–6.70 (overlapped peaks, 8H), 6.63 (d, *J* = 8.1 Hz, 1H), 6.53 (d, *J* = 8.4 Hz, 1H), 6.27 (m, 1H), 4.01–3.83 (br. peaks, 13H), 3.83–3.49 (overlapped peaks, 84H), 3.47 (t, *J* = 6.6 Hz, 6H), 2.91–2.75 (overlapped peaks, 12H, including H34, H34'), 2.70 (m, 4H), 2.07–1.89 (br. s, 10H, H27, H27'), 1.82–1.72 (m, 5H), 1.66–1.53 (m, 7H), 1.50–1.21 (overlapped signals, 85H), 1.14 (s, 3H), 1.10 (s, 3H), 0.92–0.81 (overlapped peaks, 4H). HRMS (ESI +ve) *m/z*: 1046.68555, ([M+H]$^+$, $C_{82}H_{97}N_7O_{12}{}^{35}Cl$ requires 1406.68783). Analytical HPLC (method A), t_R = 20.1 min. UV-vis (CH_3OH) λ_{max} / nm (ε / M^{-1} cm^{-1}) 555 (6.3×10^4). Fluorescence emission (CH_3OH) λ_{max} / nm: 579.

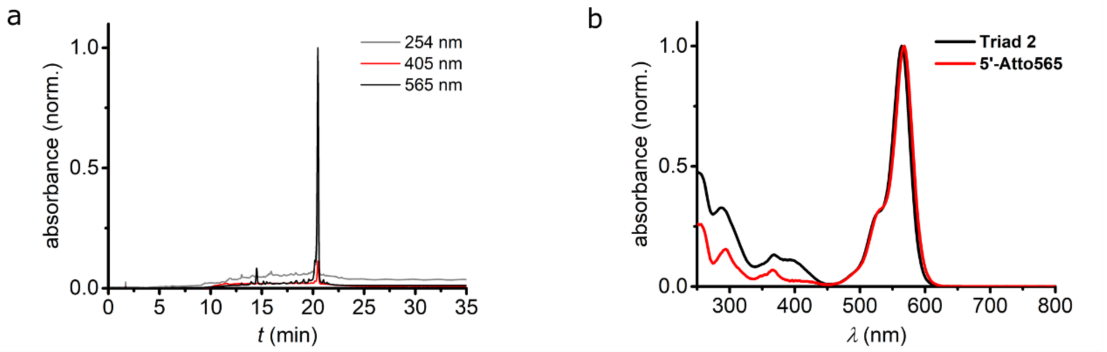

Figure 5-24 HPLC characterisation of **Triad 2** using method A. a) HPLC trace of **Triad 2** detected at 254, 405 and 565 nm. b) UV-vis absorption spectra obtained from the HPLC peaks of **Triad 2** and **5'-Atto565** dye.

Triethylammonium 6-amino-9-(2-carboxyphenyl)-3-iminio-3*H*-xanthene-4,5-disulfonate (sR110)

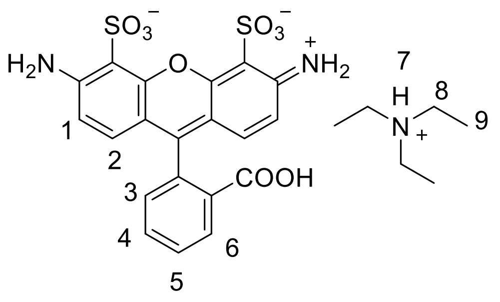

The title compound was kindly provided by Dr Andreas Vargas Jentzsch. The procedure was as follows.

The 40% fuming H_2SO_4 was made from mixing an equal amount of commercial fuming sulfuric acid, 20% free SO_3 basis (Sigma Aldrich, CAS 8014-95-7) and custom-made 55% fuming sulfuric acid solution that was prepared from addition of solid SO_3 to the commercial fuming sulfuric acid. Rhodamine 110 (100 mg, 0.30 mmol) was suspended in the 40% fuming H_2SO_4 solution (4.0 mL) at 10 °C and stirred for 5 h. The reaction mixture was carefully quenched with ice water (100 mL) containing NEt_3 (6 mL), and the solvents were removed. The crude product was purified by reverse-phased C18 silica gel chromatography (95:5 to 85:15 0.1% NEt_3 in H_2O/CH_3CN), yielding the product as a dark red solid (72 mg, 49%). R_f (RP-C18, 3:2 0.1% NEt_3 in H_2O/CH_3OH) = 0.84. ^{1}H NMR (500 MHz, D_2O) δ (ppm): 8.28 (dd, *J* = 7.2, 1.9 Hz, 1H, H6), 7.92–7.69 (m, 2H, H4, H5), 7.31 (dd, *J* = 7.2, 1.9 Hz, 1H, H3), 7.11 (d, *J* = 9.3 Hz, 2H, H2), 6.88 (d, *J* = 9.3 Hz, 2H, H1), 3.20 (q, *J* = 7.3 Hz, 9H, H8), 1.27 (t, *J* = 7.3 Hz, 12H, H9). $^{13}C\{^1H\}$ NMR (126 MHz, D_2O) δ (ppm): 171.3, 162.5, 156.5, 156.2, 133.8, 133.2, 132.7, 132.5, 131.1, 131.0, 130.7, 120.1, 114.4, 112.0, 47.3, 8.8. HRMS (ESI –ve) *m/z*: 489.00570, ($[M\text{-}HNEt_3]^-$, $C_{20}H_{13}N_2O_9S_2$ requires 489.00641). UV-vis (CH_3OH) λ_{max} / nm (ε / M^{-1} cm^{-1}) 493 (1.3×10^5). Fluorescence emission (CH_3OH) λ_{max} / nm (Φ_f): 516 (91%).

Triethylammonium 6-amino-3-iminio-9-(2-(methyl(prop-2-yn-1-yl)carbamoyl)phenyl)-3*H*-xanthene-4,5-disulfonate (28)

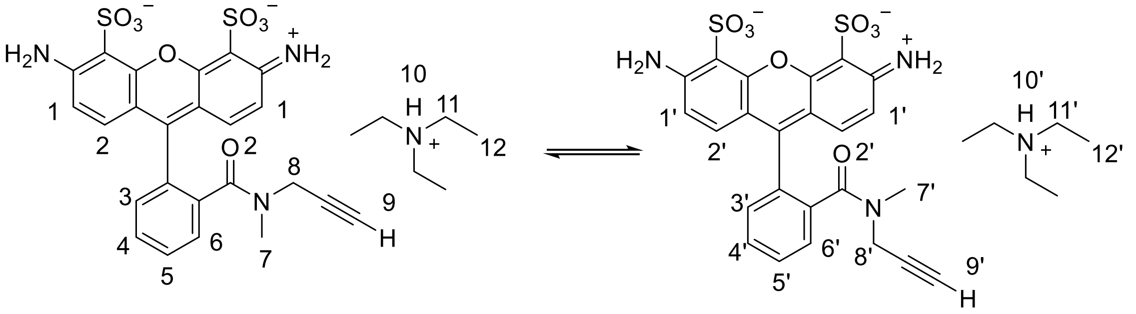

To a mixture of triethylammonium 6-amino-9-(2-carboxyphenyl)-3-iminio-3*H*-xanthene-4,5-disulfonate (**sR110**; 60 mg, 0.12 mmol) and HBTU (69 mg, 0.18 mmol) under argon was added dry DMF (5.0 mL). *N*-Methylprop-2-yn-1-amine (**32**; 24 µL, 0.24 mmol) and DIPEA (0.19 mL, 1.1 mmol) were added to the above solution. The reaction mixture was stirred at 100 °C for 30 min before being quenched with H_2O (1 mL). The solvents were removed using a distillation apparatus under 0.5 mBar at 40 °C. The crude material was purified by C18-reversed phase silica gel chromatography (1:0 to 9:1 0.1% NEt_3 in H_2O/CH_3OH) to yield a crystalline red solid (67 mg, 93%). R_f (RP-C18, 3:2 0.1% NEt_3 in H_2O/CH_3OH) = 0.71. ^{1}H NMR (500 MHz, D_2O) δ (ppm): 7.84–7.75 (overlapped m, 2H, H4, H4', H5, H5'), 7.74–7.68 (m, 0.2H, H6'), 7.68–7.62 (m, 0.7 H, H6), 7.60–7.51 (m, 1H, H3, H3'), 7.31 (d, *J* = 9.3 Hz, 2H, H2, H2'), 7.04–6.96 (overlapped d, 2H, H1, H1'), 3.99 (d, *J* = 2.5 Hz, 0.3H, H8'), 3.88 (s, 1.5H, H8), 3.20 (q, *J* = 7.3 Hz, 6H, H11, H11'), 2.79 (s, 2.4H, H7), 2.76 (s, 0.6H, H7'), 2.65 (t, *J* = 2.5 Hz, 0.1H, H9'), 2.52 (t, *J* = 2.5 Hz, 0.5H, H9), 1.28 (t, *J* = 7.3 Hz, 9H, H12, H12'). $^{13}C\{^1H\}$ NMR (126 MHz,

D_2O) δ (ppm): 170.2, 156.7, 156.1, 156.0, 155.8, 155.8, 134.3, 132.4, 132.2, 130.6, 130.2, 129.8, 129.7, 127.0, 119.6, 119.4, 113.8, 111.5, 76.9, 72.3, 46.6, 37.4, 36.5, 34.5, 32.2, 8.2. HRMS (ESI –ve) *m/z*: 540.05432, ([M-HNEt$_3$]$^-$, $C_{24}H_{18}N_3O_8S_2$ requires 540.05408).

N^2-(*tert*-Butoxycarbonyl)-N^6-diazo-*L*-lysine

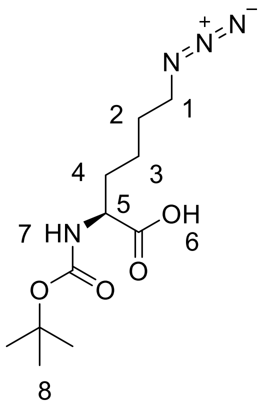

Cyclohexanaminium N^2-(*tert*-butoxycarbonyl)-N^6-diazo-*L*-lysinate (**29**; 100 mg, 0.27 mmol) was subjected to a H^+/cation exchange column on Amberlyst 15 resin using CH_3OH. The column was treated with 5% CH_3COOH/CH_3OH and rinsed with CH_3OH before. The acid product was obtained as a pale yellow oil (72 mg, 99%). ^1H NMR (400 MHz, $CDCl_3$) δ (ppm): 5.01 (d, *J* = 8.3 Hz, 1H, H7), 4.32 (m, 1H, H5), 3.29 (t, *J* = 6.7 Hz, 2H, H1), 1.97–1.82 (m, 1H), 1.78–1.57 (m, 3H), 1.56–1.35 (m, 11H).

tert-Butyl (*S*)-(6-azido-1-((2-(2-((6-chlorohexyl)oxy)ethoxy)ethyl)amino)-1-oxohexan-2-yl)carbamate (30)

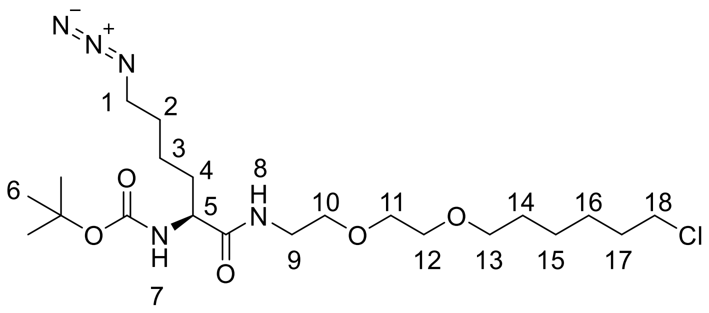

To a mixture of N^2-(*tert*-butoxycarbonyl)-N^6-diazo-*L*-lysine (53 mg, 0.19 mmol) and HBTU (112 mg, 0.30 mmol) under argon was added dry DMF (1.0 mL). (2-(2-((6-Chlorohexyl)oxy)ethoxy)ethan-1-aminium 2,2,2-trifluoroacetate (**20**; 80 mg, 0.24 mmol) and DIPEA (0.31 mL, 1.8 mmol) were added to the above solution. The reaction mixture was stirred for 3 h before being quenched with H_2O (0.2 mL). The solvents were removed using a distillation apparatus under 0.5 mBar at 40 °C. The crude product was purified by silica gel chromatography (CH_2Cl_2, 99:1 to 98:2 CH_2Cl_2/CH_3OH) to yield a yellow oil (96 mg, 99%). R_f (SiO_2, 9:1 CH_2Cl_2/CH_3OH) = 0.71. ^1H NMR (500 MHz, $CDCl_3$) δ (ppm): 6.39 (m, 1H, H8), 5.03 (d, *J* = 8.3 Hz, 1H, H7), 4.07 (m, 1H, H5), 3.64–3.59 (m, 2H), 3.59–3.51 (m, 6H), 3.47 (m, 4H), 3.27 (td, *J* = 6.8, 1.1 Hz, 2H, H1), 1.90–1.72 (m, 3H), 1.69–1.54 (m, 6H), 1.51–1.32 (m, 17H). $^{13}C\{^1H\}$ NMR (126 MHz, $CDCl_3$) δ (ppm): 171.8, 80.1, 71.4, 70.5, 70.2, 69.8, 54.5, 51.3, 45.2, 39.4, 32.7, 32.6, 29.6, 28.7, 28.5, 26.8, 25.6, 22.9. HRMS (ESI +ve) *m/z*: 478.27914, ([M+H]$^+$, $C_{21}H_{41}O_5N_5Cl$ requires 478.27907).

N-((*S*)-6-Azido-1-((2-(2-((6-chlorohexyl)oxy)ethoxy)ethyl)amino)-1-oxohexan-2-yl)-6'-(indolin-1-yl)-1,3,3-trimethylspiro[indoline-2,3'-naphtho[2,1-*b*][1,4]oxazine]-5-carboxamide (31)

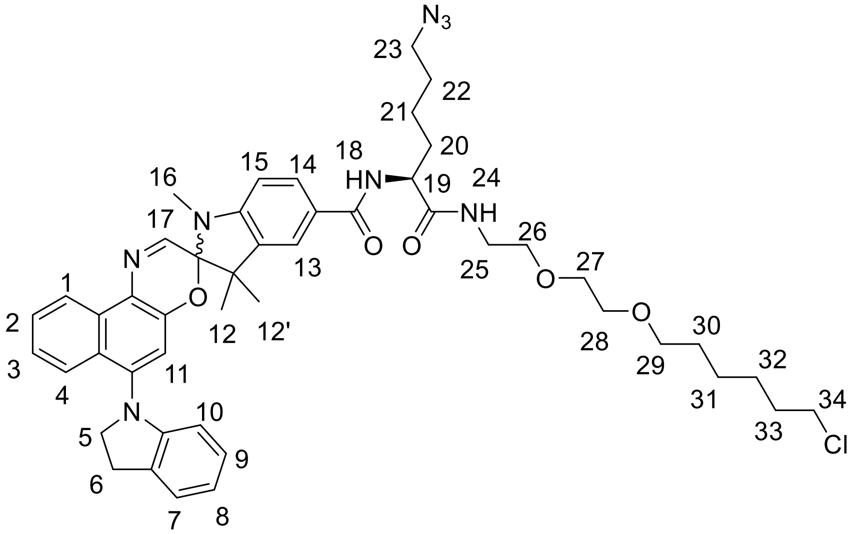

tert-Butyl (6-azido-1-((2-(2-((6-chlorohexyl)oxy)ethoxy)ethyl)amino)-1-oxohexan-2-yl)carbamate (**30**; 8.8 mg, 18 μmol) was dissolved in dry CH_2Cl_2 (1.0 mL), and the flask was purged with argon. TFA (0.10 mL) was added to the above solution, and the reaction was stirred for 1 h. The solvent was removed *in vacuo*, yielding deprotected **30** in 99% yield (9.0 mg).

To a mixture of 6'-(indolin-1-yl)-1,3,3-trimethylspiro[indoline-2,3'-naphtho[2,1-*b*][1,4]oxazine]-5-carboxylic acid (**14**; 10 mg, 20 μmol) and HBTU (8.3 mg, 22 μmol) under argon was added dry DMF (1.5 mL). Deprotected **30** (9.1 mg, 19 μmol) and DIPEA (30 μL, 17 μmol) were added to the above solution. The reaction mixture was stirred for 1 h before being quenched with H_2O (0.2 mL). The solvents were removed using a distillation apparatus under 0.5 mBar at 40 °C. The crude product was purified by silica gel chromatography (CH_2Cl_2, 99:1 to 9:1 CH_2Cl_2/CH_3OH) to yield a green solid (5.6 mg, 35%). R_f (SiO_2, 9:1 CH_2Cl_2/CH_3OH) = 0.45. Pure shift (proton-proton decoupled) ^{1}H NMR (600 MHz, $CDCl_3$) δ (ppm) (9.0–6.0 ppm): 8.61, 7.97, 7.69, 7.67, 7.60, 7.56, 7.55, 7.36, 7.19, 6.93, 6.91, 6.74, 6.69, 6.551, 6.546, 6.47, 6.30. ^{1}H NMR (600 MHz, $CDCl_3$) δ (ppm): 8.61 (d, *J* = 8.4 Hz, 1H, H1), 7.97 (d, *J* = 8.5 Hz, 1H, H4), 7.71–7.65 (overlapped 2 x d + s, 2H, H15 from both diastereomers and H18), 7.60 (ddd, *J* = 8.3, 6.7, 1.2 Hz, 1H, H2), 7.56 (d, *J* = 1.8 Hz, 0.5H, H14 from one diastereomer), 7.55 (d, *J* = 1.8 Hz, 0.5H, H14 from one diastereomer), 7.36 (ddd, *J* = 8.3, 6.7, 1.3 Hz, 1H, H3), 7.19 (d, *J* = 7.4 Hz, 1H, H7), 6.93 (t, *J* = 7.7 Hz, 1H, H9), 6.91 (d, *J* = 1.2 Hz, 1H, H11), 6.74 (t, *J* = 7.4 Hz, 1H, H8), 6.69 (dd, *J* = 8.0, 2.2 Hz, 1H, H18), 6.551 (d, *J* = 8.4 Hz, 0.5H, H16 from one diastereomer), 6.546 (d, *J* = 8.4 Hz, 0.5H, H16 from one diastereomer), 6.47 (t, *J* = 5.6 Hz, 1H, H19), 6.30 (d, *J* = 7.9 Hz, 1H, H10), 4.67–4.57 (m, 1H, H19), 3.91 (br. s, 2H, H5), 3.65–3.55 (m, 7H), 3.53 (td, *J* = 6.7, 1.6 Hz, 2H), 3.51–3.43 (m, 4H), 3.33–3.23 (m, 3H), 3.19 (br. s, 2H, H6), 2.83 (s, H17), 2.07–1.90 (m, 2H), 1.83–1.71 (m, 4H), 1.71–1.54 (m, 7H), 1.54–1.41 (m, 5H), 1.41–1.35 (m, 9H), 1.34–1.15 (m, 6H). $^{13}C\{^{1}H\}$ NMR (126 MHz, $CDCl_3$) δ (ppm): 171.8, 167.10, 167.07, 150.8, 150.0, 148.5, 144.7, 144.4, 136.5, 136.5, 131.8, 131.0, 128.7, 128.3, 128.1, 127.7, 127.0, 125.6, 125.30, 125.27, 124.9, 124.8, 123.9, 122.0, 121.3, 121.1, 120.7, 119.3, 110.0, 108.6, 106.5, 106.4, 98.9, 71.5, 70.6, 70.2, 69.7, 55.3, 53.3, 51.6, 51.3, 45.2, 39.5, 32.9, 32.7, 29.9, 29.7, 29.6, 29.1, 28.8, 25.6, 25.5, 22.8, 20.93, 20.91. HRMS (ESI +ve) *m/z*: 849.42065, ($[M+H]^+$, $C_{47}H_{58}N_8O_5Cl$ requires 849.42132).

Sodium 6-amino-9-(2-(((1-((5*S*)-6-((2-(2-((6-chlorohexyl)oxy)ethoxy)ethyl)amino)-5-(6'-(indolin-1-yl)-1,3,3-trimethylspiro[indoline-2,3'-naphtho[2,1-*b*][1,4]oxazine]-5-carboxamido)-6-oxohexyl)-1*H*-1,2,3-triazol-4-yl)methyl)(methyl)carbamoyl)phenyl)-3-iminio-3*H*-xanthene-4,5-disulfonate (Triad 3)

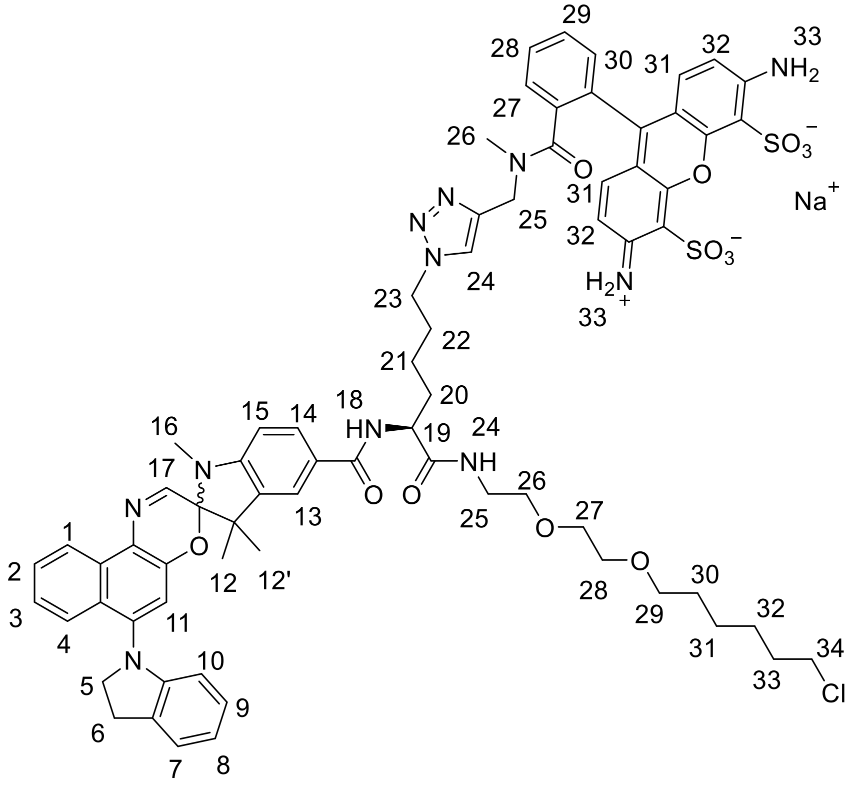

N-((*S*)-(6-Azido-1-((2-(2-((6-chlorohexyl)oxy)ethoxy)ethyl)amino)-1-oxohexan-2-yl)-6'-(indolin-1-yl)-1,3,3-trimethylspiro[indoline-2,3'-naphtho[2,1-*b*][1,4]oxazine]-5-carboxamide (**31**; 7.4 mg, 8.7 μmol) and triethylammonium 6-amino-3-iminio-9-(2-(methyl(prop-2-yn-1-yl)carbamoyl)phenyl)-3*H*-xanthene-4,5-disulfonate (**28**; 5.6 mg, 8.7 μmol) were suspended in 1:1 ^{t}BuOH/H_2O (0.4 mL). An aqueous solution of sodium ascorbate (70 μM, 0.10 mL) was added to the above suspension, followed by addition of an aqueous solution of $CuSO_4 \cdot 5H_2O$ (35 μM, 0.10 mL). The reaction mixture was stirred for 26 h before the solvents were removed using a distillation apparatus under 0.5 mBar at 40 °C. The crude product was purified by C18-reversed phase silica gel chromatography (0.1% NEt_3 in H_2O, 1:1 to 1:4 0.1% NEt_3 in H_2O/CH_3OH) to yield a pink solid (4.6 mg, 37%). R_f (RP-C18, CH_3OH) = 0.42 (streaking). ^{1}H NMR spectra recorded in different solvents reveal peaks from the diastereomers. ^{1}H NMR (400 MHz, *CDCl₃*) δ (ppm): 9.52 (br. s, 2H), 8.60 (d, *J* = 8.5 Hz, 1H, H1), 7.96 (d, *J* = 8.5 Hz, 1H, H4), 7.76 (2 x d, 1H, H15 from diastereomers), 7.69–7.42 (m, 6H), 7.35 (ddd, *J* = 8.2, 6.8, 1.3 Hz, 1H, H3), 7.22–7.13 (m, 2H), 7.03–6.83 (m, 5H), 6.79–6.70 (m, 1H), 6.68–6.60 (m, 1H), 6.59–6.48 (m, 2H), 6.29 (d, *J* = 8.0 Hz, 0.5H, H16 from a diastereomer), 6.28 (*J* = 8.0 Hz, 0.5H, H16 from a diastereomer), 4.69–4.57 (m, 1H), 4.57–4.26 (m, 4H), 3.91 (br. s, 2H), 3.70–3.26 (m, 15H), 3.17 (br. s, 2H), 2.96 (s, 1H), 2.92 (s, 1H), 2.82 (d, *J* = 5.6 Hz, 3H), 2.73 (s, 1H), 2.12–1.92 (m, 2H), 1.92–1.62 (m, 13H), 1.57 (p, *J* = 7.0 Hz, 1H), 1.50–0.95 (m, 24H). ^{1}H NMR (400 MHz, *1:1* $CDCl_3/CD_3OD$) δ (ppm): 8.53 (d, *J* = 8.5 Hz, 1H, H1), 7.93 (d, *J* = 8.4 Hz, 1H, H4), 7.86–7.72 (m, 2H), 7.69–7.51 (m, 8H), 7.33 (t, *J* = 7.8 Hz, 1H), 7.25 (d, *J* = 7.1 Hz, 1H), 7.15 (d, *J* = 7.3 Hz, 1H), 7.11 (s, 1H), 6.98–6.83 (m, 4H), 6.75–6.63 (m, 3H), 6.56 (d, *J* = 8.3 Hz, 1H), 6.26 (d, *J* = 7.9 Hz, 1H), 4.51 (d, *J* = 18.6 Hz, 2H), 4.38 (d, *J* = 26.8 Hz, 2H), 3.89 (s, 4H), 3.55 (d, *J* = 16.3 Hz, 6H), 3.49–3.45 (m, 1H), 3.42 (q, *J* = 6.2, 5.6 Hz, 3H), 3.29–3.24 (m, 5H), 2.96 (d, *J* = 4.6 Hz, 2H), 2.81 (s, 3H), 2.70 (s, 1H), 2.19–2.13 (m, 1H), 2.03–1.94 (m, 1H), 1.89–1.75 (m, 3H), 1.74–1.68 (m, 2H), 1.61–1.51 (m, 4H), 1.43–1.31 (m, 19H), 1.31–1.17 (m, 15H). HRMS (ESI –ve) *m/z*: 1388.47058, ($[M\text{-}Na]^-$, $C_{71}H_{75}N_{11}O_{13}ClS_2$ requires 1388.46812). Analytical HPLC (method D), t_R = 11.4 min. UV-vis (CH_3OH) λ_{max} / nm (ε / M^{-1} cm^{-1}) 506 (9.2×10^4). Fluorescence emission (CH_3OH) λ_{max} / nm (Φ_f): 525 (25%).

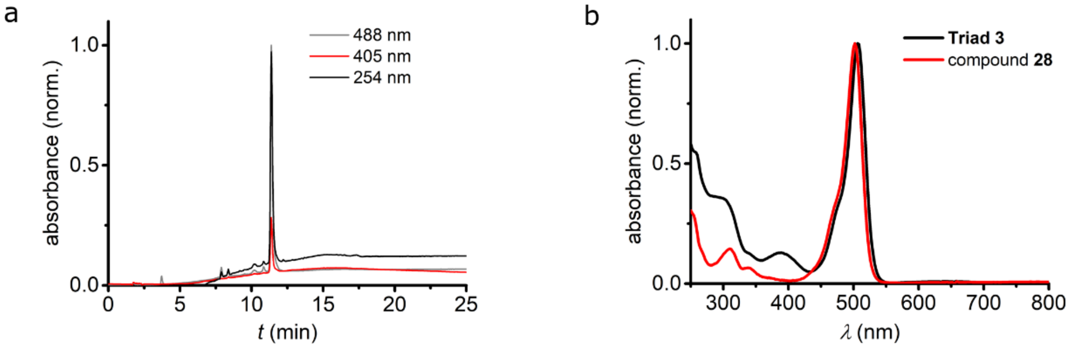

Figure 5-25 HPLC characterisation of **Triad 3** using method D. a) HPLC trace of **Triad 3** detected at 254, 405 and 565 nm. b) UV-vis absorption spectra obtained from the HPLC peaks of **Triad 3** and starting material **28**.

5-(But-3-yn-1-ylcarbamoyl)-2-(1,11-diethyl-2,2,4,8,10,10-hexamethyl-10,11-dihydro-2*H*-pyrano[3,2-*g*:5,6-*g'*]diquinolin-1-ium-6-yl)benzoate (33)

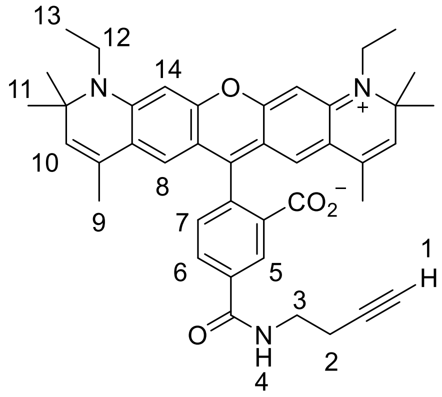

To **5’-Atto590** (15 mg, 24 µmol) under argon was added a DMF solution of HBTU (22 mᴍ, 1.3 mL, 29 µmol), followed by but-3-yn-1-amine (**32**) in dry DMF (79 mᴍ, 0.30 mL, 24 µmol) and DIPEA in dry DMF (0.17 ᴍ, 1.3 mL, 0.22 mmol). The reaction mixture was stirred for 1 h before being quenched with H_2O (1 mL). The solvents were removed using a distillation apparatus under 0.5 mBar at 40 °C, and the residue was washed with H_2O and extracted with CH_2Cl_2. The crude product was further purified by silica gel chromatography (99:1 to 92:8 CH_2Cl_2/CH_3OH) to yield the product as a deep purple solid (9.3 mg, 60%). R_f (SiO_2, 9:1 CH_2Cl_2/CH_3OH) = 0.25. ^{1}H NMR (400 MHz, CD_3OD) δ (ppm): 8.60 (d, J = 1.8 Hz, 1H, H5), 8.15 (dd, J = 7.9, 1.8 Hz, 1H, H6), 7.46 (d, J = 7.9 Hz, 1H, H7), 6.82 (s, 2H, H8), 6.81 (s, 2H, H14), 5.60 (s, 2H, H10), 3.73 (q, J = 7.0 Hz, 4H, H12), 3.59 (t, J = 7.1 Hz, 2H, H3), 2.57 (td, J = 7.1, 2.7 Hz, 2H, H2), 2.35 (t, J = 2.6 Hz, 1H, H1), 1.75 (d, J = 1.3 Hz, 6H, H9), 1.50 (s, 12H, H11), 1.37 (t, J = 7.0 Hz, 6H, H13). ^{13}C{^{1}H} NMR (101 MHz, CD_3OD) δ (ppm): 168.9, 159.5, 158.5, 153.6, 137.3, 137.0, 133.9, 131.4, 130.7, 130.2, 126.6, 124.8, 123.3, 115.0, 96.8, 82.2, 70.9, 61.4, 41.1, 40.3, 29.6, 29.5, 19.8, 18.3, 13.6. HRMS (ESI +ve) *m/z*: 642.33215, ($[M+H]^+$, $C_{41}H_{44}N_3O_4$ requires 642.33263).

tert-Butyl (*S*)-9-azido-1-(9*H*-fluoren-9-yl)-3,10-dioxo-2,14,17-trioxa-4,11-diazaicosan-20-oate (36)

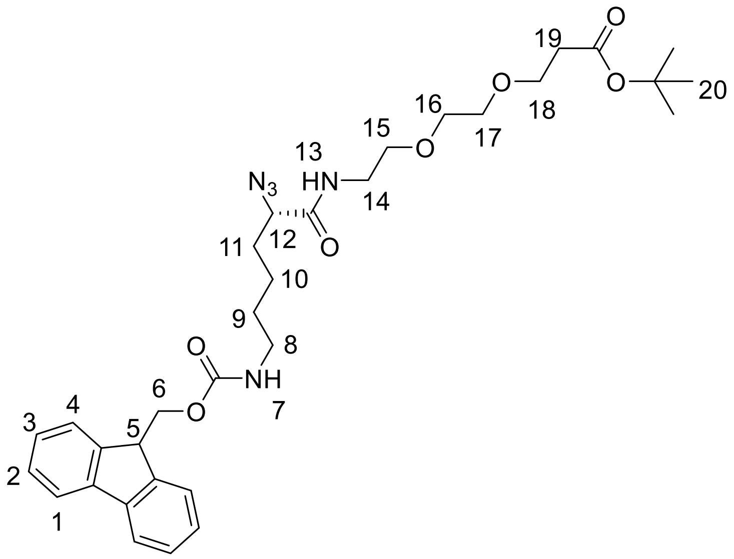

To a mixture of (*S*)-6-((((9*H*-fluoren-9-yl)methoxy)carbonyl)amino)-2-azidohexanoic acid (**34**; 334 mg, 0.85 mmol) and HBTU (387 mg, 1.0 mmol) under argon was added dry DMF (10 mL). *tert*-Butyl 3-(2-(2-aminoethoxy)ethoxy)propanoate (**35**; 217 mg, 0.93 mmol) and DIPEA (1.33 mL, 7.7 mmol) in dry DMF (10 mL) was added to the above solution. The reaction mixture was stirred for 2 h before being quenched with H_2O (1 mL). The solvents were removed using a distillation apparatus under 0.5 mBar at 40 °C. The crude product was purified by silica gel chromatography (8:2 to 3:7 petroleum ether/EtOAc) to yield a pale yellow oil (414 mg, 80%). R_f (SiO_2, EtOAc) = 0.54. ^{1}H NMR (400 MHz, $CDCl_3$) δ (ppm): 7.79 (d, J = 7.5 Hz, 2H, H1), 7.64 (d, J = 7.5 Hz, 2H, H4), 7.38 (dd, J = 7.6, 7.6 Hz, 2H, H2), 7.30 (dd, J = 7.4, 7.4 Hz, 2H, H3), 4.34 (d, J = 6.9 Hz, 2H, H6), 4.19 (t, J = 6.9 Hz, 1H, H5), 3.82 (t, J = 6.7 Hz, 1H, H12), 3.67 (t, J = 6.2 Hz, 2H, H18), 3.59–3.48 (overlapped, 6H, H15, H16, H17), 3.37 (t, J = 5.4 Hz, 2H, H14), 3.11 (t, J = 6.8 Hz, 2H, H8), 2.45 (t, J = 6.2 Hz, 2H, H19), 1.88–1.71 (m, 2H, H11), 1.57–1.48 (m, 2H, H9), 1.46–1.33 (overlapped s + m, 11H, H10, H20). ^{13}C{^{1}H} NMR (101 MHz, $CDCl_3$) δ (ppm): 171.4, 171.0, 157.5, 143.9, 141.2, 127.4, 126.7, 124.8, 119.5, 80.4, 70.0, 68.9, 66.5, 66.2, 62.8, 40.0, 39.0, 37.5, 35.8, 31.0, 29.0, 27.0, 22.4. HRMS (ESI +ve) *m/z*: 610.3262, ($[M+H]^+$, $C_{32}H_{44}N_5O_7$ requires 610.3241).

tert-Butyl (7S)-7-azido-1-(6'-(indolin-1-yl)-1,3,3-trimethylspiro[indoline-2,3'-naphtho[2,1-b][1,4]oxazin]-5-yl)-1,8-dioxo-12,15-dioxa-2,9-diazaoctadecan-18-oate (37)

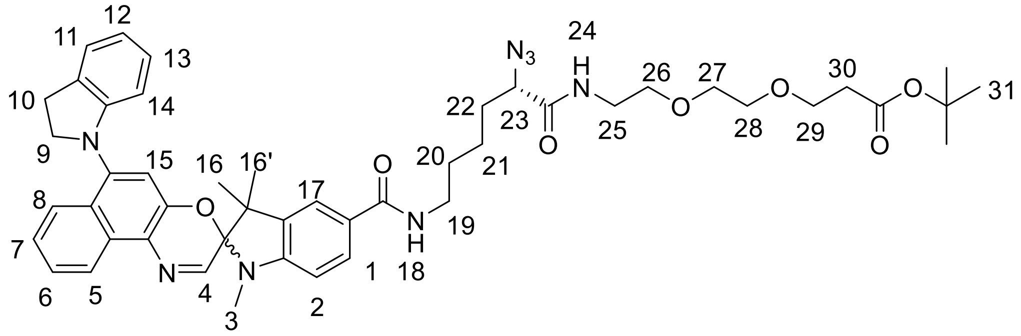

tert-Butyl (*S*)-9-azido-1-(9*H*-fluoren-9-yl)-3,10-dioxo-2,14,17-trioxa-4,11-diazaicosan-20-oate (**36**; 29 mg, 48 μmol) was dissolved in dry DMF (9.0 mL), and DBU (0.18 mL) was added to the above solution. The reaction was stirred for 0.5 h. The reaction mixture was subjected to a short plug of silica using CH_2Cl_2, 1:9 CH_3OH/CH_2Cl_2, and finally 3:10:87 $NEt_3/CH_3OH/CH_2Cl_2$ to give the deprotected product in 99% yield (18 mg).

To a mixture of 6'-(indolin-1-yl)-1,3,3-trimethylspiro[indoline-2,3'-naphtho[2,1-*b*][1,4]oxazine]-5-carboxylic acid (**14**; 17 mg, 35 μmol) and HBTU (16 mg, 42 μmol) under argon was added dry DMF (3.0 mL). *tert*-Butyl (*S*)-3-(2-(2-(6-amino-2-azidohexanamido)ethoxy)ethoxy)propanoate (Fmoc-deprotected **36**; 21 mg, 53 μmol) and DIPEA (56 μL, 0.31 mmol) in dry DMF (4.0 mL) were added to the above solution. The reaction mixture was stirred for 1.5 h before being quenched with H_2O (2 mL). The solvents were removed using a distillation apparatus under 0.5 mBar at 40 °C. The crude product was purified by silica gel chromatography (99:1 to 98:2 CH_2Cl_2/CH_3OH) to yield the product as a green oil (12 mg, 38%). R_f (SiO_2, 9:1 CH_2Cl_2/CH_3OH) = 0.44. ^{1}H NMR (400 MHz, $CDCl_3$) δ (ppm): 8.63 (d, *J* = 8.3 Hz, 1H, H5), 7.99 (d, *J* = 8.5 Hz, 1H, H8), 7.70 (s, 1H, H4), 7.66 (dd, *J* = 8.2, 1.9 Hz, 1H, H1), 7.65–7.61 (m, 1H, H6), 7.59 (d, *J* = 1.8 Hz, 1H, H17), 7.40–7.36 (m, 1H, H7), 7.22 (d, *J* = 7.2 Hz, 1H, H11), 6.98–6.92 (overlapped m+s, 2H, H13, H15), 6.85 (t, *J* = 5.6 Hz, 1H, H18), 6.79–6.74 (m, 1H, H12), 6.56 (d, *J* = 8.2 Hz, 1H, H2), 6.32 (d, *J* = 7.9 Hz, 1H, H14), 6.21 (t, *J* = 5.8 Hz, 1H, H24), 4.05–3.86 (overlapped t + br. s, 3H, H23, H9), 3.75 (t, *J* = 6.4 Hz, 2H, H29), 3.66–3.60 (m, 4H, H27, H28), 3.67–3.51 (m, 2H, H26), 3.55–3.41 (m, 4H, H19, H25), 3.21 (br. s, 2H, H10), 2.84 (s, 3H, H3), 2.53 (t, *J* = 6.4 Hz, 2H, H30), 2.05–1.86 (m, 2H, H22), 1.75–1.65 (m, 2H, H20), 1.62–1.48 (m, 2H, H21), 1.47 (s, 9H, H31), 1.42–1.36 (overlapped s, 6H, H16, H16'). $^{13}C\{^{1}H\}$ NMR (101 MHz, $CDCl_3$) δ (ppm): 171.0, 169.3, 167.4, 150.3, 149.9, 148.5, 144.3, 136.2, 131.7, 130.9, 127.6, 126.9, 126.2, 125.4, 124.73, 124.69, 124.6, 123.7, 121.9, 121.1, 120.5, 119.1, 109.9, 108.5, 106.2, 98.8, 80.7, 70.31, 70.30, 69.5, 66.9, 64.0, 55.2, 51.5, 39.5, 39.3, 36.3, 31.6, 29.6, 29.2, 28.9, 28.1, 25.3, 22.7, 20.8. HRMS (ESI +ve) *m/z*: 859.45001, ($[M+H]^+$, $C_{48}H_{59}N_8O_7$ requires 859.45012). Analytical HPLC (method A), t_R = 21.8, 23.4 min for two diastereomers.

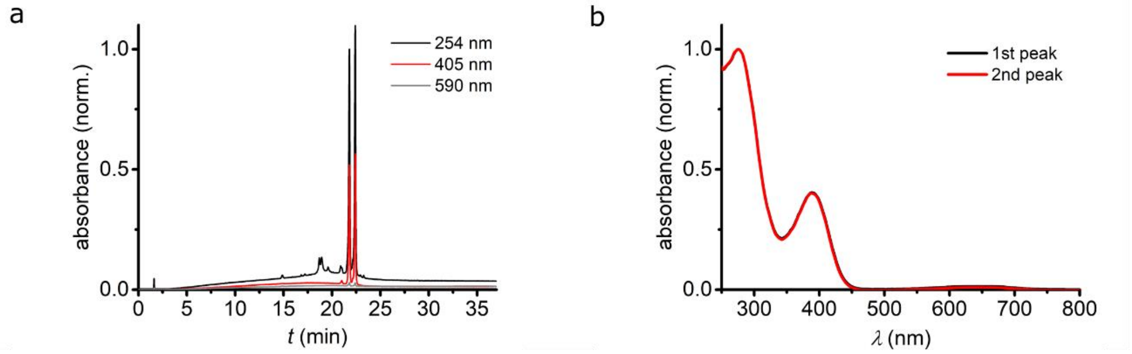

Figure 5-26 HPLC characterisation of compound **37** using method A. a) HPLC trace detected at 254, 405 and 565 nm. The two peaks represent two diastereomers of compound **37**. b) UV-vis absorption spectra obtained from the HPLC peaks in a).

2-(1,11-Diethyl-2,2,4,8,10,10-hexamethyl-10,11-dihydro-2*H*-pyrano[3,2-*g*:5,6-*g'*]diquinolin-1-ium-6-yl)-5-((2-(1-((7*S*)-1-(6'-(indolin-1-yl)-1,3,3-trimethylspiro[indoline-2,3'-naphtho[2,1-*b*][1,4]oxazin]-5-yl)-20,20-dimethyl-1,8,18-trioxo-12,15,19-trioxa-2,9-diazahenicosan-7-yl)-1*H*-1,2,3-triazol-4-yl)ethyl)carbamoyl)benzoate (38)

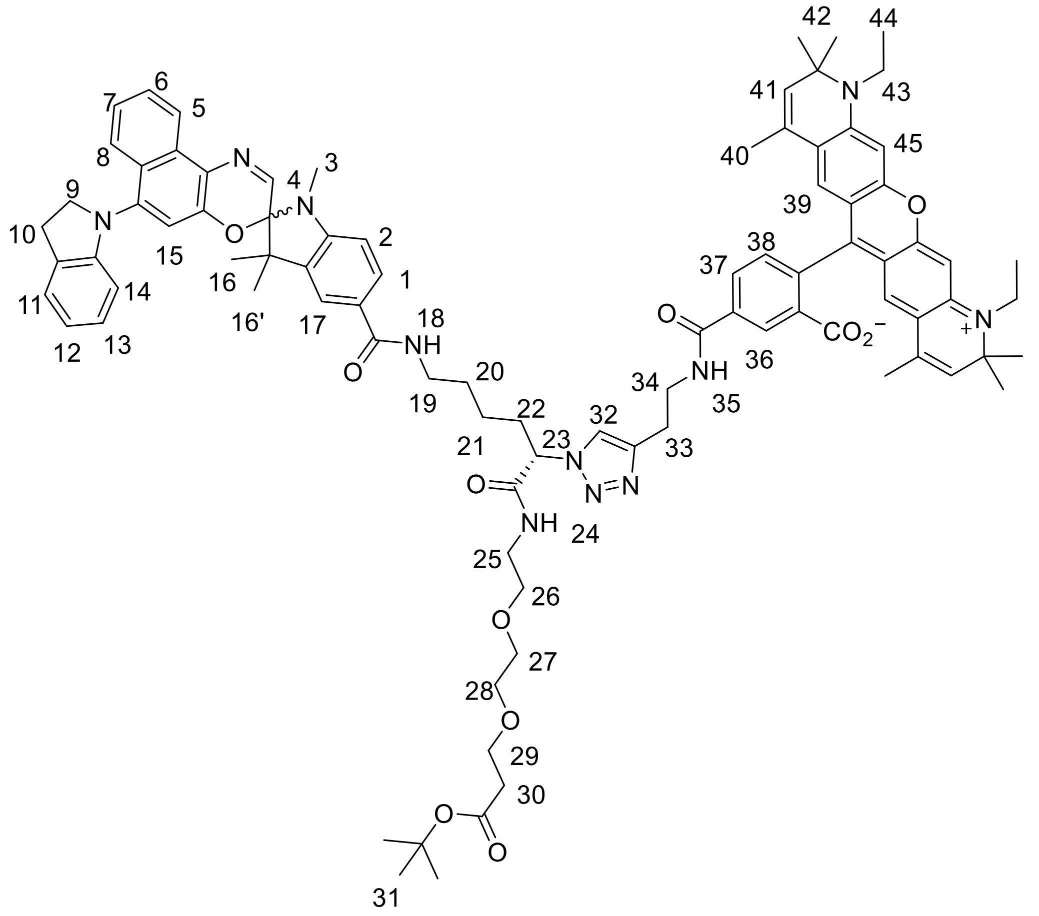

A suspension of 5-(but-3-yn-1-ylcarbamoyl)-2-(1,11-diethyl-2,2,4,8,10,10-hexamethyl-10,11-dihydro-2*H*-pyrano[3,2-*g*:5,6-*g'*]diquinolin-1-ium-6-yl)benzoate (**33**; 4.3 mg, 6.7 μmol), *tert*-butyl (7*S*)-7-azido-1-(6'-(indolin-1-yl)-1,3,3-trimethylspiro[indoline-2,3'-naphtho[2,1-*b*][1,4]oxazin]-5-yl)-1,8-dioxo-12,15-dioxa-2,9-diazaoctadecan-18-oate (**37**; 5.8 mg, 6.7 μmol), $CuSO_4 \cdot 5H_2O$ (0.67 mg, 2.7 μmol), sodium ascorbate (1.1 mg, 5.4 μmol) in 1:1 ^{t}BuOH/H_2O (2.4 mL) was stirred at room temperature for 3.5 h. ^{t}BuOH was removed on a rotatory evaporator, and the remaining aqueous solution was extracted with CH_2Cl_2. The organic layers were washed with H_2O. The combined organic fractions were dried over Na_2SO_4 and the solvents removed *in vacuo*. The crude product was purified by size exclusion chromatography (Bio-Rad, 40–60 μm styrene divinylbenzene beads, ≤ 2000 MW) with $CHCl_3$ as the eluent, and the residue was precipitated from *n*-hexane.

The product was obtained as a purple solid (8.2 mg, 81%). R_f (SiO_2, 9:1 CH_2Cl_2/CH_3OH) = 0.24. ^{1}H NMR (400 MHz, $CDCl_3$) δ (ppm): 8.60 (d, *J* = 8.5 Hz, 1H, H5), 8.45 (s, 1H, H37), 8.17 (dt, *J* = 7.8, 2.0 Hz, 1H, H38), 7.96 (d, *J* = 8.5 Hz, 1H, H8), 7.80 (s, 1H), 7.76–7.68 (m, 2H, H1 and unassigned), 7.63 (2 x s, 1H, H4, 2 diastereomers), 7.60 (t, *J* = 7.6 Hz, 1H, H6), 7.53–7.41 (m, 2H), 7.35 (t, *J* = 7.6 Hz, 1H, H7), 7.23–7.16 (m, 2H), 6.94–6.87 (m, 2H, H13 and unassigned), 6.73 (td, *J* = 7.4, 1.0 Hz, 1H, H12), 6.60–6.55 (m, 2H), 6.42 (dd, *J* = 8.1, 1.8 Hz, 1H, H2), 6.32 (t, *J* = 4.1 Hz, 2H), 6.28 (dd, *J* = 7.9, 3.3 Hz, 1H), 5.42–5.33 (m, 1H, H23), 5.22 (s, 1H, H41, diastereomer), 5.18 (s, 1H, H41, diastereomer), 4.00–3.81 (m, 4H, H9, H34), 3.73–3.62 (m, 2H, H29), 3.57–3.45 (m, 6H), 3.44–3.26 (m, 6H), 3.23–3.13 (m, 2H, H10), 3.10 (m, 2H, H33), 2.76 (2 x s, 3H, H3, 2 x diastereomers), 2.51–2.45 (m, 2H, H30), 2.19 (m, 1H, H22), 1.66 (s, 3H, H40, diastereomer), 1.64 (s, 3H, H40, diastereomer), 1.43 (s, 12H, H42), 1.38–1.32 (m, 10H), 1.31–1.06 (m, 15H). HRMS (ESI +ve) *m/z*: 750.89117, ($[M+2H]^{2+}$, $C_{89}H_{103}N_{11}O_{11}^{2+}$ requires 750.89138). HRMS (MALDI +ve) *m/z*: 1501.5946, ($[M+H]^+$, $C_{89}H_{102}N_{11}O_{11}^+$ requires 1501.7838). Analytical HPLC (method E), t_R = 16.8 min.

5-((2-(1-((7*S*)-17-Carboxy-1-(6'-(indolin-1-yl)-1,3,3-trimethylspiro[indoline-2,3'-naphtho[2,1-*b*][1,4]oxazin]-5-yl)-1,8-dioxo-12,15-dioxa-2,9-diazaheptadecan-7-yl)-1*H*-1,2,3-triazol-4-yl)ethyl)carbamoyl)-2-(1,11-diethyl-2,2,4,8,10,10-hexamethyl-10,11-dihydro-2*H*-pyrano[3,2-*g*:5,6-*g'*]diquinolin-1-ium-6-yl)benzoate (^{t}Bu-deprotected 38)

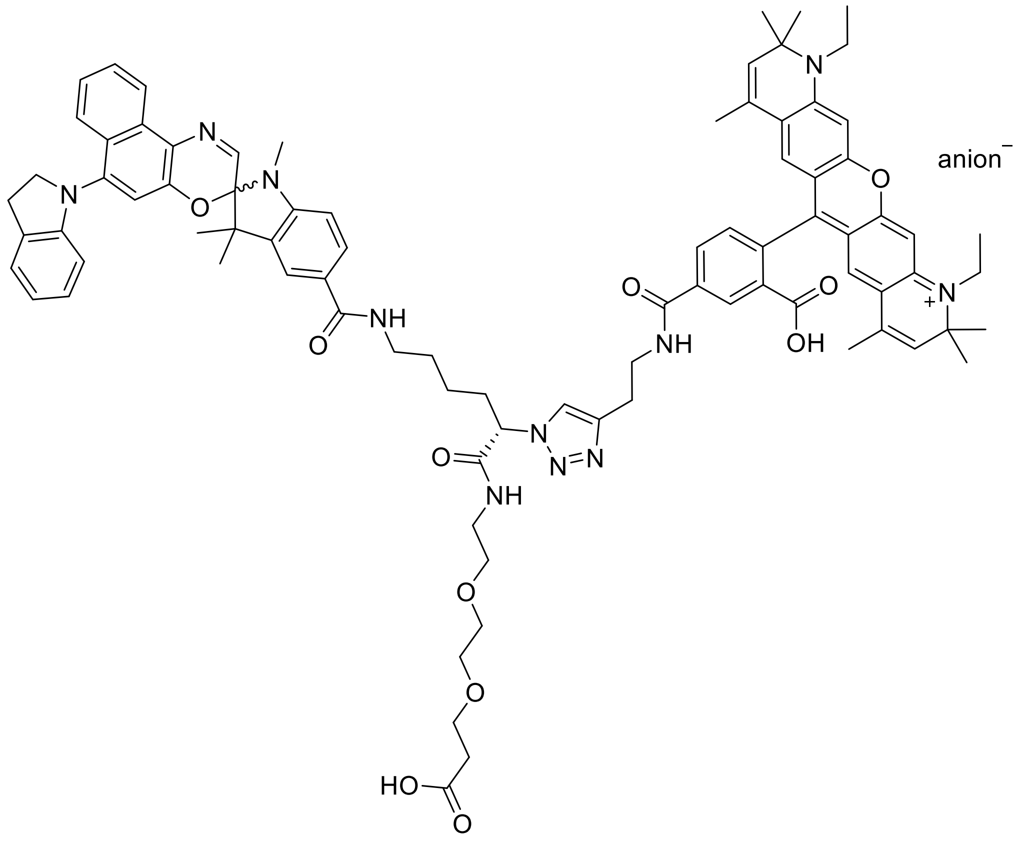

A suspension of compound **38** (4.1 mg, 2.7 μmol) and $ZnBr_2$ (20 mg, 89 μmol) in CH_2Cl_2 (2.0 mL) was stirred at room temperature for 9 h. The reaction mixture was diluted with H_2O and extracted with CH_2Cl_2. To the combined organic fractions was added H_2O, and the mixture was stirred vigorously for 30 min. The organic fraction was separated, and the solvent removed *in vacuo*. The product was obtained as a deep purple solid (2.4 mg, 61%). HRMS (ESI +ve) *m/z*: 1444.70959, ([M-anion]$^+$, $C_{85}H_{94}N_{11}O_{11}$ requires 1444.71288). Analytical HPLC (method E), t_R = 16.5 min. Analytical HPLC (method F), t_R = 15.1 min (later for reference to HPLC trace of **Triad 4**).

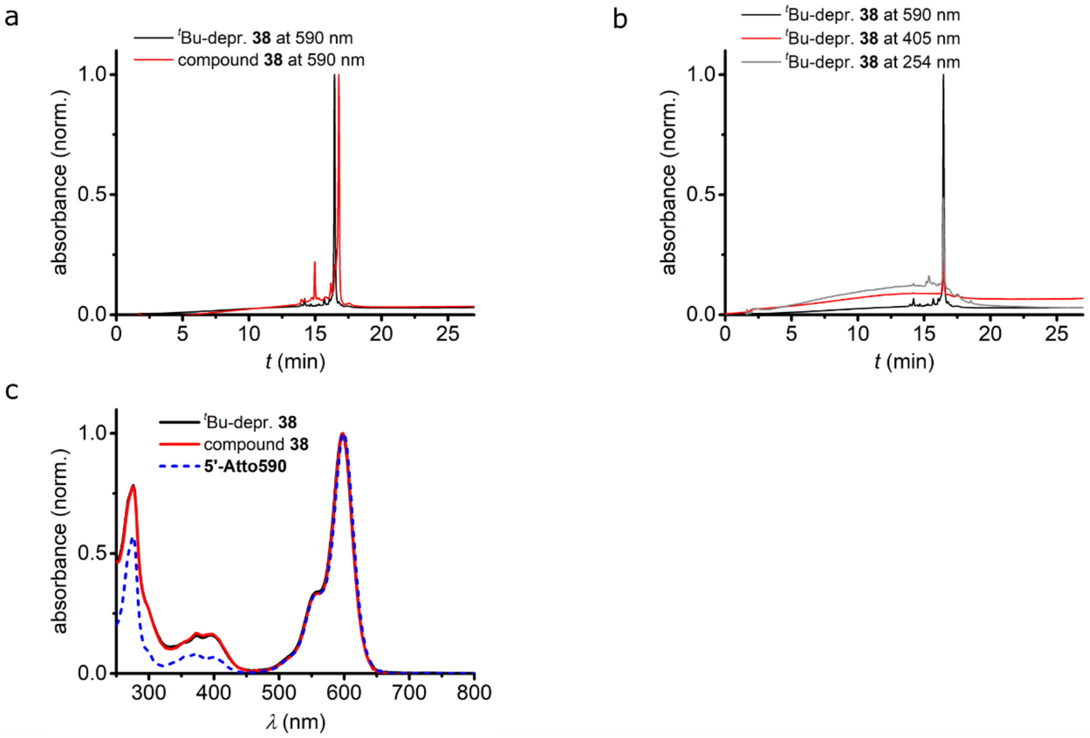

Figure 5-27 HPLC characterisation of ^{t}Bu-deprotected **38** with reference to compound **38** using method E. a) HPLC traces of the deprotected product and starting material **38**, detected at 590 nm. b) HPLC trace of the deprotected product detected at 254, 405 and 590 nm. c) UV-vis absorption spectra of the product, starting material **38** and **5’-Atto590** dye.

6-(5-((2-(1-((7*S*)-18-((2,5-Dioxopyrrolidin-1-yl)oxy)-1-(6'-(indolin-1-yl)-1,3,3-trimethylspiro[indoline-2,3'-naphtho[2,1-*b*][1,4]oxazin]-5-yl)-1,8,18-trioxo-12,15-dioxa-2,9-diazaoctadecan-7-yl)-1*H*-1,2,3-triazol-4-yl)ethyl)carbamoyl)-2-(((2,5-dioxopyrrolidin-1-yl)oxy)carbonyl)phenyl)-1,11-diethyl-2,2,4,8,10,10-hexamethyl-10,11-dihydro-2*H*-pyrano[3,2-*g*:5,6-*g'*]diquinolin-1-ium anion (Triad 4)

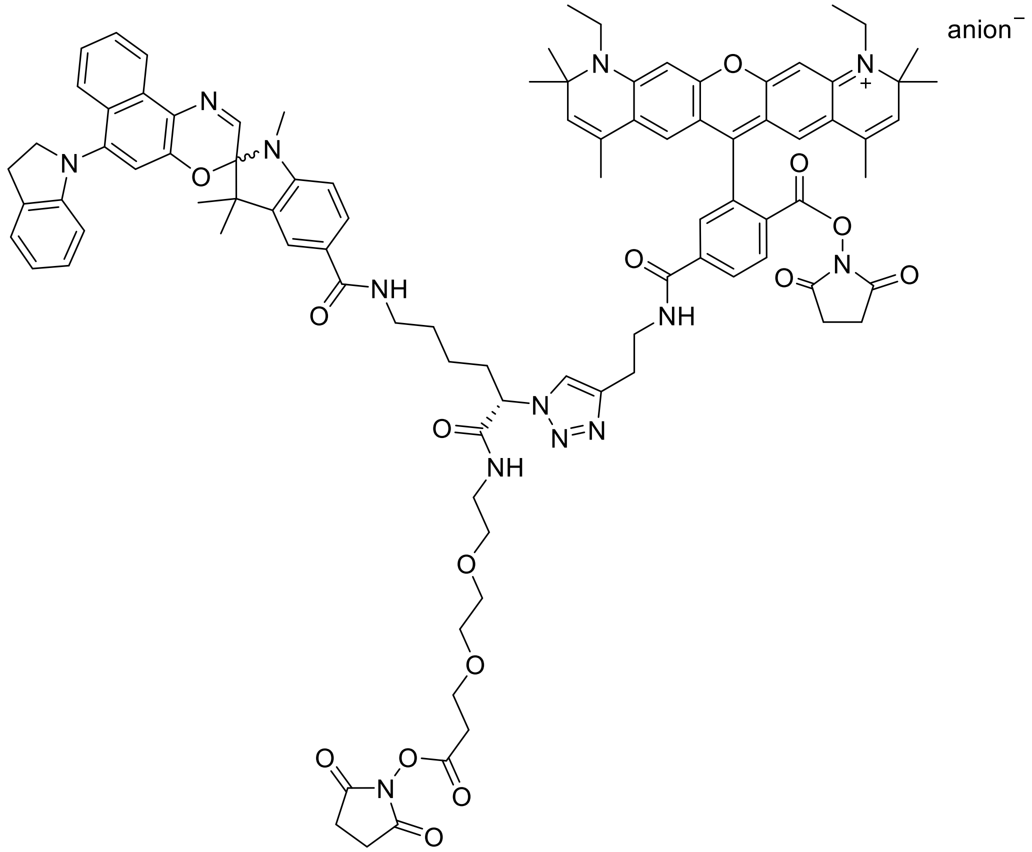

To a DMF solution (0.10 mL) of ^{t}Bu-deprotected **38** (2.4 mg, 1.7 µmol) was added DCC in dry DMF (12 mM, 0.20 mL, 2.5 µmol) and *N*-hydroxysuccinimide (NHS) in dry DMF (13 mM, 0.20 mL, 2.5 µmol), and the mixture was stirred at room temperature. Monitoring by TLC and analytical HPLC indicated only the starting material (in retrospective, the mono-ester may be formed that has a R_f almost identical to that of deprotected **38**), so more DCC and NHS were added in two batches giving a total of 14 µmol of DCC and 14 µmol of NHS. The reaction was also made more concentrated by reducing the solvent volume to ca. 0.2 mL. After two days, the reaction was heated to 50 °C for 7 h and the solvent was removed. The crude product was purified by size exclusion chromatography (Bio-Rad, 40–60 µm styrene divinylbenzene beads, ≤ 2000 MW) with $CHCl_3$ as the eluent, and the residue was precipitated from Et_2O. The product was obtained as a deep purple solid (1.7 mg, 57% based on PF_6^- as counter-ion). HRMS (ESI +ve) *m/z*: 1638.73938, ($[M\text{-anion}]^+$, $C_{93}H_{100}N_{13}O_{15}$ requires 1638.74564). Analytical HPLC (method F), t_R = 15.4 min. UV-vis (CH_2Cl_2) λ_{max} / nm (ε / M^{-1} cm^{-1}) 607 (1.0×10^5). Fluorescence emission (CH_2Cl_2) λ_{max} / nm: 633.

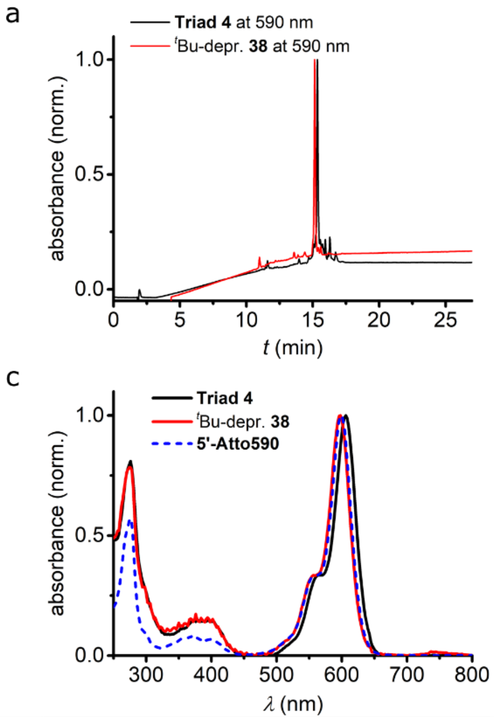

Figure 5-28 HPLC characterisation of **Triad 4** using method F. a) HPLC traces of **Triad 4** and starting material, i.e. ᵗBu-deprotected **38**, detected at 590 nm. b) HPLC trace of **Triad 4** detected at 254, 405 and 590 nm. c) UV-vis absorption spectra of **Triad 4**, deprotected **38** and **5'-Atto590** dye.

5.7 References

[1] B. N. G. Giepmans, S. R. Adams, M. H. Ellisman, R. Y. Tsien, *Science* **2006**, *312*, 217–224.
[2] T. Kogure, S. Karasawa, T. Araki, K. Saito, M. Kinjo, A. Miyawaki, *Nat. Biotechnol.* **2006**, *24*, 577–581.
[3] K. A. Lukyanov, D. M. Chudakov, S. Lukyanov, V. V. Verkhusha, *Nat. Rev. Mol. Cell Biol.* **2005**, *6*, 885–890.
[4] L. W. Miller, V. W. Cornish, *Curr. Opin. Chem. Biol.* **2005**, *9*, 56–61.
[5] I. Kumagai, K. Tsumoto, in *Encycl. Life Sci.*, American Cancer Society, **2010**.
[6] D. E. Chandler, R. W. Roberson, *Bioimaging: Current Concepts in Light & Electron Microscopy*, Jones & Bartlett Publishers, **2009**.
[7] G. Mattson, E. Conklin, S. Desai, G. Nielander, M. D. Savage, S. Morgensen, *Mol. Biol. Rep.* **1993**, *17*, 167–183.
[8] J. A. Ramos-Vara, *Vet. Pathol.* **2005**, *42*, 405–426.
[9] J. Charles A Janeway, P. Travers, M. Walport, M. J. Shlomchik, *Immunobiol. Immune Syst. Health Dis. 5th Ed.* **2001**.
[10] L. Xue, I. A. Karpenko, J. Hiblot, K. Johnsson, *Nat. Chem. Biol.* **2015**, *11*, 917–923.
[11] D. Jung, K. Min, J. Jung, W. Jang, Y. Kwon, *Mol. Biosyst.* **2013**, *9*, 862–872.
[12] T. Gronemeyer, G. Godin, K. Johnsson, *Curr. Opin. Biotechnol.* **2005**, *16*, 453–458.

[13] I. Chen, A. Y. Ting, *Curr. Opin. Biotechnol.* **2005**, *16*, 35–40.

[14] M. Z. Lin, L. Wang, *Physiology* **2008**, *23*, 131–141.

[15] B. A. Griffin, S. R. Adams, R. Y. Tsien, *Science* **1998**, *281*, 269–272.

[16] S. R. Adams, R. E. Campbell, L. A. Gross, B. R. Martin, G. K. Walkup, Y. Yao, J. Llopis, R. Y. Tsien, *J. Am. Chem. Soc.* **2002**, *124*, 6063–6076.

[17] A. Keppler, S. Gendreizig, T. Gronemeyer, H. Pick, H. Vogel, K. Johnsson, *Nat. Biotechnol.* **2003**, *21*, 86–89.

[18] A. Keppler, H. Pick, C. Arrivoli, H. Vogel, K. Johnsson, *Proc. Natl. Acad. Sci.* **2004**, *101*, 9955–9959.

[19] A. Gautier, A. Juillerat, C. Heinis, I. R. Corrêa, M. Kindermann, F. Beaufils, K. Johnsson, *Chem. Biol.* **2008**, *15*, 128–136.

[20] G. V. Los, L. P. Encell, M. G. McDougall, D. D. Hartzell, N. Karassina, C. Zimprich, M. G. Wood, R. Learish, R. F. Ohana, M. Urh, et al., *ACS Chem. Biol.* **2008**, *3*, 373–382.

[21] V. Singh, S. Wang, E. T. Kool, *J. Am. Chem. Soc.* **2013**, *135*, 6184–6191.

[22] A. Pulsipher, M. E. Griffin, S. E. Stone, L. C. Hsieh-Wilson, *Angew. Chem. Int. Ed.* **2015**, *54*, 1466–1470.

[23] Y. Zhang, M. So, A. M. Loening, H. Yao, S. S. Gambhir, J. Rao, *Angew. Chem. Int. Ed.* **2006**, *45*, 4936–4940.

[24] G. Cooper, R. Hausman, *The Cell: A Molecular Approach*, Sinauer Associates, Inc., **2006**.

[25] J. Newman, T. S. Peat, R. Richard, L. Kan, P. E. Swanson, J. A. Affholter, I. H. Holmes, J. F. Schindler, C. J. Unkefer, T. C. Terwilliger, *Biochemistry* **1999**, *38*, 16105–16114.

[26] M. J. Hynes, J. A. Maurer, *Angew. Chem. Int. Ed.* **2012**, *51*, 2151–2154.

[27] H. A. Benink, M. G. McDougall, D. H. Klaubert, G. V. Los, *BioTechniques* **2009**, *47*, 769–774.

[28] M. L. Alessi, A. I. Norman, S. E. Knowlton, D. L. Ho, S. C. Greer, *Macromolecules* **2005**, *38*, 9333–9340.

[29] N. Vennemann, M. D. Lechner, R. C. Oberthür, *Polymer* **1987**, *28*, 1738–1748.

[30] H. Li, H. Guan, X. Duan, J. Hu, G. Wang, Q. Wang, *Org. Biomol. Chem.* **2013**, *11*, 1805–1809.

[31] X. Chen, T. Pradhan, F. Wang, J. S. Kim, J. Yoon, *Chem. Rev.* **2012**, *112*, 1910–1956.

[32] J. Magano, B. G. Conway, D. Farrand, M. Lovdahl, M. T. Maloney, M. J. Pozzo, J. J. Teixeira, J. Rizzo, D. Tumelty, *Synthesis* **2014**, *46*, 1399–1406.

[33] Y. Wu, D. C. Limburg, D. E. Wilkinson, M. J. Vaal, G. S. Hamilton, *Tetrahedron Lett.* **2000**, *41*, 2847–2849.

[34] R. Kaul, Y. Brouillette, Z. Sajjadi, K. A. Hansford, W. D. Lubell, *J. Org. Chem.* **2004**, *69*, 6131–6133.

[35] D. E. Yelton, C. Desaymard, M. D. Scharff, *Hybridoma* **1981**, *1*, 5–11.

[36] C. Cizmowski, M. Jung, R. Erdmann, W. Schliebs, *Hybridoma* **2011**, *30*, 387–391.

[37] J. J. Smith, J. D. Aitchison, *Nat. Rev. Mol. Cell Biol.* **2013**, *14*, 803–817.

[38] G. Jones, P. Willett, R. C. Glen, *J. Mol. Biol.* **1995**, *245*, 43–53.

[39] Y. Liu, K. Miao, N. P. Dunham, H. Liu, M. Fares, A. K. Boal, X. Li, X. Zhang, *Biochemistry* **2017**, *56*, 1585–1595.

Chapter 6

RESOLFT Imaging on Vesicles

6 RESOLFT Imaging on Vesicles

Chapter 5 describes the unsuccessful application of the HaloTag technique with our spirooxazine-based dyads. Problems with HaloTag labelling made it difficult to test our dyads for super-resolution microscopy in live cells. Alternative strategies were explored to provide insights into the scope of our system. One is the immunolabelling method, of which the ongoing progress is reported in Chapter 5. The other is discussed here, i.e. employment of synthetic vesicles to study performance of our spirooxazine-based dyads.

6.1 Introduction to vesicles

Vesicles are supramolecular structures comprising one or more lipid bilayer membranes (with or without incorporation of proteins) that segregate the fluid in the interior compartment from the environment.[1] Bilayers are composed of amphiphiles, i.e. molecules with hydrophilic and hydrophobic components, and a typical amphiphile in biological systems is a phospholipid, e.g. 1-palmitoyl-2-oleoyl-sn-glycero-3-phosphocholine (POPC; **Figure 6-1**a, b). Bilayers made of POPC are 4 nm thick,[2] which is far below the diffraction limit of conventional confocal microscopes. The subsequent vesiculation process is driven by minimising undesirable exposure of the hydrophobic parts to water at the edge of the bilayer, and occurs when the driving force outcompetes the bending resistance.[3] Vesicles can be categorised into biological vesicles that are produced in Nature, such as peroxisomes and lysosomes, and synthetic/artificial vesicles that are prepared in laboratories.[4] The latter can be further classified into small unilamellar vesicles (SUVs; < 100 nm), large unilamellar vesicles (LUVs; 100 nm – 1000 nm), giant unilamellar vesicles (GUVs; > 1 μm), and multilamellar vesicles (MLVs), depending on the number of layers and size (**Figure 6-1**c).[1]

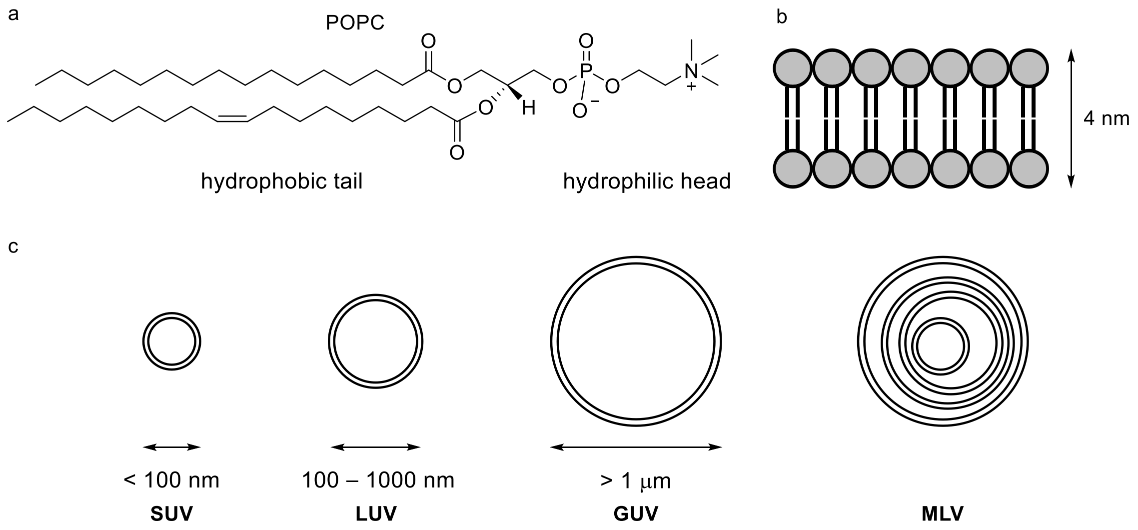

Figure 6-1 a) Chemical structure of a typical phospholipid, POPC, consisting of a hydrophilic head and hydrophobic tail. b) Formation of a lipid bilayer, with the hydrophilic head facing the aqueous environments and the hydrophobic tail being shielded away from water. The membrane thickness if POPC is used is 4 nm. c) Classification of synthetic vesicles. Small unilamellar vesicle (SUV), diameter < 100 nm. Large unilamellar vesicle (LUV), diameter 100 – 1000 nm. Giant unilamellar vesicle (GUV), diameter > 1 μm. Multilamellar vesicle (MLV).

Given the complexity of biological systems, synthetic vesicles have been developed as a close but simplified analogy to study a broad range of biophysical properties and membrane dynamics, e.g. membrane permeability, fusion and functions.[5–7] A more recent and rapidly growing field is application of synthetic vesicles in medical diagnostics and targeted drug delivery.[8–12] Additionally, much research interest has been focused on engineering and constructing artificial cells, as compartmentalisation is believed to play a key role in the origin of life.[13,14] This provides coincident development for biotechnology and biomedical application. We chose this simplified model system as it may reduce the complexity associated with cellular environments and help elucidate what causes the difficulties of our live-cell imaging. Moreover, if a proof of concept was realised by super-resolved imaging of vesicles, it would unambiguously validate the feasibility of our molecular design for such an application.

6.2 LUVs

We first explored the performance of spirooxazine-based **Dyad 3** (structure in **Figure 6-2**; detailed in Chapter 4) in large unilamellar vesicles (LUVs).

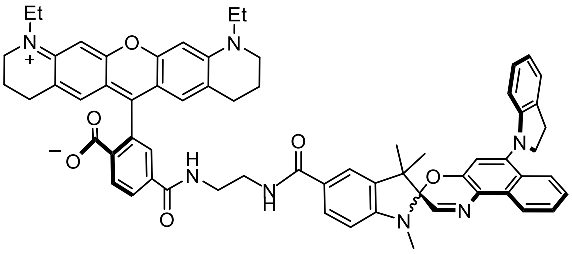

Figure 6-2 Molecular structure of spirooxazine-based **Dyad 3**.

Two techniques, i.e. sonication and extrusion, are widely used to prepare large and small unilamellar vesicles (LUVs and SUVs). The sonication method relies on ultrasonic energy to break the initially formed large and multilamellar vesicles (MLVs) into smaller vesicles that may be unilamellar or multilamellar.[15] The average size and population distribution of vesicles prepared from sonication are highly dependent on the duration and intensity of the sonication.[15,16] On the other hand, the extrusion method provides monodispersed unilamellar vesicles of a controlled size by passing the lipid suspension through membrane filters of a defined pore size under pressure.[17,18] Generally, the extrusion protocol offers higher reproducibility from batch to batch, but is more time-consuming compared to the sonication method. For the imaging purpose, we employed sonication and subsequently extrusion in order to reliably prepare a homogenous population of vesicles each time. **Dyad 3** was introduced along with other membrane compositions at the early stage. In addition to the main composition of POPC lipid, the vesicles also incorporated 0.25% w/w 1,2-distearoyl-sn-glycero-3-phosphoethanolamine-*N*-[biotinyl(polyethylene glycol)-2000] (DSPE-PEG(2000) biotin) for subsequent immobilisation on a surface that was treated with bovine serum albumin-biotin (BSA-biotin) and then streptavidin. This fixation method utilises strong non-covalent interactions between biotin and streptavidin.[19] Alternatively, the surface was treated with polylysine (PLL) before addition of vesicles. Because of nonspecific adsorption, PLL passivates the surface to prevent vesicles from collapsing in contact with the surface, and to immobilise vesicles (of large sizes) to some extent.[20] Both BSA-biotin[21] and PLL[22] methods have been reported for coverslip coating. Vesicles were prepared freshly before each imaging experiment due to their short shelf life. The details of the above procedures can be found in the Experimental Section.

6.2.1 Confocal imaging of LUVs

The biotin fixation method usually provided a denser population of LUVs compared to those from the PLL method (**Figure 6-3**). The brightness ratio of the two was 2.0:1. The higher density could be attributed to strong interaction between biotin and streptavidin as expected. A dense vesicle population is preferred as this provides a higher probability of finding suitable vesicles to image to obtain reliable and consistent data. Thus, most of the images shown below were acquired on LUVs fixed by biotin unless otherwise specified.

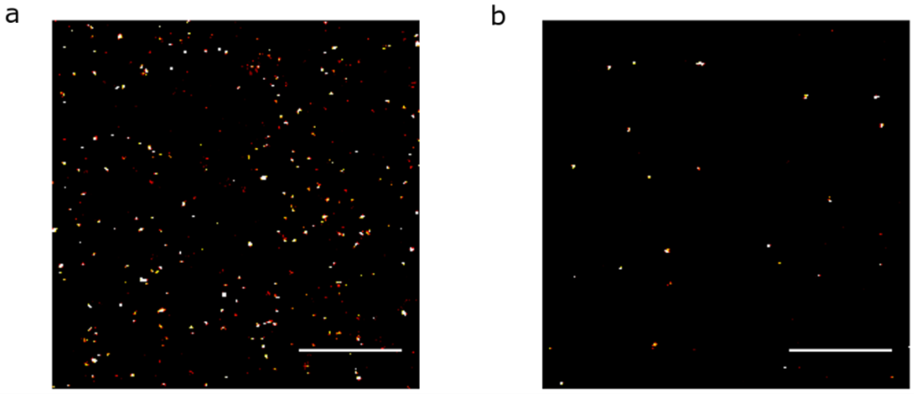

Figure 6-3 Confocal images of large unilamellar vesicles (LUVs) stained with **Dyad 3** using the same intensity of 561 nm as the excitation light. a) LUVs fixed by biotin. b) LUVs fixed by polylysine. The ratio of the average photon counts of a) and b) = 2.0: 1. Scale bar: 20 μm. Parameters: 0.92 μW of 561 nm laser, pixel size 260 nm, dwell time 1.58 μs/pixel, Zeiss LSM780 inverted confocal microscope.

The switching behaviour of the dyad was analysed using either 561 nm or 594 nm as excitation lasers under a commercial confocal microscope, i.e. Zeiss LSM780 inverted confocal microscope. While 561 nm was ideal for our dyad, which includes **6'-Atto565** dye, the ultimate goal was to test the dyad under a RESOLFT microscope (Eggeling group, Weatherall Institute of Molecular Medicine, University of Oxford) that was equipped with no 561 nm but nearby 485 nm or 594 nm lasers. Despite the similar absorbance at 485 nm and 594 nm by the **6'-Atto565** dye, we chose 594 nm as it is expected to cause less photobleaching and photodamage than 485 nm. Thus, for later comparison with RESOLFT images, we investigated the switching performance of **Dyad 3** with 561 nm as well as 594 nm on the Zeiss confocal microscope. The scanning mode was line by line, where each line is scanned with depletion light (405 nm) and then excitation light to obtain the dark state.

Surprisingly, the imaging on LUVs of **Dyad 3** delivered significantly poorer results than in live cells (Chapter 4). To begin with, LUVs showed 49%–52% quenching efficiency after optimisation of 405 nm power as the depletion light and 561 nm (**Figure 6-4**a) or 594 nm (**Figure 6-5**a) as the excitation light. This ratio was notably inferior to 75%–85% in live cells, for which we do not have a robust explanation at this time. In addition, this low contrast between bright and dark states was observed from both the vesicles and scattered background (**Figure 6-4**b, c and **Figure 6-5**b, c), which seemed to suggest that the switching was not significantly affected by the different local environments or equally affected by the presence of streptavidin/biotin on the surface. Furthermore, an inadequate fatigue resistance was observed, i.e. >60% photodegradation after 10 cycles, in contrast to 15% degradation after 23 cycles in live cells.

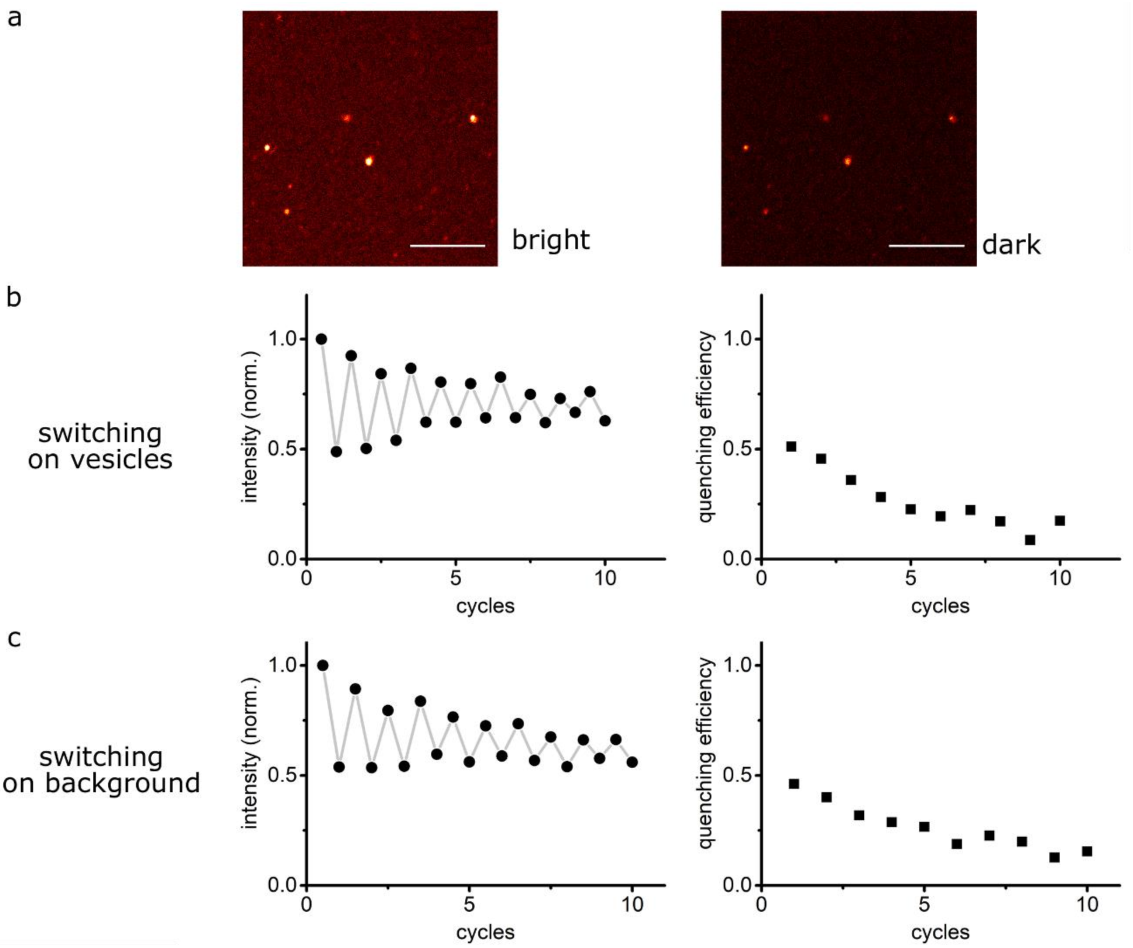

Figure 6-4 Switching behaviour of LUVs stained with **Dyad 3** using 561 nm as the excitation light. a) Bright image was obtained by excitation at 561 nm. Dark image was obtained by scanning with 405 nm immediately followed by 561 nm excitation. Scale bar: 10 µm. b) Quantification of fluorescence modulation on vesicles and the corresponding quenching efficiency. Quenching efficiency = 1 – photon counts in dark state/bright state. c) Similar fluorescence quantification at the background as in b). Parameters: 0.92 µW of 561 nm, 98 µW of 405 nm, dwell time 1.58 µs/pixel, line-by-line scanning, Zeiss LSM780 inverted confocal microscope.

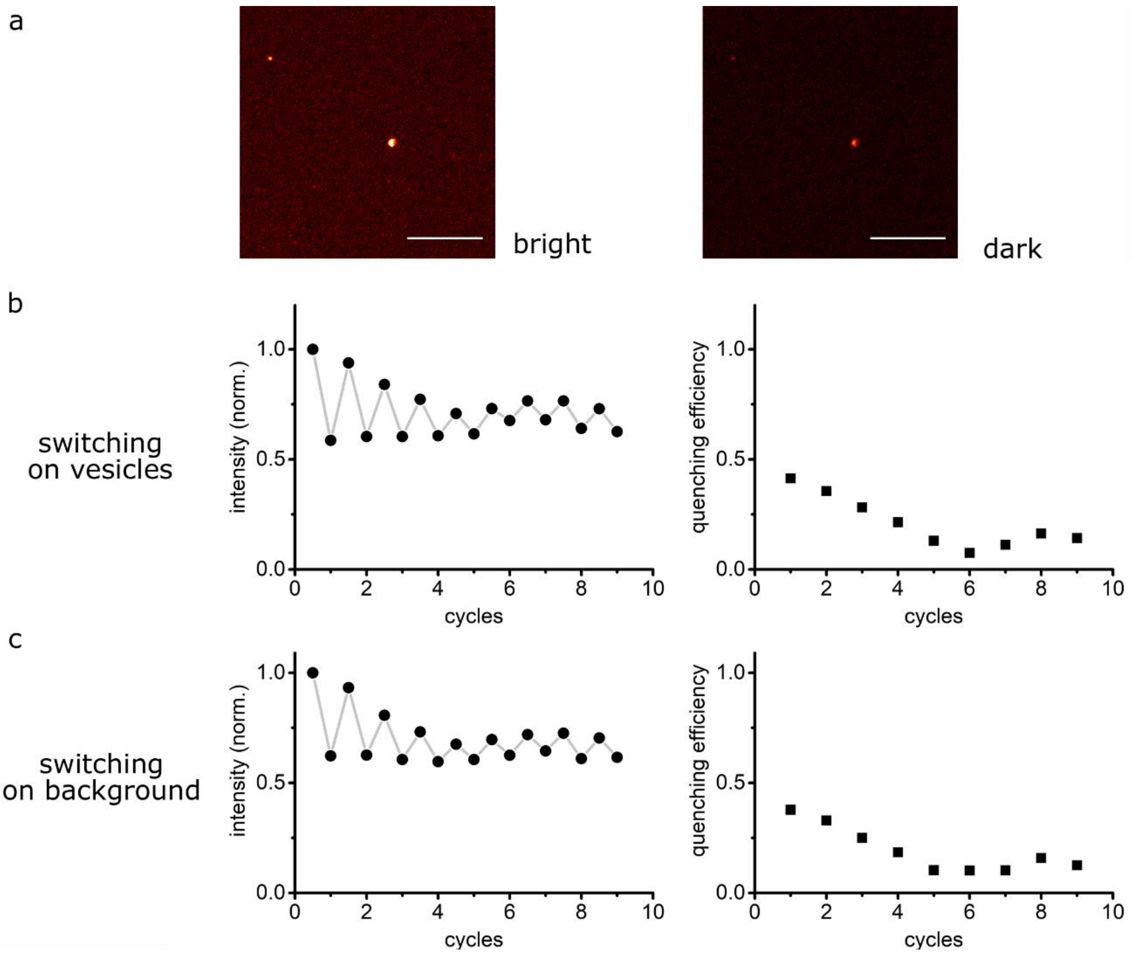

Figure 6-5 Switching behaviour of LUVs stained with **Dyad 3** using 594 nm as the excitation light. a) Bright image was obtained by excitation at 594 nm. Dark image was obtained by scanning with 405 nm immediately followed by 594 nm excitation. Scale bar: 10 μm. b) Quantification of fluorescence modulation on vesicles and the corresponding quenching efficiency. Quenching efficiency = 1 – photon counts in dark state/bright state. c) Similar fluorescence quantification at the background as in b). Parameters: 5.0 μW of 594 nm, 98 μW of 405 nm, dwell time 1.58 μs/pixel, line-by-line scanning, Zeiss LSM780 inverted confocal microscope.

Additionally, the images measured in the pixel-by-pixel scanning confocal mode displayed less than 50% quenching efficiency (**Figure 6-6**a), making it impractical to directly apply the dyad in RESOLFT microscopy. The pixel-by-pixel scanning is essential to perform RESOLFT imaging, in which depletion and excitation are performed on one pixel before repeating the process on the next pixel. We first tested the switching behaviour without the depletion donut on the RESOLFT microscope. The typical imaging sequence for each pixel is shown in **Figure 6-6**b. Strangely, the switching behaviour was observed only when a waiting time of 1 ms between 594 nm and 405 nm irradiation was inserted, as if pixels were 'tricked' to believe that they were operating in the line-by-line scanning mode.

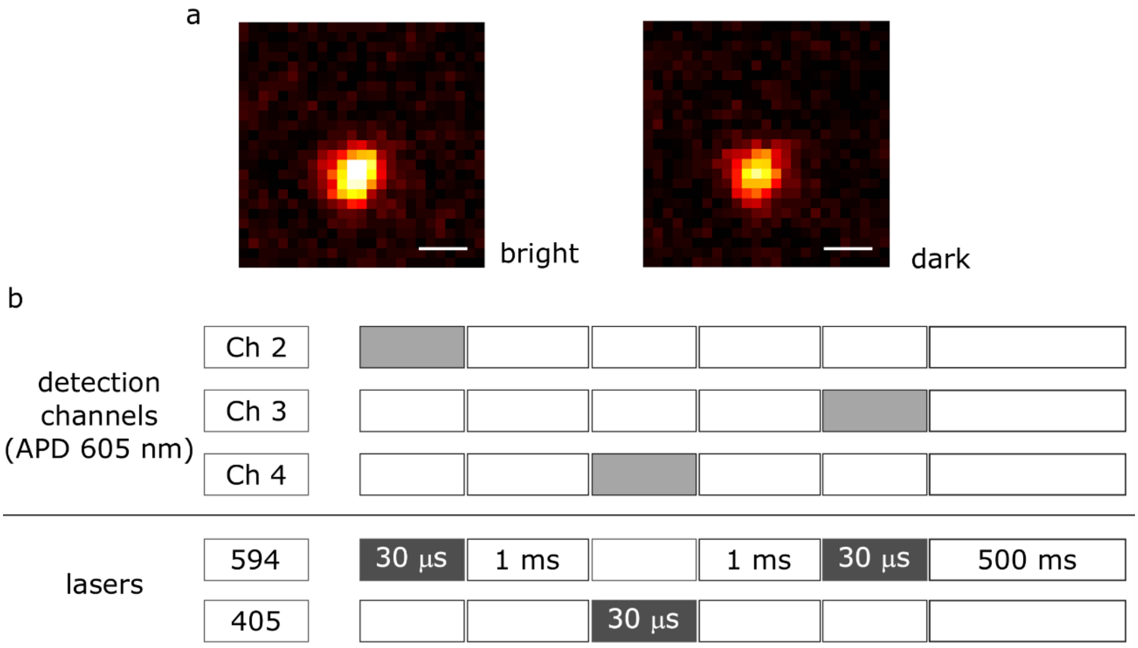

Figure 6-6 Switching behaviour of LUVs stained with **Dyad 3** in the pixel-by-pixel scanning confocal mode. a) Switching of **Dyad 3** between bright and dark states using the scanning sequence in b). Scale bar: 400 nm. b) Pixel-by-pixel scanning sequence. Detection at Channel 2 gave the image of the bright state, and Channel 3 gave the image of the dark state. Channel 4 collected emission signals resulting from the 405 nm excitation. However, these data were not required for construction of images. Parameters: 13 µW of 594 nm, 50 µW of 405 nm, pixel size 80 nm × 80 nm, confocal mode of the RESOLFT microscope. APD (605 nm) = avalanche photodiode (detected at 605–625 nm).

In conclusion, mainly due to less than 50% quenching efficiency, it was infeasible to directly apply LUVs stained with **Dyad 3** in RESOLFT microscopy. This led us to consider alternative vesicles, such as giant unilamellar vesicles (GUVs).

6.3 GUVs

The failure in imaging of either LUVs using **Dyad 3**, or live cells using triads based on the HaloTag technique (described in Chapter 5), required further investigation of the underlying causes. One postulation was that the difference in the hydrophobicity of local environments led to different imaging results in the cytoplasm and protein-ligand binding sites in cells, which could be linked to the observation in LUVs. Thus, giant unilamellar vesicles (GUVs) were initially employed to explore the distribution of the dyad between a hydrophobic and hydrophilic environment. Due to the large size (> 1 µm in diameter) of GUVs, direct observation of the dyad localisation under a conventional optical microscope is possible.

As described in Section 6.1, GUVs, like other vesicles, can serve as simplified and systematically controllable model systems of cell membranes. Furthermore, GUVs have a unique feature that makes them a closer analogue; their size is comparable to that of eukaryotic cells. These combined advantages make GUVs a popular research model to study biophysical phenomena occurring on the membrane,[2,23] and even as cell models.[24] As a result, many different preparation methods have been reported, each with their own advantages and disadvantages.[2] Two of the most widely used protocols are the ‘gentle hydration’ method,[25,26] which involves natural swelling of dried lipids deposited on a surface, and the electroformation method[27,28], where an external alternating current (AC) electric field is applied to facilitate the formation of GUVs. Despite requiring special equipment, the latter usually enables reproducible formation of monodispersed and unilamellar GUVs.[2,29] For our purpose and availability of expertise in our collaborator’s group, the electroformation method was adopted. Unlike the LUV preparation, **Dyad 3** in DMSO solution was delivered to stain the pre-formed GUVs as the dyad was observed to decompose in the presence of the electric field if it was included initially with the lipid. Either PLL or BSA was used to passivate the surface and immobilise GUVs. The details of the procedures can be found in the Experimental Section.

6.3.1 Confocal imaging of GUVs

6.3.1.1 Comparison of conditions

Compared to the vesicles fixed by just BSA, those fixed by PLL tended to be less wobbly on the surface, which was preferred due to absence of artefacts caused by movements. This would be particularly important in RESOLFT imaging as the image acquisition was relatively slow even for a small field of view, and any movements by vesicles would significantly distort the image. Thus, all the results shown from now on were acquired on the samples made using the PLL method unless otherwise specified. Similar to the imaging of LUVs described earlier, the switching behaviour of GUVs stained with **Dyad 3** was first analysed using either 561 nm or 594 nm as the excitation source on a Zeiss LSM780 inverted confocal microscope.

6.3.1.2 Confocal images

As described earlier, the initial motivation for employing GUVs was to explore the dyad preference for hydrophobic or hydrophilic environments. To our delight, confocal images revealed selective localisation of **Dyad 3** in the membrane against a dark background, indicating the hydrophobic nature of the dyad. Additionally, intensity crests and troughs were observed around the GUV membrane layer. The pattern arises due to the different interactions of the linearly polarised excitation light and dyes in different locations around the membrane. The absorption efficiency is highly dependent on the relative orientation of the transition dipole moment of the dye with respect to the plane of polarisation of the light.[30] This implies that the arrangement of the dyad in the bilayer membrane is fairly organised with restricted rotational freedom. If the dyads were not ordered, there would be dyes at random orientations at all positions around the membrane, resulting in a homogenous fluorescence intensity distribution.

Secondly, the photoswitching behaviour of **Dyad 3** was explored in GUVs using the Zeiss confocal microscope. The images acquired using the 561 nm excitation laser and 405 nm depletion laser are shown in **Figure 6-7**. The field of view was scanned first with a green laser (561 nm, 1.8 µW), to acquire the "bright" image, and then sequentially, line-by-line, with a blue laser (405 nm, 49 µW) followed immediately by the image acquisition using the green laser to obtain the "dark" image. Following this procedure, remarkable quenching efficiency, i.e. 96%–86%, was reproducibly obtained. By repeating the above photoswitching sequence, it was shown that **Dyad 3** demonstrated extremely strong fatigue resistance, losing only 9% of its quenching efficiency after 18 cycles from 96% to 87% (**Figure 6-7**b,c).

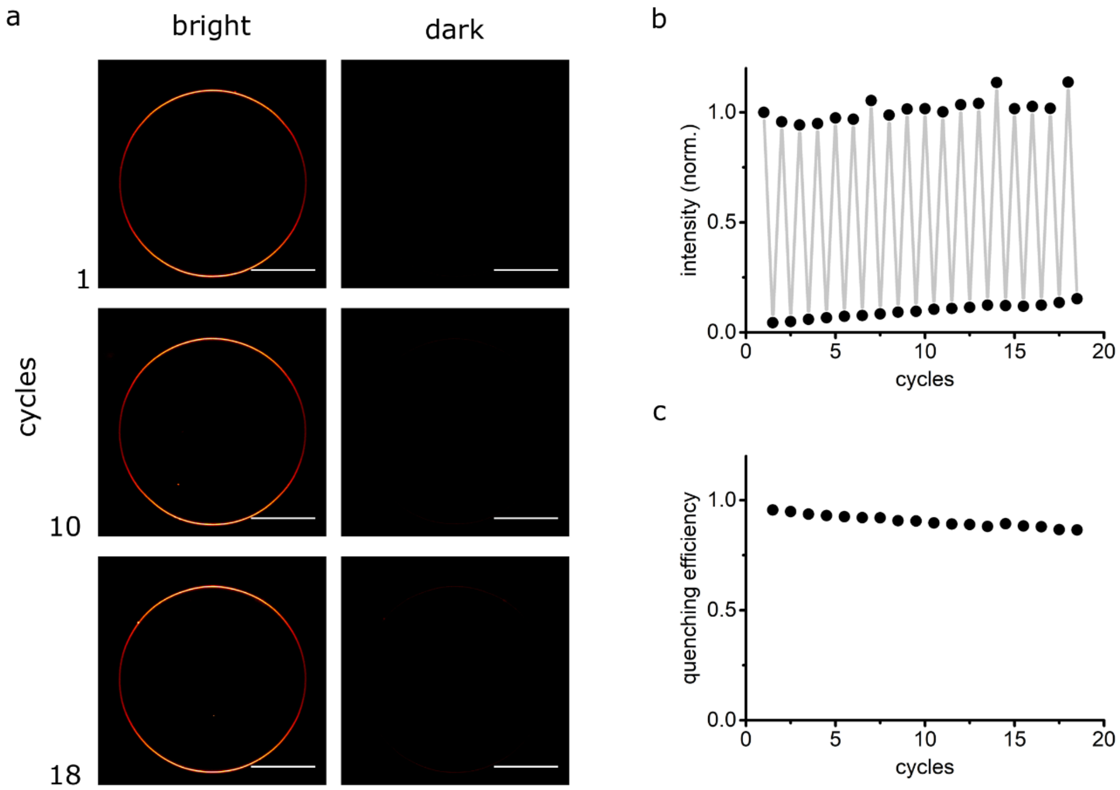

Figure 6-7 Switching behaviour of **Dyad 3** in GUVs using 561 nm as the excitation laser. a) Confocal images in bright and dark states after a number of cycles. The bright state was obtained by excitation at 561 nm. The dark state was obtained by irradiation at 405 nm followed by excitation at 561 nm. Scale bar: 20 μm. b) and c) Fluorescence quantification of **Dyad 3** over several switching cycles. Quenching efficiency refers to the effective quenching of fluorescence per cycle. Parameters: 1.8 μW of 561 nm, 49 μW of 405 nm, dwell time 1.58 μs/pixel, pixel size 80 nm × 80 nm, gain 600 (signal amplification from the photomultiplier tube), line-by-line scanning, Zeiss LSM780 inverted confocal microscope.

Equally impressive fatigue resistance was recorded using the 594 nm excitation laser, i.e. 6% loss in quenching efficiency after 21 cycles (**Figure 6-8**), despite a lower contrast between the bright and dark state (reproducibly 78%–70% quenching efficiency; **Figure 6-8**) using the same intensity of 405 nm laser power. This lower quenching efficiency was later improved to 89% when the conditions were optimised (see Section 6.4.4).

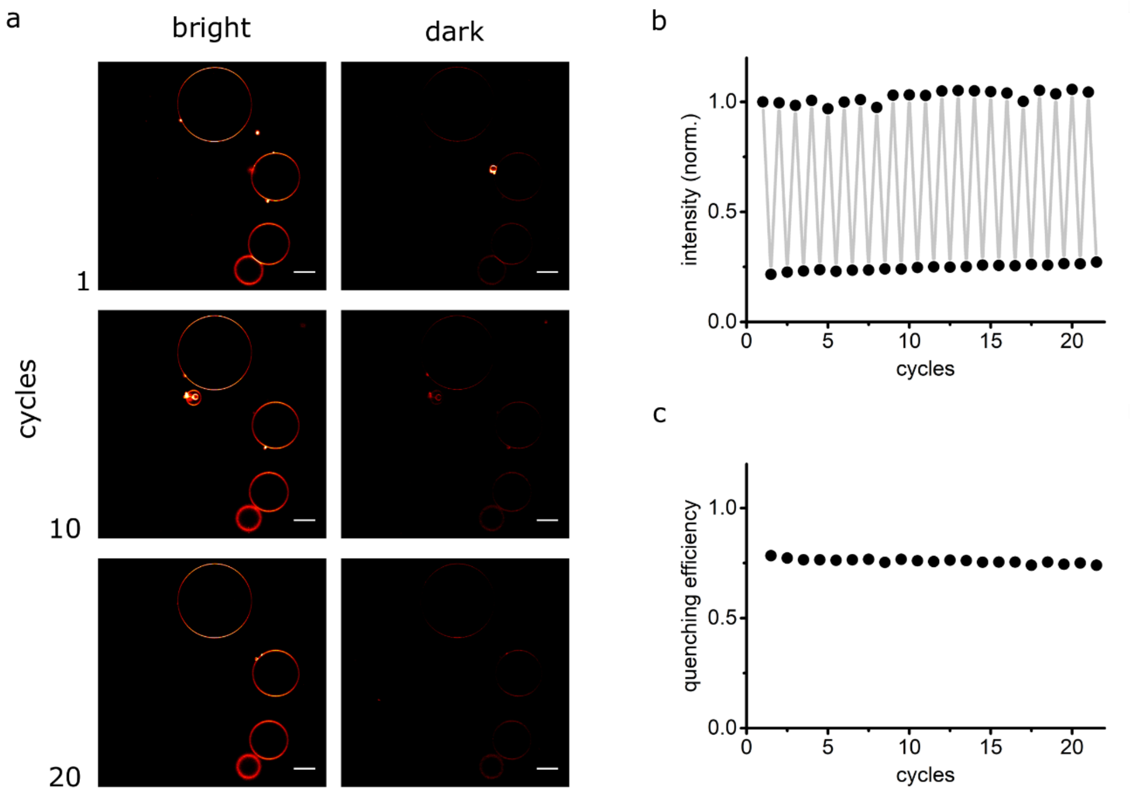

Figure 6-8 Switching behaviour of **Dyad 3** in GUVs using 594 nm as the excitation laser. a) Confocal images in bright and dark states after a number of cycles. The bright state was obtained by excitation at 594 nm. The dark state was obtained by irradiation at 405 nm followed by excitation at 594 nm. Scale bar: 20 µm. b) and c) Fluorescence quantification of **Dyad 3** over several switching cycles. Quenching efficiency refers to the effective quenching of fluorescence per cycle. Parameters: 5.0 µW of 594 nm, 49 µW of 405 nm, dwell time 1.58 µs/pixel, pixel size 80 nm × 80 nm, gain 600 (signal amplification from the photomultiplier tube), line-by-line scanning, Zeiss 780 inverted confocal microscope.

Such strong contrast and fatigue resistance of the dyad were unprecedented. Previously, the best imaging result of **Dyad 3** in live cells showed 80%–70% quenching efficiency and 15% photodegradation after 12 cycles (see Chapter 4). Nevertheless, these promising results in GUVs are comparable to what was observed for the spirooxazine switch (alone) in the cuvette, which underpins the photoswitching behaviour of the dyad. The switch demonstrated 95%–85% photoconversion upon 405 nm illumination, and even more remarkable fatigue resistance in organic solvents, <10% after 100 cycles in cyclohexane (see Chapter 3).

Here it is worth mentioning the differences in the imaging results of LUVs and GUVs. Despite their similar compositions, LUVs and GUVs have several discrepancies that might be responsible for the different switching behaviour of **Dyad 3**. Firstly, the preparation and staining procedures of LUVs and GUVs have little in common. During the LUV formation, the dyad was included at an early stage along with the lipids, and the lipid mixture underwent hydration, sonication and extrusion processes to generate the vesicles. By comparison, GUVs were pre-formed according to the electroformation method, and the dyad was added later to stain the vesicles. These procedures might alter the switching performance of the dyad. For example, because the dyad was delivered to pre-formed GUVs, it probably residues just on the outside of the membrane or/and in the bilayer, whereas in LUVs, the dyad may also occupy the inside of the membrane because of its early inclusion in the preparation. In addition, sonication energy and mechanical energy from extrusion might have effects on the dyad in the case of LUVs, as implied by the degradation of the dyad in the electric field in the case of GUVs. Secondly, the sizes of LUVs and GUVs indicate different curvatures, and suggest differences in local concentrations as well as local environments where the dyad is exposed to lipid and aqueous media to different extents. Thirdly, since LUVs are sub-diffraction sized vesicles, they appear as blurred spots under confocal imaging, meaning that the axial (*z*) position of the image cannot be determined accurately. In contrast, the midplane of GUVs could be clearly recognised and chosen for imaging, as the GUVs are much larger than the diffraction limit. If the dyad arrangement is ordered in the membrane as suggested before, different *z* positions mean varying dyad orientations, which lead to the different relative direction of the polarisation plane of incoming excitation light with respect to the transition dipole moment of the dye. Meanwhile, it is possible that in the same dyad molecule, the transition dipole moment of the dye for excitation and the transition dipole moment of the switch for activation are different. These two factors may result in a mismatch of fluorescence and switching processes, possibly leading to the differing contrasts of bright and dark states observed in LUVs and GUVs.

On account of the outstanding results under the confocal microscopy, GUVs stained with **Dyad 3** were ready to be tested under RESOLFT imaging.

6.4 RESOLFT imaging of GUVs

Super-resolution microscopy was carried out on a custom RESOLFT microscope that was adapted from an Abberior STED microscope and housed in the Eggeling group, Weatherall Institute of Molecular Medicine, University of Oxford. The following RESOLFT microscopy was carried out with assistance from Dr Silvia Galiani.

6.4.1 Reproducing previous results in the confocal mode of the RESOLFT microscope

To ensure the reproducibility of imaging results from the Zeiss confocal microscope to the super-resolution microscope, we first tested the switching in the confocal mode of the Abberior RESOLFT microscope. Using pixel-by-pixel scanning, where a switching cycle is completed on one pixel before moving to the neighbouring pixel, spherical GUVs of average diameter 10–50 µm were observed, and quenching efficiency was as high as 91% (**Figure 6-9**). Here the GUVs did not show intensity crests and troughs because unlike the Zeiss microscope that used linearly polarised light, the Abberior microscope was equipped with circularly polarised light of which the direction rotates as it propagates.

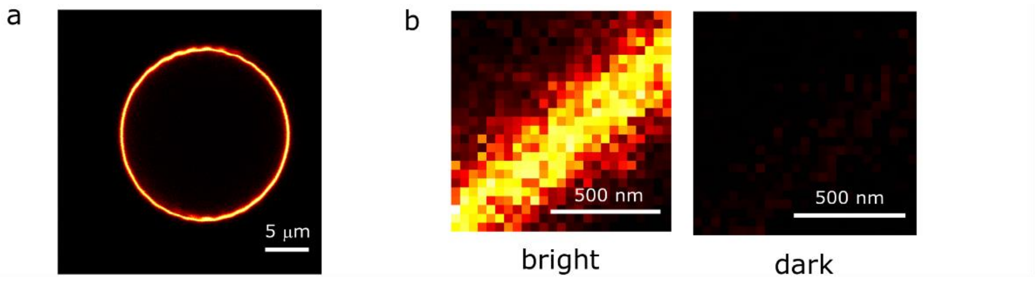

Figure 6-9 Confocal images of GUVs stained with **Dyad 3** on the RESOLFT microscope and the switching behaviour of the dyad, using pixel-by-pixel scanning. a) A large field of view (30 µm × 30 µm) of a GUV. b) Part of a GUV in bright and dark states. The bright state was obtained by excitation at 594 nm. The dark state was obtained by irradiation at 405 nm followed by excitation at 594 nm. Quenching efficiency = 1 - mean photon counts of dark/bright states = 91%. Parameters: 13 µW of 594 nm laser as the excitation source, 50 µW of 405 nm as the depletion source, 800 ms waiting time between pixels, dwell time 30 µs/pixel, pixel size 80 nm × 80 nm.

6.4.2 Beam alignment in RESOLFT mode

Before investigating the possibility of RESOLFT imaging using any switchable dye, we must ensure the proper alignment of the excitation and donut-shaped depletion laser beams on the microscope. If the two beams are misaligned to the extreme extent (**Figure 6-10**), engineering of the point spread function (PSF) based on the RESOLFT concept no longer exists, and it is simply a confocal setup.

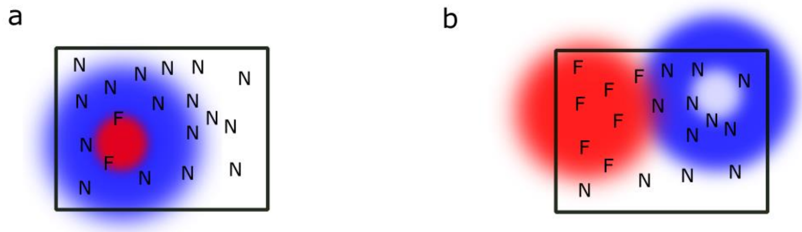

Figure 6-10 Beam alignment (a) and mis-alignment (b) of an excitation laser (red) and a donut-shaped depletion laser (blue) on a RESOLFT microscope. Note in the extreme case of beam misalignment, it is just a confocal setup. F = fluorescing object, N = non-fluorescing object.

There are very few commercial RESOLFT microscopes available, and no commercial calibration samples exist to align beams that in theory could be of any wavelength. The commonly used gold reflective beads are not sufficient on their own for the necessary fine alignment because reflection and fluorescence detection travel along different pathways in the microscope. Instead, we used gold beads (80 nm; Merck) followed by TetraSpeck Microspheres (100 nm; Thermo Fisher Scientific). The latter contain four fluorescent dyes with excitation/emission at 360/430 nm, 505/515 nm, 560/580 nm and 660/680 nm. The gold beads were used to align the phase mask (which generates the donut-shaped depletion beam) approximately in the centre, and the other beams, e.g. 594 nm as excitation light, were overlapped with the centre as much as possible. Once this rough alignment was finished, we used TetraSpeck Microspheres for the fine alignment by overlaying the centre of the donut with other beams using the same detection pathway and channel as those for the sample. A typical proper alignment is shown in **Figure 6-11** .

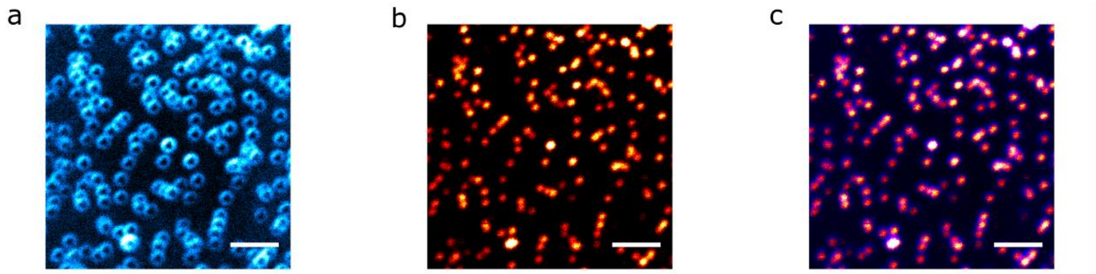

Figure 6-11 Example alignment of 405 nm (depletion) and 594 nm (excitation) beams using TetraSpeck Microspheres (100 nm; Thermo Fisher Scientific). Before this, gold beads (80 nm; Merck) were used for a rough alignment. a) Donut-shaped 405 nm laser beam. b) 594 nm laser beam. c) Overlay of a) and b). Scale bar: 2 µm. The images were acquired on the RESOLFT microscope.

6.4.3 RESOLFT images with thermal relaxation

Now with the optimal alignment of the excitation (594 nm) and the donut-shaped depletion (405 nm) laser beams fixed, acquisition of RESOLFT images was possible.

Initially, we had an empty waiting time between imaging each pixel, i.e. thermal relaxation for the switch to recover from the open to closed form without irradiation (**Figure 6-12**). The waiting time was optimised to be 800 ms for a balance of relatively fast acquisition and almost full reversion of the switch to the inactive closed form. RESOLFT imaging must be done in the pixel-by-pixel manner, and the scanning sequence is shown in **Figure 6-13**.

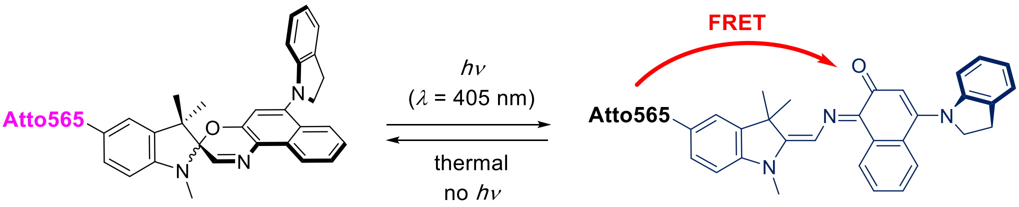

bright state
Dyad 3

dark state
Dyad 3

Figure 6-12 Reversible switching between bright and dark states of **Dyad 3** under thermal relaxation conditions.

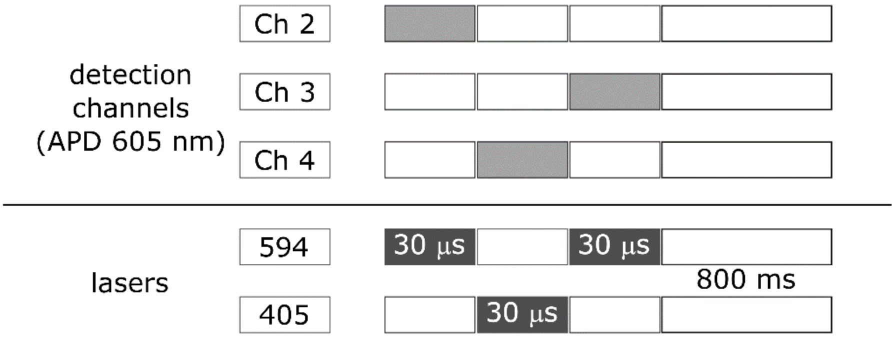

Figure 6-13 Imaging sequence with thermal relaxation between pixels on the RESOLFT microscope. Detection at Channel 2 gave the confocal image, and detection at Channel 3 gave the RESOLFT image. Channel 4 collected emission signals resulting from the 405 nm excitation. However, these data were not required for construction of images. This sequence was repeated in the pixel-by-pixel manner. Pixel size is 40 nm × 40 nm. APD (605 nm) = avalanche photodiode (detected at 605–625 nm).

Following this, we optimised the laser powers to acquire the best possible contrast between bright and dark states. Firstly, we adjusted the power of the 594 nm laser with the 405 nm laser fixed at an arbitrary value, in this case 120 µW. This adjustment was to avoid photon saturation which would give a misleadingly large spatial resolution. The spatial resolution was determined using a custom written script in ImageJ Macro language, which is provided by Dr Dominic Waithe, WIMM, University of Oxford (see Appendices). The procedure is as follows: the intensity profile perpendicular to the membrane was extracted and fitted to a Gaussian curve. The full width at half maximum (FWHM) of the Gaussian fit was used as an indication of spatial resolution (example see **Figure 6-14**). The smaller value of the FWHM, the better the spatial resolution. In our case using 594 nm as the excitation wavelength, FWHM should be approximately $d \approx \lambda/2 = 594\ \text{nm}/2 \approx 300$ nm if photon counts are below the saturation level.

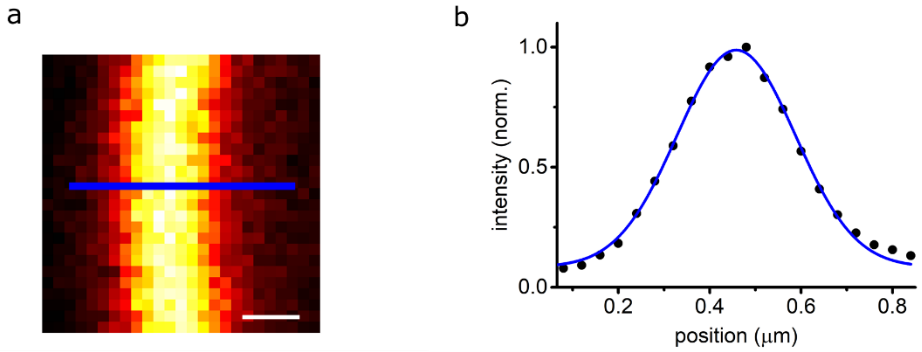

Figure 6-14 Example of calculation of full width at half maximum (FWHM) as an indication of spatial resolution. a) Confocal image of part of a GUV membrane stained with **Dyad 3** using 4.9 μW of 594 nm. Scale bar: 200 nm. b) Black dots: line profile of the intensity distribution along the line in a). Blue line: Gaussian fit, $R^2 = 0.995$, FWHM = 305 nm.

As shown in **Figure 6-15**a, between 1.3 and 4.4 μW of 594 nm laser power, the confocal FWHM is as expected (~300 nm), and the RESOLFT FWHMs are very similar (~200 nm). Once the power exceeded 4.4 μW, the RESOLFT FWHM increased to 240 nm using 6.2 μW of 594 nm power, while the corresponding confocal FWHM (325 nm) implies some detection saturation. Thus, we could choose any power between 1.3 and 4.4 μW to avoid saturation, and for the following optimisation of the 405 nm power, 4.4 μW of 594 nm was used to maximise the photon count. While the FWHMs were very similar in the range 61–155 μW of 405 nm, a slight improvement was observed using 120 μW of 405 nm compared to other powers, i.e. 185 nm *vs* 205 nm (**Figure 6-15**b). Higher laser powers were not tested because the acquisition time was long, i.e. each 2 × 2 μm image took ~33 min with a 40 nm pixel size, due to the long delay required for thermal recovery. Nevertheless, this parameter was more thoroughly optimised later when photochemical relaxation significantly sped up the acquisition.

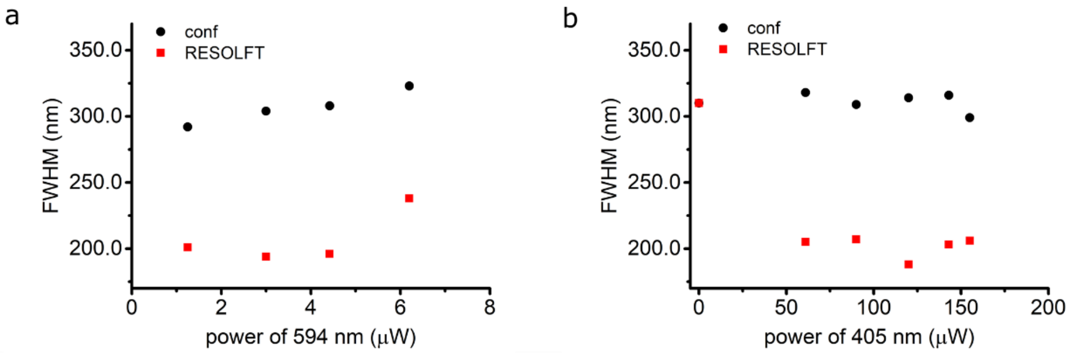

Figure 6-15 Optimisation of laser powers to acquire the best possible spatial resolution, i.e. lowest full width at half maximum (FWHM), of GUVs stained with **Dyad 3** on the RESOLFT microscope. a) Variation of 594 nm laser power with 405 nm laser power fixed at 120 μW. For subsequent 405 nm optimisation, 4.4 μW of 594 nm was chosen to maximise brightness and avoid detection saturation. Confocal values were obtained for comparison. b) Variation of 405 nm laser power with 594 nm laser power fixed at 4.4 μW. The best FWHM (185 nm) was obtained using 120 μW of 405 nm and 4.4 μW of 594 nm.

With the optimised parameters, i.e. 4.4 μW of 594 nm as the excitation light and 120 μW of 405 nm as the depletion light, the RESOLFT images of parts of GUVs were reproducibly acquired (**Figure 6-16**), with FWHM ≈ 185 nm.

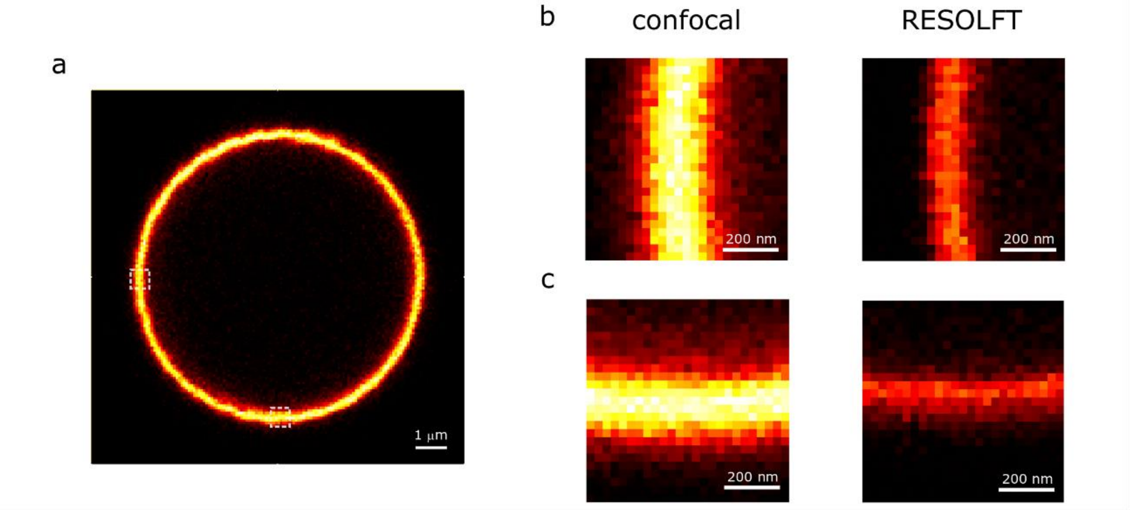

Figure 6-16 Optimised RESOLFT images of GUVs stained with **Dyad 3**. a) Confocal image of a GUV by excitation at 4.4 μW of 594 nm. b,c) Confocal and RESOLFT images of parts of the GUV as highlighted in a). The images were acquired using 4.4 μW of 594 nm (excitation) and 120 μW of 405 nm (depletion). FWHM (confocal) ≈ 300 nm, FWHM (RESOLFT) ≈ 185 nm.

6.4.4 RESOLFT images with photochemical acceleration

Despite the initial success of RESOLFT imaging on GUVs, the acquisition time was long, e.g. a 2 μm × 2 μm image took ~33 min with 40 nm pixel size. Based on the photochemical reversion of the switch in isolation (**Figure 6-17**a; reproduced from Chapter 3), in theory the recovery of the dyad from the dark to the bright state should be accelerated using visible light (**Figure 6-17**b). The lasers of relevant wavelengths available on the RESOLFT microscope were 485 nm, 594 nm and 640 nm.

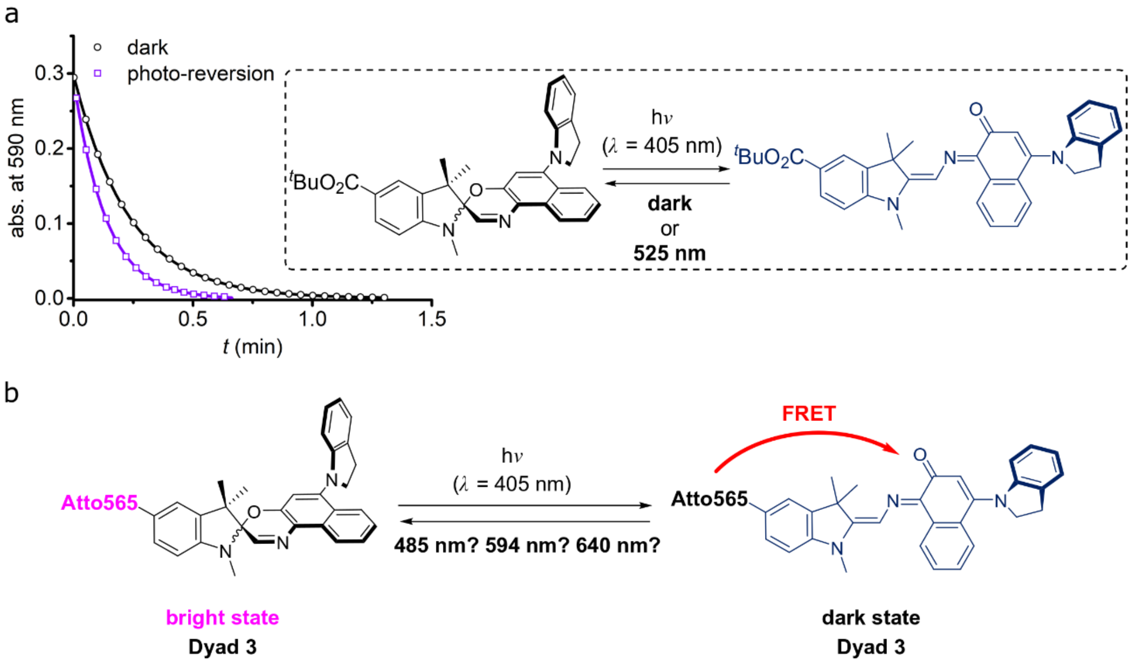

Figure 6-17 Photoreversion mechanism. a) Photochemical acceleration of the back reaction of the spirooxazine switch from the open form to the closed form, using 525 nm light. This was shown in cyclohexane solution in the cuvette using a LED light source (Chapter 3). b) Possibility of photo-acceleration from the dark state to the bright state of **Dyad 3**, using visible light sources available on the RESOLFT microscope, i.e. 485 nm, 594 nm or 640 nm.

The imaging sequence was similar to that with thermal recovery except that the previous 800 ms empty waiting (**Figure 6-13**) was replaced with irradiation at a third wavelength of much shorter time, e.g. 5 ms of 640 nm (**Figure 6-18**).

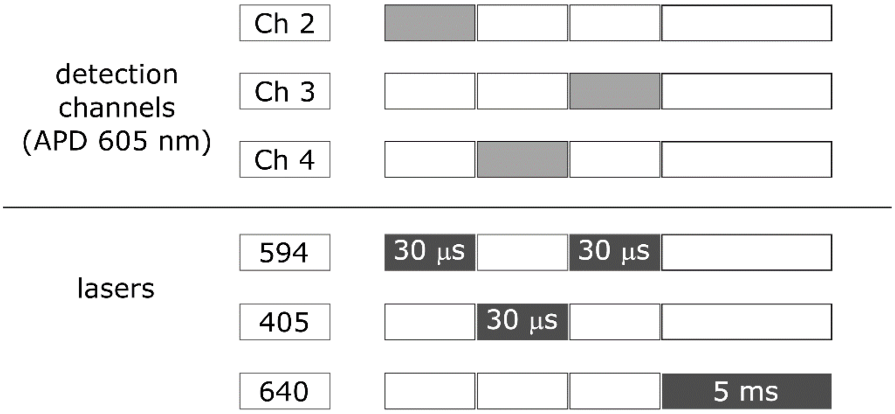

Figure 6-18 Example of an imaging sequence with photochemical recovery using 640 nm between pixels on the RESOLFT microscope. Detection at Channel 2 gave the confocal image, and detection at Channel 3 gave the RESOLFT image. Channel 4 collected emission signals resulting from the 405 nm excitation. However, these data were not required for construction of images. This sequence was repeated in the pixel-by-pixel manner. Pixel size is 40 nm × 40 nm. APD (605 nm) = avalanche photodiode (detected at 605–625 nm).

Photochemical acceleration was attempted using 485 nm, 594 nm and 640 nm; the open form of the switch absorbs at all three of these wavelengths. Firstly, with 485 nm illumination, FWHMs for both the confocal (~ 510 nm) and RESOLFT (~420 nm) images were peculiarly large, and significant photobleaching was observed due to the high energy of such short-wavelength irradiation (**Figure 6-19**).

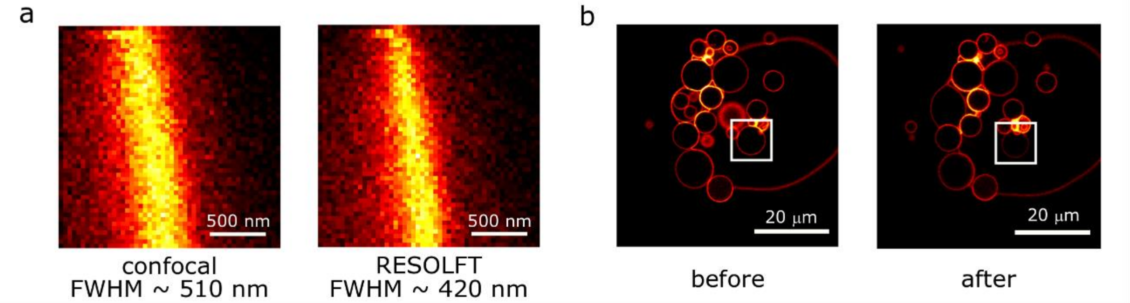

confocal
FWHM ~ 510 nm

RESOLFT
FWHM ~ 420 nm

before

after

Figure 6-19 Attempted photochemical acceleration using 485 nm light. a) Confocal and RESOLFT images of part of a GUV stained with **Dyad 3**. Despite the apparent FWHM improvement from 510 nm of confocal to 420 nm of RESOLFT, both values were unexpectedly large. b) Confocal images of GUVs before and after the RESOLFT measurement. The highlighted area was where the RESOLFT image was acquired, and photobleaching is obvious. Parameters: 1.3 μW of 594 nm laser as the excitation beam, 143 μW of donut-shaped 405 nm as the depletion beam, 30 μW of 485 nm for 30 ms as the photoreversion light, pixel size 40 nm × 40 nm. Images were acquired on the RESOLFT microscope.

Secondly, we tested the 594 nm laser, which also acts as the excitation light, to drive the back reaction. FWHM was improved from ~270 nm in the confocal image to ~230 nm in the RESOLFT image, but it was puzzling to observe that the dyad flushed into the internal volume of the vesicles during measurements (**Figure 6-20**). The re-distribution of the dyad population effected lower brightness on the membrane at higher background, leading to less reliable and sometimes irreproducible FWHM determination, arising from this apparently dynamic process.

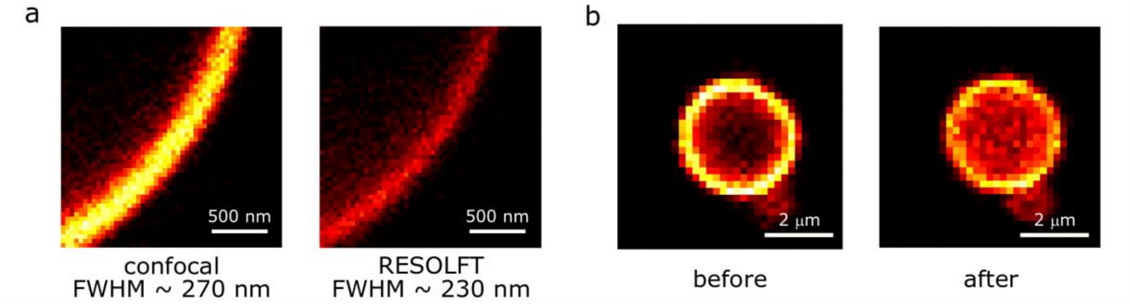

confocal
FWHM ~ 270 nm

RESOLFT
FWHM ~ 230 nm

before

after

Figure 6-20 Attempted photochemical acceleration using 594 nm light. a) Confocal and RESOLFT images of part of a GUV stained with **Dyad 3**. FWHM was improved from 270 nm in confocal to 230 nm in RESOLFT. b) Confocal images of GUVs before and after the RESOLFT measurement. Parameters: 1.3 μW of 594 nm laser as the excitation beam, 143 μW of 405 nm as the depletion beam, 1.3 μW of 594 nm for 50 ms as the photoreversion light, pixel size 40 nm × 40 nm. Images were acquired on the RESOLFT microscope.

Pleasingly, the longest wavelength laser of the three options, 640 nm, was found to accelerate the back reaction from the bright to dark state of **Dyad 3** effectively, without observation of photobleaching and re-distribution of the dyad (**Figure 6-21**). The brightness ratio before and after the RESOLFT measurement is 1: 0.96.

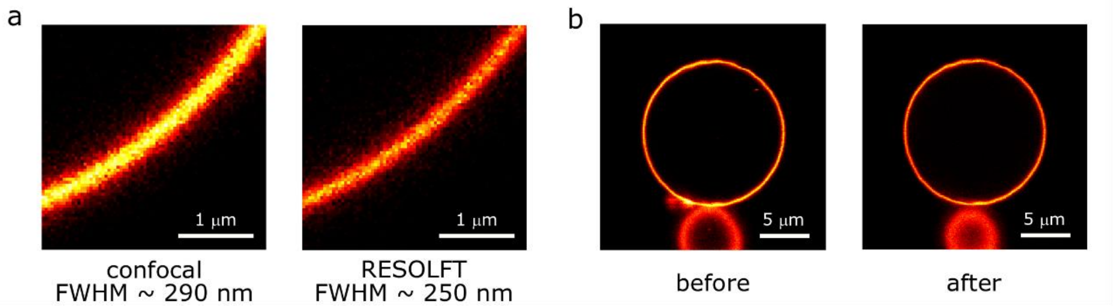

Figure 6-21 Photochemical acceleration using 640 nm light. a) Confocal and RESOLFT images of part of a GUV stained with **Dyad 3**. FWHM was improved from 290 nm in confocal to 250 nm in RESOLFT. b) Confocal images of GUVs before and after the RESOLFT measurement, and the brightness ratio is 1:0.96. Parameters: 2.0 µW of 594 nm laser as the excitation beam, 61 µW of donut-shaped 405 nm as the depletion beam, 100 µW of 640 nm for 5 ms as the photoreversion light, pixel size 40 nm × 40 nm. Images were acquired on the RESOLFT microscope.

We continued to optimise several parameters. The 640 nm laser dwell time was first adjusted to allow almost complete back reaction within a short acquisition time. With 30 µs of 1.3 µW 594 nm (excitation) and 30 µs of 143 µW 405 nm (depletion), the switch required at least 5 ms irradiation of 100 µW 640 nm to achieve the best possible spatial resolution in RESOLFT imaging (**Figure 6-22**a). Further increasing the dwell time did not reduce the FWHM of RESOLFT images noticeably, but the FWHM could be improved by optimisation of other parameters. From Section 6.4.3, we knew that adjustment of 594 nm gave little effect, as long as the power was not so high to cause detection saturation. Subsequently, the 405 nm laser power was optimised. It was found that a dip of RESOLFT FWHM was present at 90 µW of 405 nm light, while higher intensities are detrimental to the spatial resolution of RESOLFT, reaching the confocal resolution at 625 µW (**Figure 6-22**b). The best reproducible spatial resolution we have achieved is 210 nm. This is slightly larger than the 185 nm resolution obtained from the thermal recovery sequence in Section 6.4.3, but the acquisition was dramatically shortened to 0.2 s for a 2 µm × 2 µm image compared to the previous 33 min.

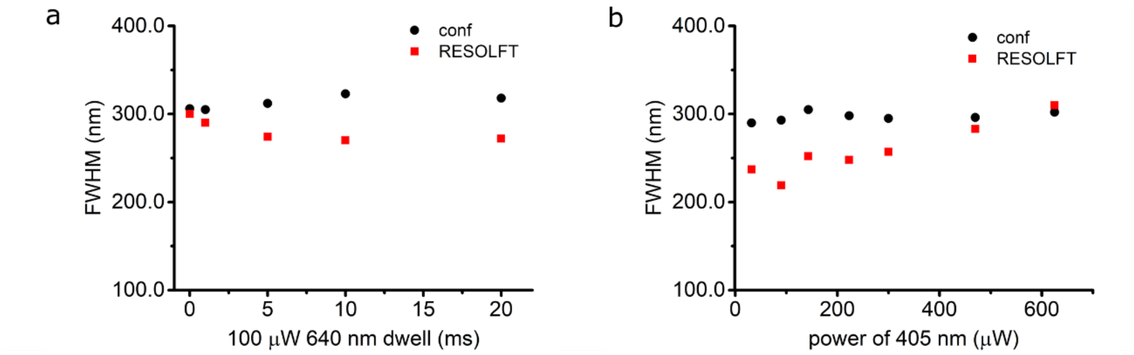

Figure 6-22 Parameter optimisation with 640 nm as the photoreversion light when imaging GUVs stained with **Dyad 3**. a) Optimisation of 640 nm laser dwell time to drive the dyad from the dark to bright state. Here, 30 μs of 1.3 μW 594 nm (excitation) and 30 μs of 143 μW 405 nm (depletion) were used, and at least 5 ms of 100 μW 640 nm was found to be most effective in accelerating the back reaction. Confocal FWHMs were presented for comparison. b) Optimisation of 405 nm laser power. With 1.3 μW of 594 nm, 90 μW of 405 nm gave the best RESOLFT FWHM ~210 nm.

Despite the fast image acquisition, the 210 nm spatial resolution is only a small improvement from 300 nm in the confocal image. We postulate that our dyad exhibits less than optimal switching above a certain threshold of the depletion power (**Figure 6-23**c, solid line). That is, quenching efficiency of the switch does not exhibit the expected behaviour of reaching a constant level due to the photostationary state (**Figure 6-23**c, dashed line). This is in contrary to the dye behaviour in STED microscopy. As described in Chapter 1, the intensity profile of the STED depletion beam shows photon saturation, represented as a flat top in quenching efficiency at stronger powers of the donut-shaped depletion light (**Figure 6-23**a,b). That is, within the lifetime, all molecules are depleted to the ground state and no more photons can be absorbed. On the other hand, for our dyad, the saturation level may contain local minima in the centre because of the poorer switching associated with maximal powers (**Figure 6-23**c,d). The result is that the measured FWHM is larger than expected (**Figure 6-23**d).

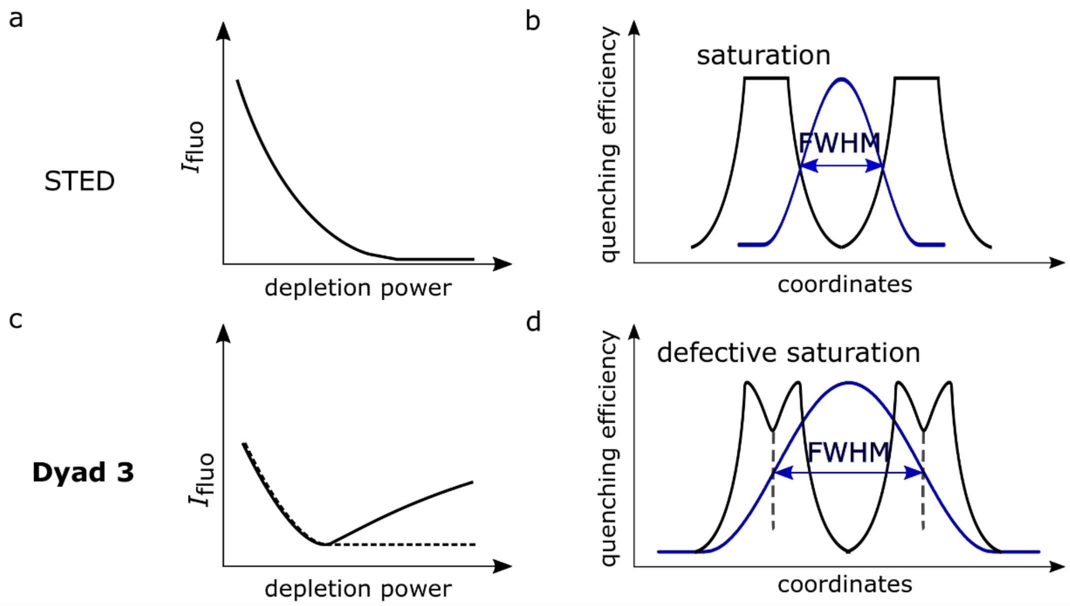

Figure 6-23 Comparison of saturation in STED dyes and our dyad. a) In STED, as depletion power goes up, fluorescence intensity decreases, and reaches ~0 beyond a threshold power. b) At strong intensities of the donut-shaped depletion light, the relation in a) leads to a saturation profile with a flat top of the highest quenching efficiency. c) Solid line: in our dyad case, fluorescence intensity initially decreases with increased depletion power, but past a critical point, stronger depletion power leads to increased fluorescence. Dashed line: the expected behaviour is that beyond a threshold depletion power, the fluorescence reaches the lowest and remains at a constant level due to the photostationary state. d) The relation in c) (solid line) leads to the defective saturation where a local minimum of quenching efficiency is observed. This leads to a larger FWHM compared to b).

This hypothesis is supported by the depletion curves shown in **Figure 6-24**. Using either 561 nm or 594 nm excitation light, quenching efficiency, i.e. ($1 - I_{\text{dark}}/I_{\text{bright}}$), increased with increasing 405 nm power in the low intensity range, but decreased as the 405 nm power increased beyond a certain threshold.

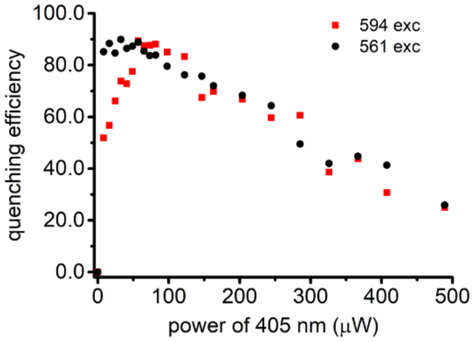

Figure 6-24 Quenching efficiency ($1 - I_{\text{dark}}/I_{\text{bright}}$) as a function of 405 nm depletion light power. With the excitation light of either 561 nm or 594 nm, quenching efficiency increases initially with increased 405 nm power, and decreases afterwards beyond a critical point. Each data point was measured on a new location on GUVs to avoid effects of accumulated photodegradation. The data were acquired on a Zeiss LSM780 confocal microscope.

The decreasing trend cannot be explained by photobleaching to the dye because the image brightness stayed approximately constant, but the dark state became brighter with increased power. Similar characteristic curves were reported previously for photoswitchable fluorescent proteins in RESOLFT imaging, which was explained by cross talk as the depletion light elicited fluorescence.[31] It is possible that a similar explanation applies in our case. We can think about the equilibrium of the bulk sample between bright and dark states where the switch is in the closed and open form respectively. The depletion laser causes ring opening of the switch population within a certain time; the open form absorbs much less at 405 nm than the closed form. During this process, because of the re-distribution of the switch population, the **6'-Atto565** component becomes the primary absorbing species of 405 nm light. This causes excitation of the dye, which accelerates ring closure of the switch *via* FRET process. Hence, the saturation level depends on the dynamics of the above processes. It is not difficult to imagine that at low power ranges, the ring opening reaction dominates, giving increased quenching efficiency, and once the power passes a critical point, quenching efficiency drops when ring closing by energy transfer outcompetes ring opening. An alternative explanation is photodegradation of the switch under intense 405 nm illumination, leading to a permanent bright state of a sub-population of the dyad.

6.5 Conclusions

We have investigated the performance of **Dyad 3** in model membrane systems, i.e. LUVs and GUVs. Switching behaviour on LUVs gave poor contrast between bright and dark states, making them unsuitable to be studied by super-resolution microscopy. Nevertheless, it laid the foundation for further analysis of the dyad in analogous GUVs. The dyad showed highly specific localisation in the membrane of GUVs and remarkable switching behaviour. For the first time, we demonstrated RESOLFT imaging on GUVs with the reproducible FWHM of 210 nm at relatively fast acquisition speed, using photochemical reversion. Despite a small improvement of the spatial resolution compared to a confocal image, this breakthrough of using a small-molecule synthetic dyad to achieve super-resolution imaging highlights the feasibility of our generic molecular design, modular versatility of which opens up many future possibilities.

6.6 Experimental

6.6.1 Protocols for preparation of LUVs

LUVs composed of POPC lipid (Avanti Polar Lipids, AL, USA) were freshly prepared (with assistance from Falk Schneider) by an extrusion method at room temperature.

1. Stock solutions were prepared as follows: POPC was dissolved in $CHCl_3$ to make a 10 mg/mL solution. DSPE-PEG(2000) biotin (Avanti Polar Lipids, AL, USA) was dissolved in $CHCl_3$ to make a 1 mg/mL solution. **Dyad 3** was dissolved in $CHCl_3$ to make 1 mM solution. 40 μL, 1 μL and 5 μL of the above solutions respectively were mixed.

2. The solvent was removed under a constant N_2 flow for 20 min. The resulting dried lipid film was suspended in 500 μL PBS buffer, and vortexed at 2500 revolutions per minute (rpm) for 5 min to form MLVs. The suspension was placed in a bath sonicator (Grant XUB5) and exposed to ultrasound of 100 W, 32–38 KHz for 45 min.

3. The sonicated vesicles were passed through polycarbonate membranes of 100 nm pore size (Avanti Polar Lipids, AL, USA) using a mini-extruder set (Avanti Polar Lipids, AL, USA). Based on the similar experiments reported previously,[32,33] this would likely give LUVs of 110–160 nm in diameter.

4. 10 μL of this suspension was diluted with 90 μL PBS buffer, and 30 μL of the diluted suspension was used for imaging.

6.6.2 Fixation of LUVs

6.6.2.1 BSA-biotin method

1. 100 μL of 1 mg/mL biotinylated BSA (Merck) was mixed with 400 μL of 1 mg/mL BSA (Merck), and 200 μL of the above solution was placed in each well of a μ-slide chamber (Ibidi, Martinsried, Germany).

2. The chamber containing the solution was left undisturbed for 90 min.

3. Meanwhile, a 1 μg/mL streptavidin solution in PBS was freshly prepared by diluting a stock solution of 0.1 mg/mL streptavidin that was made from a 10 mM solution (Thermo Fisher Scientific).

4. After removing the BSA solution, each well was washed twice with PBS, and 200 μL of the above streptavidin solution was added.
5. The chamber was left undisturbed for 90 min.
6. While part of the streptavidin solution was removed (not all the solution; streptavidin left on the surface must not be left dried), the wells were washed with PBS > 10 times. 200 μL PBS was left in each well.
7. 30 μL of the freshly prepared vesicle solution was added.
8. After 20 min, the vesicles were imaged.

6.6.2.2 Polylysine (PLL) method

1. 200 μL of a 0.01% (w/v) aqueous PLL solution was added to each well of an 8-well μ-slide chamber (Ibidi, Martinsried, Germany).
2. After 20 min, the PLL solution was removed and the cells washed twice with PBS. 200 μL PBS was left in each well.
3. 30 μL of the freshly prepared vesicle solution was added.
4. After 20 min, the vesicles were imaged.

6.6.3 Protocols for preparation of GUVs

The GUVs were freshly prepared (with assistance from Dr Erdinc Sezgin) on the same day as imaging, and their size ranged from 10 to 100 μm. The following procedure was carried out at room temperature.

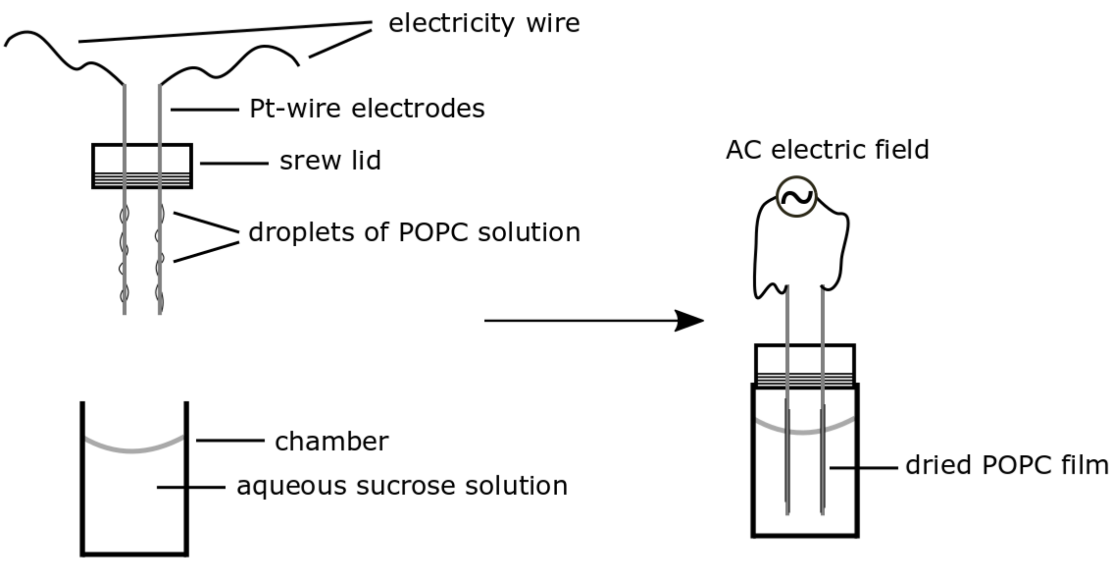

Figure 6-25 Preparation procedure of GUVs using the electroformation method.

1. POPC (Avanti Polar Lipids, AL, US) was dissolved in $CHCl_3$ to make a 1 mg/mL solution, and 5 µL was deposited on two parallel Pt-wire electrodes (distance 5 mm) located at the cap of a home-made chamber that had been cleaned with EtOH overnight and dried. Note: at this stage we did ***not*** add the dyad because such an attempt showed that our compounds were damaged by the applied electric field later.

2. The solvent was evaporated by a constant N_2 flow for 20 min.

3. 360 µL of a 300 mM aqueous sucrose solution was added in the chamber. Note: sucrose and PBS (used as an imaging medium) have similar osmotic pressure to ensure that when GUVs are suspended in PBS later, they do not burst and remain stable for a few hours. In addition, sucrose is denser than PBS, and thus, the GUVs with sucrose enclosed would sink to the passivated surface of the imaging chamber and remain relatively fixed. The surface passivation using BSA or PLL is described later.

4. After the electrodes with dried lipids were inserted into the sucrose solution, an alternating current (AC) electric field was applied using a function generator, for 1 h with a voltage of 2 V at 10 Hz of 5.7 VPP amplitude (amplitude in V from peak to peak; for formation of GUVs), and for another 30 min with a voltage of 2 V at 2 Hz of the same amplitude (for detachment of GUVs from the electrodes).

6.6.4 Preparation of BSA or PLL coated chambers

1. In a LabTek chamber (Thermo Fisher Scientific), 250 µL of a 1 mg/mL aqueous BSA (Merck) or 0.1% (w/v) aqueous PLL solution (Merck) was added into the wells and left undisturbed for 1 h.

2. After removing the above BSA or PLL solution, each well was washed twice with PBS, leaving 250 µL PBS, and 50–100 µL of the prepared GUV sucrose solution was added.

3. After 30 min, the GUVs were imaged.

6.6.5 Optical microscopy

When the Zeiss confocal microscope is mentioned, it refers to confocal imaging that was performed on a Zeiss confocal laser scanning microscope that is described in Chapter 4 Experimental Section.

When the confocal mode on the RESOLFT microscope is mentioned, it refers to confocal imaging that was performed on a custom-built RESOLFT microscope that is described in Chapter 4 Experimental Section. Either line-by-line or pixel-by-pixel scanning method was used as specified. Super-resolved images were obtained in the RESOLFT mode of the same microscope. The donut-shaped depletion beam was created by insertion of a vortex phase plate (VPP-1b, RPC Photonics, Rochester, NY) at the wavefront of the 405 nm laser path. The light sources were 405 nm (Cobolt diode laser, CW), 485 nm (LDH-D-C-485, PicoQuant, pulsed), 594 nm (PDL594, Abberior, pulsed), and 640 nm (LDH-D-C-640, PicoQuant, pulsed).

The images were processed in ImageJ (Fiji software). Calculations of FWHMs were carried out using custom written Macro scripts that can be found in Appendices. This was cross-checked with manual Gaussian fitting of hand-picked line profiles of intensity distribution.

6.7 References

[1] J. Voskuhl, B. J. Ravoo, *Chem. Soc. Rev.* **2009**, *38*, 495–505.
[2] P. Walde, K. Cosentino, H. Engel, P. Stano, *ChemBioChem* **2010**, *11*, 848–865.
[3] C. Huang, D. Quinn, Y. Sadovsky, S. Suresh, K. J. Hsia, *Proc. Natl. Acad. Sci.* **2017**, *114*, 2910–2915.
[4] F. Fernandez-Trillo, L. M. Grover, A. Stephenson-Brown, P. Harrison, P. M. Mendes, *Angew. Chem. Int. Ed.* **2017**, *56*, 3142–3160.
[5] A. C. Carreira, R. F. M. de Almeida, L. C. Silva, *Sci. Rep.* **2017**, *7*, 3949.

[6] G. Stengel, R. Zahn, F. Höök, *J. Am. Chem. Soc.* **2007**, *129*, 9584–9585.
[7] Y. Nozaki, C. Tanford, *Proc. Natl. Acad. Sci.* **1981**, *78*, 4324–4328.
[8] P. Vader, E. A. Mol, G. Pasterkamp, R. M. Schiffelers, *Adv. Drug Deliv. Rev.* **2016**, *106*, 148–156.
[9] A. Musyanovych, K. Landfester, *Macromol. Biosci.* **2014**, *14*, 458–477.
[10] F. Danhier, O. Feron, V. Préat, *J. Controlled Release* **2010**, *148*, 135–146.
[11] K. Riehemann, S. W. Schneider, T. A. Luger, B. Godin, M. Ferrari, H. Fuchs, *Angew. Chem. Int. Ed.* **2009**, *48*, 872–897.
[12] X. Guo, F. C. Szoka, *Acc. Chem. Res.* **2003**, *36*, 335–341.
[13] C. Xu, S. Hu, X. Chen, *Mater. Today Kidlington Engl.* **2016**, *19*, 516–532.
[14] F. Caschera, V. Noireaux, *Curr. Opin. Chem. Biol.* **2014**, *22*, 85–91.
[15] G. Maulucci, M. De Spirito, G. Arcovito, F. Boffi, A. C. Castellano, G. Briganti, *Biophys. J.* **2005**, *88*, 3545–3550.
[16] E. S. Richardson, W. G. Pitt, D. J. Woodbury, *Biophys. J.* **2007**, *93*, 4100–4107.
[17] L. D. Mayer, M. J. Hope, P. R. Cullis, *Biochim. Biophys. Acta BBA - Biomembr.* **1986**, *858*, 161–168.
[18] R. C. MacDonald, R. I. MacDonald, B. P. M. Menco, K. Takeshita, N. K. Subbarao, L. Hu, *Biochim. Biophys. Acta BBA - Biomembr.* **1991**, *1061*, 297–303.
[19] O. H. Laitinen, V. P. Hytönen, H. R. Nordlund, M. S. Kulomaa, *Cell. Mol. Life Sci. CMLS* **2006**, *63*, 2992–3017.
[20] M. P. Nicholas, L. Rao, A. Gennerich, *Methods Mol. Biol. Clifton NJ* **2014**, *1136*, 137–169.
[21] H. W. Schroeder, C. Mitchell, H. Shuman, E. L. F. Holzbaur, Y. E. Goldman, *Curr. Biol.* **2010**, *20*, 687–696.
[22] P. Barak, A. Rai, P. Rai, R. Mallik, *Nat. Methods* **2013**, *10*, 68–70.
[23] O. Wesołowska, K. Michalak, J. Maniewska, A. B. Hendrich, *Acta Biochim. Pol.* **2009**, *56*, 33–39.
[24] S. F. Fenz, K. Sengupta, *Integr. Biol.* **2012**, *4*, 982–995.
[25] J. P. Reeves, R. M. Dowben, *J. Cell. Physiol.* **1969**, *73*, 49–60.
[26] K. Akashi, H. Miyata, H. Itoh, K. Kinosita, *Biophys. J.* **1996**, *71*, 3242–3250.
[27] M. I. Angelova, D. S. Dimitrov, *Faraday Discuss. Chem. Soc.* **1986**, *81*, 303–311.
[28] M. I. Angelova, S. Soléau, P. Méléard, F. Faucon, P. Bothorel, in *Trends Colloid Interface Sci. VI*, Steinkopff, **1992**, pp. 127–131.
[29] L. A. Bagatolli, *Biochim. Biophys. Acta BBA - Biomembr.* **2006**, *1758*, 1541–1556.
[30] A. S. Klymchenko, S. Oncul, P. Didier, E. Schaub, L. Bagatolli, G. Duportail, Y. Mély, *Biochim. Biophys. Acta BBA - Biomembr.* **2009**, *1788*, 495–499.
[31] M. Hofmann, C. Eggeling, S. Jakobs, S. W. Hell, *Proc. Natl. Acad. Sci.* **2005**, *102*, 17565–17569.
[32] M. M. Lapinski, A. Castro-Forero, A. J. Greiner, R. Y. Ofoli, G. J. Blanchard, *Langmuir* **2007**, *23*, 11677–11683.
[33] N.-J. Cho, L. Y. Hwang, J. J. R. Solandt, C. W. Frank, *Materials* **2013**, *6*, 3294–3308.

Chapter 7

Conclusions and Future Work

7 Conclusions and Future Work

The emergence of super-resolution microscopy (SRM) triggers an ever-increasing demand for fluorescent probes. In this work, we establish a generalisable approach of developing photoswitchable synthetic dyes for application in a SRM technique, i.e. reversible saturable optical fluorescence transitions (RESOLFT) microscopy. We exploit intramolecular Förster resonance energy transfer (FRET) process in a modular molecular design, where the reversible change in spectral properties of a photoswitch is used to modulate fluorescence states of a covalently attached dye. Photoswitches and dyes from a variety of families have been explored, and the photoswitching performance of derived dyads has also been investigated by cell imaging. Achievement of super-resolved imaging using these dyads in liposomes highlights the feasibility of our generic molecular design. Furthermore, the versatility associated with each assembling component indicates high potential utility of such systems being applied in more complex environments and for more challenging biological research.

Chapter 2 describes a dyad consisting of a spiropyran photoswitch and a red-emitting silicon rhodamine dye. The system exhibits several desirable features in live cell imaging, including membrane permeability, high brightness, reversible fluorescence modulation using visible light, and strong contrast between bright and dark states. However, the relatively low fatigue resistance prevents it from being applied in RESOLFT microscopy.

Chapter 3 investigates a spirooxazine photoswitch, **SO**, that fulfils the design criteria to work as a tuneable FRET-quencher. The closed (inactive) form of the switch is readily switched to the coloured open form by 405 nm light, and combination of the relatively high quantum yield of ring-opening and poor quantum yield of ring-closing results in an uncommonly high photoconversion. The ultrafast time-resolved spectroscopy shows that the photochemistry of the switch is simpler than other related spirooxazines, which explains the good fatigue resistance due to presence of fewer side-reactions.

Chapter 4 continues to explore several related dyads by linking commercial fluorescent dyes **Atto565** with the spirooxazine switch described in Chapter 3. It is demonstrated that such dyads display high contrast between bright and dark states, and excellent fatigue resistance in live cells, which illustrates its potential to be applied in RESOLFT microscopy. Additionally, comparison of related dyes and dyads indicates that the low fluorescence quantum yields of the dyads arise from static quenching by aggregation in aqueous media and photoinduced electron transfer (PET) when the switch is not in the quencher form. This analysis points to future work which involves the use of a sufficiently long rigid linker to limit quenching by undesired PET that is more dependent on the separation distance of the switch and dye compared to FRET.

Chapter 5 further advances the spirooxazine-based dyad system by incorporating additional functionalities for specific labelling of proteins of interest. The Halo-tag technique is first exploited for live cell staining. A number of such triads are prepared from different synthetic approaches, and the preliminary imaging results imply that the spacer separating the dyad and the tag-binding ligand is of insufficient length, preventing the selective labelling and photoswitching behaviour. Another possibility is the overall hydrophobicity of the triads that dominates the localisation. Several potential solutions are proposed, including the use of a longer spacer and dyes of different hydrophilic nature. Meanwhile, initial experiments using an immunolabelling approach with an NHS-based triad were carried out, and future work on this would provide further insight into the current molecular design.

Chapter 6 reports the first RESOLFT imaging using the spirooxazine-based dyad, demonstrating the high potential of our molecular approach. The initial attempts in large unilamellar vesicles (LUVs) do not yield satisfactory contrast between bright and dark states, but it lays the foundation for investigation of our system in analogous giant unilamellar vesicles (GUVs). In a confocal microscope, our dyad exhibits extremely promising behaviour: selective localisation around the GUV membrane, impressive bright/dark contrast and strong fatigue resistance. Following this, for the first time, RESOLFT images are attained in GUVs using 405 nm and 594 nm as the depletion and excitation light respectively, with significant improvement in the spatial resolution compared to a confocal image. Furthermore, relatively fast acquisition speed is made possible by photochemical reversion by red light at 640 nm. As a simplified model system, GUVs are a good starting point to test new molecules in the project from future work.

In summary, this work has demonstrated the achievement of RESOLFT imaging using our synthetic dyad that consists of a photoswitch conjugated to a dye. The generalisability and modularity of our molecular design indicate future possibilities for functional synthetic dyes to be applied in advanced biological studies using super-resolution microscopy.

Appendices

Appendices

A1 Coordinates of DFT-optimised structures (Chapter 3)

DFT calculations were conducted by Dr Andreas Vargas Jentzsch.

SO$_{(closed)}$

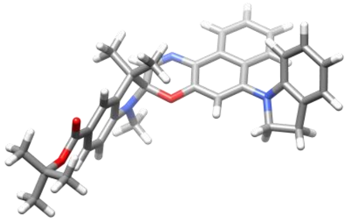

Symbol	X	Y	Z
C	-8.82887000	-1.21430800	-1.09367100
C	-8.64812900	-2.10217100	-0.02923700
C	-7.60035500	-1.93873500	0.89181600
C	-6.71065000	-0.84888400	0.74514900
C	-6.88287000	0.03549200	-0.30002500
C	-7.93689900	-0.14388600	-1.21720400
H	-9.63618400	-1.36606500	-1.80170700
H	-9.32545000	-2.94077400	0.08253500
C	-6.13495800	1.31208800	-0.65626900
C	-4.60784000	1.19965900	-0.55134100
H	-4.32512300	1.03963000	0.49372700
H	-4.21952400	0.36732400	-1.14109900
H	-4.12283100	2.12314500	-0.88477300
C	-6.63194400	2.45761700	0.26051900
H	-6.37768700	2.22012700	1.29746600
H	-6.15190900	3.40811900	0.00479900
H	-7.71686200	2.58584300	0.20106000
N	-7.92379200	0.86548000	-2.17211700
C	-6.63410200	1.52961400	-2.14897800
C	-6.74596400	2.97806900	-2.58220300
C	-4.88235600	1.46439700	-3.86564400
H	-7.56599300	3.54164800	-2.14030900
C	-4.94893300	2.84018000	-4.02215100
C	-3.91396300	0.68687600	-4.52935800
C	-4.01670000	3.48934200	-4.89381400
C	-2.97599000	1.28728200	-5.35488000
H	-3.90060400	-0.38070700	-4.34381500
C	-3.03162800	2.70995600	-5.58673000
C	-4.06765300	4.89148300	-5.12168900
C	-2.18227900	3.36098900	-6.52155400
C	-3.20660800	5.49567800	-6.01488100
H	-4.80862300	5.47396900	-4.58640600
H	-1.46818600	2.76987300	-7.08246500
C	-2.26411800	4.72239800	-6.73303800
H	-3.26273400	6.56797600	-6.17933400
H	-1.60940100	5.19911300	-7.45637000
H	-5.90440500	-0.72997600	1.46172500
C	-7.38061000	-2.87453300	2.02485400
O	-8.30114000	-3.85786400	2.06230500
O	-6.46288200	-2.75624600	2.83002300
C	-8.68909300	0.76438700	-3.40820600
H	-8.35596200	-0.07297900	-4.03518400
H	-9.74849900	0.63355700	-3.17345100
H	-8.58224000	1.69099900	-3.97559400
O	-5.76333500	0.79528000	-3.06832200
N	-5.96996900	3.57655900	-3.40822500
C	-0.61411700	0.59346000	-5.78767400
C	0.03989000	-0.47292900	-6.43593900
C	0.10641000	1.52694600	-5.03731500
C	1.42012300	-0.59988500	-6.35993200
C	1.50068900	1.38593400	-4.96811600
H	-0.39001800	2.33673900	-4.51487300
C	2.15960300	0.34014400	-5.62087000
H	1.92347800	-1.42327700	-6.86027500
H	2.07256400	2.10285800	-4.38553900
H	3.23898000	0.24743500	-5.54906200
N	-2.00389100	0.50462800	-6.00900900
C	-8.30163900	-4.92166800	3.09485800
C	-7.01559600	-5.74798600	2.99487500
H	-6.14042700	-5.16148800	3.27715100
H	-7.08991400	-6.61021300	3.66563800
H	-6.88026800	-6.12222800	1.97496800
C	-9.51768700	-5.76410900	2.70108600
H	-9.63140300	-6.59967200	3.39825700
H	-10.43149500	-5.16276100	2.72975900
H	-9.39801400	-6.16947000	1.69172100
C	-8.49827400	-4.30428300	4.48305900
H	-7.63586900	-3.70705400	4.78166600
H	-9.39191800	-3.67198100	4.49677100
H	-8.63873100	-5.10604900	5.21542700
C	-2.29866600	-0.87797600	-6.45023700
H	-3.17641000	-0.88536100	-7.10009600
H	-2.49285100	-1.53150600	-5.58663800
C	-0.99599600	-1.31316500	-7.15162600
H	-1.02849200	-1.05867700	-8.21968300

H	-0.82262100	-2.38913800	-7.06936900

SO, open form TTC

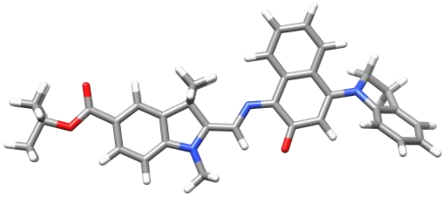

Symbol	X	Y	Z
C	-8.96271800	-0.98721700	-0.69689800
C	-8.66815200	-2.02872900	0.18563900
C	-7.47568500	-2.04274100	0.92911900
C	-6.55104200	-0.98668200	0.78761500
C	-6.83321500	0.05000500	-0.08239500
C	-8.03017700	0.04554300	-0.81607700
H	-9.88833600	-1.00002100	-1.26047700
H	-9.37350500	-2.84319600	0.29848000
C	-6.03399200	1.29550000	-0.43126800
C	-5.81811600	2.18671700	0.81588900
H	-5.29704100	3.10376000	0.53552500
H	-6.77290500	2.45315100	1.27930800
H	-5.21826000	1.64511600	1.55418800
C	-4.67634800	0.91864400	-1.07353200
H	-4.14277100	1.82011200	-1.37961000
H	-4.06673200	0.37061200	-0.34807700
H	-4.81959200	0.28129500	-1.95136800
N	-8.07992000	1.19392300	-1.61717400
C	-6.96302900	1.96805700	-1.44852300
C	-6.78838900	3.16057800	-2.14022100
C	-6.24276800	5.73728200	-3.51455700
H	-7.54720700	3.49448500	-2.83788500
C	-5.38573000	5.04119900	-2.51818400
C	-5.80658800	7.03056300	-3.98157600
C	-4.09996900	5.66644100	-2.15632000
C	-4.64215800	7.63792600	-3.58164900
H	-6.49586400	7.54602300	-4.64069100
C	-3.71190200	6.92459700	-2.69832600
C	-3.20097700	5.00530900	-1.29314000
C	-2.42035800	7.42105300	-2.42476600
C	-1.95007100	5.53346100	-1.00014100
H	-3.50325800	4.05517300	-0.87150400
H	-2.09084100	8.33844200	-2.89453400
C	-1.54617600	6.74248800	-1.58436600
H	-1.27987600	4.99675000	-0.33470600
H	-0.55672900	7.14555700	-1.39115500
H	-5.63394500	-1.00946200	1.36684100
C	-7.13927200	-3.14469700	1.87532200
O	-8.10644600	-4.07610000	1.93486900
O	-6.09630400	-3.18065800	2.51716300
C	-9.17757400	1.53111000	-2.51644800
H	-9.94366500	0.76105500	-2.45833000
H	-9.61908400	2.49066100	-2.23243600
H	-8.81772000	1.59501000	-3.54743800
O	-7.33748900	5.25925400	-3.90863300
N	-5.67266100	3.89167600	-1.93261200
C	-4.83503100	9.51813700	-5.19133300
C	-5.08432700	10.88509800	-4.99019500
C	-5.03311600	8.92551600	-6.44223000
C	-5.54159500	11.67655800	-6.03893100
C	-5.49651000	9.72993400	-7.49001500
H	-4.83065000	7.87206800	-6.60260500
C	-5.75009100	11.09359400	-7.29786400
H	-5.73709100	12.73438800	-5.88432200
H	-5.65271200	9.28531500	-8.46863700
H	-6.10468700	11.70107100	-8.12497900
N	-4.30572000	8.92262900	-4.02195900
C	-8.01460400	-5.28043600	2.79923000
C	-6.82418000	-6.14107800	2.36572500
H	-5.87474500	-5.64502100	2.57110500
H	-6.84872100	-7.08857600	2.91378600
H	-6.88491800	-6.36649700	1.29616900
C	-9.33589900	-5.99620700	2.50907900
H	-9.39441000	-6.91721200	3.09670700
H	-10.18704400	-5.36186300	2.77464500
H	-9.41144000	-6.25692100	1.44904600
C	-7.93645100	-4.86120400	4.27033700
H	-6.99698100	-4.35421700	4.49390000
H	-8.76927800	-4.19724100	4.52332300
H	-8.01043100	-5.75313400	4.90098300
C	-3.96239900	10.02510600	-3.07059700
H	-2.89536900	10.26123400	-3.14652400
H	-4.18138500	9.72223600	-2.04639300
C	-4.80038400	11.23360800	-3.54650300
H	-4.25354100	12.17257000	-3.42555300
H	-5.73592800	11.31816600	-2.97835700

SO, open form CTC

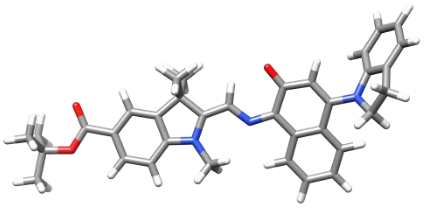

Symbol	X	Y	Z
C	-8.92595500	-0.69105300	-0.49667900
C	-8.66373200	-1.88753100	0.17521100
C	-7.48409100	-2.06650300	0.91716600
C	-6.54042900	-1.02058800	0.99430600
C	-6.79178400	0.16773600	0.33410100
C	-7.97103800	0.32421000	-0.40905400
H	-9.84737600	-0.57203700	-1.05450000
H	-9.38688700	-2.69266300	0.12605100
C	-5.97987600	1.44578300	0.24380900
C	-5.76536600	2.08079800	1.63851400
H	-5.22129600	3.02567100	1.55384200
H	-6.72006900	2.27312800	2.13652500
H	-5.17899500	1.40292400	2.26657000
C	-4.61551500	1.20077200	-0.44703000
H	-4.06080300	2.13771300	-0.54967400
H	-4.01625700	0.51113600	0.15558700
H	-4.74809700	0.76408600	-1.44114000
N	-7.99277100	1.60152100	-0.99284400
C	-6.88947200	2.32315400	-0.63066400
C	-6.54934400	3.63309700	-0.95114100
C	-5.78010300	6.37717000	-1.79891500
H	-5.58463500	3.98262200	-0.60156100
C	-7.08168800	5.69101700	-2.01409900
C	-5.60333500	7.67450300	-2.40569700
C	-8.15097300	6.43995300	-2.69833700
C	-6.57634900	8.32464500	-3.12332600
H	-4.61045700	8.10020000	-2.31504800
C	-7.92128300	7.74444000	-3.22088200
C	-9.44824300	5.89608900	-2.80546000
C	-9.00547100	8.47075300	-3.75525300
C	-10.49373300	6.61184000	-3.37543600
H	-9.62053100	4.90463000	-2.40693200
H	-8.85363900	9.48980300	-4.08615100
C	-10.27726900	7.91676900	-3.84035300
H	-11.48243400	6.16615600	-3.43791300
H	-11.09555500	8.49804800	-4.25425300
H	-5.63525900	-1.16974400	1.57352700
C	-7.18377000	-3.33431600	1.64289700
O	-8.15715200	-4.24850600	1.49212300
O	-6.16157600	-3.50512000	2.29600500
C	-9.07740500	2.04633300	-1.86202000
H	-8.67440200	2.69500800	-2.63643600
H	-9.54586700	1.17310100	-2.31649900
H	-9.82678500	2.60561100	-1.29253500
O	-4.83291700	5.83862000	-1.17139200
N	-7.36670400	4.45415500	-1.64257700
C	-5.27834600	10.42759400	-3.36560100
C	-4.69464200	11.02893300	-4.49209900
C	-4.87264600	10.77251100	-2.07268600
C	-3.69144400	11.98046000	-4.33878400
C	-3.86014000	11.72856500	-1.92946800
H	-5.32975400	10.31754000	-1.20062700
C	-3.27080600	12.33172200	-3.04731200
H	-3.23705700	12.44534700	-5.20971500
H	-3.53552100	12.00925800	-0.93165700
H	-2.49007200	13.07445400	-2.91433400
N	-6.32407300	9.55266900	-3.74393000
C	-8.10115300	-5.59650100	2.11346400
C	-6.90055200	-6.37283800	1.56425600
H	-5.95636400	-5.93616500	1.89214800
H	-6.94945300	-7.40673200	1.92118000
H	-6.92468400	-6.39044100	0.46992500
C	-9.41493800	-6.22865000	1.64812400
H	-9.49762600	-7.24457900	2.04554100
H	-10.27184500	-5.64779200	2.00262000
H	-9.45522300	-6.28022200	0.55585300
C	-8.07221500	-5.46568100	3.63917800
H	-7.13839000	-5.02160200	3.98618400
H	-8.90982900	-4.85220800	3.98629600
H	-8.17268400	-6.46045900	4.08538300
C	-5.31689200	10.44883300	-5.74215500
H	-5.54896500	11.20058500	-6.50129900
H	-4.64640900	9.70993400	-6.19999900
C	-6.59935100	9.78043400	-5.19668600
H	-7.44951600	10.46186000	-5.31052200
H	-6.83921300	8.83725200	-5.68818600

SO, open form TTT

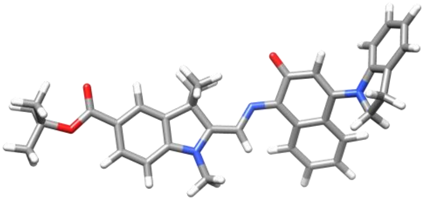

Symbol	X	Y	Z
C	-8.71267500	-1.21816300	-1.01565500
C	-8.34851900	-2.24471400	-0.14140800
C	-7.35665100	-2.05665800	0.83600500
C	-6.71129900	-0.80594400	0.94361900
C	-7.06382400	0.21726500	0.08403600
C	-8.05623900	0.00852700	-0.88803700
H	-9.48130500	-1.38897000	-1.76058000
H	-8.84147100	-3.20633900	-0.21909300
C	-6.54391700	1.64288300	-0.02204800
C	-6.81974900	2.43234700	1.28055800
H	-6.48797700	3.46646400	1.16767100
H	-7.88626700	2.42656700	1.52665100
H	-6.27479800	1.97234800	2.11123500
C	-5.03194200	1.66605300	-0.35587000
H	-4.69243300	2.69646900	-0.47526400
H	-4.47189300	1.19526200	0.45852300
H	-4.82448600	1.11275800	-1.27718100
N	-8.22670400	1.18257700	-1.62983500
C	-7.38513300	2.17654900	-1.18900300
C	-7.37191900	3.44224100	-1.74393200
C	-5.07771500	6.26732800	-1.28233500
H	-8.04307000	3.65202100	-2.57396500
C	-6.34607500	5.59220200	-1.71747200
C	-4.58645900	7.32536500	-2.14109200
C	-7.24694600	6.36348800	-2.59767400
C	-5.31327800	7.84509100	-3.18166900
H	-3.56696400	7.64471600	-1.96031700
C	-6.73509700	7.47391600	-3.32927100
C	-8.63450800	6.12138100	-2.64052300
C	-7.61886800	8.27519500	-4.07286200
C	-9.49181100	6.91445300	-3.40076700
H	-9.05972600	5.33635200	-2.02852800
H	-7.24287200	9.15285800	-4.58296100
C	-8.98205800	7.99354400	-4.12783000
H	-10.55745400	6.70559000	-3.40242300
H	-9.64330700	8.63009100	-4.70752900
H	-5.94720800	-0.67181800	1.70219300
C	-6.95020000	-3.13752600	1.77710800
O	-7.63857000	-4.27510900	1.57354500
O	-6.08574300	-2.99144900	2.63315600
C	-9.16861300	1.34134500	-2.72933600
H	-9.68009900	0.39816200	-2.90951400
H	-9.91494100	2.10473200	-2.48763300
H	-8.64209100	1.63232600	-3.64331800
O	-4.40685200	5.86165700	-0.31305500
N	-6.47776300	4.35846400	-1.29727300
C	-3.61799200	9.54922600	-3.81604500
C	-2.85730600	9.69420000	-4.98716100
C	-3.24350100	10.18531800	-2.62883400
C	-1.70297500	10.47035200	-4.98190700
C	-2.07870500	10.96216200	-2.63365300
H	-3.83825800	10.08962100	-1.72707800
C	-1.31062300	11.10716500	-3.79506600
H	-1.11139000	10.58175600	-5.88666900
H	-1.77508200	11.46486900	-1.72002400
H	-0.41263200	11.71723300	-3.77839700
N	-4.78287100	8.78317900	-4.06513900
C	-7.42097500	-5.50355300	2.37809500
C	-5.98755400	-6.00672500	2.18278100
H	-5.25929600	-5.32136400	2.61820100
H	-5.88147100	-6.98277200	2.66739900
H	-5.76788200	-6.13123900	1.11755000
C	-8.42693400	-6.48138900	1.76610500
H	-8.36677400	-7.44482700	2.28108700
H	-9.44777900	-6.09979400	1.86460200
H	-8.21487900	-6.64251700	0.70475900
C	-7.75551000	-5.23104500	3.84773800
H	-7.04242200	-4.54083900	4.30017700
H	-8.76343500	-4.81369700	3.93933000
H	-7.72762700	-6.17495300	4.40180500
C	-4.91905600	8.63913300	-5.54784400
H	-5.60767300	9.39931400	-5.93237000
H	-5.31132100	7.65321500	-5.79749300
C	-3.49738800	8.89238400	-6.09779900
H	-3.52557200	9.42081800	-7.05437300
H	-2.95777700	7.94922800	-6.25380700

SO, open form CTT

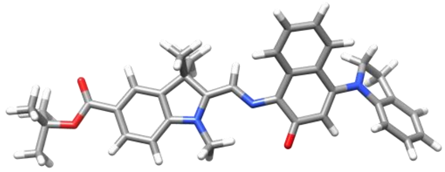

Symbol	X	Y	Z
C	-8.40651100	-0.97203900	-1.14079800
C	-8.46080200	-1.97895700	-0.17353300
C	-7.57002200	-1.99764600	0.91328600
C	-6.59715900	-0.98196000	1.04013300
C	-6.53593000	0.01802100	0.08842200
C	-7.43244600	0.01729400	-0.98982800
H	-9.10186600	-0.96982400	-1.97230300
H	-9.20512000	-2.76119400	-0.26226200
C	-5.61938500	1.22139200	-0.03977000
C	-5.77818400	2.18087000	1.16421400
H	-5.14950200	3.06762200	1.04065000
H	-6.81671800	2.50531100	1.27647000
H	-5.47425300	1.67285700	2.08480700
C	-4.14130600	0.78832200	-0.18806900
H	-3.49079400	1.65882700	-0.31426900
H	-3.82064800	0.25220100	0.71069000
H	-4.00775200	0.12724700	-1.04918000
N	-7.18338400	1.11647100	-1.81958700
C	-6.14522200	1.87007800	-1.33439700
C	-5.57865100	3.02218100	-1.85605900
C	-6.53334000	5.32517800	-4.54576400
H	-4.75310400	3.43462200	-1.27920800
C	-5.60459700	4.73003300	-3.52919300
C	-6.40197400	6.74678600	-4.78403200
C	-4.34330600	5.44880300	-3.26746700
C	-5.37240900	7.49858400	-4.27659800
H	-7.21151300	7.21146300	-5.33419100
C	-4.22960100	6.82255900	-3.63028100
C	-3.19457400	4.79056000	-2.78457800
C	-2.99139300	7.47209900	-3.48550700
C	-1.98155100	5.45809800	-2.62777800
H	-3.23231600	3.72849400	-2.58095300
H	-2.88510300	8.49804300	-3.81398300
C	-1.87891400	6.80830400	-2.97317800
H	-1.11362900	4.91709300	-2.26281400
H	-0.93369700	7.33293000	-2.87426700
H	-5.91738700	-1.00815400	1.88543500
C	-7.60912000	-3.06103300	1.95663900
O	-8.57840800	-3.96384800	1.72654300
O	-6.83851900	-3.09437500	2.90896000
C	-7.98635800	1.35116000	-3.01983300
H	-7.61209800	2.23281600	-3.53308700
H	-7.92784700	0.47401100	-3.67259600
H	-9.03182200	1.51027400	-2.73459900
O	-7.45468100	4.66425200	-5.06692000
N	-6.06089200	3.64388600	-2.95519100
C	-6.08688900	9.61984300	-5.35818700
C	-6.52854300	10.83029300	-4.80054200
C	-6.34050500	9.30697200	-6.69689500
C	-7.24141000	11.74010200	-5.57451500
C	-7.06088700	10.22838700	-7.46647500
H	-5.98547800	8.38086400	-7.13545700
C	-7.51072800	11.43492000	-6.91705600
H	-7.58617700	12.67649900	-5.14407800
H	-7.26421000	10.00160800	-8.50899700
H	-8.06441600	12.13762300	-7.53225900
N	-5.32254200	8.88375900	-4.42018900
C	-8.82873300	-5.12450400	2.61790900
C	-7.59855900	-6.03661400	2.64294800
H	-6.75245100	-5.55501800	3.13471300
H	-7.84382400	-6.95364700	3.18852800
H	-7.30825300	-6.31514900	1.62481800
C	-10.00591200	-5.82011400	1.93027800
H	-10.29379800	-6.70946600	2.49877000
H	-10.87054700	-5.15204000	1.87176100
H	-9.73478800	-6.13025900	0.91653300
C	-9.22808200	-4.63361800	4.01273700
H	-8.39673500	-4.13967500	4.51727600
H	-10.06991900	-3.93694600	3.94632600
H	-9.54380400	-5.49039700	4.61689200
C	-5.03153000	9.79014700	-3.26613400
H	-4.03986800	10.23905200	-3.38847100
H	-5.04940900	9.22993200	-2.33127000
C	-6.11694000	10.88692300	-3.34680500
H	-5.72542900	11.86161400	-3.04388200
H	-6.96826200	10.65233700	-2.69468700

A2 Overlay of UV-vis absorption spectra (Chapter 4)

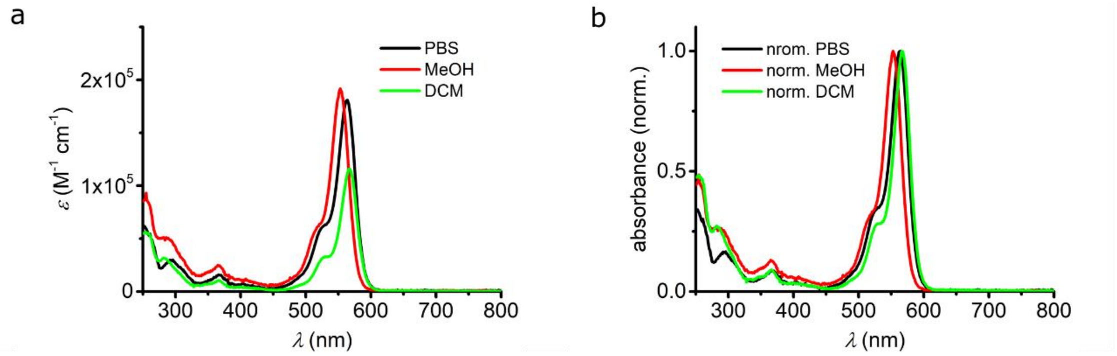

Figure 0-1 UV-vis absorption spectra of **6'-Atto565** in different solvents, a) in the unit of molar absorption coefficients. b) when normalised.

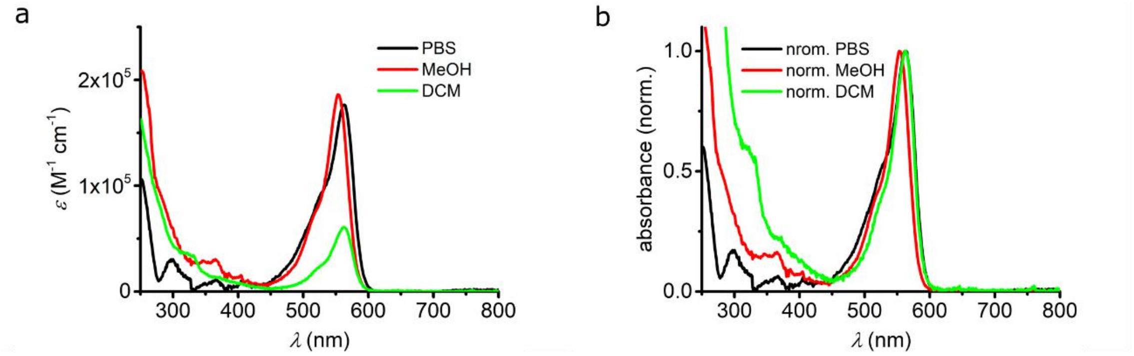

Figure 0-2 UV-vis absorption spectra of **6'-Atto565-C2linker** in different solvents, a) in the unit of molar absorption coefficients. b) when normalised.

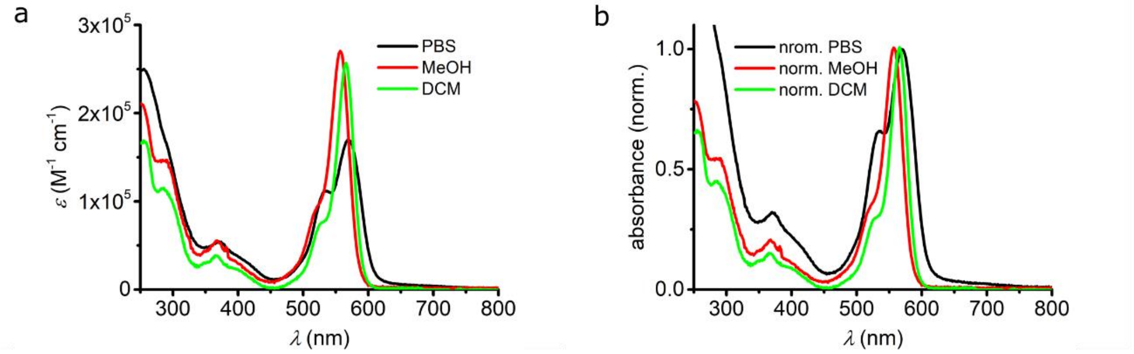

Figure 0-3 UV-vis absorption spectra of **Dyad 3** in different solvents, a) in the unit of molar absorption coefficients. b) when normalised.

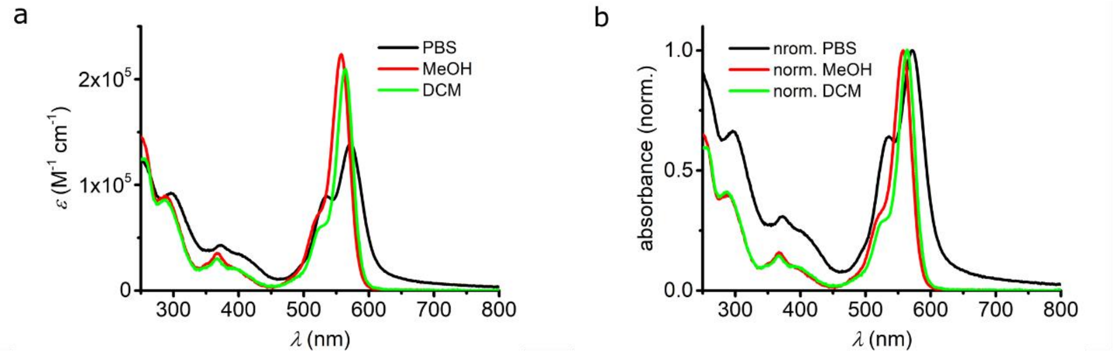

Figure 0-4 UV-vis absorption spectra of **Dyad 4** in different solvents, a) in the unit of molar absorption coefficients. b) when normalised.

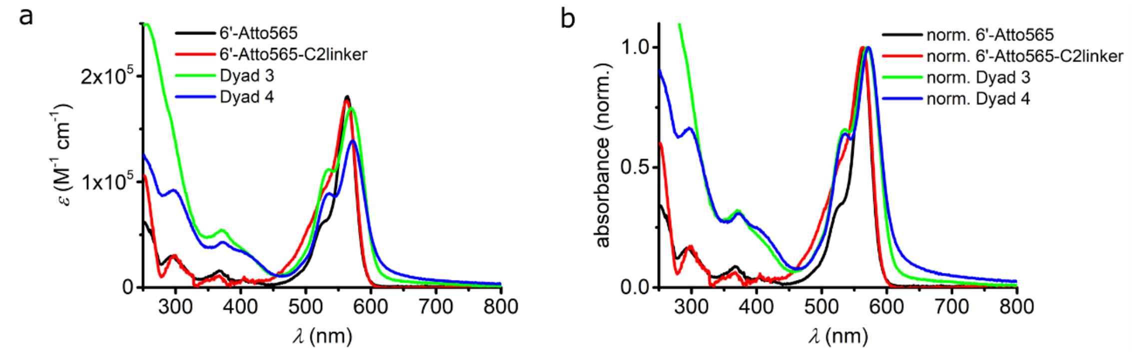

Figure 0-5 UV-vis absorption spectra of the four compounds in PBS buffer, a) in the unit of molar absorption coefficients. b) when normalised.

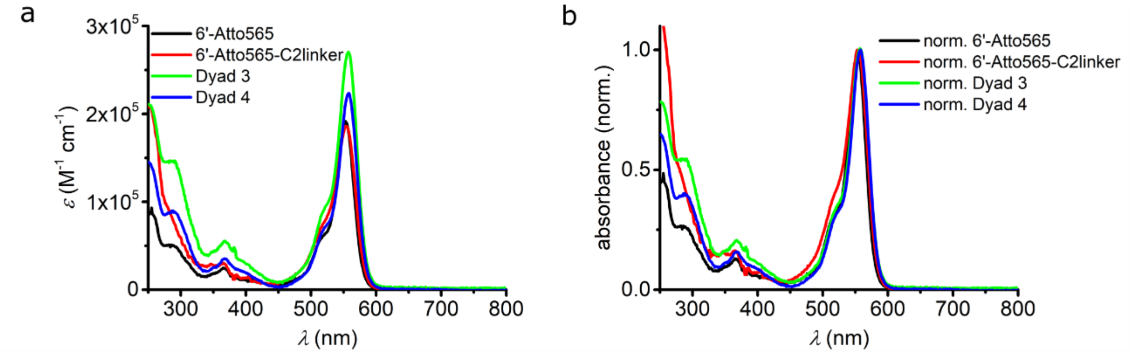

Figure 0-6 UV-vis absorption spectra of the four compounds in MeOH, a) in the unit of molar absorption coefficients. b) when normalised.

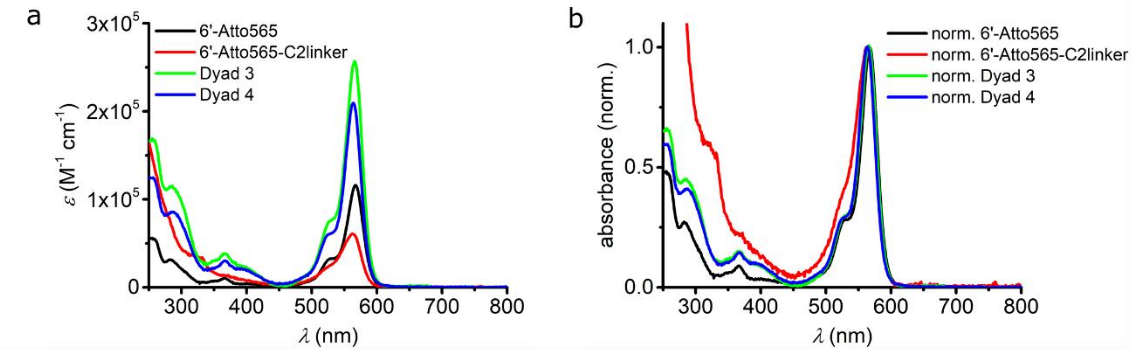

Figure 0-7 UV-vis absorption spectra of the four compounds in DCM, a) in the unit of molar absorption coefficients. b) when normalised.

A3 ImageJ macro script

We used a FWHM measuring algorithm in ImageJ macro language, which was provided by Dr Dominic Waithe, WIMM, University of Oxford. The script can be found in (https://github.com/dwaithe/generalMacros/tree/master/FWHM%20bulk%20measure).

A4 Matlab codes for photoswitch characterisations

Acknowledgements go to Dr Andreas Vargas Jentzsch who helped and guided the writing of the Matlab codes for characterising properties of photoswitches.

A4.1 Acquisition of UV-vis spectra of PSS for type T photoswitches

```
function[] = LED_blue_LS
instrumentObjects=instrfind;
delete(instrumentObjects);
clear all;
prompt={'Enter first pulse length','Enter first interval','Enter pulse
length','Enter interval','Number of cycles'};
%the pulses to maintain PSS when thermal relaxation is fast,
particular in polar solvents
dlg_title = 'Blue LED control';
num_lines = 1;
defaultans = {'2000','300','500','500','10'};
answer = inputdlg(prompt,dlg_title,num_lines,defaultans);
num=cellfun(@str2num,answer)
a=answer(1,1)
b={'0'}    %num2str(0)%answer(2,1)
c=answer(3,1)
d=answer(4,1)
e=answer(5,1)
param={'1,1,',',',',0,0,1,0,0,1@'}
param_blue={',1,',',',',0,0,1,0,0,1@'}
%  num=cellfun(@str2num,answer)
%  a=num(1)
%  b=num(2)
%  c=a+b
string_first = [strcat(param{1},a{1},param{2},b{1},param{3})]
string_second =
[strcat(e{1},param_blue{1},c{1},param_blue{2},d{1},param_blue{3})]
s1=serial('COM4')
set(s1,'baudrate',57600)
fopen(s1)
pause(2)
%fprintf(s1,'10,1,a,b,0,0,1,0,0,1@')
fprintf(s1,'%s\n',string_first)
% fclose(s1)
% pause((num(2)-100)/1000)
% fopen(s1)
pause((num(1)+num(2))/1000)
%fprintf(s1,'10,1,a,b,0,0,1,0,0,1@')
fprintf(s1,'%s\n',string_second)
fclose(s1)
instrumentObjects=instrfind;
delete(instrumentObjects);
clear all;
end
```

A4.2 Reconstruction of UV-vis spectra of PSS acquired from A4.1

```
function [noLEDfull] = reconstruct_LED(X,Y)
% This function is supposed to take the spectrum of the photogenerated
state of a switchable dye as obtained from the UV-vis
% machine (in *.SP file) and generate a version without the pulses. It
```

```
% reconstructs the abs spectrum of the photogenerated state.
%******************* The import sequence ******************************
% % A=importdata('O2 free cycle 1.TD','\t',86);
% % data=A.data;
% % X=data(:,1);
% % Y=data(:,2);
% % plot(X,Y)
% % W=reconstruct_LED(X,Y)
%*********************************************************************
lv=Y<-0.05;          % Search for the LED signal and assigns a logic
value
lv = ~lv;            % Changes false for true
%*********************************************************************
work_data2(:,1)=X(lv);
work_data2(:,2)=Y(lv);
[y_max_step,x_max_step]=findpeaks(Y(lv));
noLEDfull(:,2)=interp1(work_data2(x_max_step,1),y_max_step,X(:,1),'spl
ine');
noLEDfull(:,1)= X(:,1);
figure(2)
hold on
plot(X,Y,'g-');
plot(work_data2(x_max_step),y_max_step)
plot(X(:,1),noLEDfull(:,2),'.r-');
hold off
end
```

A4.3 Generation of time-lapse UV-vis absorbance at a single wavelength over photoswitching cycles (without or with photochemical reversion using a different wavelength)

```
function[] = LED_Blue_Red_P
instrumentObjects=instrfind;
delete(instrumentObjects);
clear all;
prompt={'Enter first pulse length','Enter first interval','Enter pulse
length','Enter interval','Number of cycles (red)','Number of cycles
(Both)'};
dlg_title = 'LED control';
num_lines = 1;
defaultans = {'1000','500','300','300','10','3'};
answer = inputdlg(prompt,dlg_title,num_lines,defaultans);
blue_pulse=answer(1,1)
blue_interval=answer(2,1)
red_pulse=answer(3,1)
red_interval=answer(4,1)
red_cycle=answer(5,1)
num=cellfun(@str2num,answer)
total_cycles=num(6)                 % to have a number for the cycles
interblue = num2str(num(2))     %num2str(num(2)+ num(3) + num(4))
interred = num2str(num(4))      %num2str(num(4)+ num(1) + num(2))
param_blue={'1,1,',',',',',0,0,1,0,0,1@'}
param_red={',1,',',',',0,0,1,0,0,1@'}
string_blue                                                          =
[strcat(param_blue{1},blue_pulse{1},param_blue{2},interblue,param_blue
{3})]
```

```
string_red                                                       =
[strcat(answer{5,1},param_red{1},answer{3,1},param_red{2},answer{4,1},
param_red{3})]
s1=serial('COM3')
set(s1,'baudrate',57600)
fopen(s1)
s2=serial('COM4')
set(s2,'baudrate',57600)
fopen(s2)
pause(2)
for n = 1:total_cycles,
    fprintf(s1,'%s\n',string_blue)
    pause((num(1)+num(2))/1000)
    fprintf(s2,'%s\n',string_red)
    pause(((num(1)+num(2)+((num(3)+num(4))*num(5))))/1000)
end
fclose(s1)
fclose(s2)
instrumentObjects=instrfind;
delete(instrumentObjects);
clear all;
end
```

A4.4 Reconstruction of time-lapse absorbance acquired from A4.3

```
function [time_drive_wo_RED,cycles] = fatigue_red(RED_time_drive)
% photochemical ring closure.
% This function is supposed to take the fatigue graph from the UV-vis
% machine (in *.TD file) and a) create an array "cycles array", which
% contains the separated cycles of fatigue, and b) creates a matrix with
% the indexes, start and end points (exact and consider to cut), and the
% max and min per cycle.
% RED VERSION
%****************** The import sequence ******************************
% % A=importdata('O2 free cycle 1.TD','\t',87);
% % data=A.data;
% % X=-data(:,1);
% % Y=data(:,2);
% % plot(X,Y)
% % [W,X]=fatigue_red(the-data-matrix)
%*********************************************************************
% Y(Y<-0.01)=-0.0000531;                                            %
assigns the -0.0000531 value to all the negatives (LED pulse)
[Z_y,Z_x]=findpeaks(RED_time_drive(:,2));
time_drive_wo_RED(:,1) = RED_time_drive(Z_x,1);
time_drive_wo_RED(:,2) = Z_y;
last_x                                                              =
find(time_drive_wo_RED(:,1)==max(time_drive_wo_RED(:,1)));          %
finds the index of the last row
time_drive_wo_RED(time_drive_wo_RED(:,2)<-0.01,2)=-
0.0000531;                   % assigns the -0.0000531 value to all the
negatives (LED pulse)
last_n=10;                                                          %
it just assigns a starting value; can be used to skip a certain start
noise (only for the MAX and MIN).
cycle_number=1;
for n=1:last_x,                                                     %
for all the data
    if time_drive_wo_RED(n,2)==-0.0000531,
```

```
        if n > last_n,                                                %
check if it's part of the last segment
            i=1;
            while time_drive_wo_RED(n+i,2)==-0.0000531,
                i=i+1;
            end
            cycles(cycle_number,1) = cycle_number;
            cycles(cycle_number,2) = n;                               %
the start value
            cycles(cycle_number,3) = n+i;                             %
the last value of the series
            last_n=n+i;
            cycle_number=cycle_number + 1;
        end
    else
    end
end
for n=1:max(cycles(:,1))-1,                                           %
Finds the index for the actual decay
    cycles(n,4) = cycles(n,3);
    cycles(n,5) = cycles(n+1,2);
end
cycles(n+1,4) = cycles(n+1,3);                                        %
Last one is longer
cycles(n+1,5) = last_x;
for n=1:max(cycles(:,1)),                                             %
Assign the Y values
    cycles(n,6) = max(time_drive_wo_RED(cycles(n,4)+1:cycles(n,5)-5,2));
    cycles(n,7) = min(time_drive_wo_RED(cycles(n,4)+1:cycles(n,5)-5,2));
end
figure(21)
hold on
plot(time_drive_wo_RED(:,1),time_drive_wo_RED(:,2),'.g-')
plot(RED_time_drive(:,1),RED_time_drive(:,2),'b-')
end
```

A4.5 Generation of UV-vis absorbance data at a single wavelength for calculation of quantum yields of ring opening reactions

```
function[] = LED_blue_JO
instrumentObjects=instrfind;
delete(instrumentObjects);
clear all;
prompt={'Enter pulse length','Enter interval'};
dlg_title = 'Blue LED control';
num_lines = 1;
defaultans = {'200','300'};
answer = inputdlg(prompt,dlg_title,num_lines,defaultans);
a=answer(1,1)
b=answer(2,1)
param={'1,1,',',',',0,0,1,0,0,1@'}
% num=cellfun(@str2num,answer)
% a=num(1)
% b=num(2)
% c=a+b
times                                                                 =
{'100','250','500','750','1000','1500','2000','2500','3000','3500','40
00','5000','6000','7000','8000','9000','10000','12500','15000','20000'}
```

```
%string = [strcat(param{1},times{n},param{2},b{1},param{3})]
s1=serial('COM4')
set(s1,'baudrate',57600)
fopen(s1)
pause(2)
%fprintf(s1,'10,1,a,b,0,0,1,0,0,1@')
%pause(200)
for n = 1:20,
    string = [strcat(param{1},times{n},param{2},b{1},param{3})]
    fprintf(s1,'%s\n',string)
    pause(450)
end
    fclose(s1)
%
instrumentObjects=instrfind;
delete(instrumentObjects);
clear all;
end
```

A4.6 Reconstruction of data acquired from A4.5 for calculations of quantum yields of ring opening reactions

```
function [cycles] = fatigue_Ptype(X,Y)
%******************* The import sequence ******************************
% % A=importdata('O2 free cycle 1.TD','\t',87);
% % data=A.data;
% % X=-data(:,1);
% % Y=data(:,2);
% % plot(X,Y)
% % W=fatigue(X,Y)
%**********************************************************************
Y(Y<-0.01)=-0.0000531;            % assigns the -0.0000531 value to all
the negatives (LED pulse)
last_x = find(X==max(X));          % finds the index of the last row
for n=1:last_x-5000,
    if Y(n)==-0.0000531,
        Y(n-1)=-0.0000531;
    end
end
last_n=10;
cycle_number=1;
blue = true;                                 % blue LED comes first
for n=1:last_x-5000,                             % for all the data
    if Y(n)==-0.0000531,
        if n > last_n,                       % check if it's part of the
last segment
            if blue == true,
                i=1;
                while Y(n+i)==-0.0000531,
                    i=i+1;
                end
                cycles(cycle_number,1) = cycle_number;
                cycles(cycle_number,2) = n;      % the start value (for
the blue pulse)
                cycles(cycle_number,3) = n+i;   % the last value of the
series (for the blue pulse)
                last_n=n+i;
                blue=false
            else
```

```
                i=1;
                while Y(n+i)==-0.0000531,
                    i=i+1;
                end
                cycles(cycle_number,4) = n;     % the start value (for
the red pulse)
                cycles(cycle_number,5) = n+i;   % the last value of the
series (for the red pulse)
                last_n=n+i;
                cycle_number=cycle_number + 1;
                blue=true
            end
        end
    else
    end
end
for n=1:max(cycles(:,1))-1,                    % Find the index for the
actual absorption plateaux
    cycles(n,6) = cycles(n,3);
    cycles(n,7) = cycles(n,4);
    cycles(n,8) = cycles(n,5);
    cycles(n,9) = cycles(n+1,2);
end
% cycles(n+1,4) = cycles(n+1,3);               % Last one is longer
% cycles(n+1,5) = last_x;
for n=1:max(cycles(:,1)),                  % Find the values of the max
and min of the cycles (means)
%    cycles(n,10) = mean(Y(cycles(n,6)+3:cycles(n,7)-3));
    cycles(n,10) = Y(cycles(n,6)+2);
    cycles(n,11) = mean(Y(cycles(n,8)+3:cycles(n,9)-3));
end
```

A4.7 Generation of UV-vis absorbance data at a single wavelength for calculation of quantum yields of ring closure reactions

```
function[] = LED_Blue_Red_P_CTR2
instrumentObjects=instrfind;
delete(instrumentObjects);
clear all;
% prompt={'Enter first pulse length','Enter first interval','Enter pulse
length','Enter interval','Number of cycles (red)','Number of cycles
(Both)'};
% dlg_title = 'LED control';
% num_lines = 1;
% defaultans = {'1000','500','300','300','10','3'};
% answer = inputdlg(prompt,dlg_title,num_lines,defaultans);
answer={'2500';'500';'50';'500';'1';'1'};  % Considering ca. 400 s
relaxation time
blue_pulse=answer(1,1)
blue_interval=answer(2,1)
red_pulse=answer(3,1)
red_interval=answer(4,1)
red_cycle=answer(5,1)
num=cellfun(@str2num,answer)
total_cycles=num(6)                  % to have a number for the cycles
interblue = num2str(num(2))     %num2str(num(2)+ num(3) + num(4))
interred = num2str(num(4))      %num2str(num(4)+ num(1) + num(2))
```

```
param_blue={'1,1,',',',',',0,0,1,0,0,1@'}
param_red={',1,',',',',',0,0,1,0,0,1@'}
%times                                                               =
{'100','150','200','300','400';'500','455','416','385','335','280'}
times                                                                =
{'1','100','250','500','750','1000';'1499','1400','1250','1000','750',
'500'} %(pulse lenght and interval; total time of 1500 ms)
%string_blue                                                         =
[strcat(param_blue{1},blue_pulse{1},param_blue{2},interblue,param_blue
{3})]
%string_red
=[strcat(answer{5,1},param_red{1},answer{3,1},param_red{2},answer{4,1}
,param_red{3})]
s1=serial('COM4')
set(s1,'baudrate',57600)
fopen(s1)
s2=serial('COM3')
set(s2,'baudrate',57600)
fopen(s2)
pause(2)
for repeat_No = 1:3,
    repeat_No
times                                                                =
{'1','100','250','500','750','1000','2000','5000';'1499','1400','1250'
,'1000','750','500','1','1'} %(pulse lenght and interval; total time of
1500 ms)
for n = 1:8,
    string_blue                                                      =
[strcat(param_blue{1},blue_pulse{1},param_blue{2},interblue,param_blue
{3})]
    string_red                                                       =
[strcat(answer{5,1},param_red{1},times{1,n},param_red{2},times{2,n},pa
ram_red{3})]
for n = 1:total_cycles,
    fprintf(s1,'%s\n',string_blue)
    pause((num(1)+num(2))/1000)
    fprintf(s2,'%s\n',string_red)
    pause(450);
%     pause(((num(1)+num(2)+((num(3)+num(4))*num(5))))/1000)
end
end
end
fclose(s1)
fclose(s2)
%
instrumentObjects=instrfind;
delete(instrumentObjects);
clear all;
end
```

A4.8 Reconstruction of data acquired from A4.7 for calculations of quantum yields of ring closure reactions

```
function [cycles,data_sorted,data_BL,values] = QY_Ttype2(X,Y)
% QY for ring closure of a T type.
% Initial slope for the Quantum yield of ring closure in T-type
% photochromes. This one works for a 3x5 measurements, other than the
% baseline.
% This function is supposed to take the fatigue graph from the UV-vis
```

```
% machine (in *.TD file) and a) create an array "cycles array", which
% contains the separated cycles of fatigue, and b) creates a matrix with
% the indexes, start and end points (exact and consider to cut), and the
% max and min per cycle.
%******************* The import sequence ******************************
% % A=importdata('O2 free cycle 1.TD','\t',87);
% % data=A.data;
% % X=data(:,1);
% % Y=data(:,2);
% % plot(X,Y)
% % W=fatigue(X,Y)
%*********************************************************************
Y(Y<-0.01)=-0.0000531;            % assigns the -0.0000531 value to all
the negatives (LED pulse)
last_x = find(X==max(X));          % finds the index of the last row
for n=1:last_x-5000,
    if Y(n)==-0.0000531,
        Y(n-1)=-0.0000531;
    end
end
last_n=10;
cycle_number=1;
%blue = true;                                 % blue LED comes first
for n=1:last_x-5000,                             % for all the data
    if Y(n)==-0.0000531,
        if n > last_n,                      % check if it's part of the
last segment
                i=1;
                while Y(n+i)==-0.0000531,
                    i=i+1;
                end
                if Y(n+i+5) > 0.6                    % There are extra
negative values so to prevent counting double.
                cycles(cycle_number,1) = cycle_number;
                cycles(cycle_number,2) = n;     % the start value (for
the blue pulse)
                cycles(cycle_number,3) = n+i;   % the last value of the
series (for the blue pulse)
                last_n=n+i;
                cycle_number=cycle_number + 1;
                else
                end
%                 i=1;
%                 while Y(n+i)==-0.0000531,
%                     i=i+1;
%                 end
%                cycles(cycle_number,4) = n;     % the start value (for
the red pulse)
%                  cycles(cycle_number,5) = n+i;   % the last value of
the series (for the red pulse)
%                 last_n=n+i;
%                 cycle_number=cycle_number + 1;
%                 blue=true
         end
    else
    end
end

% %
% % Now we need to separate the different decays
% %
```

```
data_sorted(:,1)= X(1:4000);
    for n=2:cycle_number,
        data_sorted(:,n)= Y(cycles(n-1,3)+3:cycles(n-1,3)+4002);
    end
% %
% % Substract the "blanc" (cycles 1,7,13)
% %
    for n = 3:9,
    data_BL(:,n-1) = data_sorted(:,n) - data_sorted(:,2);
    end

%     for n = 9:13,
%     data_BL(:,n-2) = data_sorted(:,n) - data_sorted(:,8);
%     end
%
%     for n = 15:19,
%     data_BL(:,n-3) = data_sorted(:,n) - data_sorted(:,14);
%     end
% %
% % Now sweep the whole and fin places where it goes straight up, then
take
% the 4 values that follow and get a mean. Change the sing (because we
% assume that everything that disapears is transformed to the SP form)
% %
numbr = size(data_BL,2)

    for i = 2:numbr,
        for n=10:4000,
            if     (data_BL(n,i)     >     (data_BL(n-1,i)+0.05))     &&
~(data_BL(n+1,i) > (data_BL(n,i)+0.05))

[data_BL(n+1,i),data_BL(n+2,i),data_BL(n+3,i),data_BL(n+4,i)]
                values(i-1,1)                    =                    -
mean([data_BL(n+1,i),data_BL(n+2,i),data_BL(n+3,i),data_BL(n+4,i)])
            else
            end
        end
    end

% for n=1:max(cycles(:,1))-1,                  % Find the index for the
actual absorption plateaux
%     cycles(n,6) = cycles(n,3);
%     cycles(n,7) = cycles(n,4);
%     cycles(n,8) = cycles(n,5);
%     cycles(n,9) = cycles(n+1,2);
% end

% cycles(n+1,4) = cycles(n+1,3);              % Last one is longer
% cycles(n+1,5) = last_x;
%for n=1:max(cycles(:,1)),                 % Find the values of the max
and min of the cycles (means)
%    cycles(n,10) = mean(Y(cycles(n,6)+3:cycles(n,7)-3));
%    cycles(n,10) = Y(cycles(n,6)+2);
%    cycles(n,11) = mean(Y(cycles(n,8)+3:cycles(n,9)-3));
%end
end
```